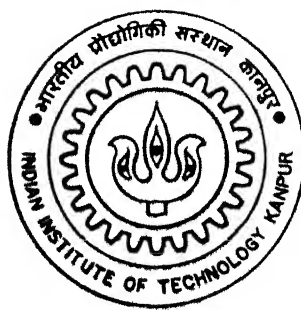


91/0964

# MÖSSBAUER SPECTROSCOPIC STUDIES OF SOME IRON-BASED ALLOYS, METALLIC GLASSES AND MINERALS

by

**DEBASHIS BANDYOPADHYAY**



DEPARTMENT OF PHYSICS

**INDIAN INSTITUTE OF TECHNOLOGY KANPUR**

May, 1996

MÖSSBAUER SPECTROSCOPIC STUDIES OF SOME IRON-BASED  
ALLOYS, METALLIC GLASSES AND MINERALS

*A Thesis Submitted in  
Partial Fulfilment of the Requirements  
for the Degree of  
DOCTOR OF PHILOSOPHY*

*by*  
**DEBASHIS BANDYOPADHYAY**

*to the*  
**DEPARTMENT OF PHYSICS**  
**INDIAN INSTITUTE OF TECHNOLOGY KANPUR**

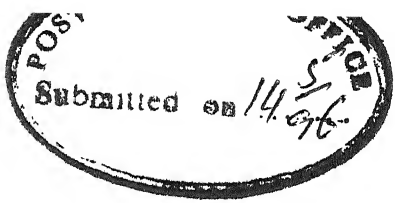
May, 1996

- 5 AUG 1997

CENTRAL LIBRARY  
I.I.T., KANPUR

No. A 123637

PHY-1896-D-BAN-MGS



## C E R T I F I C A T E

It is certified that the work contained in the thesis entitled "**MÖSSBAUER SPECTROSCOPIC STUDIES OF SOME IRON-BASED ALLOYS, METALLIC GLASSES AND MINERALS**" by **Debashis Bandyopadhyay** has been carried out under my supervision. This work has not been submitted elsewhere for a degree.

Ran Singru

( R. M. Singru )  
Professor

Department of Physics  
I I T Kanpur, INDIA

May, 1996

*dedicated to ....*

*my parents*

*EJ*

*those from whom I have learnt*

---

## A C K N O W L E D G E M E N T S

At the outset, I would like to express my profound gratitude to Professor R.M.Singru for his able guidance and continuous encouragement extended to me at all phases of my work. He had nurtured scientific outlook and provided the much needed impetus during many crucial stages of this work. His constant endeavour in tackling the problem on all fronts and understanding involvement in the minutest of the details have given this thesis the present form. I am indebted to him for the help rendered to me. I thank him for his keen interest shown in guiding me.

I am grateful to Professor D.C.Khan for extending the cooperation and the permission to use his laboratory form time to time. I am thankful to Professor A.K.Majumdar and Professor V.N.Kulkarni for providing me with samples and spending their most valuable time in discussing with me. I wish to thank Professor Y.R.Waghmare and Dr. H.C.Verma for their constant encouragement and moral support rendered to me.

I take this opportunity to thank Professor A.K.Biswas, Professor S.Bhargava and Professor G.S.Upadhyay of Materials and Metallurgical Engineering Dept., IITK, for providing me with samples and the interest shown at different stages of this work.

I express my sincere thanks to Sandeep Singh, Satyam Suwas, Gautam Sinha, Dr. U.C.Johri, Dr. Nobin Banerjee and Bidyut Halder for their timely help for execution of this work and Professor Le Caer, Dr. Paulose and Mr. Manas Maity for providing me with programme.

I am indebted to Dr. Debashis Ghosh of VECC, Calcutta and Mr. Amiya Kanti Das for their moral support provided to me.

Special thanks to Guptaji, Masoodji, Anilji and Srivprakashji for their workmanship and prompt assistance whenever I was in need.

Thanks are to Mr. Panda, Mr. Laloo Singh and Mr. A.K.Srivastava of Physics Department and Mr. Ram Singh and Mr. Bahadur Singh of the Physics workshop for their whole-hearted co-operation at various stages.

I would also like to thank the Central Library staff for

their all time smiling faces and co-operation.

I thank Mr. A.K.Ganguly for his help in many important drawings.

Thanks are also due to Arun Kumar Saha for taking some important printout from time to time.

I cherish the company of my C-TOP/V family members Tapan, Manoj, Sumanta, Bhargab, Ani, Sibu, Rahul, Sanku, Sankar-da, Mouli and Prasenjit for their friendship, love and unbelievable patience to listen to my smoky thoughts. Especially I would like to take this opportunity to thank Tapo for his brotherly presence at all good and bad stages of my stay at IIT, Kanpur.

I thank Pradip for helping me from different sides.

I would like to acknowledge the homely environment provided by all of my friends like Swapan, Tapan, Abir, Giri, Sujay, Shantilal, Dinu, Dobal, Deepak, Prabal, Alok, Gupte, Nayak, Gopal, Bachha, Nilu, Saurabh, Indra, Jethu, Susanta, Naru-da, Saurabh, Kaushik, Indra and Amrita.

Special thanks to Debashis, Sangita, Subit and Supriti for some joyful "adda" at boring moments.

I thank Mrs. and Mr. N.S.Samanta and my loving Anushree and Antara for presenting me a lot of beautiful evenings full of tea, "adda" and the flavour of the touch of a family which I badly needed during my total course of study at IIT, Kanpur.

I want to acknowledge my 'Mach-1' for its all time service rendered to me and making it possible for me to have very frequent connection with the surrounding nature.

"Kudos" to my "Sona-Ta" for her nothing is enough from my side.

At last but not the last, I would like to acknowledge my grandmother, parents, uncles, 'Bole', Boro-ma, dadas, didis, boudis and my loving brother Subhasish and younger sister Mitan along with Gopa, Babai, Bhuto, Mam, Bubun, Bhonda, Babu, Vamu, Nilika and Soma i - without whose constant inspiration and patience, I might not becoming whatever I am.

## SYNOPSIS

Name of Student: DEBASHIS BANDYOPADHYAY Roll No : 9110964

Degree for which submitted: Ph.D. Department: PHYSICS

Thesis Title: **MÖSSBAUER SPECTROSCOPIC STUDIES OF SOME IRON-BASED ALLOYS, METALLIC GLASSES AND MINERALS**

Name(s) of thesis supervisor(s) : Professor R. M. Singru

Month and Year of thesis submission: May, 1996

In 1957-58 R.L.Mössbauer discovered the phenomenon of recoilless absorption or emission of nuclear gamma rays. It was soon recognised that owing to the sharpness of the resonance the Mössbauer effect in solids provides a sensitive method to study the interactions of atomic nucleus with surrounding atoms. In particular, the use of  $^{57}\text{Fe}$  as the Mössbauer nucleus opened a door to a vast area of problems in physical metallurgy, materials science and geochemistry because there exist so many compounds, alloys, materials and minerals containing iron. As a result  $^{57}\text{Fe}$  Mössbauer spectroscopy has been used during the last two decades as a sensitive and useful method to study electric, magnetic, structural and phase identification studies of different materials having basic scientific and applied technological interest. In particular valuable information has been obtained about the binary and ternary alloys of iron, steels, iron-containing metallic glasses and iron-based minerals using  $^{57}\text{Fe}$  Mössbauer spectroscopy. The hyperfine interactions in these materials manifest itself through the Mössbauer parameters like isomer shift, electric

quadrupole moment, hyperfine magnetic field, the distribution of hyperfine fields, the width and area under the resonance lineshape etc. These Mössbauer parameters can be determined from the measured Mössbauer spectra and their systematic analysis provides valuable information which when combined with the results obtained by other characterization techniques (e.g. X-ray diffraction, magnetic measurements, differential thermal analysis etc.) can lead us to a better understanding of the electronic structure of these systems. In the present thesis we have described our  $^{57}\text{Fe}$  Mössbauer spectroscopic studies of  $\text{Fe}_{80-x}\text{Ni}_x\text{Cr}_{20}$  alloys, Fe-24 at% Al and Fe-25 at% Al alloys, Fe + 0.6 % C + 0-2 % Cr(or Mn) steels,  $\text{Fe}_{79}\text{B}_{16}\text{Si}_5$  and  $\text{Fe}_{78}\text{B}_{13}\text{Si}_9$  metallic glasses and chalcopyrite mineral. Wherever possible the results of Mössbauer spectroscopic studies have been combined with the results of other techniques like X-ray diffraction, magnetic measurements etc. to obtain a clear picture of the properties of these materials.

The present thesis is divided into seven chapters. The first chapter provides a brief introduction to the phenomenon of Mössbauer effect. The experimental methods used in the present work are described in the second chapter which also contains a description of the Mössbauer spectrometer and methods of data analysis.

In Chapter 3 we have presented our Mössbauer spectroscopic studies of the substitutionally disordered, isostructural (fcc structure)  $\gamma\text{-Fe}_{80-x}\text{Ni}_x\text{Cr}_{20}$  ( $x = 30, 26, 19, 14$ ) stainless steel alloys in the temperature range  $T = 295 - 10$  K. These alloys have several useful properties e.g. high corrosion resistance,

non-toxic, non-magnetic, creep resistance etc and therefore have many potential industrial applications. Depending on the value of  $x$  and the temperature  $T$ , these alloys exhibit paramagnetic, ferromagnetic, antiferromagnetic and spin-glass phases and provide an example of mixed or re-entrant phase alloys. Other workers have carried out detailed neutron scattering, neutron diffraction, resistivity and magnetostriction measurements, specific heat studies and magnetic measurements. However systematic  $^{57}\text{Fe}$  Mössbauer studies have not been reported for the  $\text{Fe}_{80-x}\text{Ni}_x\text{Cr}_{20}$  alloys. Our studies have provided interesting results for the evolution of Mössbauer linewidth, centre-shift, distribution of hyperfine field,  $P(H)$ , and the average hyperfine field  $\langle H \rangle$  with temperature. These results are interpreted in terms of different magnetic transitions. The observed data for the second order Doppler shift have been analyzed to obtain the Debye temperature  $\Theta_D$  for the  $x = 30$  and  $x = 26$  alloys.

Another class of Fe- alloys studied by us belong to the Fe-Al system which forms a model object of transition metal-sp element system. These studies are described in Chapter 4. Fe-Al alloys having 21 - 31 at % Al are known to exhibit several attractive physical properties which render them candidate materials for structural and magnetic applications. These alloys possess high strength, low density, extremely good corrosion and oxidation resistance which make them suitable materials for structural applications while their magnetic properties (high permeability and large magnetostriction) render them useful for technological applications. These magnetic and physical properties can be varied

by altering the composition and the process) and rate of cooling and quenching. Keeping this in mind we have studied Mössbauer spectra of five Fe-24 at% Al and Fe-25 at% Al alloy sample processed via different cooling/quenching routes. The analysis of the Mössbauer parameters, distribution of hyperfine magnetic fields, P(H) and H-values have helped us to identify various Fe-atom configurations (nearest neighbour or next nearest neighbour) responsible for different phases formed in these different processing routes. Our results also indicate that the average hyperfine field  $\langle H \rangle$  depends on the average rate of cooling followed during the precipitation of these phases.

In Chapter 5 we have described our investigations of the effect of addition of 0.5 - 2.0 mass percent of Cr or Mn to Fe + 0.6% C steels using  $^{57}\text{Fe}$  Mössbauer spectroscopy and magnetic measurements. These low alloy steels containing refractory carbides belonging to the transition metals of group IV-VI of the periodic table have useful industrial applications. The analysis of present Mössbauer spectroscopic data indicate the presence of  $\alpha\text{-Fe}$ , 1nn (nearest neighbour) and 2nn phases in the Fe-C-Cr steels and that of  $\alpha\text{-Fe}$  and 1nn phases in the Fe-C-Mn steels. These results provide interesting information about the magnetic disturbance around the solute atoms in these low alloy steels. The present magnetic measurements showed that the variation of saturation magnetic moments of Fe atoms under the external magnetic field in Fe-C-Cr and Fe-C-Mn steels show opposite but systematic behaviour.

Our Mössbauer spectroscopic studies of the metallic glasses

$\text{Fe}_{79}\text{B}_{16}\text{Si}_5$  and  $\text{Fe}_{78}\text{B}_{13}\text{Si}_9$  are presented in Chapter 6. The aim of the present study was to investigate the evolution of the hyperfine magnetic field distribution,  $P(H)$ , with the annealing temperature ( $T_a$ ) and annealing time period ( $t_a$ ) before these amorphous alloys crystallize. Keeping this aim in mind we chose  $T_a = 300, 350, 400, 450$  and  $475\text{ K}$  and  $t_a = 1 - 37\text{ h}$  (depending on  $T_a$ ). The present studies have demonstrated how the  $P(H)$  in these metallic glasses follow the kinetics of crystallization and how the time period of isothermal annealing plays an important role in the evolution of these  $P(H)$  distributions.

The last chapter describes the present studies of the kinetics of the roasting process of chalcopyrite minerals using Mössbauer spectroscopy and X-ray diffraction. Chalcopyrite minerals were roasted at  $(500 \pm 5)^\circ\text{C}$  for time intervals  $t = 1.0, 2.0, 3.0, 5.0, 10.0, 15.0, 20.0, 40.0$  and  $60.0\text{ mins}$  and at  $(650 \pm 5)^\circ\text{C}$  for time intervals  $t = 1.0, 2.5, 3.0, 5.0$  and  $10.0\text{ mins}$ . The observed Mössbauer parameters and the X-ray diffraction data have been analyzed to identify the iron compounds formed at different stages of roasting. A possible scheme of transformations has been suggested to explain the observed kinetics.

It is hoped that these measurements carried out in the Fe-Ni-Cr alloys, Fe-Al alloys, low alloy steels, Fe-B-Si metallic glasses and chalcopyrite mineral have helped to extend our present understanding of these systems.

## CONTENTS

|   | Page No.   |
|---|------------|
| LIST OF FIGURES   | <b>xv</b>  |
| LIST OF TABLES  | <b>xxv</b> |
| <br>  |            |
| <b>CHAPTER 1 :      Introduction</b>                                | <b>1</b>   |
| 1.1.      Preamble  | 1          |
| 1.2.      Mössbauer effect  | 1          |
| 1.3.      Recoil-free fraction                                      | 5          |
| 1.4.      Hyperfine interactions                                    | 8          |
| 1.4.1.      Isomer shift  | 11         |
| 1.4.2.      Quadrupole splitting                                    | 20         |
| 1.4.3.      Magnetic hyperfine interaction                          | 22         |
| 1.5.      Scope of the present work                                 | 25         |
| References  | 30         |
| <br>  |            |
| <b>CHAPTER 2 :      Experimental methods and data analysis</b>      | <b>31</b>  |
| 2.1.      Introduction  | 31         |
| 2.2.      Radioactive source  | 31         |
| 2.3.      Mössbauer spectrometer                                    | 33         |
| 2.4.      Gamma-ray detection system                                | 34         |
| 2.5.      The multichannel analyzer: Data acquisition system        | 35         |
| 2.6.      Performance and calibration of the Mössbauer spectrometer | 37         |
| 2.7.      Data analysis   | 39         |

|                    |   |           |
|--------------------|---|-----------|
| 2.7.1.             | Determination of Mössbauer parameters   | 39        |
| 2.7.2.             | Determination of hyperfine field distribution, P(H)   | 42        |
| 2.8.               | Other measurements  | 45        |
|                    | References  | 48        |
| <b>CHAPTER 3 :</b> | <b>Magnetic phase transition study of Fe<sub>80-x</sub>Ni<sub>x</sub>Cr<sub>20</sub> ternary alloy system</b> | <b>50</b> |
| 3.1.               | Introduction  | 50        |
| 3.2.               | Experimental  | 54        |
| 3.3.               | Results and discussions   | 58        |
| 3.3.1.             | Introduction  | 58        |
| 3.3.2.             | Alloy with x = 30.  | 58        |
| 3.3.3.             | Alloy with x = 26   | 73        |
| 3.3.4.             | Alloy with x = 19.  | 79        |
| 3.3.5.             | Alloy with x = 14.  | 84        |
| 3.4.               | Summary and conclusions   | 86        |
|                    | References  | 87        |
| <b>CHAPTER 4 :</b> | <b>Mössbauer spectroscopic study of heat-treated and control-cooled Fe - 24 at% Al and Fe - 25 at% Al</b>     | <b>89</b> |
| 4.1.               | Introduction  | 89        |
| 4.2.               | Experimental procedure  | 99        |
| 4.3.               | Results and discussion  | 102       |
| 4.3.1.             | Analysis using least-squares - fitting to the Mössbauer spectra.  | 102       |

|             |  |     |
|-------------|--|-----|
| 4.3.1.1.    | Introduction   | 102 |
| 4.3.1.2.    | Sample AA1; Fe-24 at% Al processed by route 1.   | 115 |
| 4.3.1.3.    | AA2 to AA4 samples: Fe-24 at% Al processed by routes 2, 3 and 4.   | 116 |
| 4.3.1.4.    | AA5 sample: Fe-25 at% Al processed by route 5.   | 116 |
| 4.4.        | Summary and conclusions  | 121 |
|             | References   | 123 |
| CHAPTER 5 : | Mössbauer spectroscopic study of low alloy steels containing Chromium or Manganese   | 125 |
| 5.1.        | Introduction   | 125 |
| 5.2.        | Experimental procedure   | 128 |
| 5.3.        | Results and discussion   | 129 |
| 5.3.1.      | Mössbauer spectroscopic studies  | 129 |
| 5.4.        | Conclusions  | 141 |
|             | References   | 142 |
| CHAPTER 6 : | Study of hyperfine field distributions in $\text{Fe}_{79}\text{B}_{16}\text{Si}_5$ and $\text{Fe}_{78}\text{B}_{13}\text{Si}_9$ metallic glasses | 144 |
| 6.1.        | Introduction   | 144 |
| 6.2.        | Experimental procedure and data analysis   | 150 |
| 6.3.        | Results and discussion   | 153 |
| 6.3.1.      | Study of as-received samples of  | 153 |

|                    |  |            |
|--------------------|--|------------|
|                    | Si <sub>5</sub> and Si <sub>9</sub>  |            |
| 6.3.2.             | Study of heat-treated samples  | 155        |
| 6.3.2.1.           | Fe <sub>79</sub> B <sub>16</sub> Si <sub>5</sub> (or Si <sub>5</sub> )   | 155        |
| 6.3.2.2.           | Fe <sub>78</sub> B <sub>13</sub> Si <sub>9</sub> (or Si <sub>9</sub> )   | 173        |
| 6.4.               | Conclusions  | 186        |
|                    | References   | 188        |
| <b>CHAPTER 7 :</b> | <b>Study of the roasting of chalcopyrite minerals by Mössbauer spectroscopy</b>  | <b>191</b> |
| 7.1.               | Introduction   | 191        |
| 7.2.               | Experiment   | 193        |
| 7.3.               | Results and discussion   | 194        |
| 7.3.1.             | As - received sample   | 194        |
| 7.3.2.             | Samples roasted at (500 ± 5)°C<br>for different time intervals t<br>= 1.0, 2.0, 3.0, 5.0, 10.0,<br>15.0, 20.0, 40.0 and 60.0 mins. | 199        |
| 7.3.3.             | Samples roasted at (650 ± 5)°C<br>for t = 1.0, 2.5, 3.0, 5.0 and<br>10.0 min.  | 203        |
| 7.4.               | Conclusions  | 207        |
|                    | References   | 208        |

## LIST OF FIGURES

Page No.

- Fig.1.1.** (a) Intensity  $I(E)$  of spectral line as a function of transition energy  $E_{\gamma}$ . (b) Nucleus receiving recoil energy  $E_R$  during the emission of photon. (c) The schematic nuclear energy level diagram of emission and absorption. 2
- Fig.1.2.** Overlap of the emission and absorption lines showing the relation between  $E_{\gamma}$ ,  $E'_{\gamma}$ ,  $E''_{\gamma}$  for two cases: (a) optical case  $E_R \ll \Gamma$  and (b) nuclear case  $E_R \gg \Gamma$ . The energy scales are shown only schematically and not realistically. 4
- Fig.1.3.** (a) Effect of monopole interaction on the energy levels of source and absorber nuclei. (b) Mössbauer spectrum showing monopole interaction. 12
- Fig.1.4.** Review of isomer shift data of iron in various ionisation state [13]. 16
- Fig.1.5.** Review of  $^{57}\text{Fe}$  Mössbauer parameters (a) IS (isomer shift) and (b) QS (quadrupole splitting) for iron plotted against the coordination number for ionic high spin and low spin compounds and minerals. Arrows indicate that the values outside the range of boxes have been observed. 17

- Fig.1.6.** Data for the  $^{57}\text{Fe}$  isomer shift with respect to natural iron ( $\alpha\text{-Fe}$ ) at room temperature. Units of the IS values are  $\text{mms}^{-1}$  and signs of the velocity for the source are to be read from the bottom row while the signs of velocity for the absorber are to be read from the top row. 19
- Fig.1.7.** Effect of the quadrupole interaction on the nuclear energy levels of source / absorber and the resulting Mössbauer spectrum showing the quadrupole splitting and isomer shift. 21
- Fig.1.8.** Effect of quadrupole interaction and a strong magnetic interaction on the energy levels of  $^{57}\text{Fe}$ . The number 1 to 6 indicating the line positions in the Mössbauer spectrum. 24
- Fig.2.1.** Schematic block diagram of Mössbauer spectrometer. 32
- Fig.2.2.** Pulse height spectrum of  $^{57}\text{Co}$  in Rh matrix (Mössbauer source) measured using proportional counter. 36
- Fig.2.3.** Hyperfine field distribution,  $P(H)$ , for natural iron (absorber) at room temperature, (b) corresponding Mössbauer spectrum. Dots are experimental data points and continuous line shows the fit. 44
- Fig.2.4.** Variation of (a)  $\langle H \rangle$  and (b)  $\chi^2$  with N (number of cosine terms) for  $\text{Fe}_{78}\text{B}_{13}\text{Si}_9$  metallic glass sample in as-received condition. 46

|                 |   |    |
|-----------------|---|----|
| <b>Fig.2.5.</b> | Variation of $\chi^2$ -with N (number of cosine terms) for $Fe_{79}B_{16}Si_5$ metallic glass sample annealed at 748 K for 8h.  | 47 |
| <b>Fig.3.1.</b> | Ternary diagram of FeNiCr system showing crystallographic and magnetic phases. The dotted-dashed line separates the $\gamma$ phase from $\alpha$ , $\delta$ and $\sigma$ phases at room temperature. The solid line for $T_C = 0$ separates the ferromagnetic (FM) phases from the paramagnetic (P) one [taken from ref.3]. | 53 |
| <b>Fig.3.2.</b> | Temperature (T) vs Ni concentration (x in units of at. %) magnetic phase diagram of $Fe_{80-x}Ni_xCr_{20}$ alloys ( $10 \leq x \leq 30$ ) [Taken from Ref.3].   | 53 |
| <b>Fig.3.3.</b> | Helium cryostate used for low-temperature Mössbauer spectroscopic studies.  | 57 |
| <b>Fig.3.4.</b> | Mössbauer spectra of $Fe_{50}Ni_{30}Cr_{20}$ sample at different temperatures and corresponding hyperfine field distributions.  | 59 |
| <b>Fig.3.5.</b> | Temperature dependence of full width at half maximum (FWHM) of $Fe_{50}Ni_{30}Cr_{20}$ sample.  | 64 |
| <b>Fig.3.6.</b> | Temperature dependence of Centre Shift of $Fe_{50}Ni_{30}Cr_{20}$ sample.   | 64 |
| <b>Fig.3.7.</b> | Temperature dependence of resonance area of $Fe_{50}Ni_{30}Cr_{20}$ sample.   | 65 |
| <b>Fig.3.8.</b> | Temperature dependence of average hyperfine field $\langle H \rangle$ of $Fe_{50}Ni_{30}Cr_{20}$ sample.  | 65 |

- Fig.3.9.** Variation of normalized average hyperfine field versus reduced temperature. The open circles (o) represent data for  $x = 30$  while crosses (+) represent data for  $x = 26$ . The continuous lines are drawn through the data points for visual guidance. 67
- Fig.3.10.** Two-Gaussian fits to the  $P(H)$  distributions vs.  $H$  curves at different temperatures. (a) represent the low-field side Gaussian (+) and (b) the high-field side Gaussian (o). 69
- Fig.3.11.** Temperature dependence of the most probable hyperfine field ( $H_{peak}$ ) corresponding to two-Gaussian components (Fig.3.10). (a) represent low-field side Gaussian (+) and (b) represents high-field side Gaussian (o). 70
- Fig.3.12.** Curve fitted (continuous line) to the second order Doppler shift values for determining the Debye temperature ( $\Theta_D$ ) of  $Fe_{50}Ni_{30}Cr_{20}$  alloy. 72
- Fig.3.13.** Mössbauer spectra of  $Fe_{54}Ni_{26}Cr_{20}$  sample at different temperatures and corresponding hyperfine field distributions. 74
- Fig.3.14.** Temperature dependence of full width at half maximum (FWHM) of  $Fe_{54}Ni_{26}Cr_{20}$  sample. 77
- Fig.3.15.** Temperature dependence of Centre Shift of  $Fe_{54}Ni_{26}Cr_{20}$  sample. 77
- Fig.3.16.** Temperature dependence of resonance area of  $Fe_{54}Ni_{26}Cr_{20}$  sample. 78

|  |           |
|--|-----------|
| <b>Fig.3.17.</b> Temperature dependence of average hyperfine field $\langle H \rangle$ of $Fe_{54}Ni_{26}Cr_{20}$ sample.  | <b>78</b> |
| <b>Fig.3.18.</b> Curve fitted (continuous line) to the second order Doppler shift values for determining the Debye temperature ( $\Theta_D$ ) of $Fe_{54}Ni_{26}Cr_{20}$ alloy.  | 80        |
| <b>Fig.3.19.</b> Mössbauer spectra of $Fe_{61}Ni_{19}Cr_{20}$ sample at different temperatures.  | 82        |
| <b>Fig.3.20.</b> Temperature dependence of full width at half maximum (FWHM) of $Fe_{61}Ni_{19}Cr_{20}$ sample.  | 85        |
| <b>Fig.3.21.</b> Temperature dependence of full width at half maximum (FWHM) of $Fe_{66}Ni_{14}Cr_{20}$ sample.  | 85        |
| <b>Fig.4.1.</b> Variation of $\mu$ and $H$ with Fe and Al nn's.<br>[taken from Ref.5].   | 91        |
| <b>Fig.4.2(a).</b> Phase diagram of Fe-Al system.  | 96        |
| <b>Fig.4.2(b).</b> Route of the sample processing schedules in phase diagram.  | 97        |
| <b>Fig.4.3.</b> Structure of $Fe_3Al$ ( $DO_3$ ).  | 98        |
| <b>Fig.4.4.</b> Mössbauer spectra of the sample AA1. Open circles (lower spectrum) represent the experimental data points. The upper Figure shows the five subspectra providing the best fit with $\square$ , $\Delta$ , $+$ , $\blacksquare$ and $\blacktriangle$ representing sites I, II, III, IV and V (see Table 4.2) respectively. | 103       |
| <b>Fig.4.5.</b> Mössbauer spectra of the sample AA2. Open circles (lower spectrum) represent the experimental data points. The upper Figure  | 104       |

shows the five subspectra providing the best fit with  $\square$ ,  $\Delta$ ,  $+$ ,  $\blacksquare$  and  $\blacktriangle$  representing sites I, II, III, IV and V (see Table 4.2) respectively.

**Fig. 4.6.** Mössbauer spectra of the sample AA3. Open 105

circles (lower spectrum) represent the experimental data points. The upper Figure shows the five subspectra providing the best fit with  $\square$ ,  $\Delta$ ,  $+$ ,  $\blacksquare$  and  $\blacktriangle$  representing sites I, II, III, IV and V (see Table 4.2) respectively.

**Fig. 4.7.** Mössbauer spectra of the sample AA4. Open 106

circles (lower spectrum) represent the experimental data points. The upper Figure shows the five subspectra providing the best fit with  $\square$ ,  $\Delta$ ,  $+$ ,  $\blacksquare$  and  $\blacktriangle$  representing sites I, II, III, IV and V (see Table 4.2) respectively.

**Fig. 4.8.** Mössbauer spectra of the sample AA5. Open 107

circles (lower spectrum) represent the experimental data points. The upper Figure shows the five subspectra providing the best fit with  $\square$ ,  $\Delta$ ,  $+$ ,  $\blacksquare$  and  $\blacktriangle$  representing sites I, II, III, IV and V (see Table 4.2) respectively.

**Fig. 4.9.** Variation of hperfine field of different sites 111

in samples AA1 - AA5.

|   |            |
|---|------------|
| <b>Fig.4.10.</b> Dependence of local hyperfine field $H_K$ on the number of K nearest-neighbour Al atoms of the Fe atoms [Taken from Ref.22].   | <b>113</b> |
| <b>Fig.4.11.</b> Hyperfine field distributions in (a) AA1, (b) AA2, (c) AA3, (d) AA4 and (e) AA5 samples.   | <b>118</b> |
| <b>Fig.5.1.</b> $^{57}\text{Fe}$ Mössbauer spectra of different Fe-C-Cr steels fitted by using least square fit method. (a) 0.0% Cr, (b) 0.5% Cr, (c) 1.0% Cr, (d) 2.0% Cr.                                     | <b>130</b> |
| <b>Fig.5.2.</b> $^{57}\text{Fe}$ Mössbauer spectra of different Fe-C-Mn steels fitted by using least square fit method. (a) 0.0% Mn, (b) 0.5% Mn, (c) 1.0% Mn, (d) 2.0% Mn.                                     | <b>131</b> |
| <b>Fig.5.3.</b> Hyperfine field distribution in Fe-C-Cr steels. ——— 0.5% Cr, ----- 1.0% Cr, - - - - - 2.0% Cr.  | <b>136</b> |
| <b>Fig.5.4.</b> Hyperfine field distribution in Fe-C-Mn steels. ——— 0.5% Mn, ----- 1.0% Mn, - - - - - 2.0% Mn.  | <b>137</b> |
| <b>Fig.5.5.</b> Variation of Magnetic moment of Fe atoms under the external magnetic field at room temperature of Fe-C-Cr steels for various compositions : o - 0.0% Cr, Δ - 0.5% Cr, □ - 1.0% Cr, ♦ - 2.0% Cr. | <b>139</b> |
| <b>Fig.5.6.</b> Variation of Magnetic moment of Fe atoms under the external magnetic field at room temperature of Fe-C-Mn steels for various  | <b>140</b> |

compositions : o - 0.0% Mn, Δ - 0.5% Mn, □ - 1.0% Mn, ♦ - 2.0% Mn.

- Fig.6.1.** Mössbauer spectra of as-received Si5 & Si9 samples. 154
- Fig.6.2.** P(H) distribution for as-received Si5 & Si9 samples. 154
- Fig.6.3.** P(H) distribution for Si5 samples annealed at 573 K (300 °C) for different  $t_a$ . 157
- Fig.6.4.** P(H) distribution for Si5 samples annealed at 623 K (350 °C) for different  $t_a$ . 158
- Fig.6.5.** P(H) distribution for Si5 samples annealed at 673 K (400 °C) for different  $t_a$ . 159
- Fig.6.6.** P(H) distribution for Si5 samples annealed at 723 K (450 °C) for different  $t_a$ . 160
- Fig.6.7.** P(H) distribution for Si5 samples annealed at 748 K (475 °C) for different  $t_a$ . 161
- Fig.6.8.** Mössbauer spectrum of Si5 sample annealed at 723 K (450°C) for 16h. 163
- Fig.6.9.** (a) Dependence of  $\langle H \rangle$  for the  $Fe_{79}B_{16}Si_5$  metallic glasses on annealing time period ( $t_a$ ) at (i)  $T_a = 573$  K (o); (ii)  $T_a = 623$  K (Δ); (iii)  $T_a = 673$  K (■) and (iv)  $T_a = 723$  K (●); (b) Dependence of  $\langle H \rangle$  for the  $Fe_{79}B_{16}Si_5$  metallic glasses on annealing time period ( $t_a$ ) at (i)  $T_a = 723$  K (o) and (ii)  $T_a = 748$  K (●). 170
- Fig.6.10.** A model for structural relaxation in amorphous alloys. (The small arrows indicate the spin 171

direction of Fe atoms and the empty arrows shows the average direction of magnetization in a cluster).

- Fig.6.11.** Difference in P(H) for  $Fe_{79}B_{16}Si_5$  between  $t = t_a$  (after annealing) and  $t = 0$  (before annealing) at (a)  $T_a = 723$  K and (b)  $T_a = 748$  K 172
- Fig.6.12.** P(H) distribution for Si9 samples annealed at 573 K ( $300^\circ C$ ) for different  $t_a$ . 174
- Fig.6.13.** P(H) distribution for Si9 samples annealed at 623 K ( $350^\circ C$ ) for different  $t_a$ . 175
- Fig.6.14.** P(H) distribution for Si9 samples annealed at 673 K ( $400^\circ C$ ) for different  $t_a$ . 176
- Fig.6.15.** P(H) distribution for Si9 samples annealed at 723 K ( $450^\circ C$ ) for different  $t_a$ . 177
- Fig.6.16.** P(H) distribution for Si9 samples annealed at 748 K ( $475^\circ C$ ) for different  $t_a$ . 178
- Fig.6.17.** (a) Dependence of  $\langle H \rangle$  for the  $Fe_{78}B_{13}Si_9$  metallic glasses on annealing time period ( $t_a$ ) at (i)  $T_a = 573$  K ( $\circ$ ) ; (ii)  $T_a = 623$  K ( $\Delta$ ) ; (iii)  $T_a = 673$  K ( $\blacksquare$ ) and (iv)  $T_a = 723$  K ( $\bullet$ ) ; (b) Dependence of  $\langle H \rangle$  for the  $Fe_{78}B_{13}Si_9$  metallic glasses on annealing time period ( $t_a$ ) at (i)  $T_a = 723$  K ( $\circ$ ) and (ii)  $T_a = 748$  K ( $\bullet$ ). 184
- Fig.6.18.** Difference in P(H) for  $Fe_{78}B_{13}Si_9$  between  $t = t_a$  (after annealing) and  $t = 0$  (before annealing) at (a)  $T_a = 723$  K and (b)  $T_a = 748$  K 185
- Fig.7.1.** Room temperature Mössbauer spectrum of the 195

chalcopyrite mineral in the as received form.

**Fig. 7.2.** Room temperature Mössbauer spectra of chalcopyrite samples roasted at  $(500 \pm 5)^\circ\text{C}$  for different time intervals  $t =$  (a) 1.0, (b) 2.0, (c) 3.0, (d) 5.0, (e) 10.0, (f) 15.0, (g) 20.0 and (h) 40.0 min. The zero of the velocity scale refers to the centre of the inner peaks of  $\alpha$ -Fe Mössbauer spectrum. The lines at the top indicate the characteristic peak positions in the Mössbauer spectra of (A)  $\text{Fe}_2(\text{SO}_4)_3$ , (B) pyrite, (C) see text, (D)  $\text{FeSO}_4$ , (E) chalcopyrite and (F)  $\alpha\text{-Fe}_2\text{O}_3$ .

**Fig. 7.3.** Room temperature Mössbauer spectra of chalcopyrite samples roasted at  $(650 \pm 5)^\circ\text{C}$  for different time intervals  $t =$  (a) 1.0, (b) 2.5, (c) 3.0, (d) 5.0, (e) 10.0. The zero of the velocity scale to the centre of the peaks of  $\alpha$ -Fe Mössbauer spectrum. The lines at the top indicate the characteristic peak positions in the Mössbauer spectra of (A) pyrite, (B) see text, (C)  $\text{FeSO}_4$ , (D) chalcopyrite and (E)  $\alpha\text{-Fe}_2\text{O}_3$ .

LIST OF TABLES

Page No.

|  |     |
|--|-----|
| <b>Table 1.1.</b> Parameters [11,12] for the 14.4 keV Mössbauer transition in $^{57}\text{Fe}$ .   | 9   |
| <b>Table 1.2.</b> Isomer shift and quadrupole splitting for iron in various electron configuration $d^n(+)$ .  | 15  |
| <b>Table 3.1.</b> Values of transition temperature $T_C$ , $T_{SG}$ , $T_N$ and saturation magnetization $4\pi M_S$ in $\text{Fe}_{80-x}\text{Ni}_x\text{Cr}_{20}$ ( $x = 30, 26, 19$ and $14$ ) alloys as reported by Majumdar and Blanckenhagen [3]. | 55  |
| <b>Table 4.1.</b> Routes and Schedule of heat-treatment and processing of different samples of Fe-Al alloys. See Figs.4.2(b) for the explanation of the symbols $a_1$ , $b_1$ , etc. used for describing the route.                                    | 100 |
| <b>Table 4.2.</b> Mössbauer parameters ( $H$ , $\Gamma$ , intensity) of samples AA1-AA5 measured at room temperature and the proposed assignment of configurations giving rise to each of the hyperfine magnetic field.                                | 108 |
| <b>Table 4.3.</b> Magnetic hyperfine field values for different Fe atom configuration in Fe-Al alloys as proposed by different workers. All values are in kOe.   | 114 |
| <b>Table 4.4.</b> The results for $H_{peak}$ , $\langle H \rangle$ , $\Delta H_1$ , $\Delta H_2$ and $\langle IS \rangle$  | 119 |

for the samples AA1 - AA5.

|  |     |
|--|-----|
| <b>Table 5.1.</b> Mössbauer parameters of Fe-C, Fe-C-Cr and Fe-C-Mn steels for different mass percentages (x) of Cr and Mn.  | 133 |
| <b>Table 5.2.</b> Parameters obtained from the analysis of Mössbauer spectra of steel samples by Window's method. $\Delta H_R$ and $\Delta H_L$ are the right and left half-width of a peak in the hyperfine field distribution.   | 138 |
| <b>Table 6.1.</b> Details of the heat-treatment schedule.  | 152 |
| <b>Table 6.2.</b> Summary of parameters of peaks decomposed from the P(H) curves for Si5 shown in Figs. 6.6 and 6.7.   | 166 |
| <b>Table 6.3.</b> Results for $H_{eff}$ , $H_p$ , $\langle H \rangle$ , $\Delta H_1$ and $\Delta H_2$ for the $Fe_{79}B_{16}Si_5$ metallic glass for different annealing temperatures ( $T_a$ ) and time periods ( $t_a$ ). The errors in $H_{eff}$ , $H_p$ and $\langle H \rangle$ are typically $\pm 4$ kOe. | 168 |
| <b>Table 6.4.</b> Summary of parameters of peaks decomposed from the P(H) curves for Si9 shown in Figs. 6.15 and 6.16.   | 180 |
| <b>Table 6.5.</b> Results for $H_{eff}$ , $H_p$ , $\langle H \rangle$ , $\Delta H_1$ and $\Delta H_2$ for the $Fe_{78}B_{13}Si_8$ metallic glass for different annealing temperatures ( $T_a$ ) and time periods ( $t_a$ ). The errors in $H_{eff}$ , $H_p$ and $\langle H \rangle$ are typically $\pm 4$ kOe. | 182 |
| <b>Table 7.1.</b> Roasting of chalcopyrite at $(500 \pm 5)^\circ C$ for  | 196 |

different time intervals. Values of Mössbauer parameters and assignments<sup>†</sup> of different compounds.

Table 7.2. Roasting of chalcopyrite at  $(650 \pm 5)^\circ\text{C}$  for

205

ifferent time intervals. Values of Mössbauer parameters and assignments<sup>†</sup> of different compounds.

# CHAPTER 1

## Introduction

### **1.1. Preamble**

In 1957 R.L.Mössbauer [1] discovered the phenomenon of recoil-less nuclear absorption and emission of  $\gamma$ -radiation from a radiating atom embedded in a solid and this phenomenon came to be known as Mössbauer effect. In view of its very high energy sensitivity, the technique of Mössbauer spectroscopy was soon applied to diverse research areas in physics, chemistry, physical metallurgy, biochemistry, geochemistry, materials science etc. Several good books and excellent review articles describing the Mössbauer effect and its applications have been published in the literature [2-10] and hence no attempt will be made to go into these details here. However, for the sake of completeness, we shall briefly outline below the basic principles of Mössbauer effect and its methodology.

### **1.2. Mössbauer effect**

Consider the decay phenomenon of a radioactive nucleus from a higher excited energy state ( $E_{ex}$ ) to the ground state ( $E_g$ ) with an emission of gamma photon of energy  $E_\gamma$  such that

$$E_\gamma = E_{ex} - E_g \quad (1.1)$$

The excited state has a finite width of energy  $\Gamma$  which is related to its mean lifetime  $\tau$  by  $\Gamma \approx \hbar/\tau$  (Fig.1.1).

The total linear momentum is conserved during this nuclear

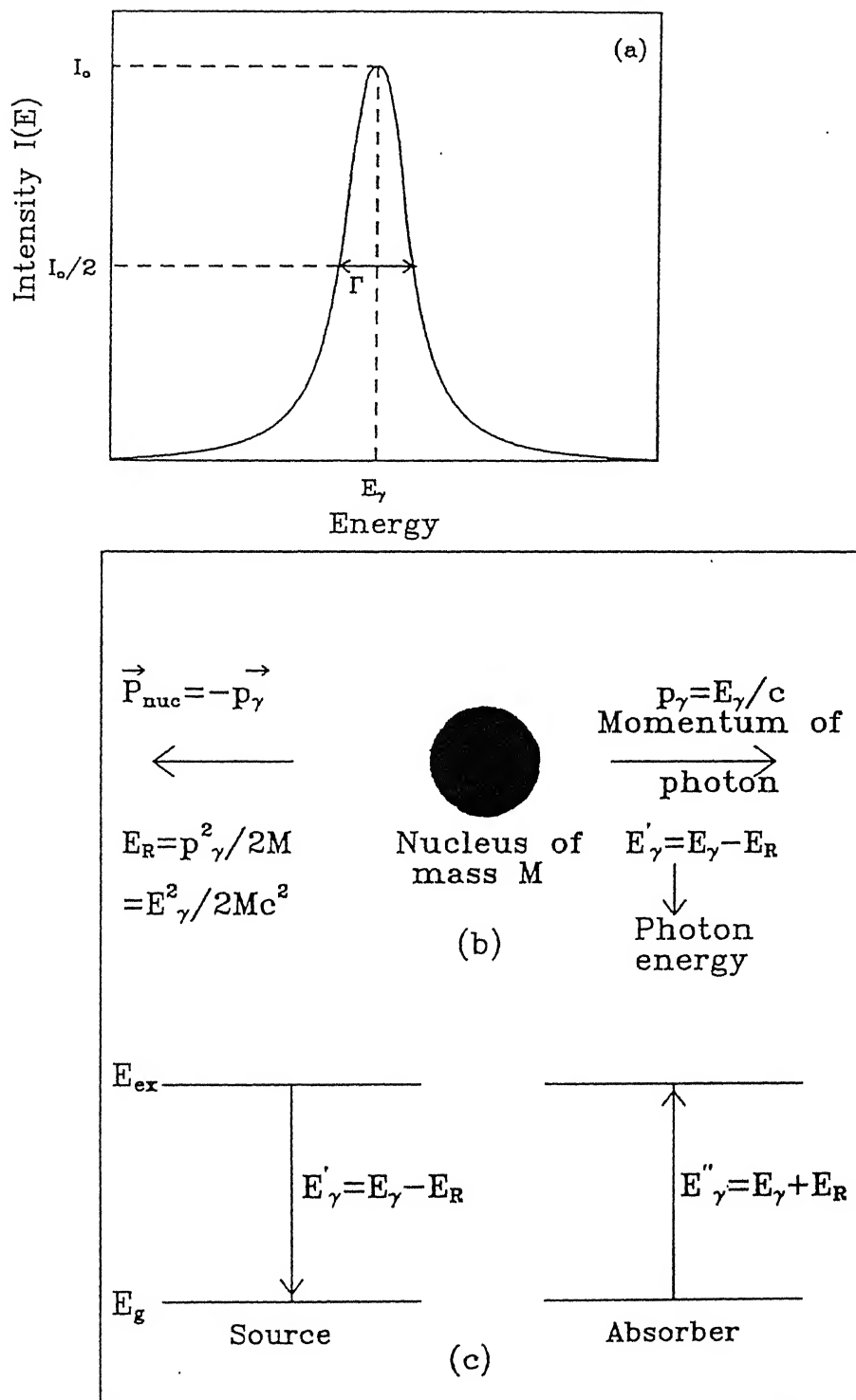


**Fig.1.1.** (a) Intensity  $I(E)$  of spectral line as a function of transition energy  $E_\gamma$ . (b) Nucleus receiving recoil energy  $E_R$  during the emission of photon. (c) The schematic nuclear energy level diagram of emission and absorption.

decay and as a result the emitting nucleus undergoes a recoil (Fig.1.1). This recoil energy ( $E_R$ ) is related to the energy of the emitted gamma photon ( $E_\gamma$ ) by the following relation:

$$E_R = p_\gamma^2 / 2M = E_\gamma^2 / 2Mc^2 \quad (1.2)$$

where  $p_\gamma$  is the momentum of the emitted photon,  $M$  is the mass of the emitting nucleus and  $c$  is the speed of light. Consequently the energy of the emitted gamma photon is modified from  $E_\gamma$  to  $E'_\gamma$  where

$$E'_\gamma = E_\gamma - E_R \quad (1.3)$$

Similar process takes place when the nucleus is excited from the ground state to the higher energy state by the absorption of a gamma photon of energy  $E_\gamma$  such that

$$E''_\gamma = E_\gamma + E_R \quad (1.4)$$

where  $E_R$  is the recoil energy for the absorbing nucleus. The energy profile diagrams of  $E'_\gamma$  and  $E''_\gamma$  are shown in Fig.1.2 for different values of the recoil energy  $E_R$ . When  $E_R$  is small the two profiles will overlap each other and give a resonance. However in real situation with nuclei,  $E_R \gg \Gamma$  (almost  $10^8$  times) where  $\Gamma$  is the natural linewidth of the gamma-ray photon (Fig.1.1.c). As a result there will be a wide gap between the energy profiles corresponding to  $E'_\gamma$  and  $E''_\gamma$  and no resonance will occur. The recoil energy  $E_R$  should be of the order of  $\Gamma$  for resonance to occur. Mössbauer found out that when the radioactive nucleus is well embedded in the crystal lattice the mass of the nucleus will be effectively replaced by the total mass of the lattice in the

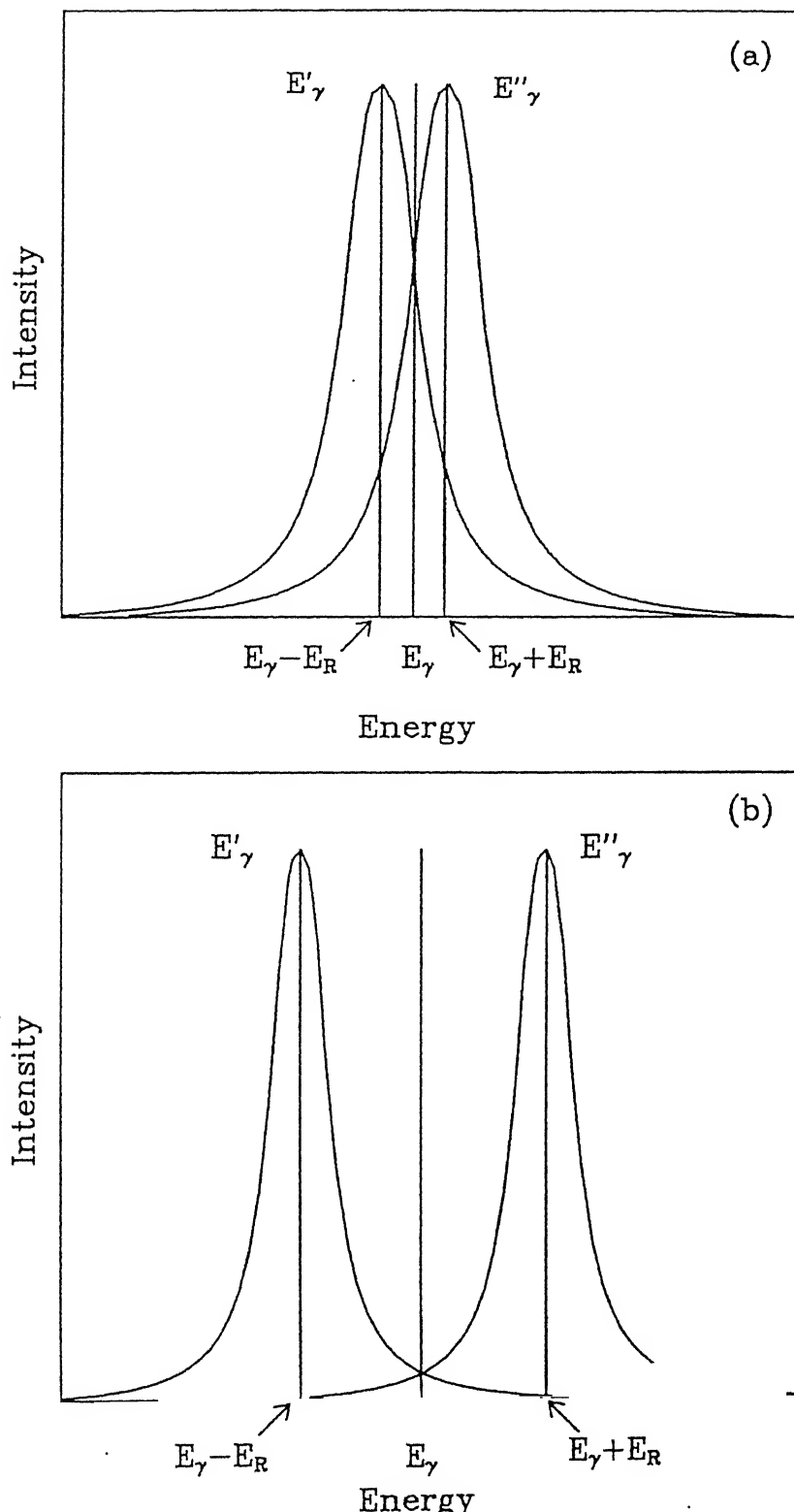


**Fig.1.2.** Overlap of the emission and absorption lines showing the relation between  $E_\gamma$ ,  $E'_\gamma$ ,  $E''_\gamma$  for two cases: (a) optical case  $E_R \ll \Gamma$  and (b) nuclear case  $E_R \gg \Gamma$ . The energy scales are shown only schematically and not realistically.

equation

$$E_R = p_\gamma^2 / 2M = E_\gamma^2 / 2Mc^2 \quad (1.2)$$

Under this condition  $E_R$  becomes negligible and the source and absorber energy profiles overlap completely and both will have widths approaching  $\Gamma_H$  (or the Heisenberg linewidth) and resonance will occur. The gamma rays will thus be emitted (or absorbed) without any recoil and this is how recoilless emission or absorption will occur.

### 1.3. Recoil-free fraction

When the atom are well embedded in a crystal, a fraction 'f' of the total number of gamma-ray photons is emitted without any loss of recoil energy. Same is true for the absorption process. A more detailed analysis [2-10] shows that the probability of recoilless emission or absorption is given by the following expression

$$f = \left[ \left| \int \Psi_n^*(x) \Psi_n(x) \exp(-i \vec{k} \cdot \vec{x}) \right|^2 dx \right]^{1/2} \quad (1.5)$$

where  $\Psi_n(x)$  represents the vibrational state of lattice,  $x$  the positional coordinate of the centre-of-mass of the emitting nucleus and  $\vec{k}$  is the wave vector of the gamma ray.

A general expression for the probability,  $f$ , of emission or

absorption of gamma-photon without recoil is given by

$$f = \exp \left[ -k^2 \langle x^2 \rangle \right]$$

$$= \exp \left[ -\frac{\hbar^2 k^2}{2m} \int \left[ g(\omega)/\hbar \right] \coth (\hbar\omega/2k_B T) d\omega \right] \quad (1.6)$$

where  $\langle x^2 \rangle$  is the mean square displacement of the nucleus from the equilibrium position and  $g(\omega)$  is the normalized density of phonon states of angular frequency  $\omega$ . In the Debye model of solids, the frequency distribution is given by

$$G(\omega) = \text{constant} * \omega^2 \quad \text{for } 0 \leq \omega \leq \omega_{\max}$$

$$= 0 \quad \text{for } \omega > \omega_{\max}$$

Using this model the expression for  $f$  reduces [8] to

$$f = \exp \left[ -\frac{6E_R}{k_B \theta_D} \left\{ \frac{1}{4} + \left( \frac{T}{\theta_D} \right)^2 \int_0^{\theta_D/T} \frac{x dx}{e^x - 1} \right\} \right] \quad (1.7)$$

where  $\theta_D$  is the Debye temperature. In the limit of low ( $T \ll \theta_D$ ) and high ( $T \gg \theta_D$ ) temperatures the expression for  $f$  becomes

$$f = \exp \left[ -\frac{E_R}{k_B \theta_D} \left( \frac{3}{2} + \frac{\pi^2 T^2}{\theta_D^2} \right) \right] \quad \text{for } T \ll \theta_D \quad (1.8a)$$

and at absolute zero

$$f = \exp \left[ -\frac{3E_R}{2k_B \theta_D} \right]$$

In the high temperature limit

$$f = \exp \left[ -\frac{6E_R T}{k_B \Theta_D^2} \right] \quad \text{for } T \geq \frac{1}{2} \Theta_D \quad (1.8b)$$

The following conclusions can, therefore, be drawn about the properties of recoilless fraction:

(i)  $f$  increases with decreasing recoil energy  $E_R$  (i.e. decreasing  $E_\gamma$ ).

(ii)  $f$  increases with the decrease of temperature.

(iii)  $f$  increases with the increase of Debye temperature  $\Theta_D$ . So  $\Theta_D$  may be considered as the measure of the strength of the bonds between Mössbauer atoms and the lattice. One often writes  $f = e^{-2W}$  and the factor  $W$  is generally called the Debye-Waller factor or the Lamb-Mössbauer factor [8].

The nature of energy distribution of emitted and absorbed gamma photons show Breit-Wigner or Lorentzian shape. Using the concept of recoil-free fraction, the energy distribution of the recoilless emitted radiation can be written as

$$I(E) = I_0 f_s \left[ \frac{\Gamma^2/4}{(E - E_\gamma)^2 + \Gamma^2/4} \right] \quad (1.9)$$

While the energy distribution of the resonant absorption can be described as

$$\sigma(E) = \sigma_0 f_a \left[ \frac{\Gamma^2/4}{(E - E_\gamma)^2 + \Gamma^2/4} \right] \quad (1.10)$$

where  $f_s$  and  $f_a$  are the recoilless fraction for the source and absorber respectively,  $I_0$  is the intensity of emitted radiation from the source and  $\sigma_0$  is the effective photon cross-section for the Mössbauer nucleus in the absorber.

The above discussion indicates that the chief requirements for suitable Mössbauer nuclide are low gamma-ray energy  $E_\gamma$  (preferably in the range 10 - 150 keV) and high Debye temperature  $\epsilon_D$ . Considering all these aspects,  $^{57}\text{Fe}$  nucleus has been found to be the most suitable nuclide. Although the Mössbauer effect has been observed for 100 different nuclear transitions in about 80 nuclides distributed over 43 elements in the periodic table, about 75% of the Mössbauer spectroscopic studies have been carried out using  $^{57}\text{Fe}$ . The important parameters of  $^{57}\text{Fe}$  which make it most suitable and popular Mössbauer nuclide are listed in Table 1.1 [11,12].

#### 1.4. Hyperfine interactions

When a nucleus is embedded in a lattice, it can interact with the electric and magnetic fields produced by the extranuclear environment due to the charge and currents in the surrounding electronic/atomic surroundings. These effects are described by "hyperfine interactions", a name given to the interactions between a nuclear (moment) property and an appropriate electronic or atomic property. Study of such hyperfine interactions is of great interest because they provide valuable information regarding electron- and spin- density distributions. The hyperfine

Table 1.1. Parameters [11,12] for the 14.4 keV Mössbauer transition Fe in  $^{57}\text{Fe}$

1. Isotopic abundance = 2.14 %
2. Energy E = 14.41303 (8) keV
3. Half-life,  $t_{1/2} = 97.81$  (14) ns
4. Ratio of the excited and ground state nuclear magnetic moment  
 $R_\mu = -1.7145$  (5)
5. Nuclear magnetic dipole moment of the excited state =  $\mu = -0.15534$  (5) nm
6. Nuclear electric quadrupole moment of the excited state =  $Q = 0.209$  (15) barns
7. Total internal conversion coefficient,  $\alpha_T = 8.21$  (12)
8. Debye temperature,  $\Theta_D = 440$  K.
9. Mössbauer cross-section =  $256$  (3)  $\times 10^{-20}$  cm $^{-2}$
10. Mössbauer linewidth (theoretical full width at half maximum)  
 $\Gamma = 0.194$  mms $^{-1}$
11. Recoil energy,  $E_R = 1.957 \times 10^{-3}$  eV
12. Conversion factor 1 mms $^{-1} = 11.6248$  (1) MHz.

interactions could be written as

$$H = H_0 + E_0 + M_1 + E_2 + \dots \quad (1.11)$$

where

$H_0$  = Hamiltonian excluding hyperfine interaction,

$E_0$  = Electric monopole interaction between the nucleus and the surrounding electrons,

$M_1$  = Magnetic dipole interaction between nuclear magnetic dipole moment and the magnetic field produced at the nucleus by the surrounding environment,

$E_2$  = Electric quadrupole interaction between nuclear electric quadrupole moment and electric field gradient of the surrounding electrons.

Higher order terms (e.g.  $M_2$ ,  $E_3 \dots$ ) are usually small and can be neglected. There are thus three main terms to be considered in the expression for the hyperfine interactions, viz.  $E_0$ ,  $M_1$  and  $E_2$ . The electric monopole interaction ( $E_0$ ) describing the interaction of the nuclear charge distribution with the electron density at the nuclei in the source and absorber gives rise to the so-called "isomer shift" in Mössbauer spectroscopy. The magnetic dipole interaction ( $M_1$ ) causes the magnetic splitting (or nuclear Zeeman effect) in Mössbauer spectra. The so-called quadrupole splitting in the Mössbauer spectra is caused by the electric quadrupole interaction ( $E_2$ ). The subject of hyperfine interaction and its relevance to Mössbauer spectroscopy has been discussed in detail in the literature [2-11] and in the following we shall give only a barest outline for the sake of completeness.

#### 1.4.1. Isomer shift

Isomer shift is one of the most important Mössbauer parameters. It measures the difference between the Mössbauer transition energy in the source and the absorber when both of them are at the same temperature. It arises out of the fact that the nucleus is not a point charge but has a finite size and spatial charge distribution. The electrostatic interaction between nucleus and surrounding electron clouds (because electrons have a finite probability of being found inside the volume of the nucleus) is, therefore, not purely Coulombic point-interaction. As a result of this interaction the nuclear energy levels do not show any splitting. Instead, the nuclear energy levels, both in the ground ( $E_g$ ) and excited ( $E_{ex}$ ) state, show a shift. When the source and the absorber nuclei have different environment, the energy difference between  $E_{ex}$  and  $E_g$  will also be different. Let us denote the energy of the Mössbauer gamma ray in the source by  $E_\gamma^S$  and that in the absorber by  $E_\gamma^A$ . Then in the above case  $E_\gamma^S$  is not equal to  $E_\gamma^A$ . The difference between  $E_\gamma^S$  and  $E_\gamma^A$  is typically of the order of  $10^{-9}$  eV. In order to observe a resonance one should apply a Doppler velocity  $v$  to the source (or absorber) such that  $[E_\gamma^S \pm (v/c)E_\gamma^S] = E_\gamma^A$ . In the absence of electric quadrupole or magnetic dipole interaction, isomer shift manifests itself as a shift of single resonance from the zero velocity (Fig.1.3). If the electric quadrupole or magnetic dipole interactions are also present, the isomer shift is from the position of the centre of gravity (on the velocity scale) of Mössbauer spectrum and it gives a measure of the strength of electric monopole interaction. The subject of

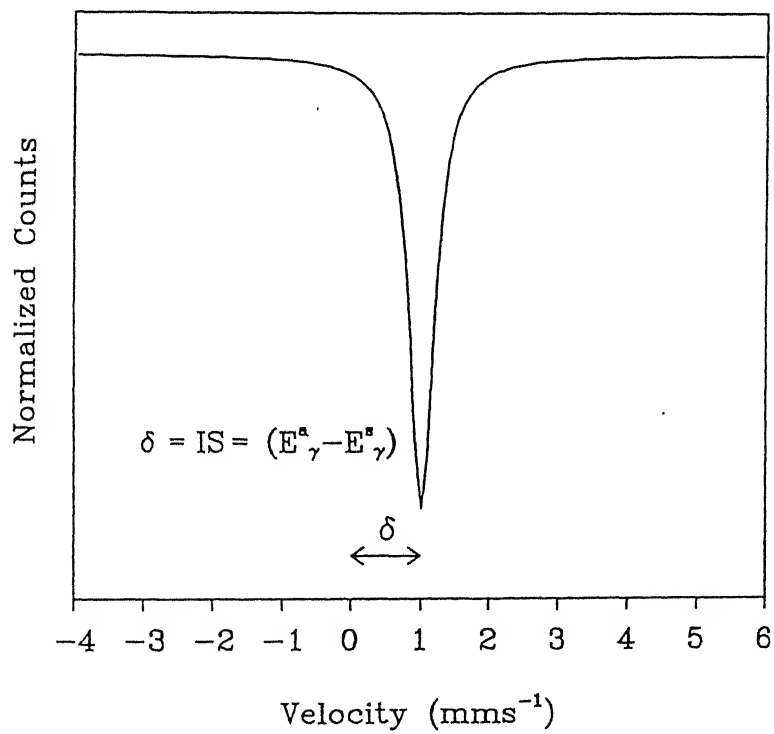
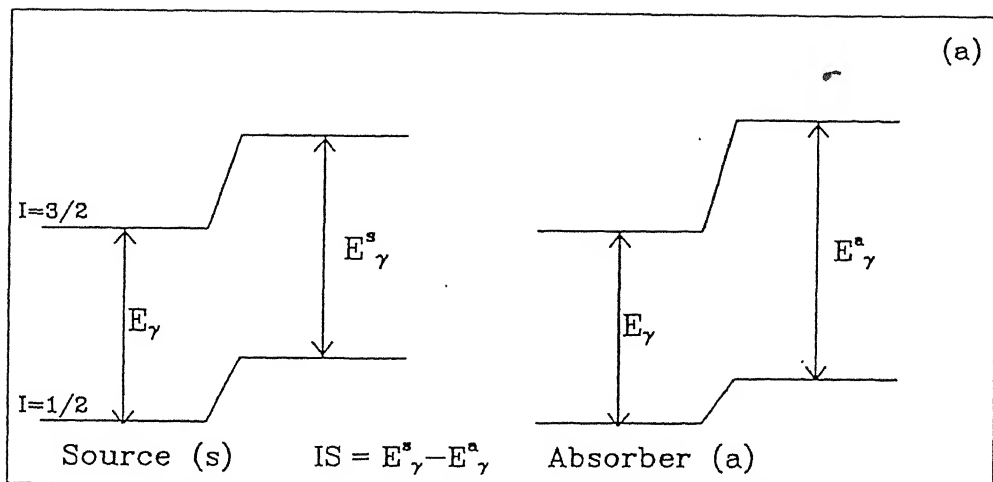


**Fig. 1.3.** (a) Effect of monopole interaction on the energy levels of source and absorber nuclei. (b) Mössbauer spectrum showing monopole interaction.

isomer shift has been discussed in detail in several reviews [2-13] and we shall not go into these details here. To illustrate the connection between isomer shift and the electron density at the nucleus, we shall outline a simple calculation of isomer shift using non-relativistic approximation [9,10] and by assuming charge distribution of nucleus to be uniform and spherically symmetric. Let  $\delta E$  denote the difference between the electrostatic interaction of a point nucleus and a nucleus with finite volume. It can be shown that

$$\delta E = K \left| \Psi_s(0) \right|^2 R^2 \quad (1.12)$$

where  $K$  is a nuclear constant ( $= 2\pi Z e^2 / 5$ ),  $\left| \Psi_s(0) \right|^2$  is the s-electron density at the nucleus and  $R$  is the nuclear radius. The value of  $\delta E$  will be different for the nucleus in the ground and excited state because the nuclear radii ( $R$ ) are different in these two states. The difference between these two  $\delta E$ 's is given by

$$\delta E_{ex} - \delta E_g = K \left[ \left| \Psi_s(0) \right|^2 (R_{ex}^2 - R_g^2) \right] \quad (1.13)$$

For a given nucleus (e.g.  $^{57}\text{Fe}$ )  $R_{ex}$  and  $R_g$  are constant but the value of  $\left| \Psi_s(0) \right|^2$  will vary from one compound to another. An expression for isomer shift (IS or  $\delta$ ) can be obtained by writing the difference of eq. (1.13) for source and absorber as

$$IS = \delta = K (R_{ex}^2 - R_g^2) \left[ \left| \Psi_s(0) \right|_a^2 - \left| \Psi_s(0) \right|_s^2 \right] \quad (1.14)$$

where the subscripts  $a$  and  $s$  correspond to the absorber and source

respectively. For a source material (e.g. radioactive  $^{57}\text{Co}$  in Rh matrix for  $^{57}\text{Fe}$  Mössbauer spectroscopy),  $R_{\text{ex}}$ ,  $R_g$  and  $\left| \Psi_s(0) \right|_s^2$  are constant and we can rewrite eq. (1.14) by using  $\delta R = (R_{\text{ex}} - R_g)$  as

$$\text{IS} = \delta = K R^2 \left( \frac{\delta R}{R} \right) \left[ \left| \Psi_s(0) \right|_a^2 - C \right] \quad (1.15)$$

where  $C$  is a constant whose value depends on the source used. In this way the expression for IS depends on two factors, the first one being the nuclear factor  $\delta R$  while the second is the extranuclear factor  $\left| \Psi_s(0) \right|_a^2$ . For a given nucleus  $\delta R$  is constant and the value of IS (or  $\delta$ ) is directly proportional to the s-electron density at nucleus. For  $^{57}\text{Fe}$ ,  $\delta R$  is negative and the IS-value becomes more negative with an increase in s-electron density of the absorber. Although the p and d electron clouds do not directly interact with the nuclear charge density, they induce changes in the IS-values.

Mössbauer spectroscopic studies of different compounds of iron have shown that the range of values of IS (or  $\delta$ ) falls in different intervals depending on the ionization states of iron. This is brought out by the data presented in Table 1.2 and Fig.1.4 [13] for compounds in which iron ion has high spin configuration. In this way the examination of the measured IS-value can help us to determine the oxidation state of iron compounds. The plot of  $^{57}\text{Fe}$  IS against the coordination number is shown in Fig.1.5(a) for ionic high spin and low spin compounds and minerals. The arrows marked on the boxes indicate that values outside the boxes have also been observed.

Table 1.2. Isomer shift and quadrupole splitting for iron in various electron configuration  $d^n(+)$ .

| $d^n$ | Oxidation state | IS* [9]<br>( $\text{mms}^{-1}$ ) | $\Delta E$ [5]<br>( $\text{mms}^{-1}$ ) |
|-------|-----------------|----------------------------------|---|
| $d^7$ | +1              | 1.90                             | _____                                   |
| $d^6$ | +2              | 1.20                             | 1.5-3.7                                 |
| $d^5$ | +3              | 0.45                             | 0.0-1.0                                 |
| $d^4$ | +4              | 0.00                             | _____                                   |
| $d^2$ | +6              | -0.90                            | _____                                   |

(+) IS = Isomer shift,  $\Delta E$  = Quadrupole splitting with respect to  $\alpha\text{-Fe}$ .

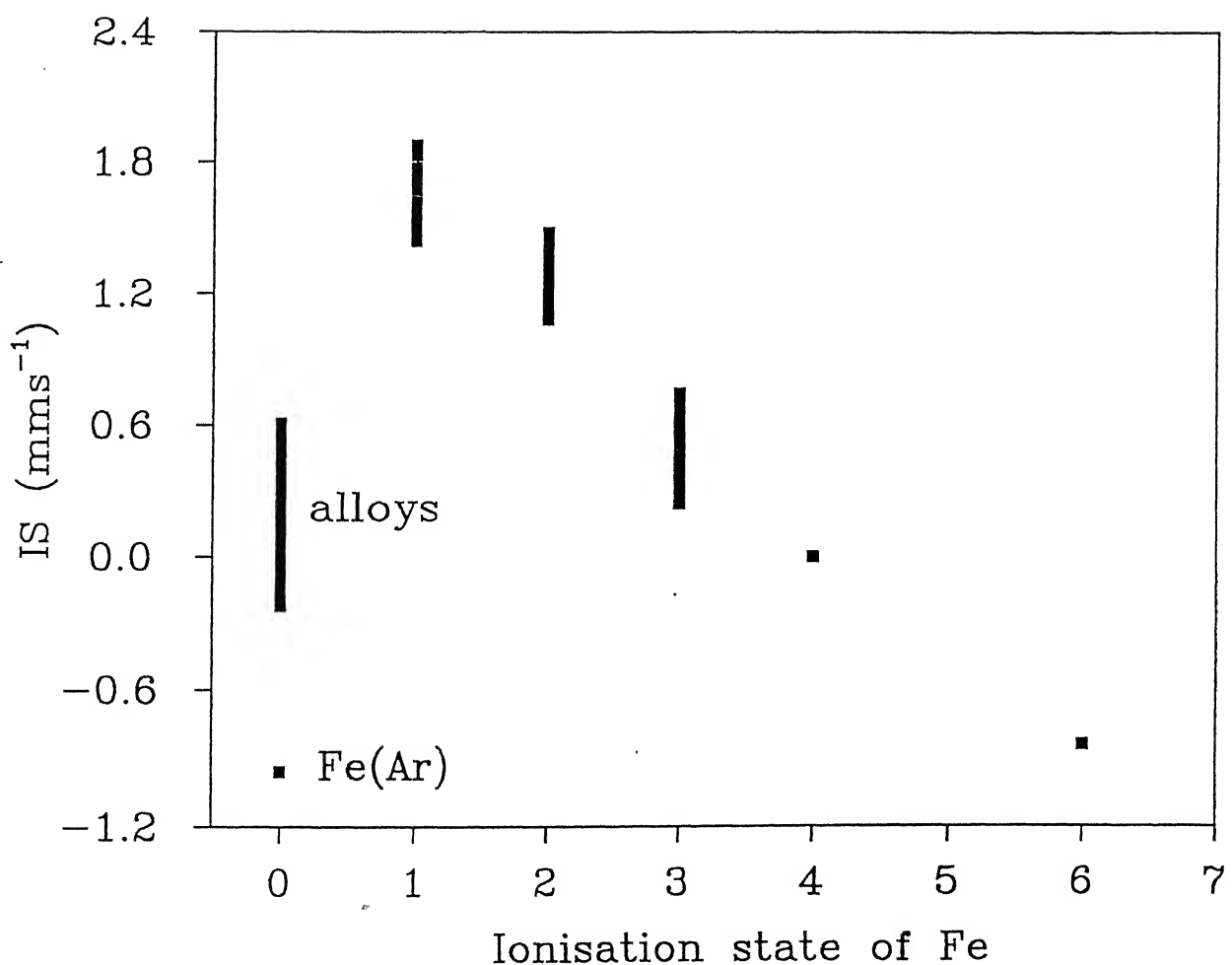


**Fig.1.4.** Review of isomer shift data of iron in various ionisation state [13].

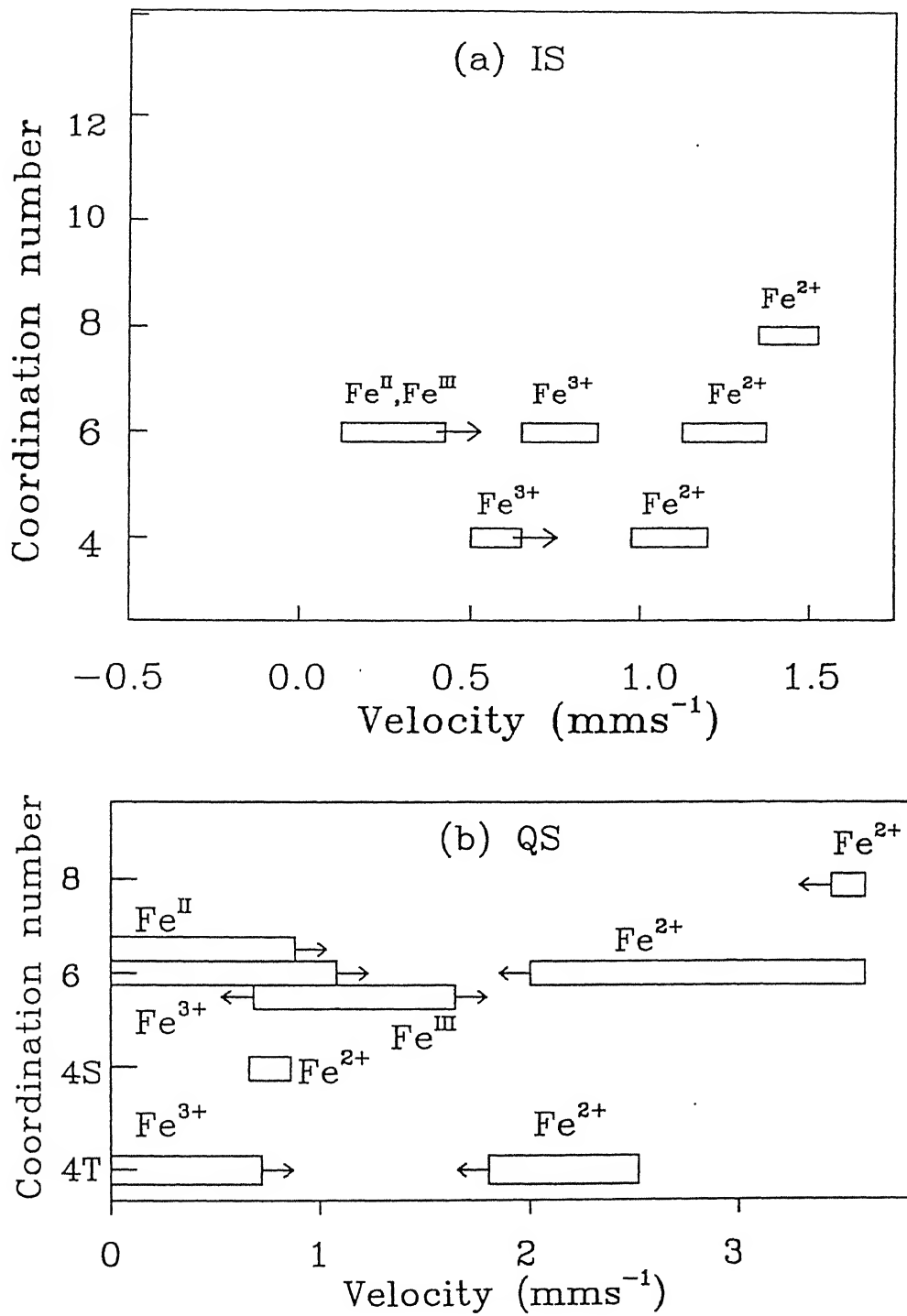


Fig.1.5. Review of  ${}^{57}\text{Fe}$  Mössbauer parameters (a) IS (isomer shift) and (b) QS (quadrupole splitting) for iron plotted against the coordination number for ionic high spin and low spin compounds and minerals. Arrows indicate that the values outside the range of boxes have been observed.

Different values of IS relative to different sources (or to different absorbers) have been reported by different workers. In order to have a universal comparison it is necessary to use a IS scale for  $^{57}\text{Fe}$  sources (or absorber) as shown in Fig.1.6.

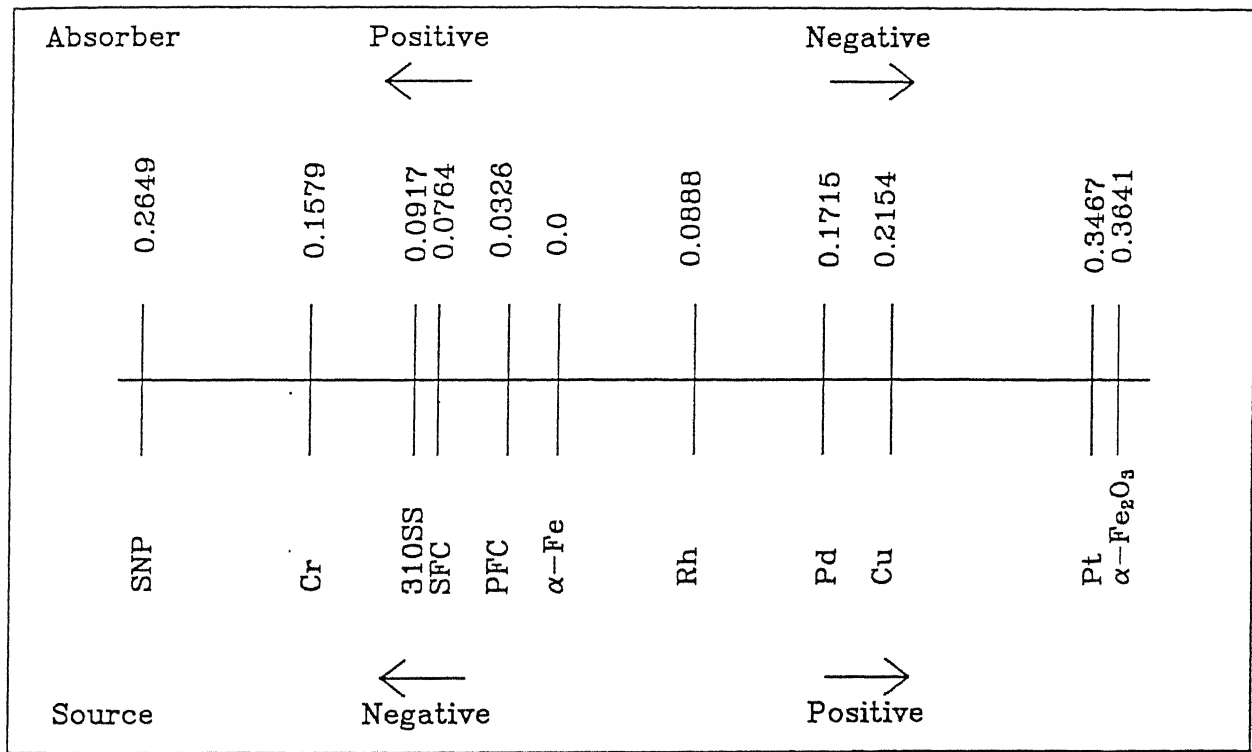
In addition to the IS discussed above, Mössbauer spectral lines also exhibit a temperature shift if the source and absorber are kept at different temperatures. This shift arises due to the fact that at the lattice site, the Mössbauer atom has sufficient mean square velocity depending on the temperature of the solid and hence the Doppler shift is a function of the mean square velocity of the Mössbauer atoms in solids. This phenomenon is known as second order Doppler shift ( $\delta_{\text{SOD}}$ ) and the total shift in the energy of the spectral lines in Mössbauer effect can be written as

$$\delta_{\text{Total}} = \delta_{\text{IS}} + \delta_{\text{SOD}} \quad (1.16)$$

For a Debye solid, the expression of  $\delta_{\text{SOD}}$  becomes [14],

$$\delta_{\text{SOD}} = -\frac{1}{2c} \left[ \frac{9}{8} \frac{k_B \Theta_D}{M} + \frac{3k_B T}{M} f\left(\frac{T}{\Theta_D}\right) \right] \quad (1.17)$$

$$\text{where, } f\left(\frac{T}{\Theta_D}\right) = 3\left(\frac{T}{\Theta_D}\right) \int_0^{\Theta_D/T} \frac{x^3}{e^x - 1} dx$$



SNP =  $\text{Na}_2\text{Fe}(\text{CN})_6\text{NO}, 2\text{H}_2\text{O}$

SFC =  $\text{Na}_4\text{Fe}(\text{CN})_6, 10\text{H}_2\text{O}$

PFC =  $\text{K}_4\text{Fe}(\text{CN})_6, 3\text{H}_2\text{O}$

SS = Stainless steel

**Fig.1.6.** Data for the  $^{57}\text{Fe}$  isomer shift with respect to natural iron ( $\alpha\text{-Fe}$ ) at room temperature. Units of the IS values are  $\text{mms}^{-1}$  and signs of the velocity for the source are to be read from the bottom row while the signs of velocity for the absorber are to be read from the top row.

At finite temperature T the expression of  $\delta_{SOD}$  [14] becomes

$$\delta_{SOD} = -\frac{3k_B T}{2Mc} \left[ 1 + \frac{1}{20} \left( \frac{\epsilon_D}{T} \right)^2 \right] \quad \text{for } T > \epsilon_D \quad (1.18a)$$

$$= -\frac{9}{16} \frac{k_B \epsilon_D}{Mc} \left[ 1 + \frac{8\pi^4}{15} \left( \frac{T}{\epsilon_D} \right)^4 \right] \quad \text{for } T \ll \epsilon_D \quad (1.18b)$$

In view of the above discussion it is clear that the contributions from  $\delta_{SOD}$  should be considered only when temperature dependent measurements are made.

#### 1.4.2. Quadrupole splitting

In case of nuclei having (i) nuclear spin  $I>1/2$  and (ii) nuclear charge distribution that is non-uniform and deviating from spherical symmetry, there will be an interaction between the nuclear charge distribution and the extranuclear electric field. More precisely the z-component of the electric field gradient (EFG) tensor will interact with the electric quadrupole moment of the nucleus. Such an electric quadrupole interaction leads to the splitting of nuclear energy levels. Let us consider the case of  $^{57}\text{Fe}$  nucleus for which the spins of the excited and ground states are  $I = 3/2$  and  $I = 1/2$  respectively. The higher level ( $I=3/2$ ) splits into two levels, ( $m_I = \pm 3/2, \pm 1/2$ ) while the lower level ( $I=1/2$ ) remains unsplit (or degenerate) as shown in Fig.1.7. Selection rule allows both the transitions :

$$m_I = \pm 3/2 \rightarrow m_I = \pm 1/2 \quad \text{and} \quad m_I = \pm 1/2 \rightarrow m_I = \pm 1/2$$

and this gives rise to a doublet or a two-line Mössbauer spectrum from which the quadrupole splitting (QS or  $\Delta E$ ) is obtained as the

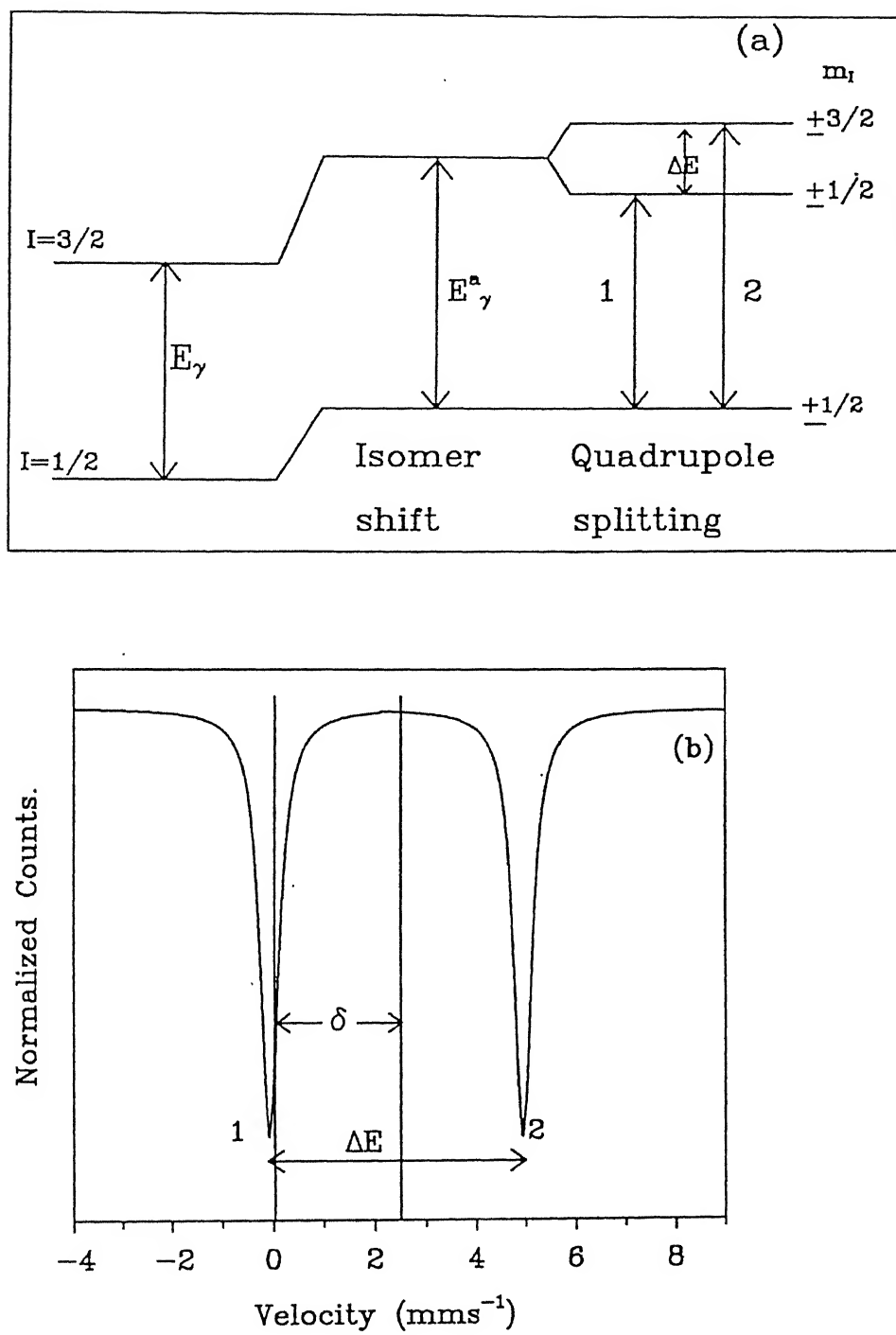


**Fig.1.7.** Effect of the quadrupole interaction on the nuclear energy levels of source / absorber and the resulting Mössbauer spectrum showing the quadrupole splitting and isomer shift.

separation between the two peak positions.

The theory of quadrupole splitting has been discussed in detail by several authors [2-12]. In the case of  $^{57}\text{Fe}$  the quadrupole splitting can be expressed as

$$QS = \Delta E = 1/2 e^2 qQ \left[ 1 + \eta^2/3 \right]^{1/2} \quad (1.19)$$

where,  $Q$  = electric quadrupole moment of the nucleus

$eq = V_{ZZ}$  = the negative  $z$ -component of the electric field gradient (EFG)

$e$  = protonic charge

$\eta$  = the asymmetry parameter =  $(V_{XX} - V_{YY})/V_{ZZ}$ .

$q = (1-R)_{\text{qval}} + (1-\gamma_{\alpha})_{\text{qlat}}$

The analysis of  $\Delta E$  (or  $QS$ ) values determined from the observed Mössbauer spectra provide valuable information for studying solids. The plot of  $\Delta E$ -values versus the coordination number for different ionic high spins is shown in Fig.1.5(b).

#### 1.4.3. Magnetic hyperfine interaction

The existence of magnetic hyperfine interaction in Mössbauer spectra has led to several interesting applications of Mössbauer spectroscopy for the study of magnetism and magnetic materials. Let us consider the magnetic hyperfine splitting in  $^{57}\text{Fe}$ .

A nucleus having a total spin  $I > 0$ , possesses a magnetic dipole moment ( $\vec{\mu} = g_N \mu_N \vec{I}$ ) which can interact with the magnetic field  $\vec{H}$  present at the site of the nucleus. This interaction gives rise to a splitting of the energy levels and this phenomenon is

known as nuclear Zeeman effect. The interaction Hamiltonian is given by

$$H = - \vec{\mu} \cdot \vec{H} = -g_N \mu_N (\vec{I} \cdot \vec{H}) \quad (1.20)$$

where  $g_N$  is the nuclear g-factor,  $\mu_N$  is the nuclear Bohr magneton ( $e\hbar/2M_N c = 5.04929 * 10^{-27} \text{ JT}^{-1}$ ) and  $I$  is the nuclear spin.

Using the first order perturbation theory the eigenvalues of the above Hamiltonian become

$$E_m = \langle I m_I | H | I m_I \rangle = - g_N \mu_N H m_I \quad (1.21)$$

and as a result the energy level splits into  $(2I+1)$  equally spaced states having magnetic quantum number  $m_I = I$  to  $-I$ . Gamma-ray transitions then take place according to the selection rule  $\Delta I = \pm 1$  and  $\Delta m_I = 0, \pm 1$ . In the case of  $^{57}\text{Fe}$  nucleus the magnetic hyperfine interaction splits excited state (energy level with  $I=3/2$ ) into four states while the ground state ( $I = 1/2$ ) is split into two states (Fig. 1.8). Gamma-ray transitions between these energy levels obey the selection rules stated above and consequently they give rise to a six-line (sextet) pattern in the Mössbauer spectrum. The relative intensities of these six transitions in the  $^{57}\text{Fe}$  nucleus are in the ratio [6]

$$\begin{aligned} & \left( \frac{3}{2}, \frac{3}{2} \rightarrow \frac{1}{2}, \frac{1}{2} \right) : \left( \frac{3}{2}, \frac{1}{2} \rightarrow \frac{1}{2}, \frac{1}{2} \right) : \left( \frac{3}{2}, \frac{3}{2} \rightarrow \frac{1}{2}, -\frac{1}{2} \right) :: \\ & \left( \frac{3}{2}, -\frac{1}{2} \rightarrow \frac{1}{2}, \frac{1}{2} \right) : \left( \frac{3}{2}, -\frac{1}{2} \rightarrow \frac{1}{2}, -\frac{1}{2} \right) : \left( \frac{3}{2}, -\frac{3}{2} \rightarrow \frac{1}{2}, -\frac{1}{2} \right) \\ & \qquad \qquad \qquad = 3:Z:1::1:Z:3 \quad (1.22) \end{aligned}$$

where  $Z = 4/(1+\cot^2\theta)$  with  $\theta$  being the angle between the gamma-photon beam and the magnetic field axis. In the case of polycrystalline samples the value of  $Z$  in equation (1.22) has to

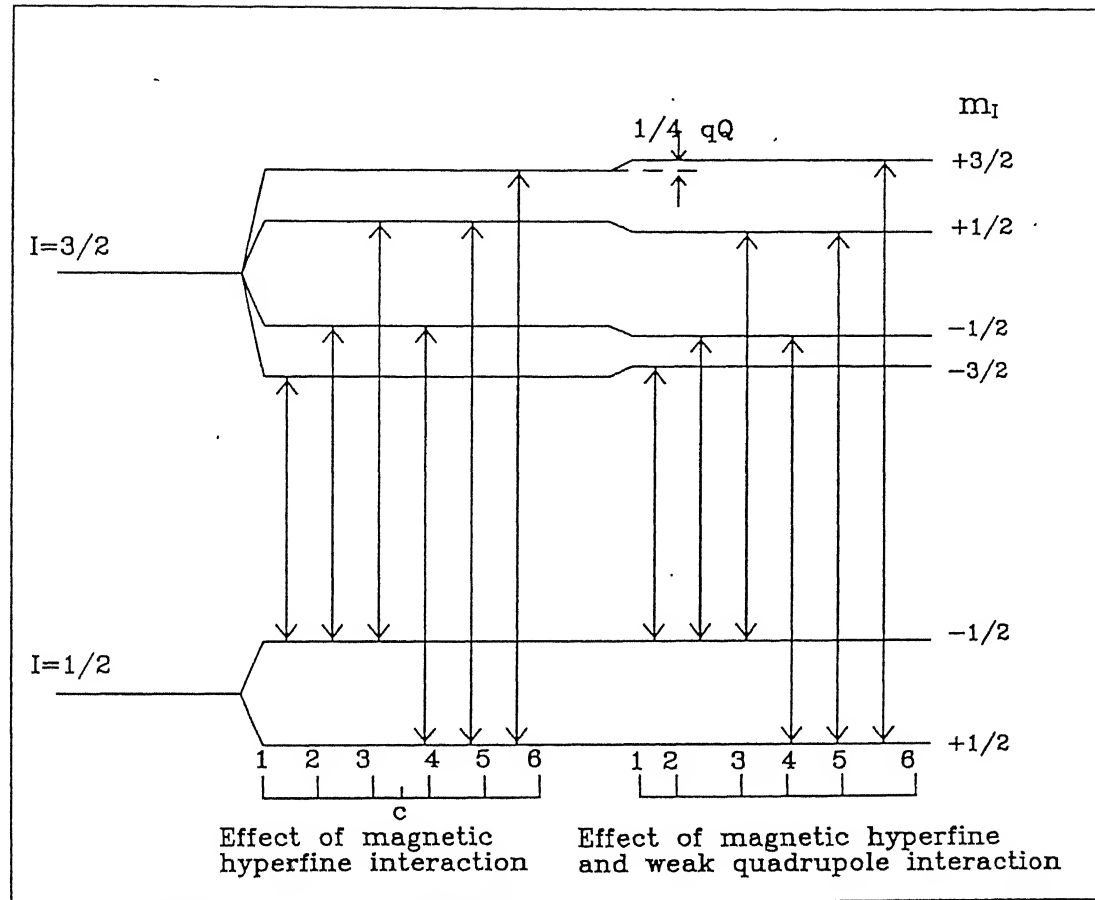


Fig.1.8. Effect of quadrupole interaction and a strong magnetic interaction on the energy levels of  $^{57}\text{Fe}$ . The number 1 to 6 indicating the line positions in the Mössbauer spectrum.

be averaged over all possible  $\theta$  and the relative intensities of the six hyperfine lines [equation (1.22)] follow the simple ratios

$$3:2:1::1:2:3 \quad (1.23)$$

Introduction of Doppler velocity  $v$  between the source and the absorber leads to a modification of the gamma-ray energy from  $E_\gamma$  to  $E_\gamma^D$  with

$$E_\gamma^D = E_\gamma \pm vE_\gamma/c \quad (1.24)$$

The internal magnetic field  $H_{int}$  at the  $^{57}\text{Fe}$  nucleus can be determined by measuring the peak positions of the resonance lines in the Mössbauer spectrum. In the case of  $^{57}\text{Fe}$  nucleus, the value of  $H_{int}$  can be shown to be

$$H_{int} = 0.843 * 10^5 (L_5 - L_3) * (\text{calibration constant}) \quad (1.25)$$

where  $L_3$  and  $L_5$  are the peak positions of the third and fifth line in the Mössbauer spectrum.

### 1.5. Scope of the present work

It is now well recognised that the  $^{57}\text{Fe}$  Mössbauer spectroscopy can be used as a sensitive and useful method to study electronic, magnetic, structural and phase properties of different iron-bearing materials having basic scientific and applied technological interest. We have carried out such studies of some technologically interesting iron-bearing materials and the results of these studies are described in the present thesis.

There are seven chapters in the present thesis. After providing an introduction to Mössbauer spectroscopy in the present chapter, the experimental methods used by us are described in the next chapter.

Our Mössbauer spectroscopic studies of the substitutionally disordered isostructural (fcc structure)  $\gamma\text{-Fe}_{80-x}\text{Ni}_x\text{Cr}_{20}$  ( $x = 30, 26, 19$  and  $14$ ) stainless steel alloys in the temperature range  $T = 10 - 295$  K are described in Chapter 3. These alloys exhibit paramagnetic, ferromagnetic, antiferromagnetic and spin-glass phases and provide an example of mixed or reentrant phase alloys. They have been systematically studied using other physical methods like neutron scattering, resistivity, magnetostriiction, specific heat etc. However equally systematic  $^{57}\text{Fe}$  Mössbauer spectroscopic measurements have not yet been reported for the  $\text{Fe}_{80-x}\text{Ni}_x\text{Cr}_{20}$  alloys. Theoretically the magnetic properties of these alloys provide interesting problems which need to be answered and Mössbauer spectroscopy can provide a wealth of experimental data in this respect. These alloys also have many potential industrial applications because of their useful properties e.g. high corrosion resistance, non-toxic, non-magnetic, creep resistance etc. Keeping all these aspects in mind we have experimentally measured the evolution of Mössbauer parameters like linewidth, centre-shift, distribution of hyperfine magnetic field and average hyperfine field etc. with temperature for different values of  $x$  (viz.  $x = 30, 26, 19$  and  $14$ ). These results are interpreted in terms of the magnetic transition and magnetic phase diagram. Debye temperature  $\Theta_D$  for the  $x = 30$  and  $x = 26$  alloys have been determined from the analysis of the second order Doppler shift.

In Chapter 4 we have presented our Mössbauer spectroscopic studies of Fe - 24 at% Al and Fe - 25 at% Al. The Fe-Al system forms a model object of transition metal-sp element system. Fe-Al

alloys having 21 - 31 at % Al are known to exhibit several attractive physical properties which render them candidate materials for structural and magnetic applications. These alloys possess high strength, low density, extremely good corrosion and oxidation resistance which make them suitable materials for structural applications while their magnetic properties (high permeability and large magnetostriction) render them useful for technological applications. These magnetic and physical properties can be varied by altering the composition and the process and rate of cooling and quenching. Keeping this in mind we have studied Mössbauer spectra of five Fe-24 at% Al and Fe-25 at% Al alloy sample processed via different cooling/quenching routes. The analysis of the Mössbauer parameters, distribution of hyperfine magnetic fields,  $P(H)$  and H-values have helped us to identify various Fe-atom configurations (nearest neighbour or next nearest neighbour) responsible for different phases formed in these different processing routes. Our results also indicate that the average hyperfine field  $\langle H \rangle$  depends on the average rate of cooling followed during the precipitation of these phases.

In Chapter 5 we have described our investigations of the effect of addition of 0.5 - 2.0 mass percent of Cr or Mn to Fe + 0.6% C steels using  $^{57}\text{Fe}$  Mössbauer spectroscopy and magnetic measurements. These low alloy steels containing refractory carbides belonging to the transition metals of group IV-VI of the periodic table have useful industrial applications. The analysis of present Mössbauer spectroscopic data indicate the presence of  $\alpha\text{-Fe}$ , 1nn (nearest neighbour) and 2nn phases in the Fe-C-Cr steels

and that of  $\alpha$ -Fe and 1nn phases in the Fe-C-Mn steels. These results provide interesting information about the magnetic disturbance around the solute atoms in these low alloy steels. The present magnetic measurements showed that the variation of saturation magnetic moments of Fe atoms under the external magnetic field in Fe-C-Cr and Fe-C-Mn steels show opposite but systematic behaviour.

Our Mössbauer spectroscopic studies of the metallic glasses  $\text{Fe}_{79}\text{B}_{16}\text{Si}_5$  and  $\text{Fe}_{78}\text{B}_{13}\text{Si}_9$  are presented in Chapter 6. The aim of the present study was to investigate the evolution of the hyperfine magnetic field distribution,  $P(H)$ , with the annealing temperature ( $T_a$ ) and annealing time period ( $t_a$ ) before these amorphous alloys crystallize. Keeping this aim in mind we chose  $T_a = 300, 350, 400, 450$  and  $475\text{ K}$  and  $t_a = 1 - 37\text{ h}$  (depending on  $T_a$ ). The present studies have demonstrated how the  $P(H)$  in these metallic glasses follow the kinetics of crystallization and how the time period of isothermal annealing plays an important role in the evolution of these  $P(H)$  distributions.

The last chapter describes the present studies of the kinetics of the roasting process of chalcopyrite minerals using Mössbauer spectroscopy and X-ray diffraction. Chalcopyrite minerals were roasted at  $(500 \pm 5)^\circ\text{C}$  for time intervals  $t = 1.0, 2.0, 3.0, 5.0, 10.0, 15.0, 20.0, 40.0$  and  $60.0\text{ mins}$  and at  $(650 \pm 5)^\circ\text{C}$  for time intervals  $t = 1.0, 2.5, 3.0, 5.0$  and  $10.0\text{ mins}$ . The observed Mössbauer parameters and the X-ray diffraction data have been analyzed to identify the iron compounds formed at different stages of roasting. A possible scheme of transformations

has been suggested to explain the observed kinetics.

It is hoped that these measurements carried out in the Fe-Ni-Cr alloys, Fe-Al alloys, low alloy steels, Fe-B-Si metallic glasses and chalcopyrite mineral have helped to extend our present understanding of these systems. The author has gained valuable experience of applying  $^{57}\text{Fe}$  Mössbauer spectroscopic technique to different types of materials and analyzing the results.

### References

- [1] R.L.Mössbauer, Z.Physik, 151, 124 (1958).
- [2] H.J.Lipkin, Ann. Phys. 9, 332 (1960).
- [3] H.Frauenfelder, "The Mössbauer Effect", (W.A.Benjamin Inc., New York 1962).
- [4] G.K.Wertheim, "Mössbauer Effect: Principles and Applications", (Academic Press, New York, 1964).
- [5] R.Herber, Ann. Rev. Phys. Chem. 17, 261 (1966).
- [6] "Chemical Applications of Mössbauer Spectroscopy", edited by V.I.Goldanskii and R.H.Herber, (Academic Press, New York, 1968).
- [7] "An Introduction to Mössbauer Spectroscopy", edited by L.May, (Plenum Press, New York, 1971).
- [8] N.N.Greenwood and T.C.Gibb, "Mössbauer Spectroscopy", (Chapman and Hall Ltd., London, 1971).
- [9] G.M.Bancroft, "Mössbauer Spectroscopy", (McGraw - Hill Book Co., Maidenhead, 1973).
- [10] H.Wegener, "Der Mössbauer Effekt", (Bibliographisches Institut AG, Mannheim, 1966).
- [11] "Mössbauer Spectroscopy", edited by U.Gönser, (Springer - Verlag, Berlin, 1975).
- [12] J.G.Stevens and L.H.Bowen, Analy. Chemistry, 48, 232R (1976).
- [13] G.K.Shenoy and F.E.Wagner, "Mössbauer Isomer Shifts", (North - Holland Publishing Co., Amsterdam 1978).
- [14] R.M.Housley and F.Hess, Phys. Rev. 146, 517 (1966).

## CHAPTER 2

### Experimental methods and data analysis

#### 2.1. Introduction

In this chapter we shall provide a brief description of the apparatus and methods of data analysis used in the present work. We shall begin with the Mössbauer spectrometer which is schematically shown in the block diagram of Fig.2.1. Mössbauer spectroscopy is now routinely used as an experimental technique and its methodology has been well described in the literature [1-9]. The present discussion dwells on various units shown in Fig.2.1 i.e.

(i) Radioactive source, (ii) Mössbauer spectrometer, (iii) Sample absorber, (iv) Gamma-ray detector and (v) Electronic instruments.

#### 2.2. Radioactive source

The desirable properties of the radioactive sources used in Mössbauer spectroscopy have been discussed in the literature [1-9]. All the present Mössbauer spectroscopic measurements were carried out by using the 14.4 keV gamma ray in the  $^{57}\text{Fe}$  nuclei for observing Mössbauer effect. A radioactive  $^{57}\text{Co}$  source deposited in Rh metal (host matrix) foil and supplied by the Amersham International Limited, Amersham, U.K. was used. The initial activity of this source was 25 mCi. According to the specifications provided by the suppliers the recoil-free fraction

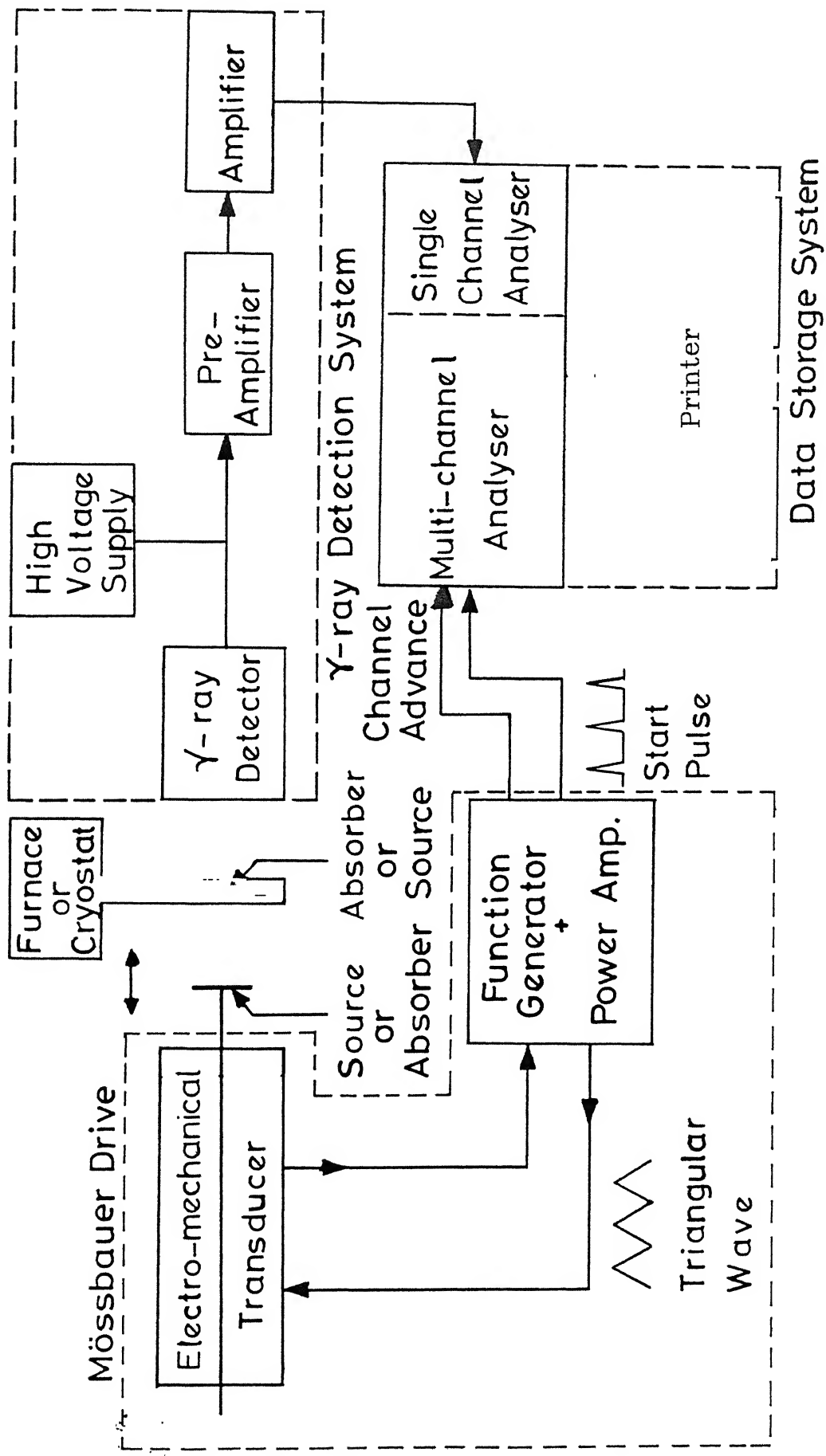


Fig. 2.1 Schematic block diagram of Mössbauer spectrometer.

of this source was 0.77. This source yielded a single Mössbauer line when observed with our Mössbauer spectrometer using potassium ferrocyanide absorber (at room temperature) and this line showed a full-width-at-half-maximum (FWHM) of  $0.30 \text{ mms}^{-1}$ . At room temperature linewidths observed with stainless steel (SS310) and sodium nitroprusside as absorbers were  $0.43 \text{ mms}^{-1}$  and  $0.24 \text{ mms}^{-1}$  respectively.

### 2.3. Mössbauer spectrometer

The heart of a Mössbauer spectrometer is the Mössbauer drive system which is a combination of units that provides measurable relative velocities (usually with constant acceleration) between the source and the absorber. In the present work we used the Mössbauer drive assembly supplied by WISSEL (Wissenschaftliche Electronik GmbH), Germany. This assembly consisted of a velocity transducer, a function generator and constant acceleration drive unit or power amplifier. In our setup WISSEL model MA-260 formed the velocity transducer while WISSEL model DFG-1200 formed the function generator. The latter unit produced a triangular reference signal which was fed to the power amplifier (model WISSEL MR-360). The output taken from the power amplifier is proportional to the ideal velocity of the transducer and it is fed to the driving coil of the transducer. The pickup coil mounted in the velocity transducer senses the actual velocity in the form of a pickup signal. A difference or error signal is obtained as the difference between the reference signal and the pickup signal and

this error signal is proportional to the deviation of the actual velocity from its stipulated value. After amplifying this error signal is fed back to the driving coil through a feedback loop so that the deviation from the stipulated velocity is minimised. The function generator provides a triangular voltage waveform (or reference signal) to the velocity transducer so that the radioactive source (mounted on the transducer) can be swept in both directions with velocities ranging between  $-V_{max}$  to  $+V_{max}$ . This gives rise to a relative velocity between the moving source and the stationary absorber and the absorption and transmission of the gamma rays through the absorber is then measured in terms of this relative velocity.

#### **2.4. Gamma-ray detection system**

A gas-filled proportional counter (Model I-1331, ECIL, India) was used to detect the 14.4 keV gamma rays transmitted through the absorber. This proportional counter contained krypton as ionizing gas and has a thin beryllium window and was provided with high voltage with the help of high voltage power supply (EG & G Ortec, Model 456) capable of supplying upto 3000 V at 10mA current. A gamma ray of given energy, when detected by the proportional counter, is converted into a linear charge pulse of a given amplitude. The charge pulse is then passed through a preamplifier (Canberra, Model 2006) which produces a gaussian voltage pulse. Next in line is a linear spectroscopy amplifier (Canberra, Model 2021) which amplifies these pulses to provide output pulses having

pulse heights in the range 0 to 10 volts. These analog pulses coming from the amplifier are then fed into the multichannel analyzer for data acquisition. A typical pulse height spectrum of gamma rays from the radioactive  $^{57}\text{Co}$  (in Rh) source is shown in Fig.2.2.

## 2.5. The multichannel analyzer: Data acquisition system

The multichannel analyzer (MCA) used by us consisted of an EG & G Ortec MCA card incorporated in a personal computer (PC). It is necessary to ensure that the appropriate Mössbauer gamma ray (i.e. having an energy of 14.4 keV) is selected before recording the Mössbauer spectrum. This selection is achieved by using the energy window of the MCA in the pulse height analysis (PHA) mode. The pulse height spectrum of  $^{57}\text{Co}$  in Rh always contains low-energy X-rays and their intensity was reduced by placing an aluminium foil between the source and the absorber. The selection of the 14.4 keV gamma ray was completed by using the upper level (ULD) and lower level (LLD) discriminators in the MCA. Such a careful selection is very important for increasing the signal - to - noise ratio. The resulting Mössbauer spectrum is finally stored in the 512 channels of the MCA operated in the multiscaling (MCS) mode. It was necessary to obtain a synchronization of the channel number of the MCA with the increment in the relative velocity ( $\Delta V$ ) of the source and this was achieved by advancing the address of the MCA memory in steps with the help of an external clock. This process involves dividing the reference signal (a triangular waveform)

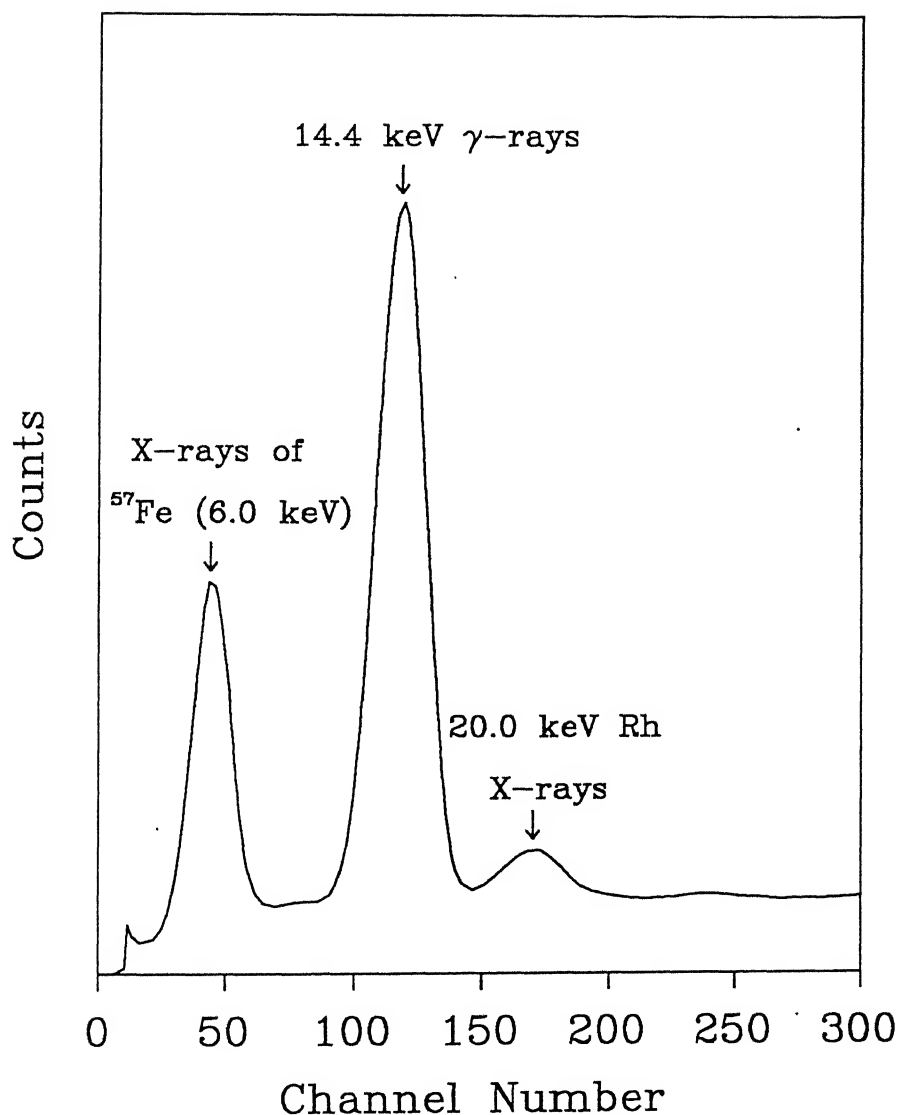


Fig.2.2. Pulse height spectrum of  $^{57}\text{Co}$  in Rh matrix  
(Mössbauer source) measured using proportional counter.

into 512 pulses by the external clock, with the first pulse coinciding with the beginning of the reference signal. The address of the memory is advanced to record the signal in the next channel, each time the MCA receives such a pulse. Because the reference signal fed to the transducer is of symmetric nature, two identical Mössbauer spectra (each extending over 256 channels) are recorded in the 512 channels of the MCA.

## 2.6. Performance and calibration of the Mössbauer spectrometer

The following standard absorbers were used to check the performance and calibration of the Mössbauer spectrometer:

- (i) natural iron ( $\alpha$ -Fe) foil 25  $\mu\text{m}$  thick
- (ii) enriched iron foil (containing 1.9 mg/cm<sup>2</sup> of  $^{57}\text{Fe}$ )
- (iii) potassium ferrocyanide (5mg/cm<sup>2</sup> of iron)
- and (iv) sodium nitroprusside (5mg/cm<sup>2</sup> of iron).

All these absorbers were obtained from the Amersham International Limited, Amersham, U.K. For each measurement reported in the following chapters, the Mössbauer absorbers were prepared according to the special requirements of the problem involved. These methods of preparation are explained in the following chapters at appropriate places. However the absorber thickness and the geometry of the absorber (vis - a -vis the source and gamma ray detector) had to be optimised to keep the broadening of the Mössbauer lines to a possible minimum. This broadening is usually described in terms of  $\Gamma_{\text{ex}}$ , the experimentally determined full-width-at-half-maximum (FWHM) of the Mössbauer lineshape (which is Lorentzian in character) [4]. The Mössbauer line is

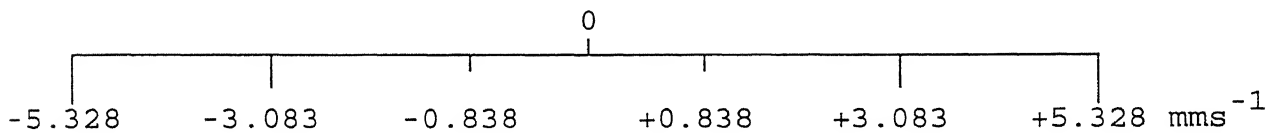
broadened (or  $\Gamma_{\text{ex}}$  increased) due to the thickness of the source as well as the absorber. These effects are well studied and reviewed in the literature [1-9] and will not be discussed here. When the thickness of sample absorber is too small, the number of active particles (i.e. which can cause resonance during the absorption) are very small and as a result the peak intensity of the Mössbauer line is poor. Hence a very thin absorber is not suitable for good spectrum. On the other hand, larger thickness increases  $\Gamma_{\text{ex}}$  and hence an optimum thickness is desirable. In the present case, this optimum thickness had to be determined by performing trial runs and analyzing the results.

Another important effect which determines the shape and width  $\Gamma_{\text{ex}}$  of a Mössbauer line is the so-called effect of the relative geometry between the source, the absorber and the detector [10-13]. There are two major causes for these effects. The first one arises because the distance between the source and the detector is continuously changed in the acceleration mode. The second effect is the so-called cosine effect. In our work we considered both these effects while arranging the geometry of the experiment and tried to minimise the FWHM,  $\Gamma_{\text{ex}}$ , of the Mössbauer lines observed with our spectrometer. It was found that for natural iron FWHM of Mössbauer spectrum is  $0.24 \text{ mms}^{-1}$ .

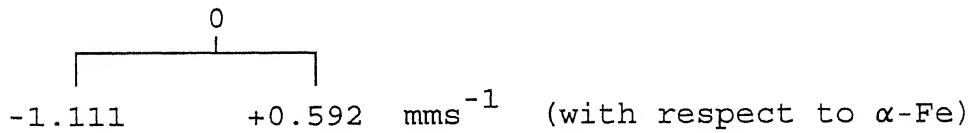
After ensuring satisfactory performance of the Mössbauer spectrometer, it was necessary to calibrate it regularly so that each measured spectrum could be appropriately labelled with the velocity scale on the x-axis. Standard absorbers of natural iron ( $\alpha$ -Fe enriched in  $^{57}\text{Fe}$ ) and sodium nitroprusside were used to

calibrate the Mössbauer spectrometer and MCA. The Mössbauer spectra of these standard absorbers were recorded before every run and the channel numbers corresponding to each peak position were carefully determined. The peak positions of the Mössbauer spectra from these two absorbers in terms of the velocity ( $\text{mms}^{-1}$ ) of the source are known quantities in the literature as quoted below:

(a)  $\alpha$ -Fe (natural iron), a sextet



(b) Sodium nitroprusside, a doublet



Various parameters obtained for  $\alpha$ -Fe absorber using present Mössbauer spectrometer are summarised below to indicate the level of its performance,

- (1) centroid position  $\Rightarrow$  128.134 channel
- (2) FWHM of the inner lines  $\Rightarrow$   $0.24 \text{ mms}^{-1}$
- (3) Velocity/channel  $\Rightarrow$   $0.086 \text{ mms}^{-1}$

## 2.7. Data analysis

### 2.7.1. Determination of Mössbauer parameters

Several computer programs have been developed by different workers for analyzing measured Mössbauer spectra with an aim of

precise determination of Mössbauer parameters (i.e. isomer shift, quadrupole splitting, hyperfine magnetic field), linewidths, intensities etc. In our work we used computer program based on the method proposed by Law and Bailey [14]. This method is based on the assumption that the relaxation effect is small and the Mössbauer absorption line can be approximated by a Lorentzian curve. The computer program is then written with an aim to perform a satisfactory curve-fitting so that the "guess values" of the parameters are found and close agreement between experimental data and the values predicted by assumed function are found.

Let the experimental data points describing the Mössbauer spectrum be denoted by  $y_i$  and let the function  $\phi_i = \phi_i(B_1, B_2, \dots, B_n)$  be the functional form chosen for these data points. The condition for obtaining the set of parameters  $B_k$  is to minimise the quantity

$$S^2 = \sum_{i=1}^N s_i^2 = \sum_{i=1}^N (y_i - \phi_i)^2 \quad (2.1)$$

where  $N$  is the number of experimental points. This leads to the condition for minimum as

$$\frac{ds^2}{dB_k} = 0 \quad (2.2)$$

and it leads to  $n$  simultaneous equations. Solving these equations, we can obtain a correction  $\Delta B_k$  for the initial approximate value  $B_k$ . The new parameters  $B_k^{i+1} = B_k^i + \Delta B_k$  are then obtained, with the superscript  $i$  referring to  $i^{\text{th}}$  iteration. An examination of new parameters is made to ensure that  $S^2$  is minimum and this gives better results if the increment of the parameters is restricted

such that

$$B_k^{i+1} = B_k^i + \alpha \Delta B_k \quad (2.3)$$

where  $\alpha$  is less than 1. Convergence is reached when successive values differ by an amount less than the preassigned tolerances. Calculation of chi-square ( $\chi^2$ ) value is made to test the goodness-of-fit. The standard error in the fitted parameters  $B_k$  can be determined with the help of error matrix which can be calculated from the inversion matrix. The values of Mössbauer parameters obtained for natural iron using least-squares-fit computer program are as follows:

- (i) Isomer shift:  $(0.00 \pm 0.01) \text{ mms}^{-1}$
- (ii) Quadrupole splitting:  $(0.00 \pm 0.01) \text{ mms}^{-1}$
- (iii) Internal magnetic field:  $(330 \pm 2) \text{ kOe}$
- (iv) Full-width-at-half-maximum:  $(0.24 \pm 0.01) \text{ mms}^{-1}$

Mössbauer parameters obtained for other standard absorbers using least-squares-fit program are as follows:

#### 1. Stainless steel (SS310):

- (i) Isomer shift:  $(-0.074 \pm 0.01) \text{ mms}^{-1}$
- (ii) Quadrupole splitting:  $0.00 \text{ mms}^{-1}$
- (iii) Internal magnetic field:  $0.00 \text{ kOe}$
- (iv) Full-width-at-half-maximum:  $(0.43 \pm 0.01) \text{ mms}^{-1}$

#### 2. Sodium nitroprusside:

- (i) Isomer shift:  $(-0.257 \pm 0.01) \text{ mms}^{-1}$
- (ii) Quadrupole splitting:  $(1.7 \pm 0.01) \text{ mms}^{-1}$
- (iii) Internal magnetic field:  $0.00 \text{ kOe}$
- (iv) Full-width-at-half-maximum:  $(0.24 \pm 0.01) \text{ mms}^{-1}$

### 2.7.2. Determination of hyperfine field distribution, $P(H)$

In many cases, the sample studied by Mössbauer spectroscopy shows a distribution of magnetic hyperfine fields,  $P(H)$ . One such familiar system is iron-rich metallic glass system (which we have studied, see Chapter 6 ) where the presence of  $P(H)$  is attributed to the presence of large number of inequivalent sites in the glass with the strength of hyperfine interaction changing from site to site. It, therefore, becomes necessary to unfold the measured Mössbauer spectrum to yield a graph of the probability,  $P(H)$ , of the magnetic hyperfine field  $H$  versus  $H$ . Several methods have been proposed in the literature [15-20] to achieve this. The simplest methods developed for this purpose assume analytical expressions for  $P(H)$  and determine the parameters of these functions by a least-squares-fit to the data [15-17]. Other and more realistic methods do not assume any special expression for  $P(H)$ . In the method developed by Window[18],  $P(H)$  is described in terms of a Fourier series, while Hesse and Rübartsch [19] make use of discrete step functions. Both these methods have been found to give similar results. In another method Vincze [20] determined  $P(H)$  of subspectra obtained by linear combinations of spectra measured with different polarizations. Although this method is model independent, it is limited to very soft ferromagnetic systems only [21].

Many workers have widely used the method developed by Window [18] to determine hyperfine field distributions in amorphous magnetic systems. In this method  $P(H)$  is expressed in a series of

cosine terms in the interval  $H = 0$  to  $H = H_{\max}$ :

$$P(H) = \sum_{n=1}^N b_n \left[ \cos(n\pi H/H_{\max}) - (-1)^n \right] \quad (2.4)$$

where  $n = 1, 2, 3 \dots N$  and the boundary conditions  $P(H=0) = 0$  and  $P(H = H_{\max}) = 0$ ;  $(dP/dH)_{H=0} = 0$  and  $(dP/dH)_{H=H_{\max}} = 0$  apply. In practice the Fourier coefficients  $b_n$  are determined from the best least-squares-fit to the data, by solving  $N+1$  simultaneous equations. This makes the computation time very long if  $N$  is assumed to be very large, although larger  $N$  assures good convergence of the series in equation (2.4). On the other hand smaller value of  $N$  can lead to truncation errors which appear in the form of oscillations and negative values of  $P(H)$ . In addition to the truncation of the Fourier expansion, the incorrect intrinsic parameters and the statistical fluctuations give rise to such nonphysical artifacts to the  $P(H)$  curves. Usually the assumptions of single average isomer shift and negligible electric quadrupole moment are made [23], and we also followed this scheme.

Previous work [19, 21] has shown that the choice of the values of  $N$ ,  $H_{\max}$  etc. has to be made carefully before applying Window's method [18]. Keeping this in mind we carried out some tests with the version of computer program which was based on Window's method and which was used by us. The computer program was first tested by analysing the six-finger Mössbauer spectrum observed for  $\alpha$ -Fe. The resulting  $P(H)$  distribution is shown in Fig.2.3 along with the Mössbauer spectrum (observed as well as fitted). These results gave  $H_{\text{peak}} = 330$  kOe,  $\langle H \rangle = 316$  kOe and  $\Gamma(\text{FWHM}) = 26$  kOe with the

$\chi^2$ - value being 2.96 when N = 30, with  $H_{\max}$  = 400 kOe.

Another test involved the analysis of the Mössbauer spectrum of the as-quenched sample of the metallic glass  $Fe_{78}B_{13}Si_9$  measured at room temperature. In this test  $H_{\max}$  = 400 kOe and N was varied from 2 to 17. A plot of average hyperfine field  $\langle H \rangle$  and the  $\chi^2$ -value against N showed that a choice of the optimum value N = 15, was a satisfactory choice (Fig.2.4). It may be mentioned that the value N = 15 was also chosen by Ganesan et al. [24] in their analysis of  $Fe_{95-x}W_5B_x$  metallic glasses. In the case of semicrystalline sample of metallic glass  $Fe_{79}B_{16}Si_5$  annealed at 748 K for 8h, our results (Fig.2.5) shows that the choice of the optimum value N = 20 is a satisfactory choice.

## 2.8. Other measurements

In order to corroborate the results obtained for various samples with Mössbauer measurements, we also carried out other measurements using X-ray powder diffraction and magnetization measurements.

X-ray powder diffraction patterns of the samples were recorded by using Rich and Seifert ISO-Debyeflex 2002 diffractometer with a Cr  $K_\alpha$  target. All these studies were performed at room temperature.

Magnetization measurements were done by using vibrating sample magnetometer (Model 155, PAR) and using a field upto 10 KG. All these measurements were done at room temperature.

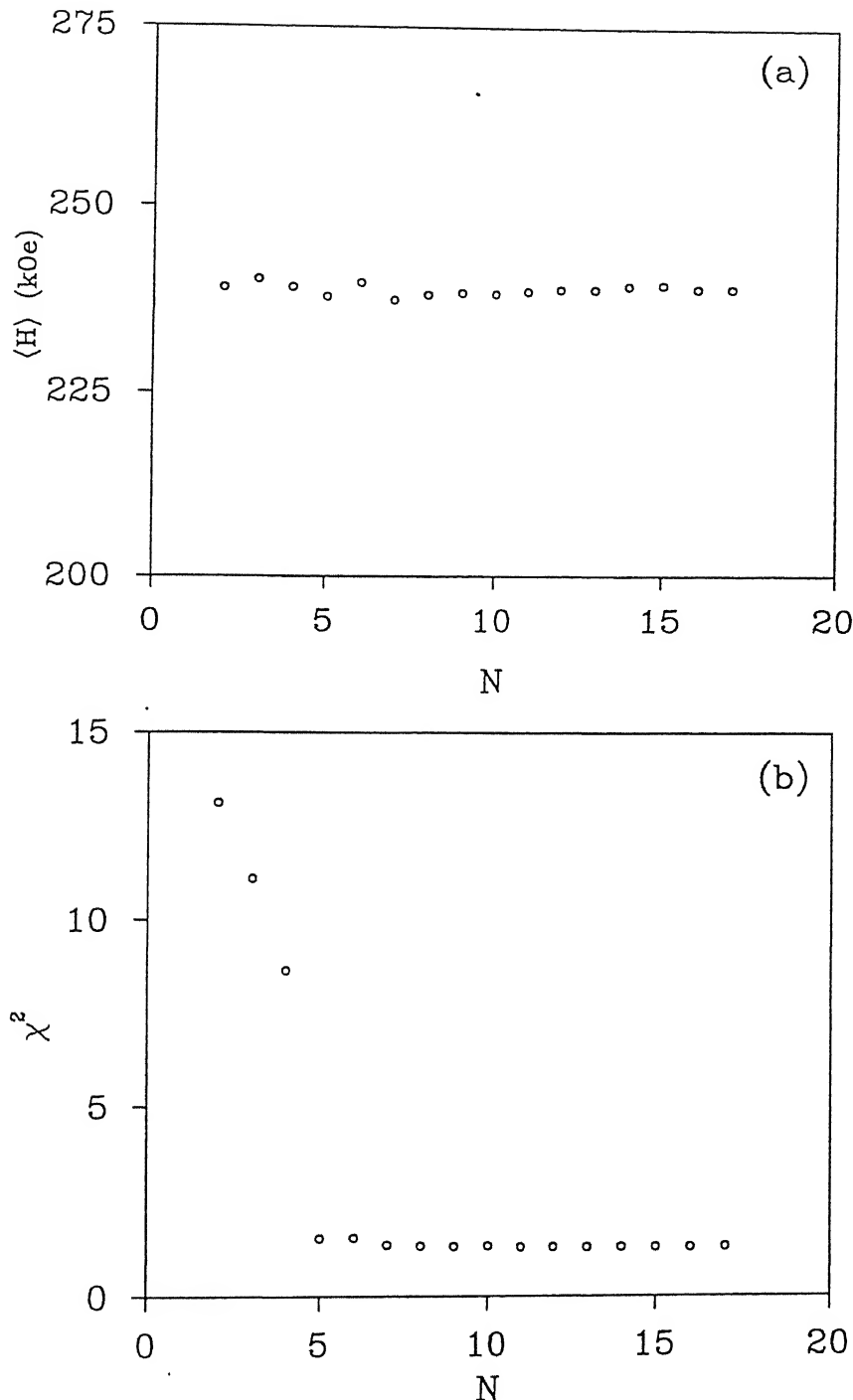


**Fig. 2.4.** Variation of (a)  $\langle H \rangle$  and (b)  $\chi^2$  with  $N$  (number of cosine terms) for  $\text{Fe}_{78}\text{B}_{13}\text{Si}_9$  metallic glass sample in as-received condition.

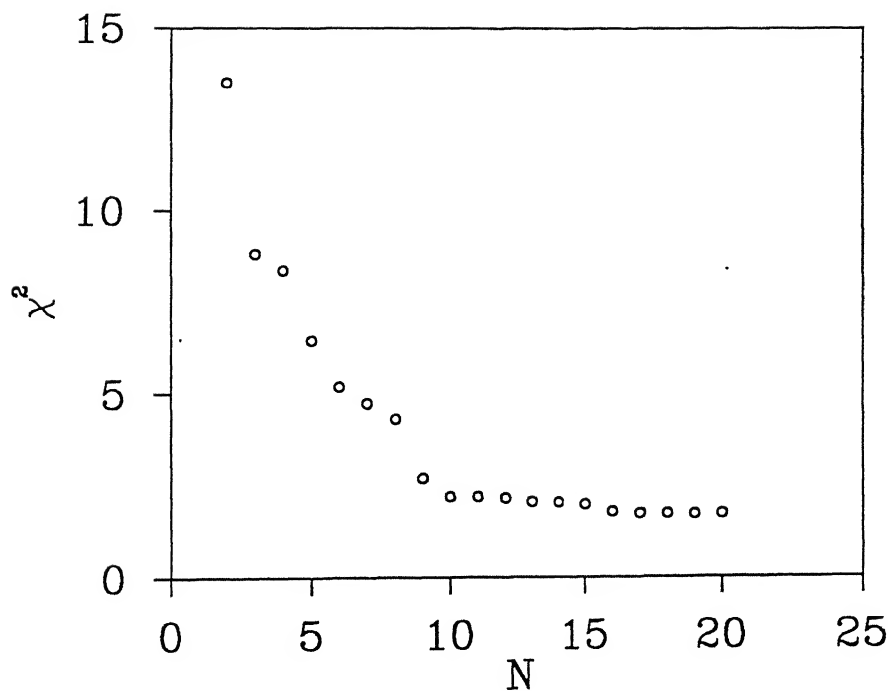


Fig. 2.5. Variation of  $\chi^2$ -with N (number of cosine terms) for  $\text{Fe}_{79}\text{B}_{16}\text{Si}_5$  metallic glass sample annealed at 748 K for 8h.

References

- [1] . N.Benczer-Koller and R.H.Herber in "Chemical Applications of Mössbauer Spectroscopy", edited by V.I.Goldanskii and R.H.Herber (Academic Press, New York, 1968), p.
- [2] U.Gonser in "Mössbauer Spectroscopy", edited by U.Gonser, (Springer-Verlag, Berlin-Heidelberg, 1975) p.
- [3] N.N.Greenwood and T.C.Gibb, "Mössbauer Spectroscopy", (Chapman and Hall Ltd., London, 1971).
- [4] G.M.Bancroft, "Mössbauer Spectroscopy, an Introduction for Inorganic Chemists and Geochemists", (McGraw-Hill, London, 1973).
- [5] A.Vertes, A.Korecs and K.Burger, "Mössbauer Spectroscopy", (Elsevier Scientific Publishing Co., Amsterdam, 1979).
- [6] V.G.Bhide, "Mössbauer Effect and its Applications", (Tata McGraw-Hill Publishing Co. Ltd., New Delhi, 1973).
- [7] "Mössbauer Effect Methodology", vols. 1-9, edited by I.J.Gruverman, (Plenum Press, New York, 1965 - 74).
- [8] J.J.Spijkerman in "An Introduction to Mössbauer Spectroscopy", edited by L.May, (Plenum Press, New York, 1971).
- [9] H.Wegener, "Der Mössbauer-Effekt", (Bibliographisches Institut AG, Mannheim, 1966).
- [10] S.Margulies and J.R.Ehrman, Nucl. Instr. and Meth. 12, 131 (1961).
- [11] D.A.Shirley, M.Kaplan and P.Axel, Phys. Rev. 123, 816 (1961).
- [12] D.A.O'Connr, Nucl. Inst. and Meth. 21, 318 (1963).

- [13] A.J.Stone, Nucl. Inst. and Meth., 107, 285 (1973).
- [14] V.J.Law and R.V.Bailey, Chem. Eng. Sc. 18, 189 (1963).
- [15] T.E.Sharon and C.C.Tsuei, Solid State Commun. 9, 1923 (1971).
- [16] T.E.Sharon and C.C.Tsuei, Phys. Rev. B5, 1047 (1972)
- [17] J.Logan and E.Sun, J.Non-Cryst. Solids, 20, 285 (1976).
- [18] B.Window, J.Phys. E: Sci. Instrum. 4, 401, (1971).
- [19] J.Hesse and A.Rübartsch, J.Phys. E: Sci. Instrum. 7, 526, (1974).
- [20] I.Vincze, Solid State Commun. 25, 689, (1978).
- [21] H.Keller, J.Appl.Phys. 52, 5268 (1981).
- [22] C.L.Chien and H.S.Chen, J.Phys. C2, 118 (1979).
- [23] C.L.Chien, D.Musser, E.M.Gyorgy, R.C.Sherwood, H.S.Chen, F.E.Luborsky and J.L.Walter, Phys.Rev. B20, 283 (1979).
- [24] K.Ganesan, A.Narayanasamy and T.Nagarjan, J.Phys. Condens. Matter 2, 4227 (1990).

## CHAPTER 3

### Magnetic phase transition study of $Fe_{80-x}Ni_xCr_{20}$ ternary alloy system

#### 3.1 Introduction

There has been considerable interest in the study of magnetic materials having a random mixture of ferromagnetic and antiferromagnetic interactions. One such class of materials is the Fe-Ni binary alloy system which is very interesting from the point of view of basic magnetism as well as industrial applications [1]. The iron-rich Fe-Ni alloys having 35 at% Ni are known as Invar alloys while the nickel-rich Fe-Ni alloys with Ni concentrations of around 75 at% Ni are well known as permalloys which are characterised by very high permeability and have a wide range of applications in the industry. For practical applications a third alloying element (e.g., Mo, Si, Ge, Cr, etc.) is added to the Fe-Ni system so that the permeability can be increased while costs can be reduced by replacing expensive nickel by a cheaper element. In particular, it has been found that the magnetic properties of the Fe-Ni alloys can be very much improved by the addition of Cr. Thus Nakamura [2] has shown that the initial permeability of the Fe-Ni-Cr alloys increased with increasing Cr concentration and at 12 at% Cr, it becomes almost ten times as large as that for the binary Fe-Ni alloys. To cite some typical industrial applications,

$\text{Fe}_{54}\text{Ni}_{38}\text{Cr}_8$  alloys are used for manufacturing shield plates of floppy disc drives and video tape recorders, iron cores of watches, etc. From the physicist's point of view the Fe-Ni-Cr system provides several challenging problems. Firstly, there is no unique theory yet found to explain the magnetism of 3d transition metal alloys although a wealth of experimental data have been collected. Secondly, the antiferromagnetism of Fe in the fcc  $\gamma$  phase of the Fe-Ni alloys arises out of the negative exchange integral of electrons of nearest neighbour Fe atoms in the fcc  $\gamma$  phase. However, owing to the  $\gamma$ - $\alpha$  phase transformation it is not possible to study the antiferromagnetic phase of Fe below 1180 K. This difficulty can be circumvented by the addition of Cr or Mn or V so that the  $\gamma$ - phase is stabilised and then the complete transformation region from antiferromagnetism (Fe-rich) to ferromagnetism (Ni-rich) within the same crystallographic fcc phase can be studied. In the alloy system Fe-Ni-Cr, nature has thus provided us with a convenient system whose ternary and magnetic phase diagrams are well studied [3]. By varying the composition and the temperature it is possible to study different magnetic phases of the Fe-Ni-Cr alloys. Keeping these interests in mind the Fe-Ni-Cr alloys have been studied with different experimental methods like neutron scattering [3-6], magnetic measurements [3, 4], resistivity measurements [7], magnetoresistance studies [8], etc.  $^{57}\text{Fe}$  Mössbauer spectroscopy has proved to be a valuable microscopic tool for studying the magnetic properties of iron-based alloys. As early as 1963 the  $^{57}\text{Fe}$  hyperfine field in the Fe-Ni alloys was studied by Johnson et

CENTRAL LIBRARY  
1977  
KANPUR

Ref No A 123637

al. [9] using Mössbauer spectroscopy. Many other Mössbauer spectroscopic studies of the Fe-Ni alloys have followed during the last three decades [10]. However, not many reports are found in the literature about the application of Mössbauer spectroscopy to the study of Fe-Ni-Cr alloys. Although Bendick and Pepperhoff [11] have determined the Neel and Curie temperatures of the  $\text{Fe}_{80-x}\text{Ni}_x\text{Cr}_{20}$  alloys using  $^{57}\text{Fe}$  Mössbauer spectroscopy, the main emphasis of their work was on the investigation of specific heat anomalies. Recent Mössbauer investigations of the Fe-Ni-Cr alloys by Gaffari et al. [12] dealt with the difference between magnetic moments for the as-rolled and annealed samples and secondly the Cr content in their samples was low (<0.01 to 11.8 wt%). Other Mössbauer spectroscopic studies [13,14] of the Fe-Ni-Cr alloys have involved the study of corrosion protection and electrochemical processes.

On the other hand the Fe-Ni-Mn alloys have been well studied by Mössbauer spectroscopy [10,15]. Keeping all these aspects in mind we have measured Mössbauer spectra of the polycrystalline substitutionally disordered  $\gamma$ -  $\text{Fe}_{80-x}\text{Ni}_x\text{Cr}_{20}$  ( $x = 30, 26, 19$  and  $14$ ) stainless steel alloys in the temperature range of 10 to 295 K. The choice of the composition of the alloy (i.e. Cr = 20 at% and the x-values) and the temperature range was made with the help of the ternary phase diagram (Fig.3.1) and the magnetic phase diagram (Fig.3.2) of the Fe-Ni-Cr system as reported by Majumdar and Blanckenhagen [3]. The values of the transition temperatures, viz., Curie temperature ( $T_C$ ), spin-glass temperature ( $T_{SG}$ ) and the Neel temperature ( $T_N$ ), as given by Majumdar and Blanckenhagen [3],

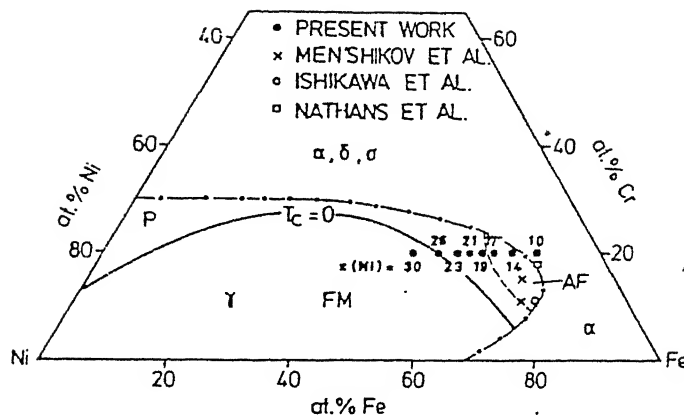


Fig. 3.1. Ternary diagram of FeNiCr system showing crystallographic and magnetic phases. The dotted-dashed line separates the  $\gamma$  phase from  $\alpha$ ,  $\delta$  and  $\sigma$  phases at room temperature. The solid line for  $T_C = 0$  separates the ferromagnetic (FM) phases from the paramagnetic (P) one [Taken from Ref.3].

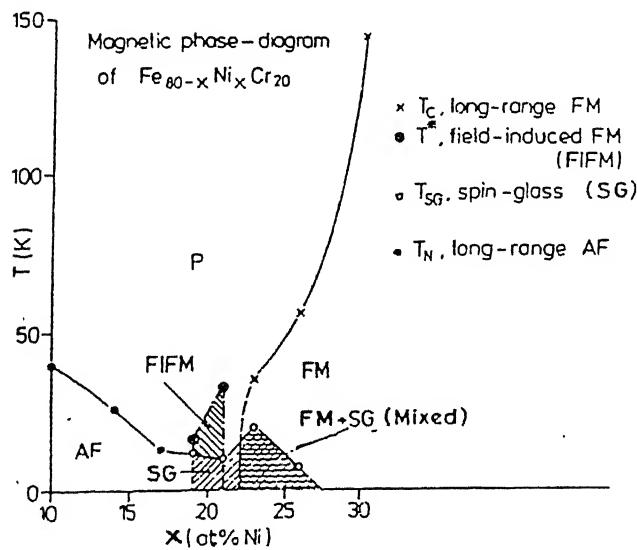


Fig. 3.2. Temperature ( $T$ ) vs Ni concentration ( $x$  in units of at. %) magnetic phase diagram of  $\text{Fe}_{80-x}\text{Ni}_x\text{Cr}_{20}$  alloys ( $10 \leq x \leq 30$ ) [Taken from Ref.3].

are shown in Table 3.1. These results show that by varying x and temperature the  $\text{Fe}_{80-x}\text{Ni}_x\text{Cr}_{20}$  alloys can be transformed from long-range ferromagnetic (FM) to long-range antiferromagnetic (AFM) phases through spin-glass (SG) and reentrant spin-glass (RSG) phases, retaining the fcc  $\gamma$ -phase throughout. It is well recognised that the  $^{57}\text{Fe}$  Mössbauer spectroscopy provides an useful microscopic point-probe for the identification and study of different magnetic phases. Further the  $^{57}\text{Fe}$  Mössbauer spectroscopy has been applied to study other mixed or reentrant phase alloys like Au-Fe, Fe-Ni-Mn, etc. It can thus be seen that our choice of the x-values and temperature ranges provide a rich menu which can allow the technique of  $^{57}\text{Fe}$  Mössbauer spectroscopy to systematically study the hyperfine magnetic fields in different phases. As far as we know such a systematic study of the hyperfine magnetic fields in the  $\text{Fe}_{80-x}\text{Ni}_x\text{Cr}_{20}$  alloys using Mössbauer spectroscopy has not been reported in the literature so far.

### 3.2. Experimental

The samples of  $\text{Fe}_{80-x}\text{Ni}_x\text{Cr}_{20}$  ( $x = 30, 26, 19$  and  $14$ ) used in the present experiments are from the same lot of alloys which were used for magnetic measurements and neutron diffraction experiments [3]. The method of their preparation has been described previously [3]. The Mössbauer absorbers were prepared from powdered samples and were used to record transmission Mössbauer spectra in the temperature range of  $10$  to  $295$  K. The details of the Mössbauer spectrometer have already been described in Chapter 2. However, the requirement of temperature-dependent studies for the present

Table. 3.1. Values of transition temperatures  $T_C$ ,  $T_{SG}$   $T_N$  and saturation magnetization  $4\pi M_S$  in  $Fe_{80-x}Ni_xCr_{20}$  ( $x = 30, 26, 19$  and  $14$ ) alloys as reported by Majumdar and Blanckenhagen [3].

| $x$<br>(at %) | $T_C$<br>(K) | $T_{SG}$<br>(K) | $T_N$<br>(K) | $4\pi M_S$<br>(KG) |
|---------------|--------------|-----------------|--------------|--------------------|
| 30            | 144          | —               | —            | 3.8                |
| 26            | 56           | 7               | —            | 1.92               |
| 19            | —            | 12              | —            | —                  |
| 14            | —            | —               | 26           | —                  |

work needed a modification of the Mössbauer spectrometer. This was achieved by installing an exchange gas variable temperature system obtained from JANIS. The system was installed as an integral part of a closed-cycle helium refrigerator and it consisted of a copper tube (with mylar windows) mounted on a cold head. The tube was surrounded by a double-walled steel shroud in order to isolate the cold head and the sample holder area from the surroundings (Fig.3.3). The sample was positioned inside the copper tube and the sample holder was separated from the shroud by metallic bellows so that they could absorb the vibrations generated during the operation of the refrigerator. The entire assembly was fixed on a cement concrete bench. The partition above the vibration-isolation stage was fixed to a thick aluminium plate which in turn was rigidly bolted to two supporting columns. The transducer and the detector were separated from the concrete bench by thick foam to eliminate any transmission of vibrations present in the bench. An oil diffusion pump (IBP type 0-500) was used to evacuate the shroud. The temperature of the sample was determined by using a Si-diode sensor (LAKESHORE Cryotronics model DRC-91C) which could achieve a temperature stability of 0.01 K. For the measurement purposes the Mössbauer absorbers were wrapped in a thin aluminium foil and they were firmly anchored to the copper mount of the sample holder. This additional instrumentation led to a longer separation between the source - absorber - detector as well as greater absorption of the 14.4 keV gamma rays. However, good statistics in the counting rate was maintained by using a stronger source of  $^{57}\text{Co}$  and longer counting periods.

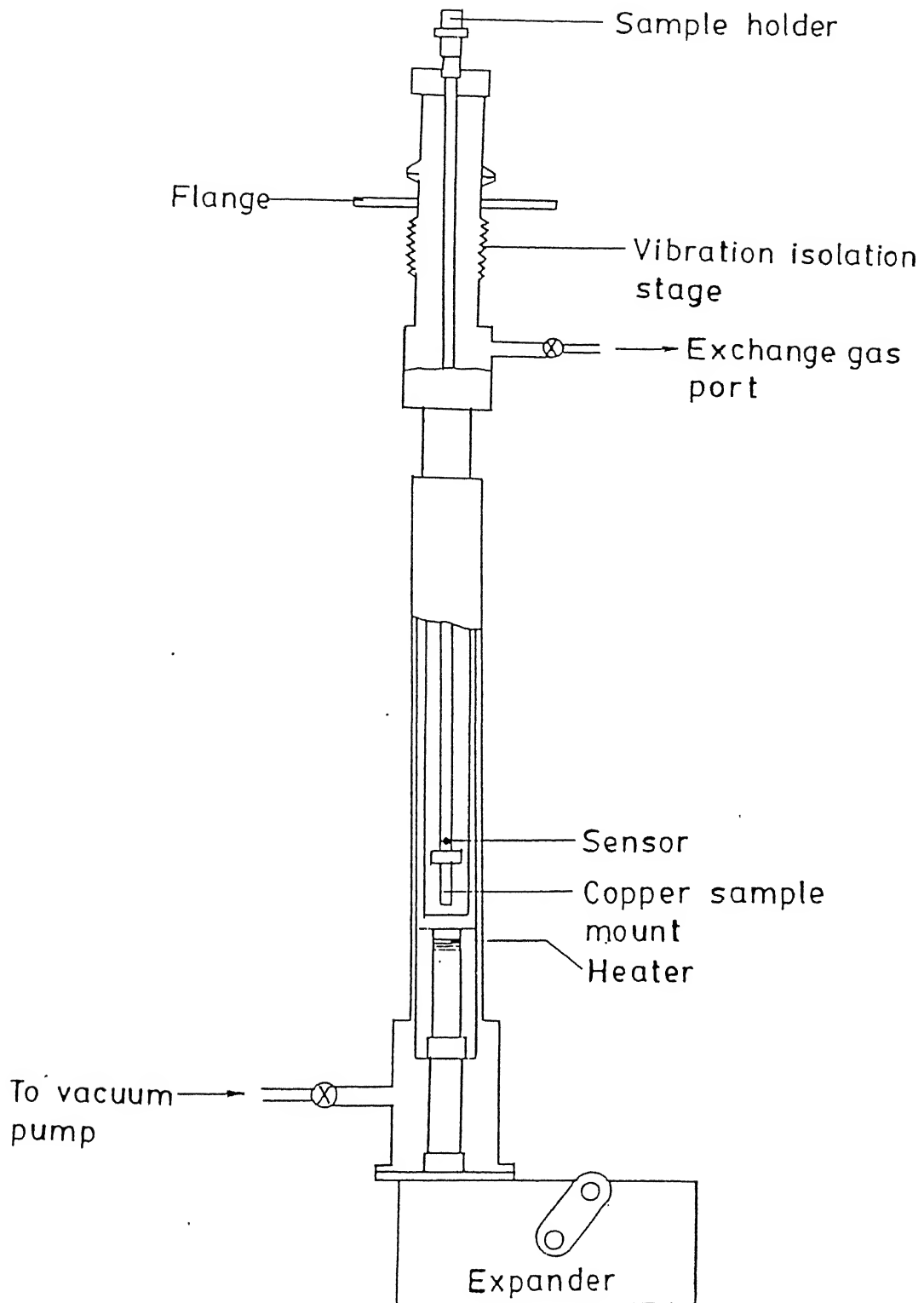


Fig. 3.3. Helium cryostate used for low-temperature Mössbauer spectroscopic studies.

The analysis of the Mössbauer spectra was carried out with computer programs using two methods. In the first method a least-squares-fitting program employing Lorentzian shapes for the peaks and an iterative procedure was used. In the second method we followed the procedure of Window [16] to obtain hyperfine field distributions,  $P(H)$ , from the measured Mössbauer spectra.

### 3.3. Results and discussions

#### 3.3.1 Introduction

We shall now present and discuss the  $^{57}\text{Fe}$  Mössbauer spectra of  $\text{Fe}_{80-x}\text{Ni}_x\text{Cr}_{20}$  alloys according to their  $x$ -values in the following sections.

#### 3.3.2 Alloy with $x = 30$ .

The magnetic phase diagram (Fig.3.2) indicates that the alloy with  $x = 30$  is paramagnetic in the range of 144 to 295 K and is ferromagnetic below 144 K. Mössbauer spectra of this alloy measured at 10, 20, 50, 60, 70, 75, 90, 110, 115, 120, 125, 130, 135, 140, 175, 200, 240, and 295 K along with the hyperfine field distributions,  $P(H)$  are shown in Fig.3.4. At  $T = 295$  K the Mössbauer spectrum consists of a single, narrow peak having a center shift  $CS = -0.092 \text{ mm s}^{-1}$  and a full width at half maximum,  $\Gamma = 0.40 \text{ mm s}^{-1}$  which is slightly broader than the natural linewidth due to the effective finite thickness of the absorber when mounted in the cryostat. This narrow single-line spectrum at 295 K is attributed to the paramagnetic phase as expected from the magnetic phase diagram (Fig.3.2). As the temperature of the sample was

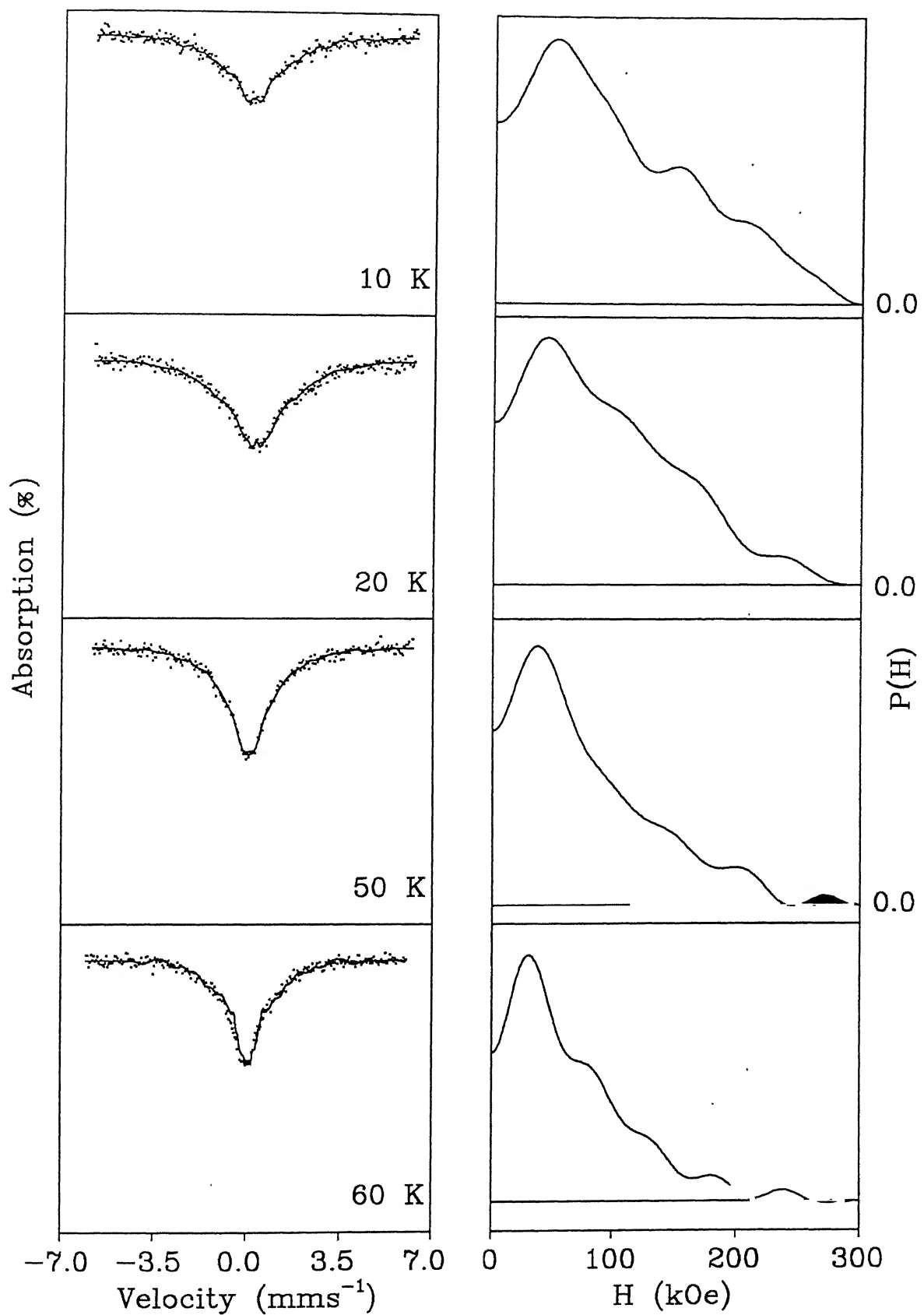


**Fig. 3.4.** Mössbauer spectra of  $\text{Fe}_{50}\text{Ni}_{30}\text{Cr}_{20}$  sample at different temperatures and corresponding hyperfine field distributions. (Continued on the next page)

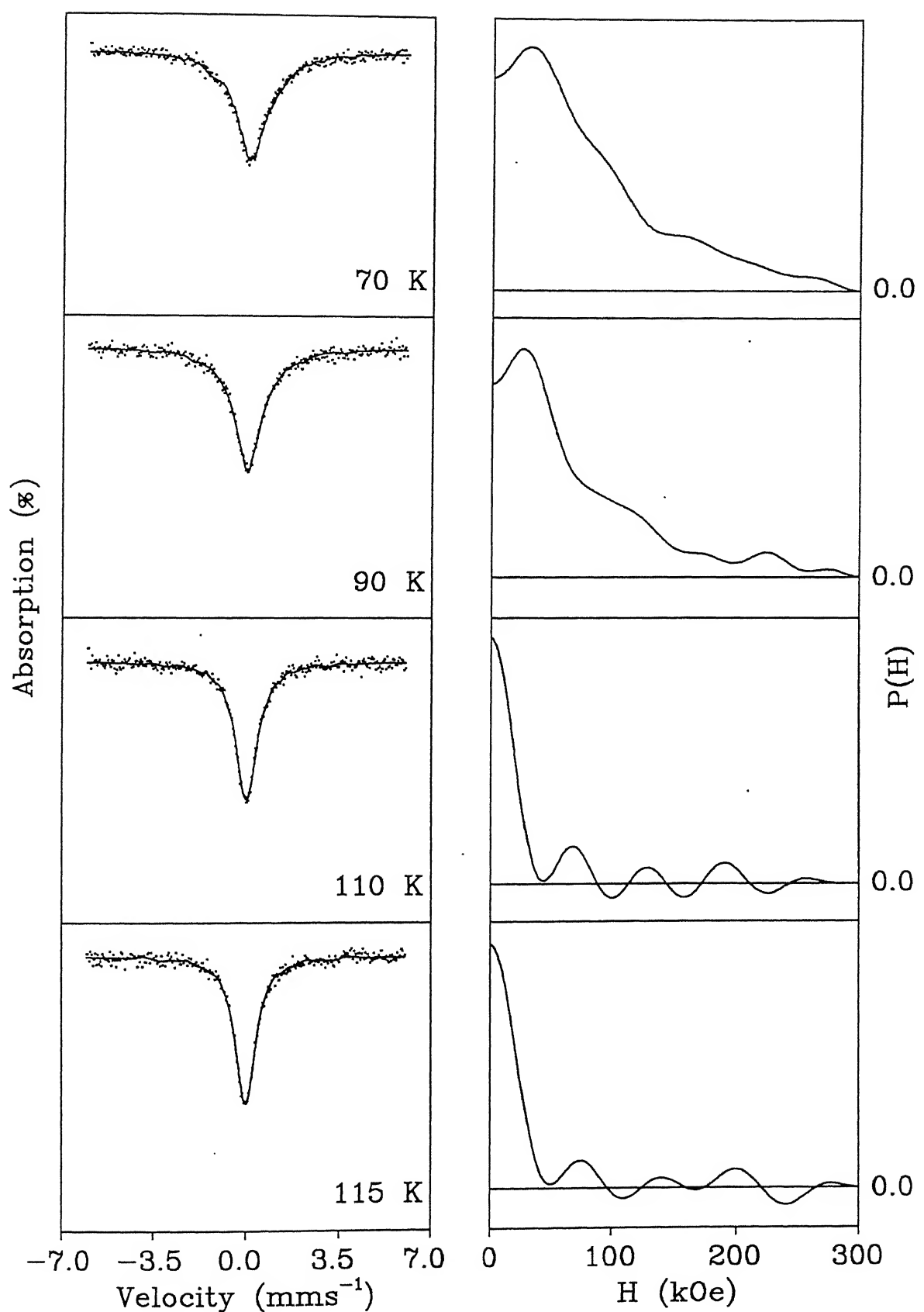


Fig. 3.4. (Continued)

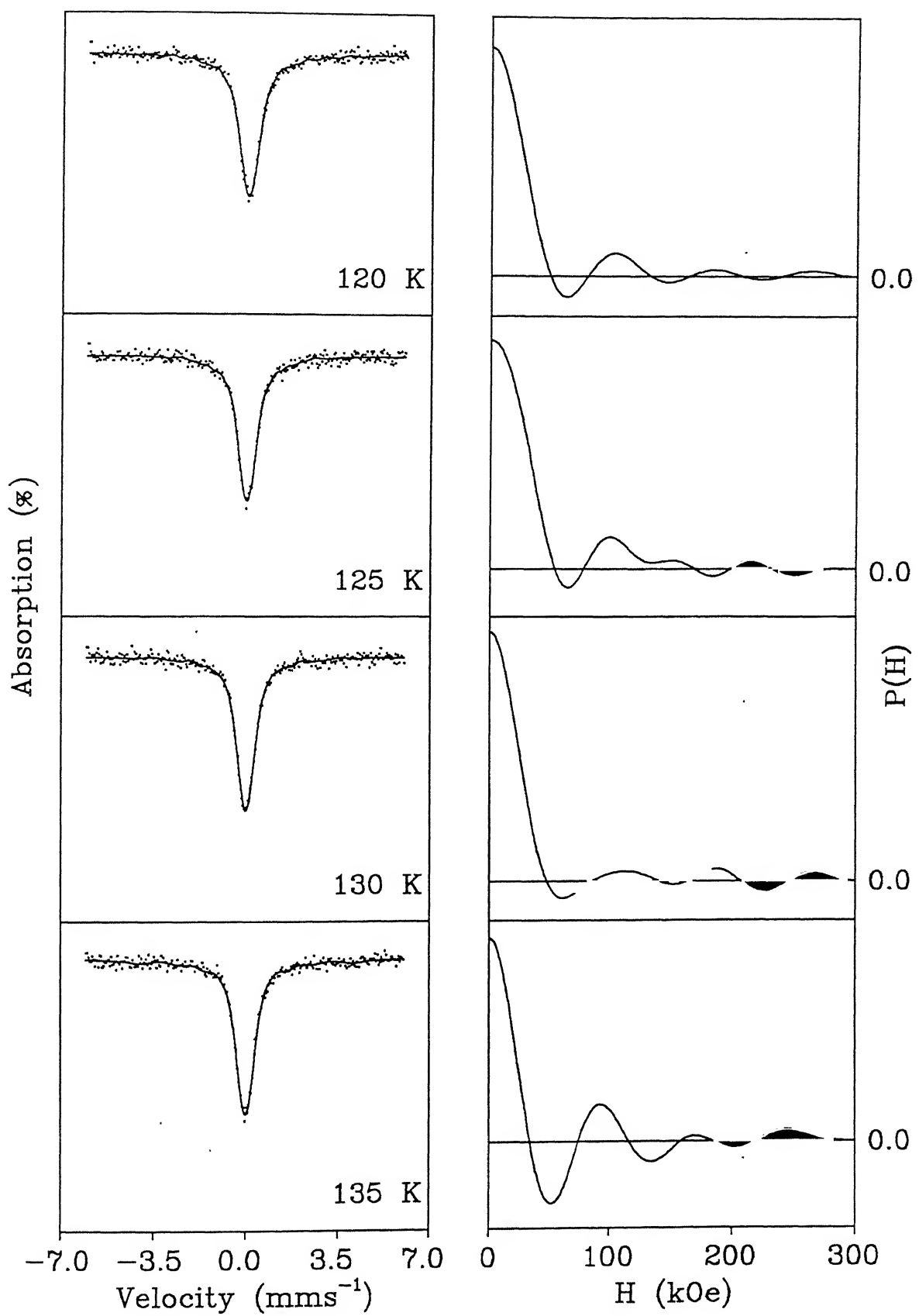


Fig. 3.4. (Continued)

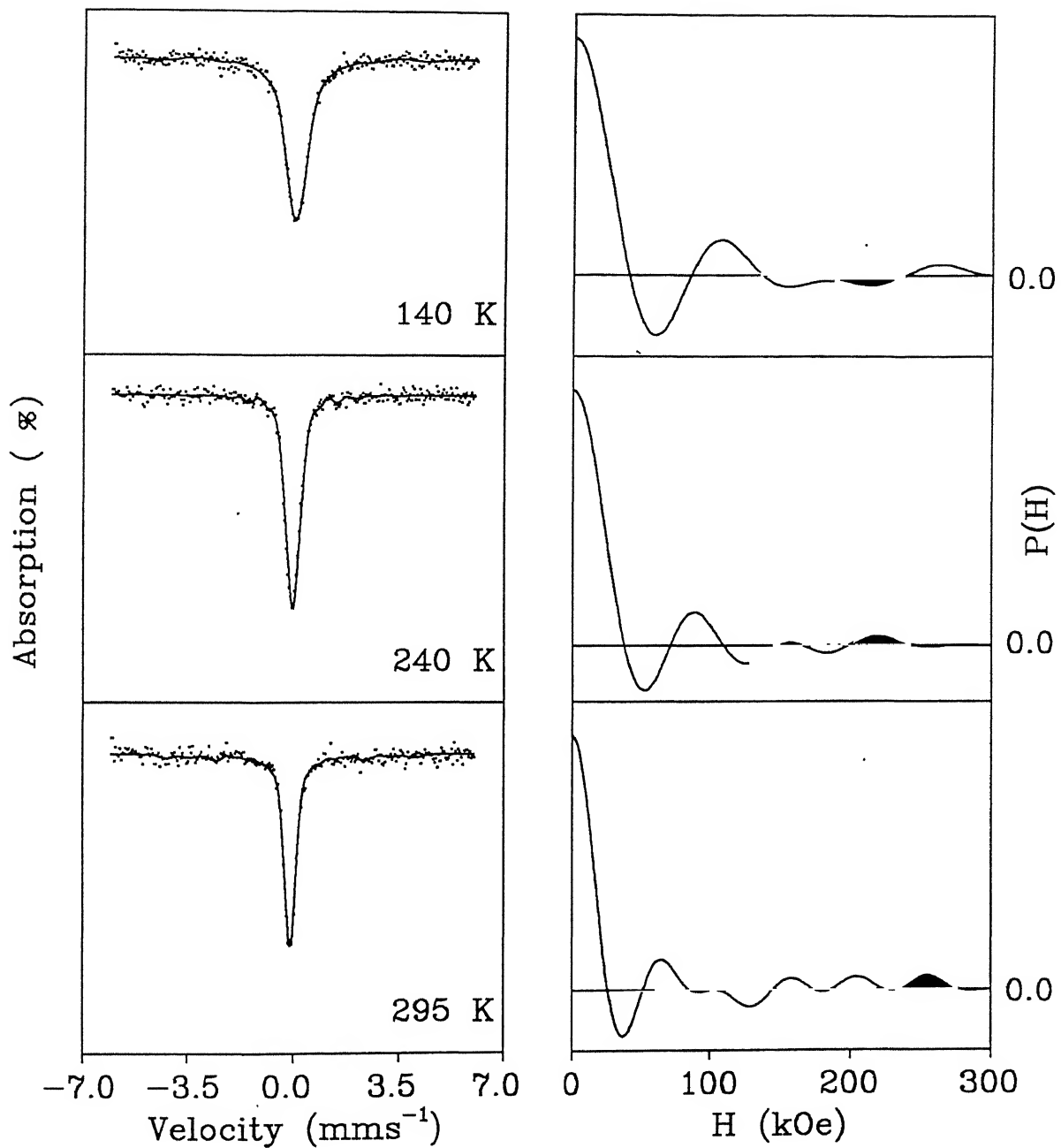


Fig. 3.4. (Continued)

reduced below 295 K, the Mössbauer spectra continue to exhibit a single-peak lineshape but the lines get progressively wider. The variations of the Mössbauer parameters, viz., linewidth  $\Gamma$ , centre shift and the area under the resonance peak with temperature are shown in Figs.3.5-3.7 respectively. Using the results for the  $P(H)$  shown in Fig.3.4, the average hyperfine field  $\langle H \rangle = \int HP(H)dH / \int P(H)dH$  was also determined and the variation of  $\langle H \rangle$  with temperature is shown in Fig.3.8. It is interesting to observe that the paramagnetic to ferromagnetic phase transition at  $T = T_C$  [3] is reflected in the temperature dependence of  $\Gamma$  (Fig.3.5), peak area (Fig.3.7) and  $\langle H \rangle$  (Fig.3.8). However the analysis of the present results for  $\langle H \rangle$  versus  $T$  (Fig.3.8) gave a value of  $T_C = 130 \pm 2$ K. This result for the Curie temperature obtained from Mössbauer spectroscopy differs from the value  $T_C = 144$  K reported by Majumdar and Blanckenhagen [3] and this difference could be attributed to the different sensitivities of the different methods used to determine  $T_C$ .

As observed in Fig.3.5 the linewidth  $\Gamma$  shows a slight increase as the temperature is reduced from 295 K to about 175 K. This behaviour is attributed to an increase in the effective absorber thickness which is proportional to the Debye-Waller factor [17]. More steep increase in  $\Gamma$  observed at  $T < 140$  K (Fig.3.5) is attributed to the ferromagnetic ordering. The area under the resonance peak shows a similar variation with temperature (Fig.3.7) and it can be explained in a similar way.

We now turn our attention to the results for the evolution of  $P(H)$  (Fig.3.4) and  $\langle H \rangle$  (Fig.3.8) with temperature. The shape of

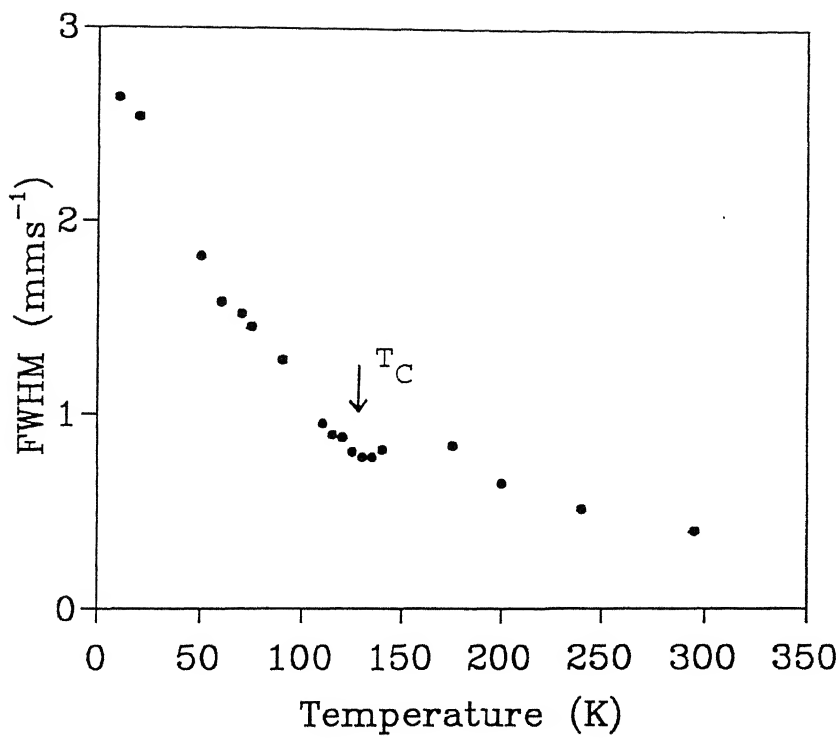


Fig. 3.5. Temperature dependence of full width at half maximum (FWHM) of  $\text{Fe}_{50}\text{Ni}_{30}\text{Cr}_{20}$  sample.

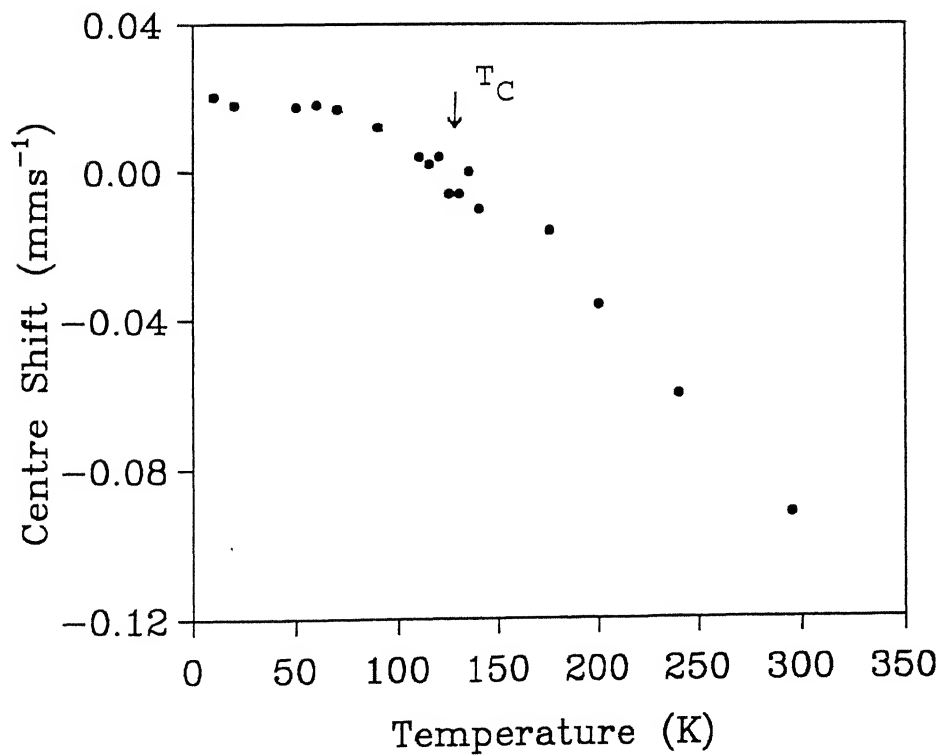


Fig. 3.6. Temperature dependence of Centre Shift of  $\text{Fe}_{50}\text{Ni}_{30}\text{Cr}_{20}$  sample.

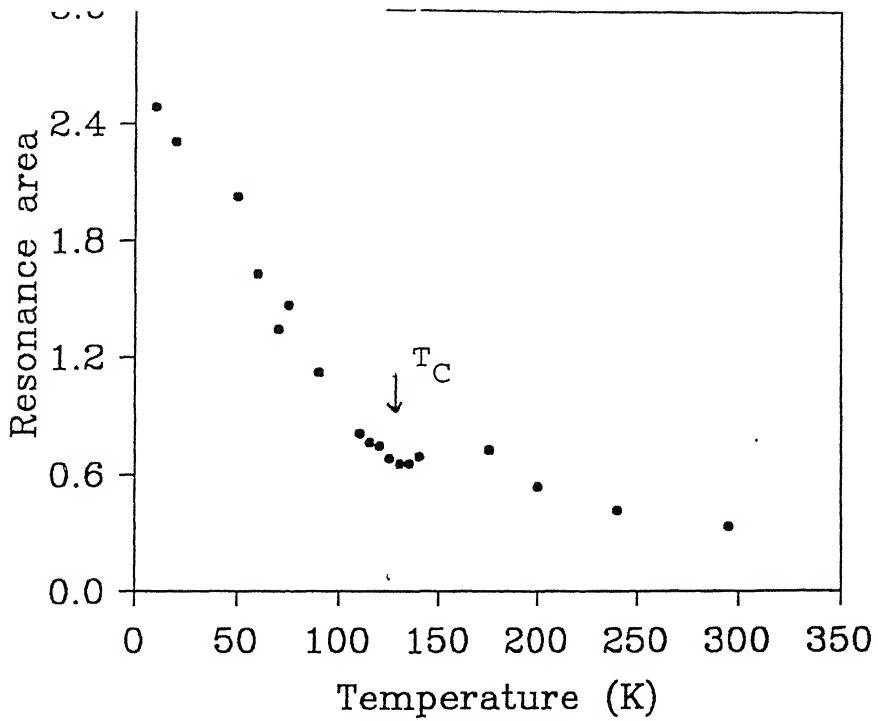


Fig. 3.7. Temperature dependence of resonance area of  $\text{Fe}_{50}\text{Ni}_{30}\text{Cr}_{20}$  sample.

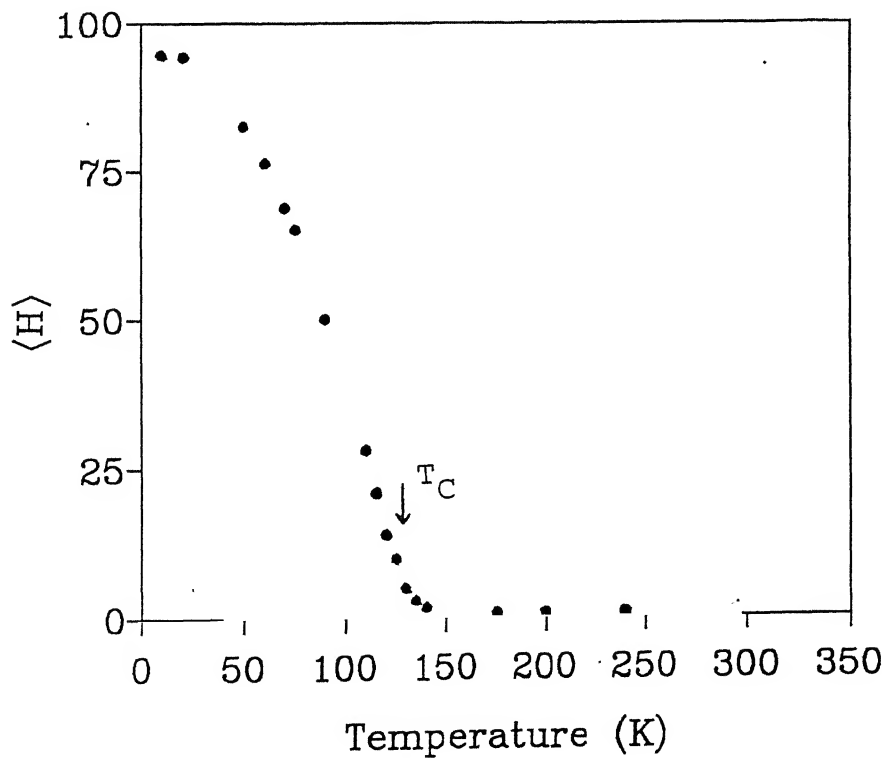
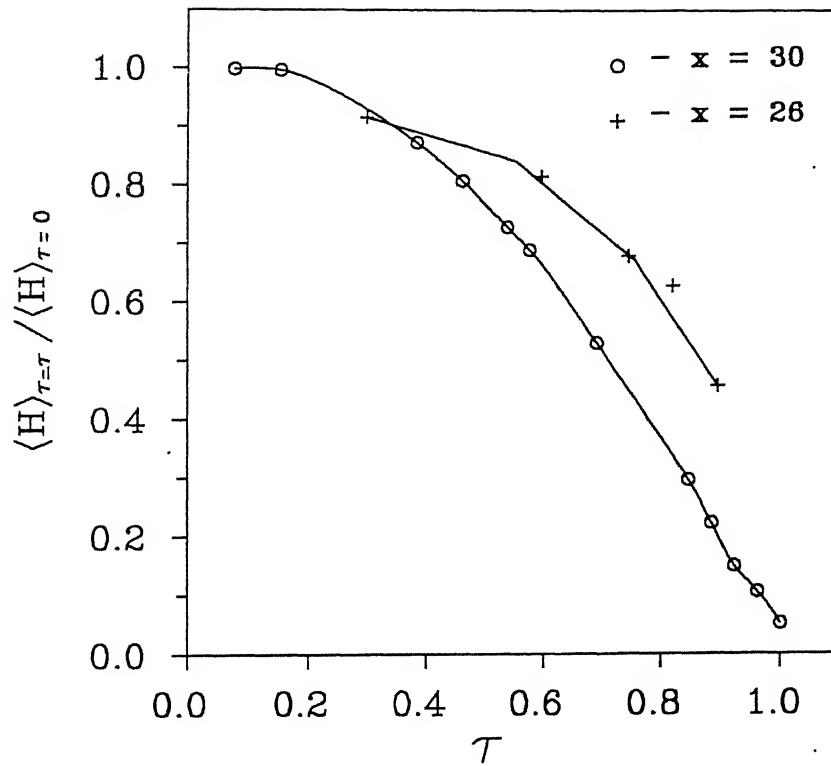


Fig. 3.8. Temperature dependence of average hyperfine field  $\langle H \rangle$  of  $\text{Fe}_{50}\text{Ni}_{30}\text{Cr}_{20}$  sample.

the  $P(H)$  distribution observed at  $T = 295$  K is characteristic of the paramagnetic phase [18] and this shape persists upto 140 K. After crossing  $T = T_C$  the  $P(H)$  distribution settles into a different shape for  $T \leq 90$  K. This behaviour is understood in terms of the effect of ferromagnetic ordering of  $\text{Fe}_{80-x}\text{Ni}_x\text{Cr}_{20}$  at  $T \leq T_C$ . As the temperature is decreased from 295 K the average hyperfine field  $\langle H \rangle$  remains negligibly small down to 175 K and then around 140 K it starts to rise with decreasing temperature. This rise is particularly steep in the region of 115 to 20 K. The observed temperature dependence of  $\langle H \rangle$  can be explained in terms of a long-range ferromagnetic phase below its  $T_C$  ( $\approx 130$  K, derived from our Mössbauer data). The temperature dependence of  $\langle H \rangle$  is very similar to that of dc-magnetization of this alloy [3]. In the previous studies, the results for the average hyperfine fields for the Fe-Ni [10] and Fe-Ni-Mn [19] alloys obtained by  $^{57}\text{Fe}$  Mössbauer spectroscopy have been plotted versus the reduced temperature and a behaviour similar to the normalized plot of spontaneous magnetization versus reduced temperature [20] was observed. Keeping this in mind we have also plotted the normalized average hyperfine fields  $\langle H \rangle_{\tau=\tau} / \langle H \rangle_{\tau=0}$  versus  $\tau = T/T_C$  in Fig.3.9 and the curves show an "inverted bell" - like shape very analogous to the plot of the normalized spontaneous magnetization [10, 19, 20]. It is interesting to note that the hyperfine magnetic fields in Fe-34 at% Ni are of the order of 300 kOe as determined by Mössbauer spectroscopy [10]. The results in Fig.3.8 show that  $\langle H \rangle$  is about 95 kOe at  $T < 20$  K in the  $\text{Fe}_{50}\text{Ni}_{30}\text{Cr}_{20}$  alloy. This decrease of  $\langle H \rangle$  in going from Fe-Ni to Fe-Ni-Cr alloys can be



**Fig. 3.9.** Variation of normalized average hyperfine field versus reduced temperature. The open circles (o) represent data for  $x = 30$  while crosses (+) represent data for  $x = 26$ . The continuous lines are drawn through the data points for visual guidance.

understood from the different type of antiferromagnetic interactions present in Fe-Ni-Cr alloys. The hyperfine field distributions for the  $x = 30$  alloy for  $T < 100$  K show a broad shape extending from  $H = 0$  to  $H = 300$  kOe. We tried to fit two independent sub-distributions (each having a Gaussian shape but characterized by different FWHM) to the total  $P(H)$  observed by us at  $T = 10, 20, 50, 60$  and  $90$  K. The results of this two-Gaussian fit are shown in Fig.3.10 where the Gaussian representing the subdistributions on the lower (higher) field side is labelled as a (b). Similar two-Gaussian fit to the  $P(H)$  distributions in  $\text{Fe}_{90}\text{Zr}_{10}$  alloy have been observed by Kaul et al. [21]. The temperature variation of the peak (or most probable) value for the a and b curves are shown in Fig.3.11. It is seen that in each case (a or b) the peak values decrease with temperature. This behaviour needs to be understood better.

The variation of the centre shift (CS) with temperature for the  $\text{Fe}_{50}\text{Ni}_{30}\text{Cr}_{20}$  sample is shown in Fig.3.5. It is well known that the centre shift is the sum of the chemical isomer shift ( $\delta_{\text{IS}}$ ) and the contribution from the second order Doppler shift ( $\delta_{\text{SOD}}$ ).  $\delta_{\text{Total}}$  can be expressed as

$$\delta_{\text{Total}} = \delta_{\text{IS}} + \delta_{\text{SOD}}. \quad (3.1)$$

This has been discussed in Chapter 1 in detail. A non-zero contribution from the second term of the above expression arises due to the relativistic effect whenever the source and absorber are at different temperatures and is also known as thermal shift. This temperature dependent part of the centre shift is caused by the time dilation resulting from the thermal motion of the  $\gamma$ -ray

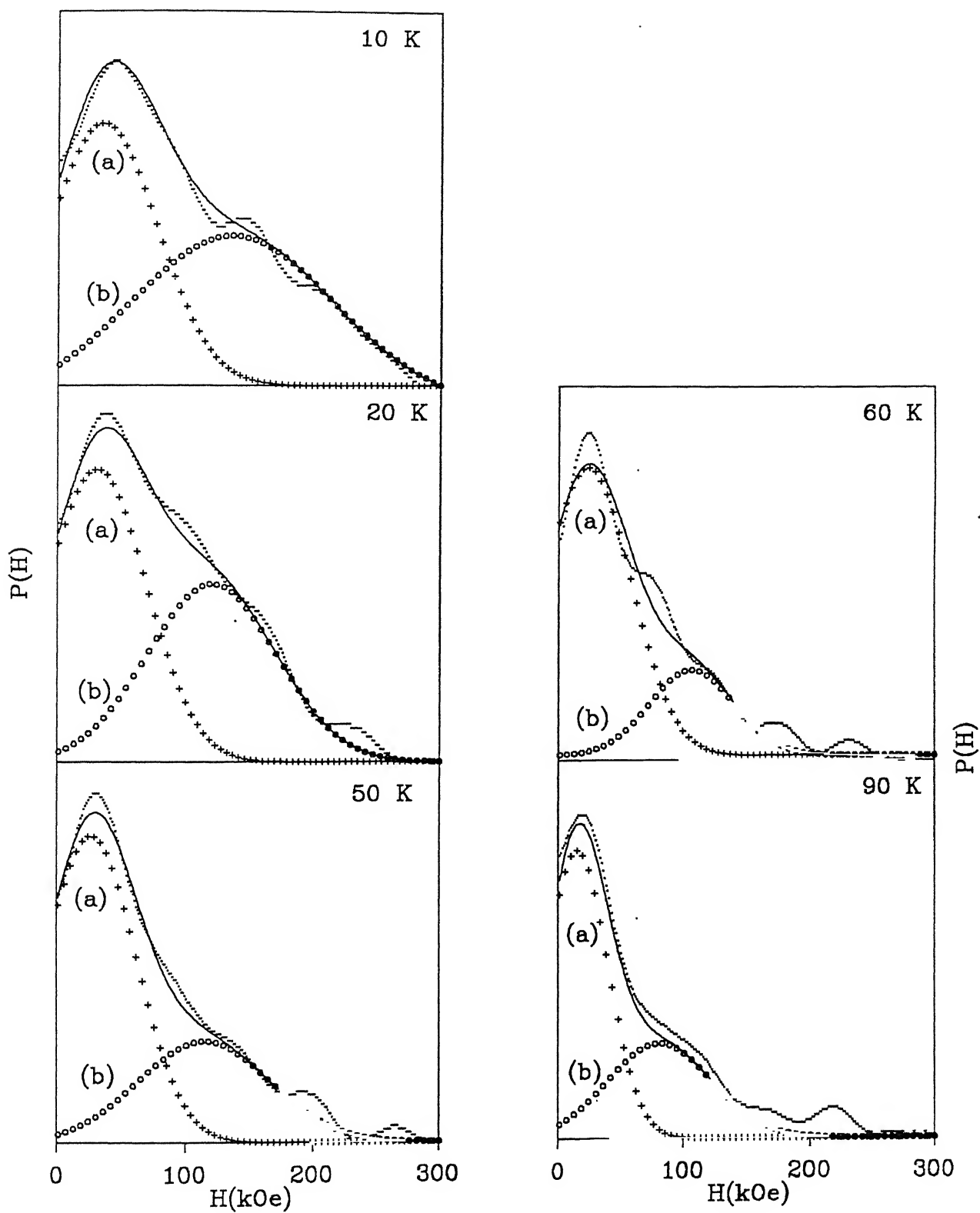


**Fig. 3.10.** Two-Gaussian fits to the  $P(H)$  distributions vs.  $H$  curves at different temperatures. (a) represent the low-field side Gaussian (+) and (b) the high-field side Gaussian (o).

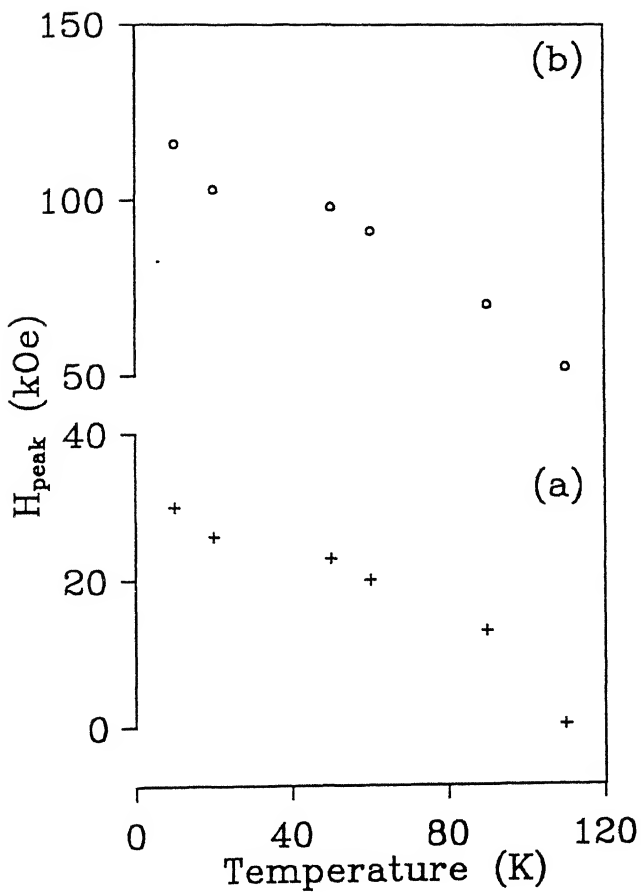


**Fig.3.11.** Temperature dependence of the most probable hyperfine field ( $H_{\text{peak}}$ ) corresponding to two-Gaussian components (Fig.3.10). (a) represent low-field side Gaussian (+) and (b) represents high-field side Gaussian (o).

emitting and absorbing nuclei. If  $\langle v^2 \rangle$  is the mean square velocity of the Mössbauer atom in the lattice, then  $\delta_{SOD}$  can be expressed as

$$\delta_{SOD} = -\langle v^2 \rangle / 2c \quad (3.2)$$

which is Eq.(1.17) of Chapter 1 [14]. In this way the Doppler shift is related to the lattice dynamics of Debye solids. Temperature dependence of centre shift gives information about the vibrational state of Debye solids. For calculating the Debye temperature we have fitted the experimental data on the centre shift by using the following equation:

$$\delta(T_1) - \delta(T_2) = \frac{9K}{2Mc} \left[ T_2 \left( \frac{T_2}{\epsilon_D} \right)^3 \int_0^{\epsilon_D/T_2} \frac{x^3}{x^3 - 1} dx - T_1 \left( \frac{T_1}{\epsilon_D} \right)^3 \int_0^{\epsilon_D/T_1} \frac{x^3}{x^3 - 1} dx \right], \quad (3.3)$$

where we have assumed that the isomer shift ( $\delta_{IS}$ ) is independent of temperature, and  $T_2$  is the lowest temperature. By using the minimum standard deviation method we have obtained  $\epsilon_D$  as shown in Fig.3.12. The solid line represents the curve fitted with the experimental data points. It is clear from the experimental data that there is hardly any change in  $\delta_{SOD}$  below the transition temperature ( $T_C$ ). This indicates that below the transition temperature ( $T_C$ ) there is no effect of electronic structural anomaly or phonon softening for the  $Fe_{50}Ni_{30}Cr_{20}$  sample. The softening corresponds to the case of lattice vibration when the average velocity decreases. Again the expression for  $\langle v^2 \rangle$  which we have used for fitting the experimental data is true for a harmonic

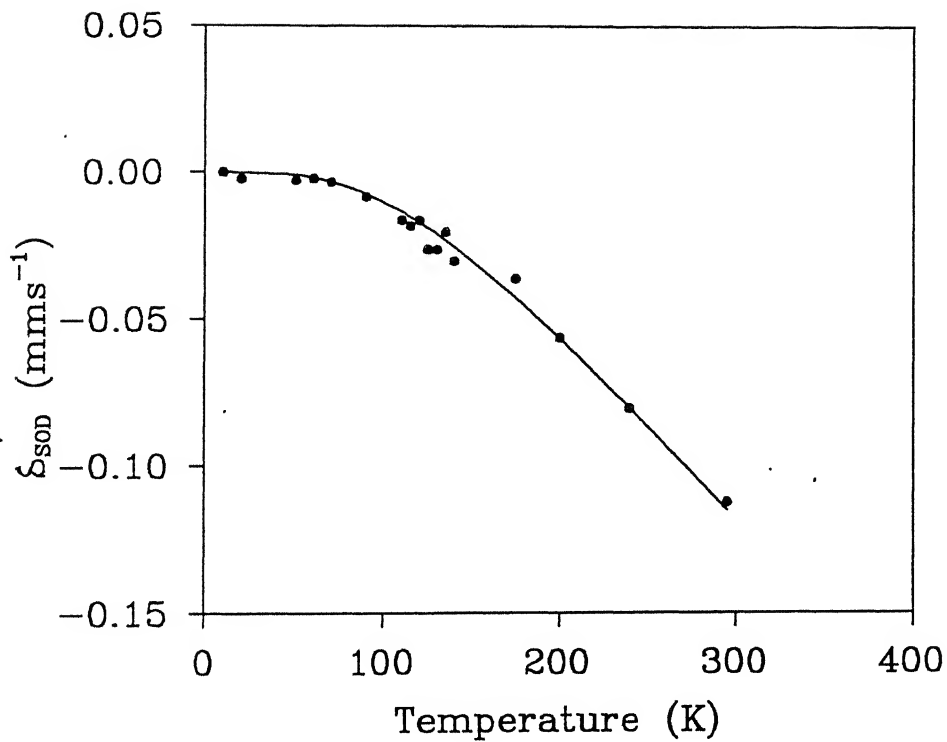


**Fig.12.** Curve fitted (continuous line) to the second order Doppler shift values for determining the Debye temperature ( $\Theta_D$ ) of  $\text{Fe}_{50}\text{Ni}_{30}\text{Cr}_{20}$  alloy.

crystal. So one could conclude that below the transition temperature vibrational motion of  $^{57}\text{Fe}$  atoms remains harmonic. The average velocity decreases below  $T_C$  as discussed earlier. The decrease of  $\langle v^2 \rangle$  reflects the absence of vibrational instabilities in the lattice below  $T_C$ . Therefore the temperature dependence of the centre shift shows that the motion of Fe atoms remains harmonic and no phonon softening is observed below the Curie temperature.

### 3.3.3 Alloy with $x = 26$

Figure 3.13 shows the Mössbauer spectra of the  $\text{Fe}_{54}\text{Ni}_{26}\text{Cr}_{20}$  sample measured at 13, 16, 20, 40, 50, 55, 60, 64, 67, 70, 75, 95, 125, 160, 200, 240, and 295 K. The general pattern of the temperature evolution of these spectra is similar to that obtained for the alloy with  $x = 30$ . The temperature dependence of the linewidth  $\Gamma$ , centre shift CS, resonance-peak area and  $\langle H \rangle$  are shown in Figs. 3.14 - 3.17, respectively. According to the magnetic phase diagram (Fig.3.2) the alloy with  $x = 26$  is paramagnetic above  $T_C$  ( $= 56$  K) and is in a mixed phase (ferromagnetic + spin glass) in the range of 7 to 56 K. The results shown in Figs.3.15, 3.16 and 3.17 appear to support such a magnetic transition at a temperature  $T_C$  determined by us to be around  $T_C = 65$  K. We wish to point out that the value of  $T_C$  for  $x = 26$  cannot be determined with the same precision as for  $x = 30$ . This uncertainty arises from the fact that there are only five data points in the  $\langle H \rangle$  versus T curve (Fig.3.17) in the range  $T = 20 - 70$  K and this made it difficult to provide accurate fit and

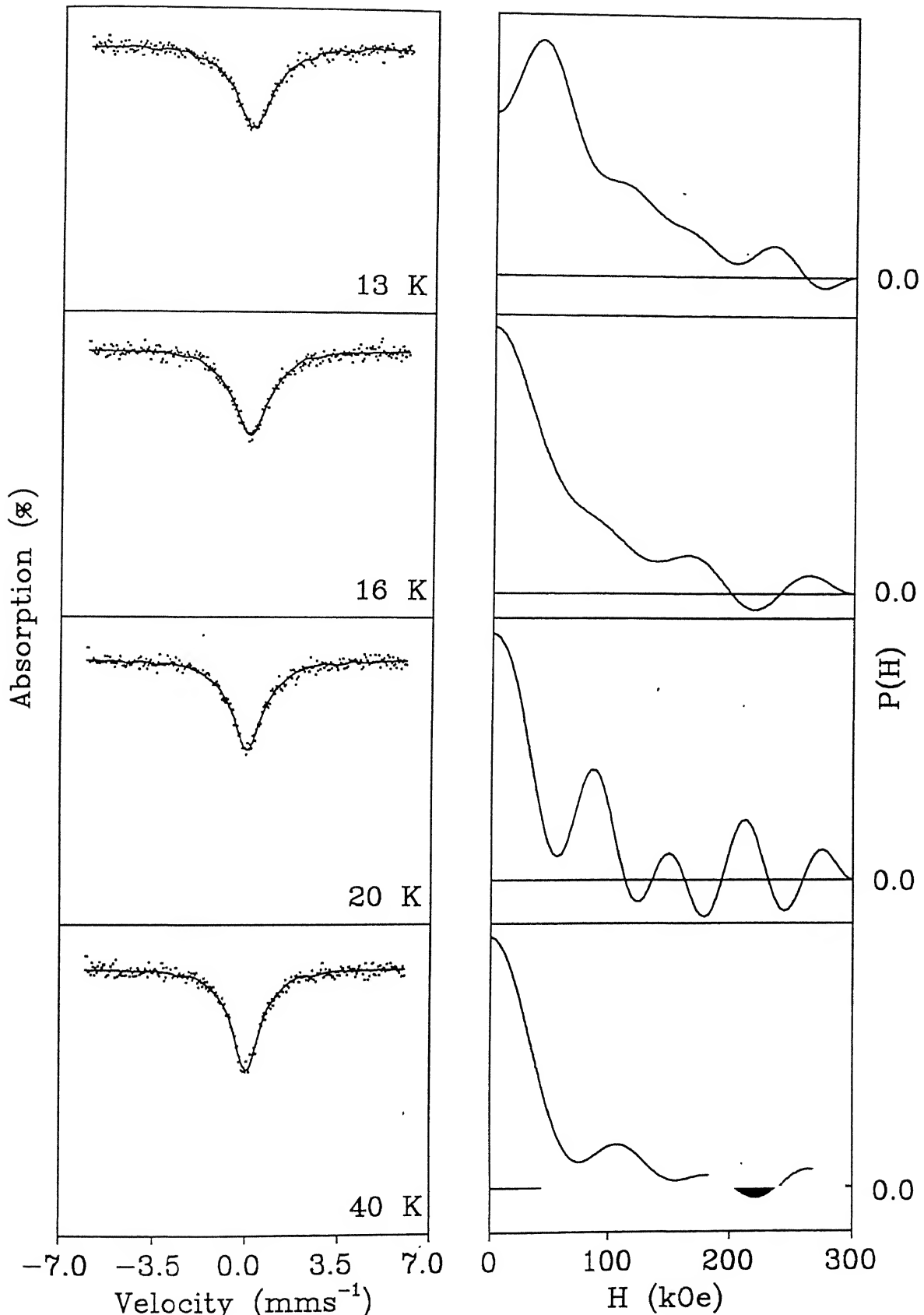


Fig. 3.13. Mössbauer spectra of  $\text{Fe}_{54}\text{Ni}_{26}\text{Cr}_{20}$  sample at different temperatures and corresponding hyperfine field distributions.  
 (Continued on the next page)

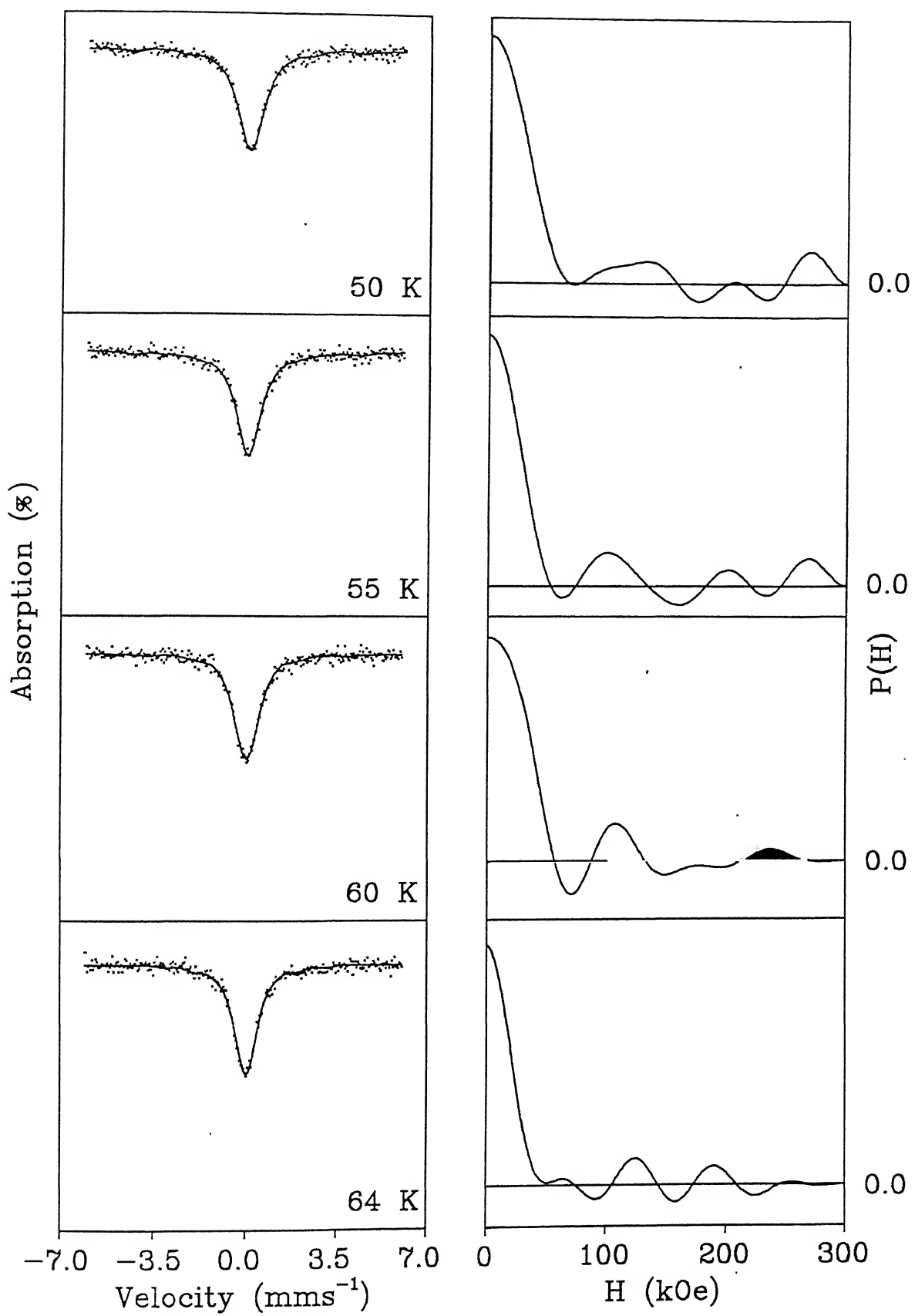


Fig. 3.13. (Continued)

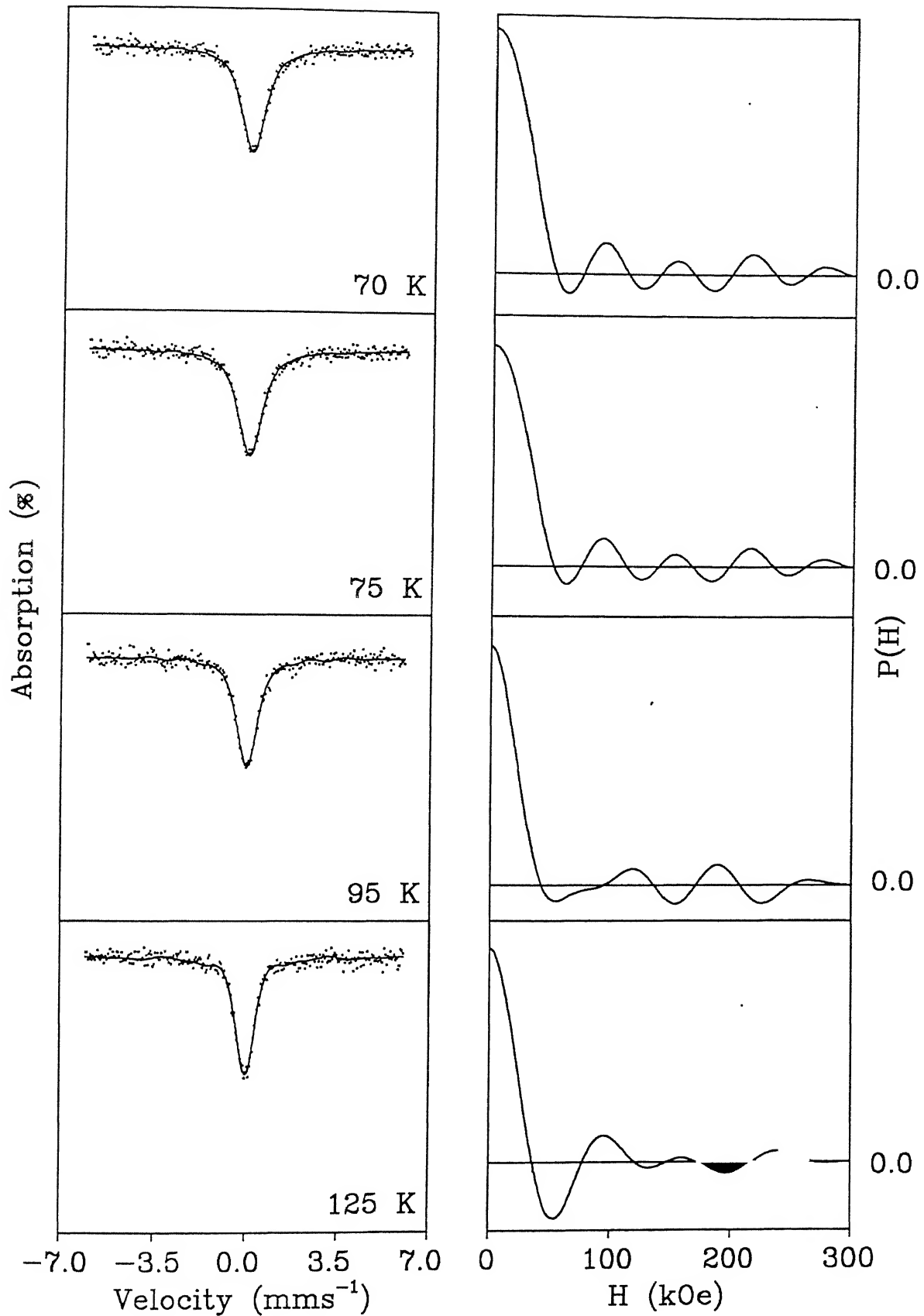


Fig. 3.13. (Continued)

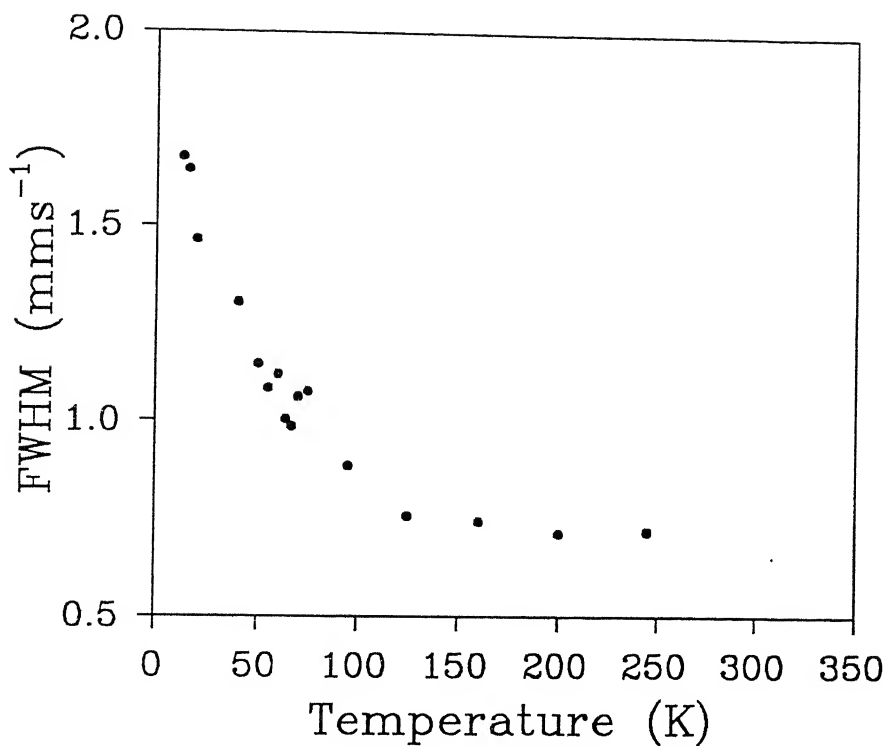


Fig. 3.14. Temperature dependence of full width at half maximum (FWHM) of  $\text{Fe}_{54}\text{Ni}_{26}\text{Cr}_{20}$  sample.

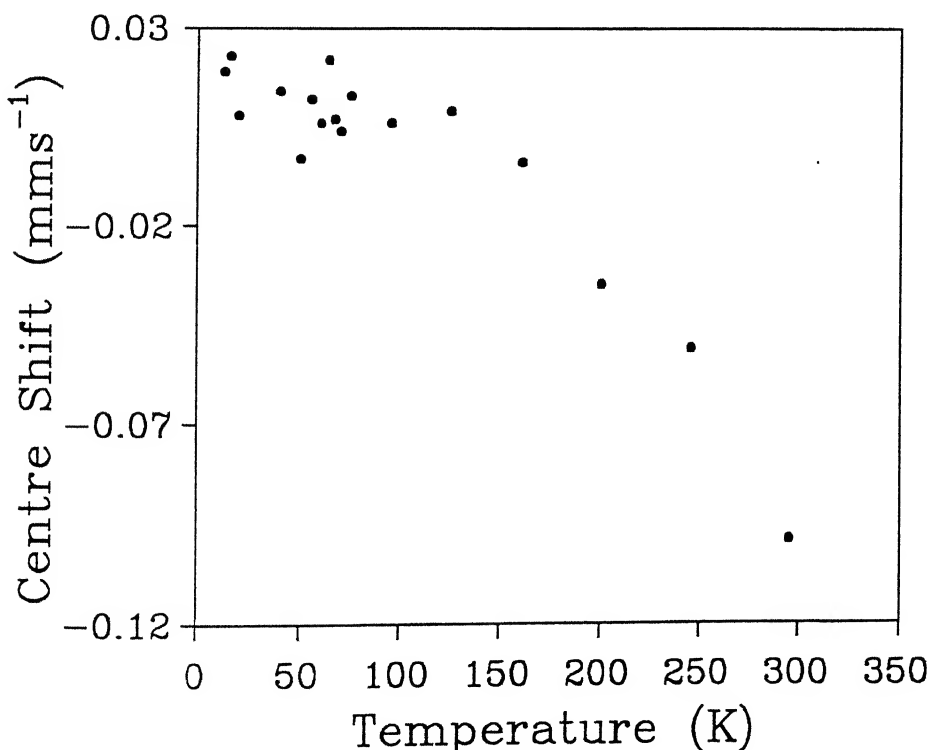


Fig. 3.15. Temperature dependence of Centre Shift of  $\text{Fe}_{54}\text{Ni}_{26}\text{Cr}_{20}$  sample.

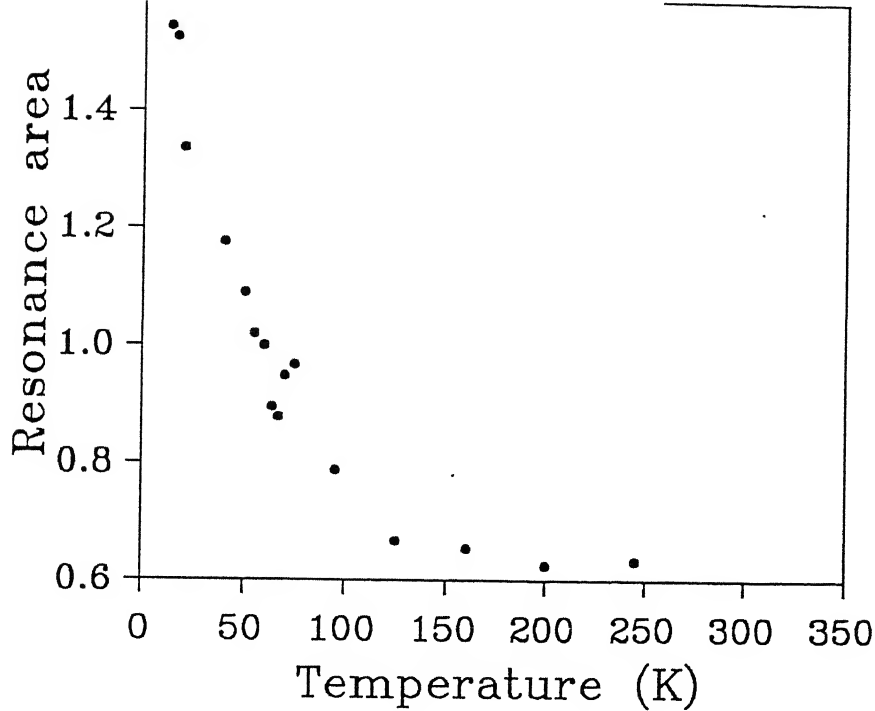


Fig. 3.16. Temperature dependence of resonance area of  $\text{Fe}_{54}\text{Ni}_{26}\text{Cr}_{20}$  sample.

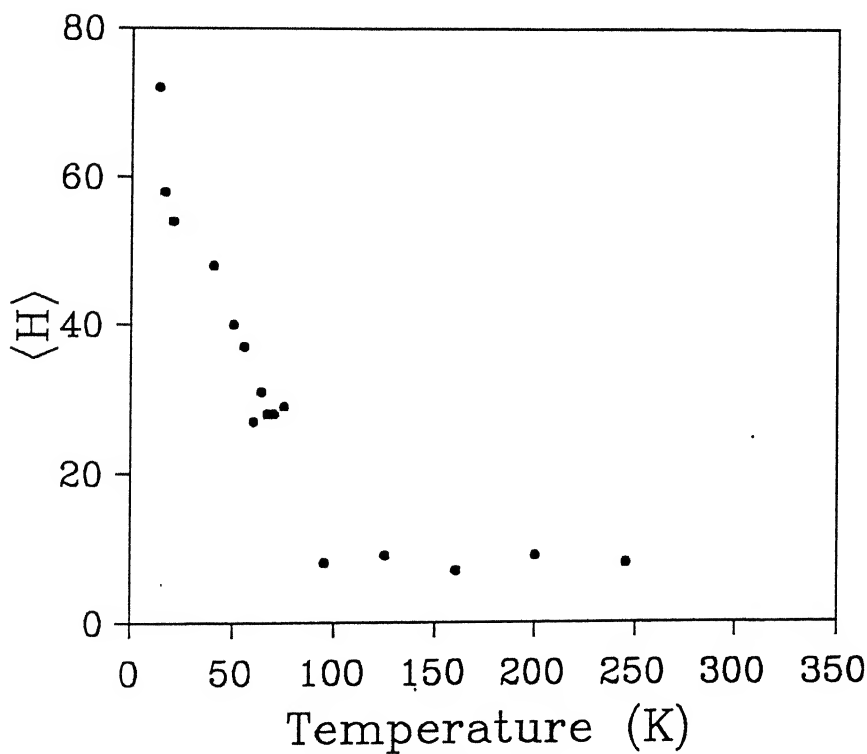


Fig. 3.17. Temperature dependence of average hyperfine field  $\langle H \rangle$  of  $\text{Fe}_{54}\text{Ni}_{26}\text{Cr}_{20}$  sample.

obtain a precise determination of  $T_C$ . As in the case of  $x=30$ , the present value of  $T_C \approx 65$  K (for  $x = 26$ ) is different from the value ( $T_C = 56$  K) reported by Majumdar and Blanckenhagen [3]. An interesting point emerges from a close examination of Fig.3.17. The values of  $\langle H \rangle$  for  $x = 26$  lie in the range of 70 to 40 kOe in the temperature range of 16 to 50 K. In the case of  $x = 30$  the value  $\langle H \rangle$  in the same temperature interval lie in the range of 90 to 80 kOe. The saturation magnetization for alloys with  $x = 26$  and 30, as reported by Majumdar and Blanckenhagen, were  $4\pi M_S = 1.92$  and 3.8 kG, respectively. Thus one finds that the average hyperfine field scales with the spontaneous magnetization. The variation of normalized average hyperfine field versus reduced temperature  $\tau$  (see previous section) for  $x = 26$  is shown in Fig.3.9. Although there are only five data points, they show an "inverted-bell" shape with a greater flatness. Earlier work on  $Fe_{1-x}Ni_x$  [19] has shown that the degree of flatness depends on the concentration of Fe in the alloy sample.

The temperature dependence of the centre shift and second order Doppler shift  $\delta_{SOD}$  for the sample with  $x = 26$  is shown in Figs.3.15 and 3.18, respectively. An analysis of these data by a method similar to that followed for the  $x = 30$  yielded  $e_D = 507$  K for the best fit for  $x = 26$ . This shows that for the  $Fe_{80-x}Ni_xCr_{20}$  alloys  $e_D$  depends on the  $x$ -value.

### 3.3.4. Alloy with $x = 19$ .

The magnetic phase diagram (Fig.3.2) indicates that as the temperature of the  $Fe_{61}Ni_{19}Cr_{20}$  alloy is lowered from 295 K it

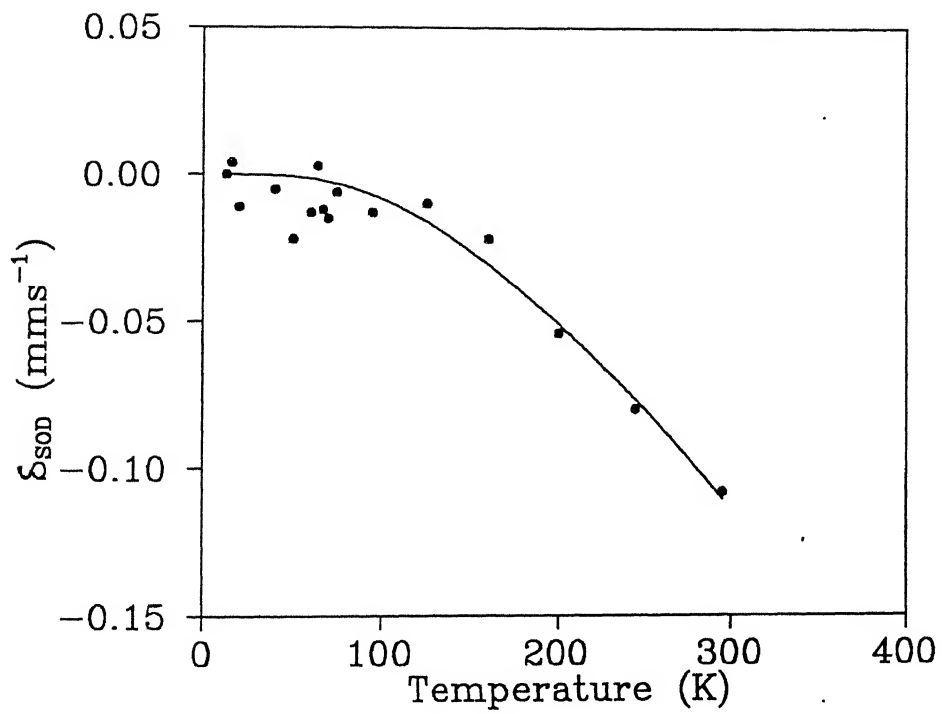


**Fig. 3.18.** Curve fitted (continuous line) to the second order Doppler shift values for determining the Debye temperature ( $\Theta_D$ ) of  $\text{Fe}_{54}\text{Ni}_{26}\text{Cr}_{20}$  alloy.

transforms from paramagnetic to a field-induced ferromagnetic phase (FIFM) at about  $T = 16$  K and upon further cooling it enters a spin-glass phase at 12 K. The present Mössbauer measurements of  $x = 19$  were carried out at  $T = 14, 15, 17, 19, 20, 27, 30, 35, 45, 50, 70, 90$ , and 295 K. No measurements were made in the range of 90 to 295 as the sample was expected to be paramagnetic throughout. Further, no external field was applied. As a result of these conditions we were unable to explore either the FIFM or the SG phase reported for  $x = 19$  by Majumdar and Blanckenhagen [3]. The Mössbauer spectra observed in the above temperature range are shown in Fig.3.19 while the observed variation of  $\Gamma$  with temperature is shown in Fig.3.20. It was observed that the  $\Gamma$ -values remained in the narrow range of 0.44 to 0.55  $\text{mms}^{-1}$  (which was characteristic of a paramagnetic phase) as the temperature was decreased from 295 K to 30 K. A further decrease of temperature of the sample led to a steep rise in  $\Gamma$  in the temperature range of 14 K to 30 K. This behaviour suggested an onset of a phase transformation, even before  $T_{SG}$  ( $= 12$  K) was reached. It may be pointed out that Mössbauer spectroscopic studies of the Au-3 at% Fe and Rh-5 at% Fe spin glasses by Mayer et al. [22] showed a similar behaviour and this led these authors to suggest that the true paramagnetic state only sets in at a temperature appreciably higher than the cusp temperature. This behaviour was attributed to the relaxation effects associated with pre-transition fluctuations. Several canonical spin-glasses show deviations from the Curie-Wiess law at temperatures which are much larger than their  $T_{SG}$ 's [23]. This indicates correlation between 3d moments at

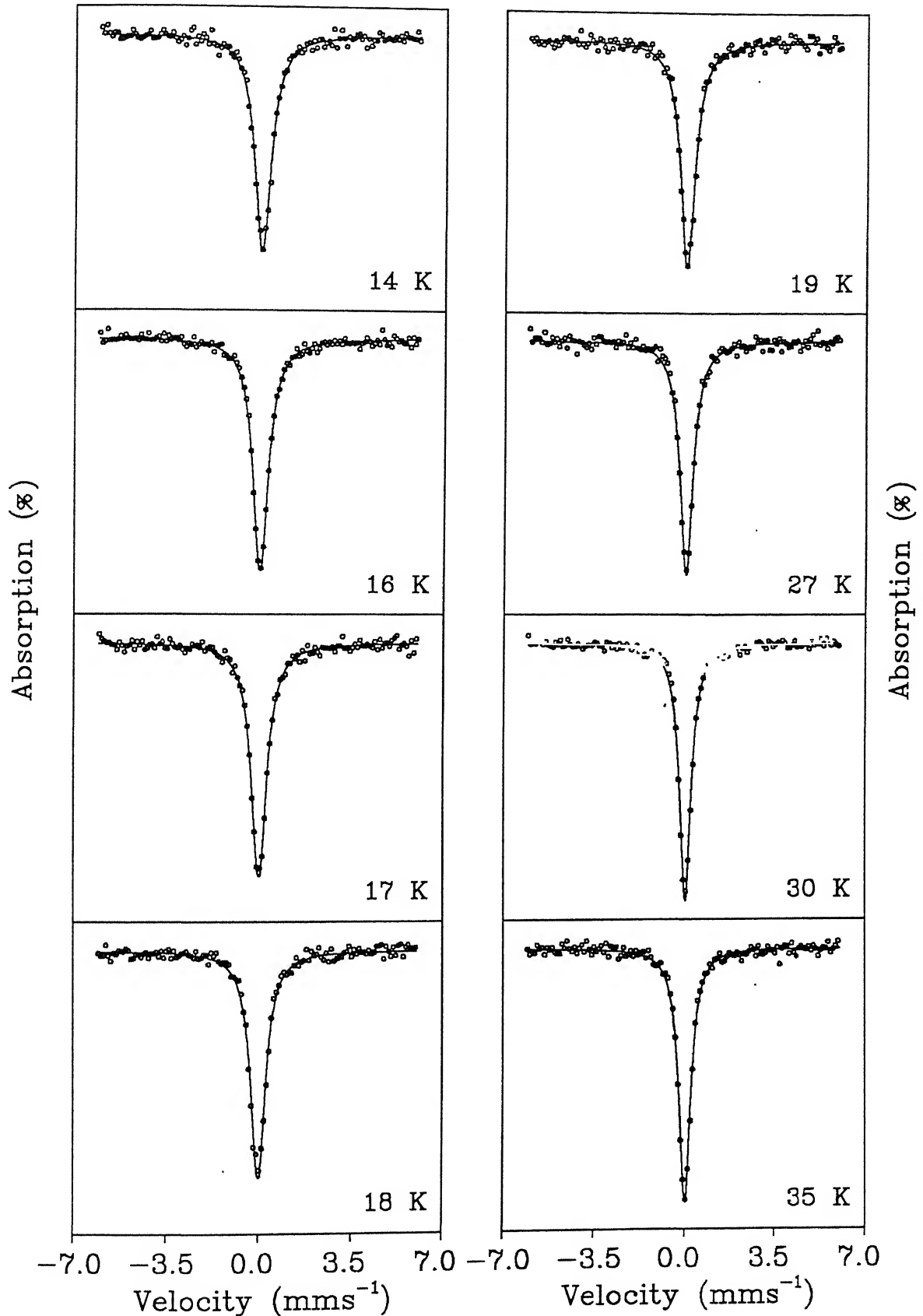


**Fig. 3.19.** Mössbauer spectra of  $\text{Fe}_{61}\text{Ni}_{19}\text{Cr}_{20}$  sample at different temperatures.

(Continued on the next page)

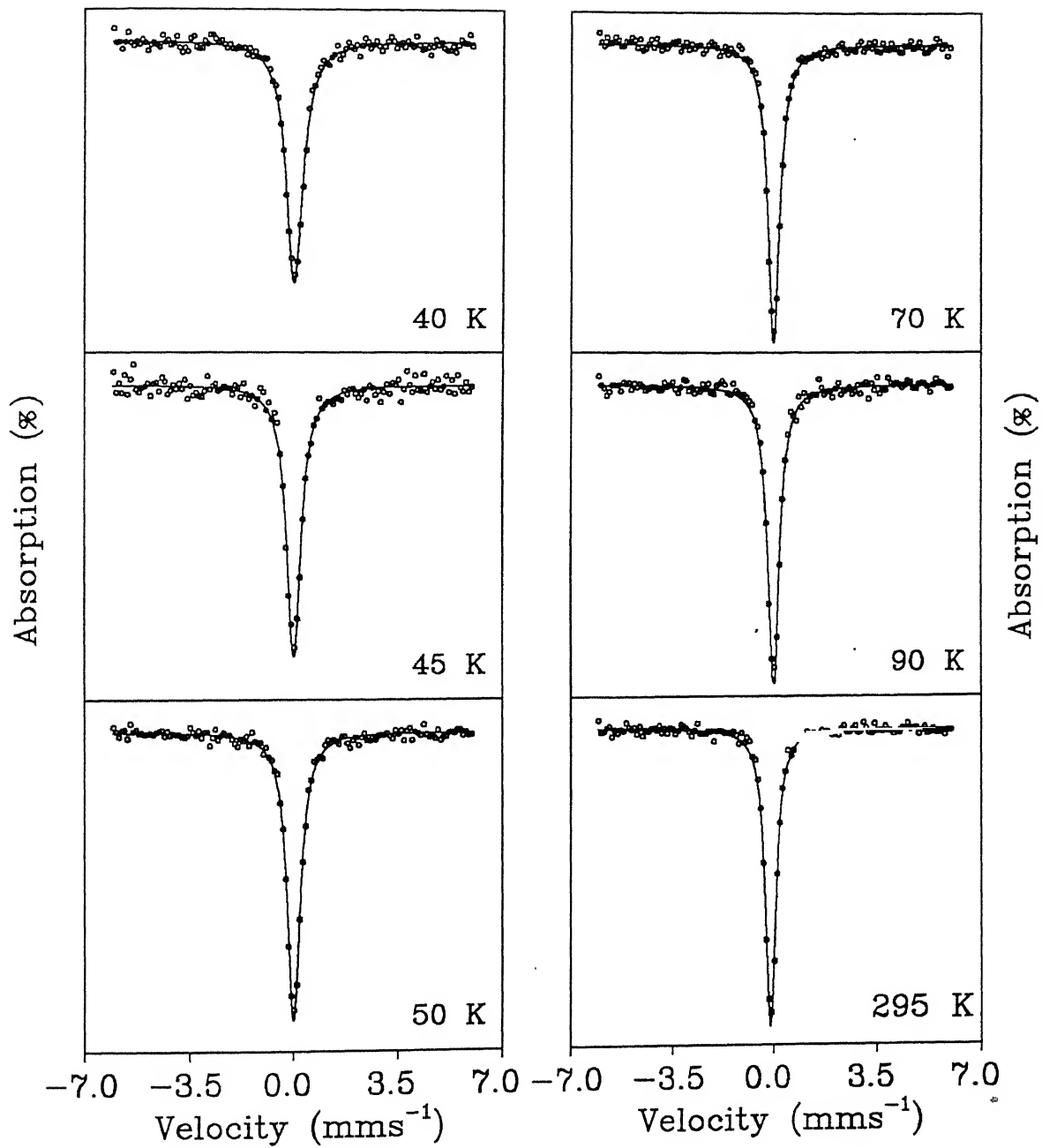


Fig. 3.19. (Continued)

$T \gg T_{SG}$ .

The narrow linewidths observed for the sample with  $x = 19$  did not allow any determination of  $P(H)$  or  $\langle H \rangle$  by Window's method. We interpret this result to mean that  $\langle H \rangle$  in  $x = 19$  have vanishingly small values at low ( $T < 30$  K) temperatures. This result is in agreement with the interpretation by Majumdar and Blanckenhagen [3] who concluded that the alloy with  $x = 19$  is too poor in Ni content to support long-range ferromagnetism at any temperature.

Mössbauer studies of the  $Fe_{65}(Ni_{1-x}M_x)_{35}$  alloys by Nakamura et al. [24] have shown that the hyperfine magnetic field acting on  $^{57}Fe$  nuclei is about 300 kOe in the ferromagnetic alloys and changes rapidly to about 45 kOe in the antiferromagnetic alloys.

### 3.3.5. Alloy with $x = 14$ .

The magnetic phase diagram shows that the alloy  $Fe_{66}Ni_{14}Cr_{20}$  is paramagnetic above the Neel temperature,  $T_N = 26$  K. The Mössbauer spectra of this sample measured at  $T = 20, 22, 24, 26, 35, 45, 60, 120, 170$ , and 210 K, although not presented here, showed a single-peak lineshape throughout, with the linewidth,  $\Gamma$ , varying with temperature as shown in Fig.3.21. It is observed that the linewidth  $\Gamma$  is almost constant as the temperature is lowered from 210 K to 60 K. Further lowering of temperature leads to a steep rise in  $\Gamma$  especially in the range of 20 to 35 K. This behaviour is attributed to the paramagnetic - antiferromagnetic transition. The linewidths observed in the range of 20 to 35 K are relatively narrow, lying in the range of 0.96 to 0.60  $mms^{-1}$ . This makes it difficult to determine  $P(H)$  or  $\langle H \rangle$ . This result could be

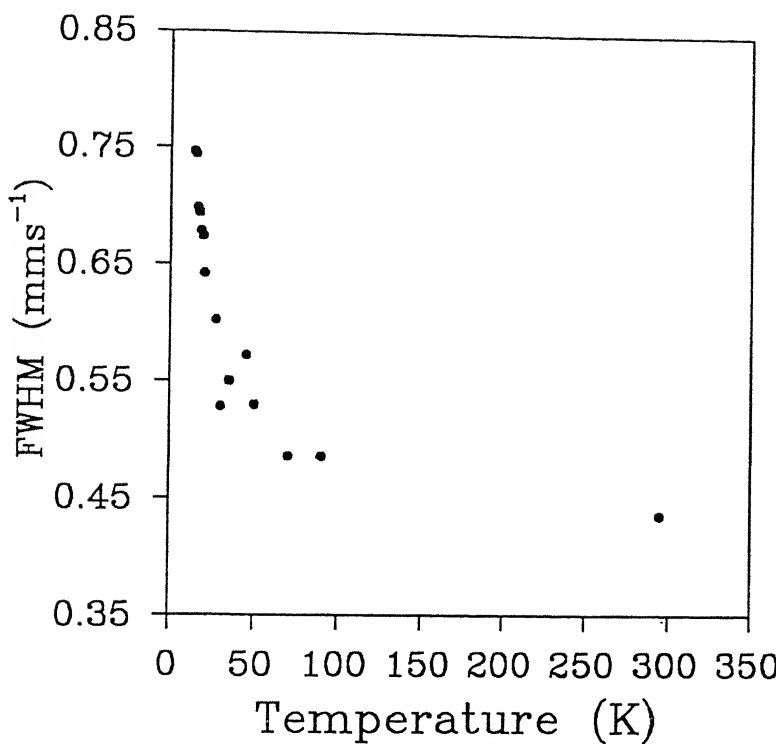


Fig. 3.20. Temperature dependence of full width at half maximum (FWHM) of  $\text{Fe}_{61}\text{Ni}_{19}\text{Cr}_{20}$  sample.

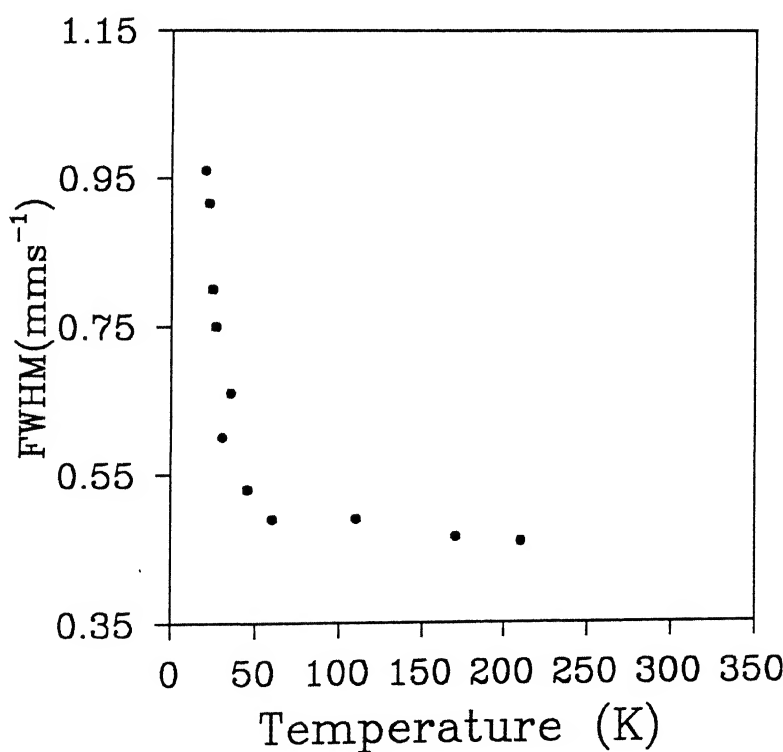


Fig. 3.21. Temperature dependence of full width at half maximum (FWHM) of  $\text{Fe}_{66}\text{Ni}_{14}\text{Cr}_{20}$  sample.

understood in terms of the antiferromagnetic ordering of this sample at low temperature.

### 3.4 Summary and conclusions

Mössbauer spectra were measured for the  $\text{Fe}_{80-x}\text{Ni}_x\text{Cr}_{20}$  ( $x = 30, 26, 19$  and  $14$ ) alloys in the temperature range of  $10$  to  $295$  K. The results were analyzed to obtain different Mössbauer parameters as well as the hyperfine field distributions,  $P(H)$  and the average hyperfine field  $\langle H \rangle$ . The variation of these quantities with temperature can be understood in terms of the magnetic phase diagram of the alloy system. In particular the temperature-evolution of  $P(H)$  and  $\langle H \rangle$  provide useful new information about these alloys. The present studies are preliminary in the sense they suggest that more systematic studies involving lower temperature ranges and closer temperature values should be carried out. More specifically, one should measure  $\langle H \rangle$  below  $T_{SG}$  ( $7$  K) for  $x = 26$ . This will distinguish between the two possible lowest temperature phases, viz, a pure spin-glass or a ferro-spin-glass phase. We were unable to carry out such detailed studies because of the limitations of our facilities. Nevertheless, the present work has brought out the usefulness of Mössbauer technique for this alloy system and has emphasized need to perform further Mössbauer spectroscopic studies of the  $\gamma\text{-Fe}_{80-x}\text{Ni}_x\text{Cr}_{20}$  alloys. The present results for the temperature variation of  $\langle H \rangle$  should provide interesting clues to theorists to apply the physics of solid state to explain our variations.

References

- [1] "Physics and Engineering Applications of Magnetism", edited by Y.Ishikawa and N.Miura (Springer-Verlag, Berlin, 1991).
- [2] Y.Nakamura, Hyperfine Interactions, 83, 55 (1994).
- [3] A.K.Majumdar and P.v.Blanckenhagen, Phys. Rev. B 29, 4079 (1984); J. Magn. Magn. Mat. 40, 227 (1983).
- [4] A.Z.Men'shikov, S.K.Sidorov and A.Ye.Teplykh, Phys. Met. Metallogr. (USSR), 45, 42 (1979).
- [5] A.Z.Men'shikov and A.Ye.Teplykh, Phys. Met. Metallogr. (USSR), 44, 78 (1979).
- [6] R.Nathans and S.J.Pickart, J.Phys.Chem.Solids 25, 183 (1964).
- [7] S.Banerjee and A.K.Raychaudhuri, Solid State Commun. 83, 1047 (1992); T.K.Nath and A.K.Majumdar, Phys. Rev.B, May, 1996.
- [8] S.Banerjee and A.K.Raychaudhuri, J.Phys.Condens.Mat. 5, L295 (1993).
- [9] C.J.Johnson, M.S.Ridout and T.E.Cranshaw, Proc.Phys.Soc. (London), 81, 1069 (1963).
- [10] J.Hesse, Hyperfine Interactions, 47, 357 (1989) and the references therein. See also "Invar Problem", edited by A.J.Freeman and M.Shimizu, J. Magn. and Magn. Mat. 10, 109 (1979).
- [11] W.Bendick and W.Pepperhoff, J.Phys.F:Metal Phys. 11, 57 (1981).
- [12] M.Ghafari, T.Okiyama, T.Takemato, Y.Kawai and Y.Nakamura, Nucl. Instr. and Methods, B 76, 37 (1993).

- [13] A.Verter, Hyperfine Interactions, 45, 113 (1989) .
- [14] E.Kuzmann, I.Czako-Nagy, A.Verter, C.U.Chisholm, A.Watson, M.K.El-Sharif, J.Kerti, and G.Konczos, Hyperfine Interactions, 45, 397 (1989) .
- [15] H.H.Ettwig and W.Pepperhoff, Phys. Status Sol. (a), 23, 105 (1974) and references therein.
- [16] B.Window, J.Phys. E4, 401 (1971) .
- [17] G.M.Bancroft, "Mössbauer Spectroscopy" (McGraw-Hill, Maidenhead, 1973) .
- [18] R.G.Pillay, A.K.Grover, S.N.Mishra, D.Ramababu and P.N.Tandon, Hyperfine Interactions, 34, 527 (1987) .
- [19] B.Huck and J.Hesse, J. Magn. Magn. Mat. 78, 247 (1989) .
- [20] J.Crangle and G.C.Hallam, Proc. Roy. Soc. London A272, 125 (1963) .
- [21] S.N.Kaul, V.Siruguri and G.Chandra, Phys. Rev. B 45, 12343 (1992) .
- [22] C.Meyer, F.Hartmann-Boutron, Y.Gros and I.A.Campbell, J.Magn and Magn. Mat. 46, 254 (1985) .
- [23] A.K.Majumdar, V.Oestreich and D.Weschenfelder, Solid State Commun. 45, 907 (1983) .
- [24] Y.Nakamura, M.Shiga and Y.Takeda, J.Phys.Soc.Japan, 27, 1470 (1969) .

## CHAPTER 4

### Mössbauer spectroscopic study of heat-treated and control-cooled Fe - 24 at% Al and Fe - 25 at% Al

#### 4.1. Introduction

Among the alloys of iron, the iron-aluminium alloy system has invoked considerable research interest because it is a model object of transition metal-sp element system. Most of the interest in this system has been focussed on the investigation of the phase diagram, order - disorder transformations and magnetic and structural properties. In particular the magnetic properties of Fe-Al alloys have been studied using the methods of neutron diffraction [1], magnetization measurements [2] and  $^{57}\text{Fe}$  Mössbauer spectroscopy [3-5]. Since Al is a low - z element, it does not contribute much to the non-resonant absorption in Mössbauer effect. Secondly Al is non-magnetic and hence the solute in the Fe-Al system does not make appreciable contribution of its own. The microscopic technique of  $^{57}\text{Fe}$  Mössbauer spectroscopy has, therefore, been widely applied for studying the hyperfine interactions, phase analysis and order-disorder phenomenon in the Fe-Al system and such work can be divided into two categories: the study of iron-rich alloys, (see review by Gonser and Ron [6]) and the study of aluminium-rich alloys (see papers by Nasu et al. [7]). Most of the Mössbauer spectroscopic investigations of the iron-rich Fe-Al system have aimed at the determination of the hyperfine magnetic field H in the  $\text{Fe}_{1-x}\text{Al}_x$  alloys either as a

function of  $x$  or as a function of temperature. It was pointed out by Srinivasan et al. [8] that the magnetic moment,  $\mu$ , of an Fe atom in these alloys is determined primarily by its nearest neighbour (nn) configuration. As a result the hyperfine magnetic field,  $H$ , at an Fe nucleus will also vary with the number of Fe and Al nn's and a reported variation [5] of  $\mu$  and  $H$  with Fe and Al nn's is shown in Fig.4.1.

At this stage an examination of the Fe-Al phase diagram will be useful. Several workers [9-14] have investigated the phase stability and phase diagram of the Fe-Al system and the well-accepted phase diagram is that suggested by Kubaschewski [15] and it is shown in Fig.4.2(a). Depending on the composition and temperature a number of phases:  $\text{FeAl}_3$  ( $\text{Fe}_4\text{Al}_{13}$ ),  $\text{Fe}_2\text{Al}_5$ ,  $\text{FeAl}_2$ ,  $\text{FeAl}$  and  $\text{Fe}_3\text{Al}$  and ordered structures are exhibited by the Fe-Al system.

The Fe-Al alloys which have been slowly ( $\sim 1^\circ\text{C}/\text{min}$ ) cooled to room temperature can be divided into three classes having basic structural and magnetic properties [5]. This approximate division can be made according to the concentration of Al falling in the ranges 0-18, 18-32 and 32-52 at%. In the first range (the so-called  $\alpha$ -region) one can think of the alloy to be a solid solution in which dilute Al impurities are added in the bcc lattice. The magnetic moment of the Fe atoms is almost same as in  $\alpha$ -Fe. The Mössbauer spectra observed for these alloys closely resemble that of  $\alpha$ -Fe with some minor differences [16]. The alloys containing more than  $\sim 32$  at% Al form the ordered B2 or CsCl structure and are nonmagnetic. Their structure consists of two

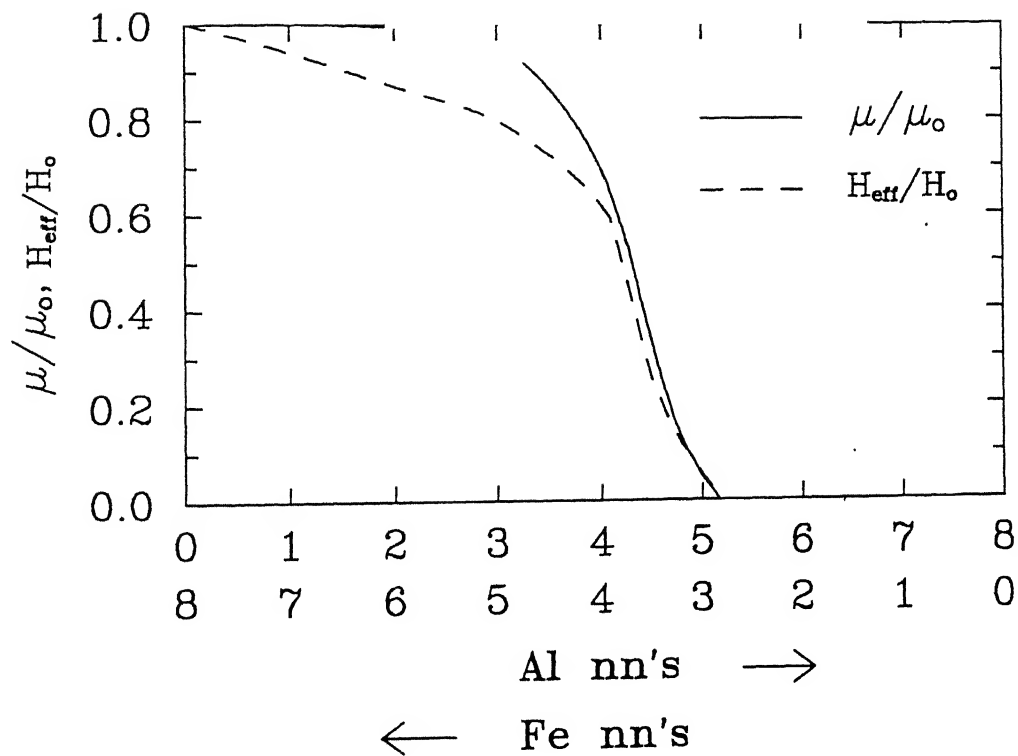


**Fig. 4.1.** Variation of  $\mu$  and  $H$  with Fe and Al nn's. [taken from ref. 5].

interpenetrating simple cubic lattices, one of pure Fe and the other of pure Al. On the other hand the structure of the alloys having ~ 18-32 at% Al is complicated and cannot be described in a straightforward manner. Mössbauer spectra for this composition of alloys show a complex nature which appears to strongly depend on the history and heat-treatment of the samples. Unfolding these spectra into constituent subspectra and identifying them has been a challenging problem in Mössbauer spectroscopy [6]. In the case of Fe-Al alloys having ~ 18-32 at% Al, two ordered phases having stoichiometric compositions  $\text{Fe}_3\text{Al}$  and  $\text{FeAl}$  are of interest. The structure of the ordered state  $\text{Fe}_3\text{Al}$  (shown in Fig.4.3) consists of two sublattices A and D. The sublattice A contains only Fe atoms, each having four Fe and four Al nearest neighbours (nn). On the other hand the sublattice D contains alternately Al and Fe atoms, each having eight Fe nn atoms. Such a crystallographic ordering (Fig.4.3) is called  $\text{DO}_3$ . In the case of the stoichiometric compound  $\text{FeAl}$ , the ordered state is described by CsCl or B2 structure and is formed by two interpenetrating simple cubic lattices. The B2 structure can be understood with the help of Fig.4.3 by disregarding the use of different symbols for atoms in the D sublattice (i.e. sublattice A is formed entirely by Fe atoms and sublattice D is formed entirely by Al atoms). Complete disorder prevails at high temperature and it is then not possible to distinguish between the sublattices and all sites are randomly populated by the constituent atoms giving rise to  $\alpha$ -Fe cell type structure (Fig.4.3). The nn and nnn (next nearest neighbour) configurations for  $\text{Fe}_3\text{Al}$  and  $\text{FeAl}$  can thus be summarized as

follows. In  $\text{Fe}_3\text{Al}$  there are two types of Fe atoms, one having 8Fe nn's and 6Al nnn's, the other having 4Fe and 4Al nn's and 6Fe nnn's. On the other hand the configuration for FeAl has Fe atoms having 8Al nn's and 6Fe nnn's. Previous work [16-22] has shown that the hyperfine magnetic field,  $H$ , at an  $^{57}\text{Fe}$  nucleus is determined by the particular nn and nnn configuration of the extranuclear atom and this in turn influences the hyperfine interaction parameters which can be experimentally measured by Mössbauer spectroscopy. It is also known that the phase boundaries shown in Fig.4.2 are somewhat uncertain because they depend on the exact nature of the heat treatment and processing carried out for preparing the samples.

It is well known that by varying composition and process of heat treatment (and quenching) a series of Fe-Al alloys having different soft magnetic and physical properties can be obtained. For example the Fe - 22 at% Al show high magnetic permeability, the Fe - 25 at% Al have large magnetostriction and the Fe - 28 at% Al possess high magnetic permeability and these three alloys have emerged as important materials having wide engineering applications [23]. Although the Al-concentration in these three alloys does not differ much, the process routes by which they are heat-treated and quenched for practical use differ significantly amongst themselves. The variations in the magnetic properties of these Fe-Al alloys are expected to arise from the different atomic configurations in their crystal structure [5]. It has been recognised that  $^{57}\text{Fe}$  Mössbauer spectroscopy offers a sensitive microscopic point-probe to identify the type of  $^{57}\text{Fe}$ -atom

configurations responsible for different hyperfine fields,  $H$ , observed in iron-based alloys [16-22]. Other possible technique available for the study of atomic configurations are the transmission electron microscopy (TEM) and X-ray diffraction (XRD). The former technique, TEM, provides only a localized probe while the latter technique (XRD) suffers from some limitations for the present purpose. These drawbacks arise because the superlattice reflections are very weak in intensity and the changes in the lattice parameters for fundamental reflections bring complications in data analysis. Again the sensitivity of each technique to bulk effects is different. Considering all these aspects, Mössbauer spectroscopy is the best and most sensitive technique to identify different phases (arising out of different atomic configurations) and estimate their volume fractions. Although the Fe-Al system has been extensively studied using  $^{57}\text{Fe}$  Mössbauer spectroscopy, most of the investigations have been carried out to examine the effect of either the composition or the temperature of the sample [16-22]. Not many studies have attempted to measure the Mössbauer spectra at room temperature keeping the composition fixed but using different processing routes (i.e. heat-treatment and quenching) for the samples.

In the present work we report Mössbauer spectroscopic studies of the Fe-24 at% Al and Fe-25 at% Al alloys. Fe-Al alloys having 22-31 at% Al are known to exhibit several attractive properties which render them potential materials for structural and magnetic applications. These alloys possess high strength, low density, extremely good corrosion and oxidation resistance which make them

suitable materials for structural applications [24]. Regarding their magnetic properties, their high magnetic permeability and large magnetostriction qualify these alloys as important materials useful for technological applications [23]. Further it is observed that a series of Fe-Al alloys having different soft magnetic and physical properties can be obtained by varying the composition and the process of heat treatment [23].

Keeping these aspects in mind we have investigated, using  $^{57}\text{Fe}$  Mössbauer spectroscopy, the effect of quenching or cooling process (involved during the sample preparation) on the hyperfine magnetic field H present in various phases due to different Fe sites having different Fe atom configurations. The phases were stabilized through equilibrium slow cooling or rapid quenching involving a schedule described in the next section. The composition of the alloys was chosen with an aim of bringing the cooling path through the triangular region of the  $\lambda$  transition of the phase diagram [Fig.4.2(b)]. Thus the Fe-24 at% alloy corresponds to the left region whereas the Fe-25 at% Al alloy corresponds to the right corner of the triangle.

Although in the processing of each of the five alloy samples studied by us we started with a disordered phase of the alloy, the different processing routes followed by us lead to a partial ordering in which Fe and Al atoms occupy random atomic sites. Hence the samples of the quenched alloys cannot be described in terms of unique crystal structure (e.g.  $\text{DO}_3$ , B2 ... etc) and they consist of various phases assigned to different atomic configurations. The aim of the present Mössbauer spectroscopic

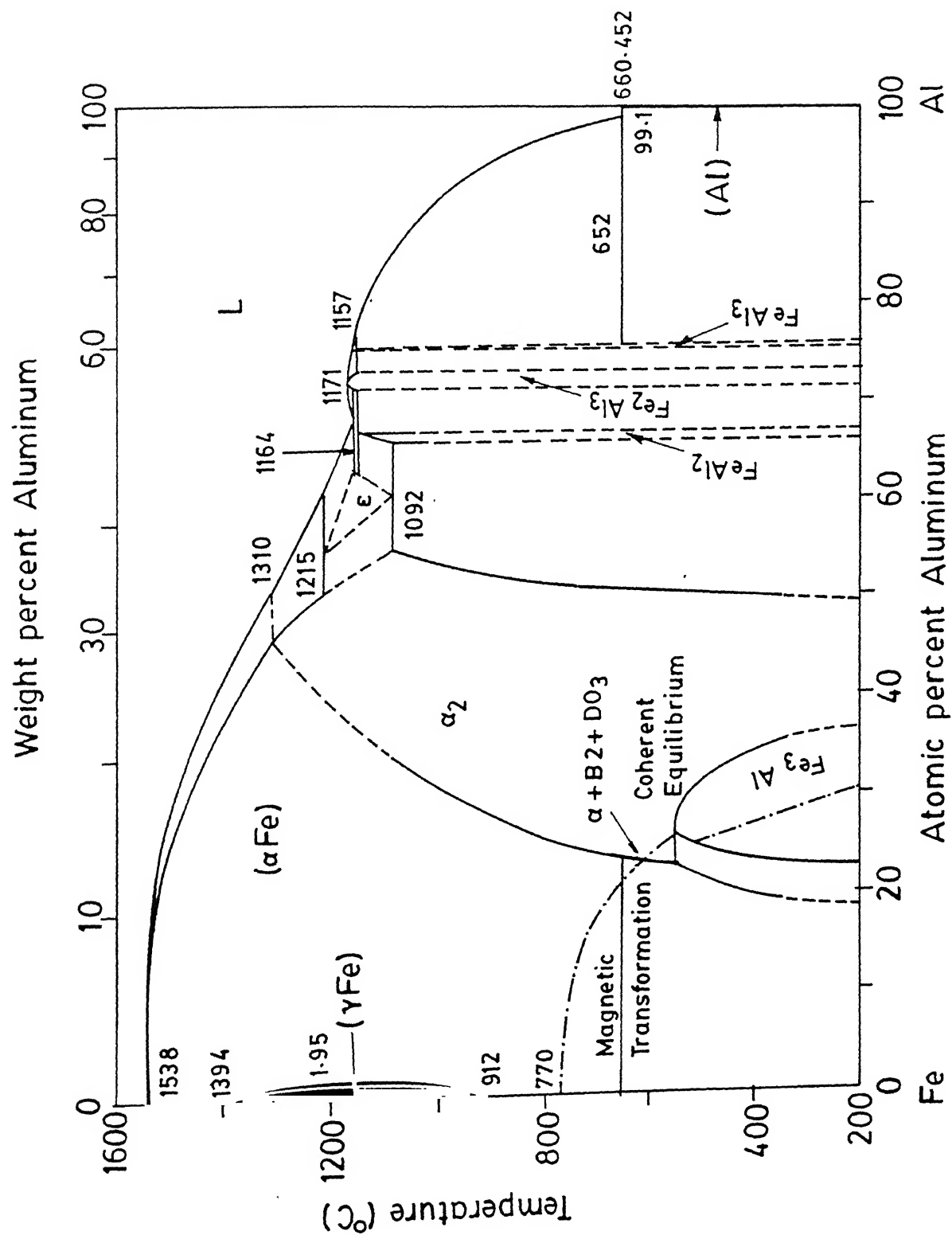


Fig. 4.2 (a). Phase diagram of Fe-Al system.

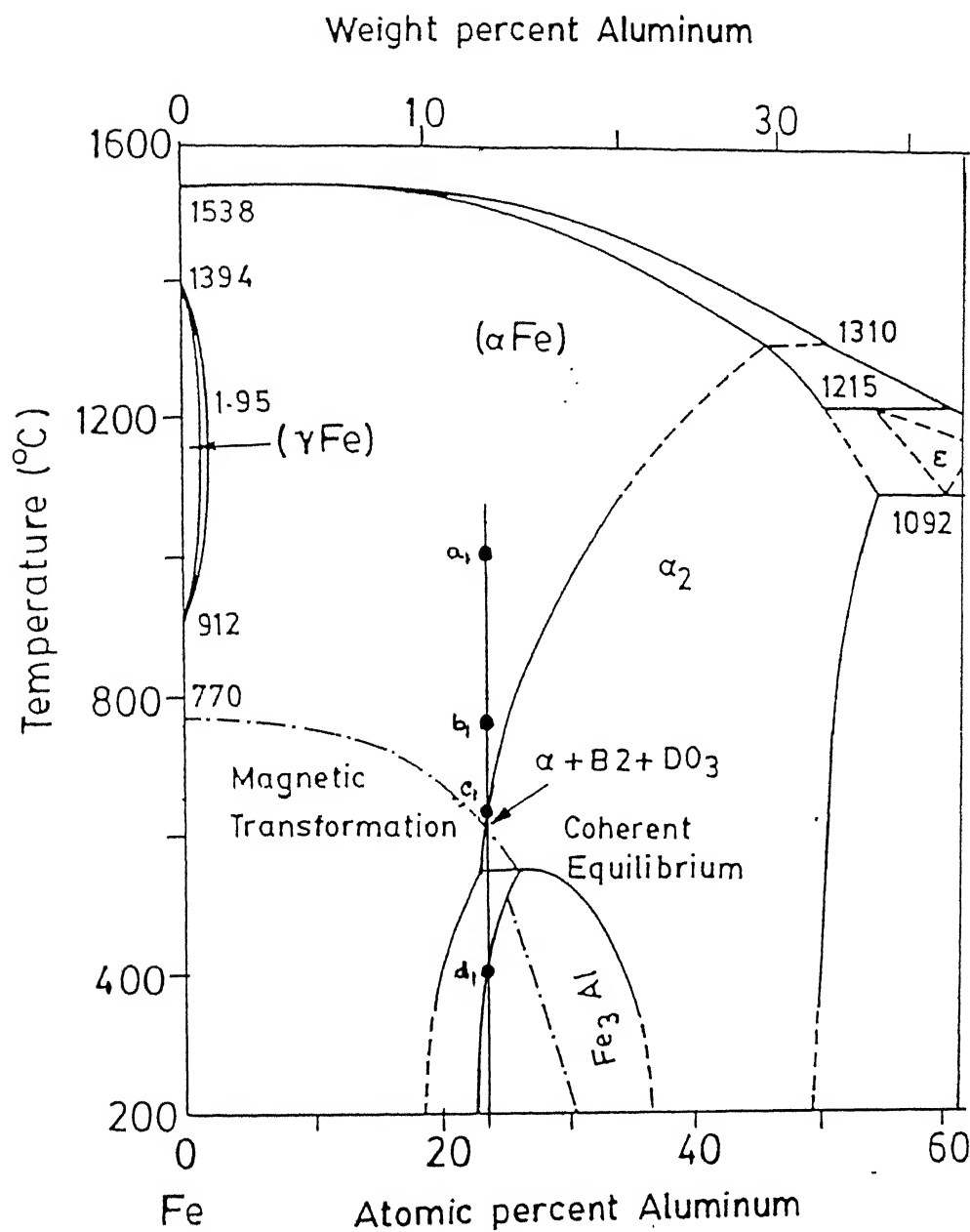
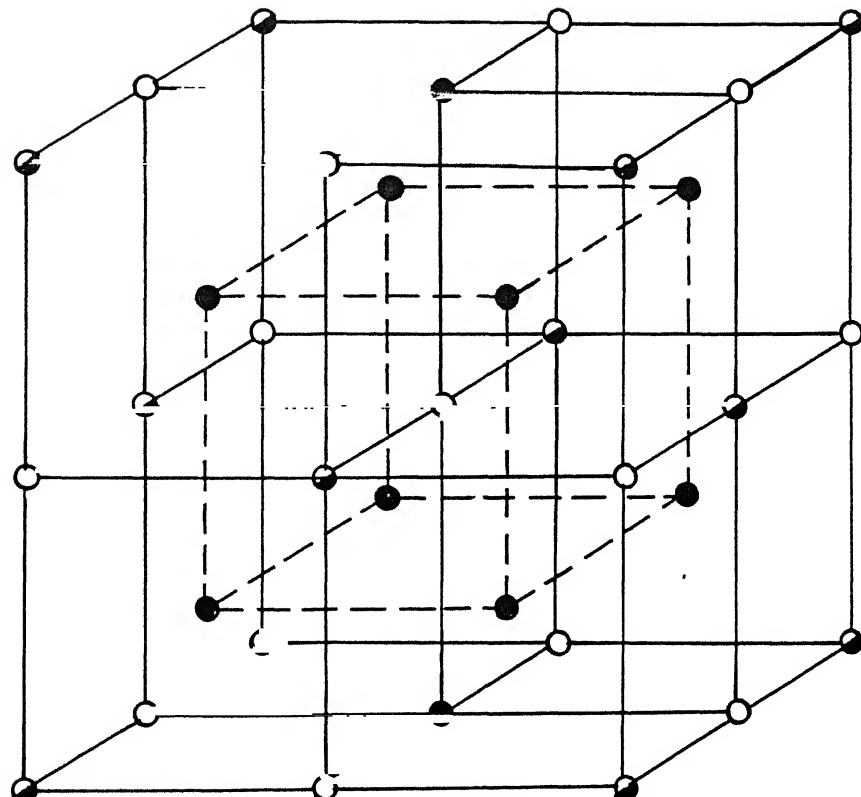


Fig. 4.2(b). Route of the sample processing schedules in phase diagram.



Sublattice A ● Fe

Sublattice D { ● Fe  
○ Al

Fig. 4.3.

Structure of  $\text{Fe}_3\text{Al}$  ( $\text{DO}_3$ ).

studies is to identify these phases and the atomic configurations responsible for them, and to determine the volume fraction of these phases. By studying the five different samples it should be possible to examine the effect of processing routes on the nature and volume fraction of these phases.

#### 4.2. Experimental procedure

The Fe-Al alloys were prepared from high purity Fe and Al metals having 99.99% purity by consumable electrode arc melting in a water-cooled copper crucible. The ingots were homogenized at  $1000^{\circ}\text{C}$  for 168 hours to remove any compositional inhomogeneity. The homogeneity was checked by characterizing the homogenized alloys by electron probe analyzer. Small pieces of the homogenized ingots were cut and encapsulated in quartz capsules in high vacuum ( $\sim 10^{-6}$  Torr). These capsules were then heated in a vertical tube furnace by following the processing schedule shown in Table 4.1 so that five Fe-Al alloys each having a different route of processing and rate of cooling were prepared. It is well known that the extent of phase formation depends upon the rate of cooling of each of these five alloys.

The absorbers for Mössbauer spectroscopy were prepared from powdered (particle size less than  $53 \text{ m}\mu$ ) samples of these five alloys (designated as AA1 - AA5, see Table 4.1.) and they were used to record transmission Mössbauer spectra at room temperature ( $23^{\circ}\text{C}$ ). A Mössbauer spectrometer coupled to a multichannel analyzer and operated in a constant acceleration mode was used. A  $^{57}\text{Co}$  source embedded in rhodium matrix (Amersham International

Table 4.1. Routes and Schedule of heat-treatment and processing of different samples of Fe-Al alloys. See Figs.4.2(b) for the explanation of the symbols  $a_1$ ,  $b_1$ , etc. used for describing the route.

| Sample | Composition | Route used for heat treatment and processing   |
|--------|-------------|--|
| AA1    | Fe-24at% Al | <u>Route 1:</u> $a_1 \longrightarrow$ ice quenching.<br>As-cast alloy was heated at $1000^{\circ}\text{C}$ for 168 h. It was then ice quenched from disordered $\alpha$ -phase field.  |
| AA2    | Fe-24at% Al | <u>Route 2:</u> $a_1 \longrightarrow b_1 \longrightarrow$ ice quenching.<br>As-cast alloy was heated at $1000^{\circ}\text{C}$ for 168 h. It was then cooled from $1000^{\circ}\text{C}$ to $750^{\circ}\text{C}$ at the rate of $2^{\circ}\text{C}/\text{min}$ . After keeping it at $750^{\circ}\text{C}$ for 48 h, it was ice quenched from ( $\alpha$ + imperfectly ordered B2) phase field  |
| AA3    | Fe-24at% Al | <u>Route 3:</u> $a_1 \longrightarrow b_1 \longrightarrow c_1 \longrightarrow$ ice quenching.<br>As-cast alloy was heated at $1000^{\circ}\text{C}$ for 168 h. It was then cooled from $1000^{\circ}\text{C}$ to $750^{\circ}\text{C}$ at the rate of $2^{\circ}\text{C}/\text{min}$ . Next it was cooled from $750^{\circ}\text{C}$ to $575^{\circ}\text{C}$ at the rate of $2^{\circ}\text{C}/\text{min}$ . After keeping it at $575^{\circ}\text{C}$ for 48 h, it was ice-quenched from the triple phase field $\alpha$ , B2 and $\text{DO}_3$ . |

(Continued on the next page)

Table 4.1. (Continued)

|     |             |   |
|-----|-------------|---|
| AA4 | Fe-24at% Al | <p><u>Route 4:</u> <math>a_1 \rightarrow b_1 \rightarrow c_1 \rightarrow d_1 \rightarrow</math> cooled to RT</p> <p>As-cast alloy was heated at <math>1000^{\circ}\text{C}</math> for 168 h. It was then cooled from <math>1000^{\circ}\text{C}</math> to <math>750^{\circ}\text{C}</math> at the rate of <math>2^{\circ}\text{C}/\text{min}</math>. Next it was cooled from <math>750^{\circ}\text{C}</math> to <math>575^{\circ}\text{C}</math> at the rate of <math>2^{\circ}\text{C}/\text{min}</math>. It was kept at <math>575^{\circ}\text{C}</math> for 48 h and then it was cooled to <math>400^{\circ}\text{C}</math> at <math>2^{\circ}\text{C}/\text{min}</math>. It was then furnace cooled to room temperature from (RT) in the <math>\text{DO}_3</math> phase field.</p> |
| AA5 | Fe-25at% Al | <p><u>Route 5:</u> <math>a_2 \rightarrow b_2 \rightarrow c_2 \rightarrow d_2 \rightarrow</math> cooled to RT</p> <p>As-cast alloy was heated at <math>1000^{\circ}\text{C}</math> for 168 h. It was then cooled at the rate of <math>1^{\circ}\text{C}/\text{min}</math> to <math>650^{\circ}\text{C}</math> in the imperfectly ordered B2 phase. Next it was cooled <math>550^{\circ}\text{C}</math> for 6h to ensure the transformation from B2 <math>\rightarrow \text{DO}_3</math> phase. It was then cooled to <math>450^{\circ}\text{C}</math> at the rate of <math>1^{\circ}\text{C}/\text{min}</math> and held at <math>450^{\circ}\text{C}</math> for 48h in order to stabilise the <math>\text{DO}_3</math> phase. Next it was slowly cooled to RT</p>                        |

Ltd., Amersham, U.K.) was used and the spectrometer was calibrated using a standard  $\alpha$ -Fe foil.

The analysis of the Mössbauer spectra was carried out with computer programs using two methods. In the first method a least-squares-fitting computer program employing Lorentzian shapes for the peaks and an iterative procedure was used. It was assumed that the total Mössbauer spectrum was a superposition of a number of contributing subspectra each having different Mössbauer parameters (i.e. hyperfine field  $H$ , isomer shift  $IS$ , relative intensity etc).

In the second method we followed the procedure of Window [27] to obtain the hyperfine field distributions  $P(H)$ , and the average hyperfine field  $\langle H \rangle = \int HP(H) dH / \int P(H) dH$ .

#### 4.3. Results and discussion

##### **4.3.1. Analysis using least-squares-fitting to the Mössbauer spectra.**

###### **4.3.1.1. Introduction**

Mössbauer spectra observed for the five different samples AA1-AA5 (Table 4.1) at room temperature are shown in Figs.4.4-4.8 respectively and they appear similar. Each of these spectra was found to be complex and could be decomposed into five sextets (subspectra) without any trace of a paramagnetic component.

The hyperfine magnetic fields,  $H$ , obtained for each of these subspectra are given in Table 4.2. The width of the lines in each of these subspectra appeared broader, showing the FWHM - values in the range  $0.35 - 0.40 \text{ mms}^{-1}$  as compared to the value  $0.25 \text{ mms}^{-1}$

Normalized Counts.

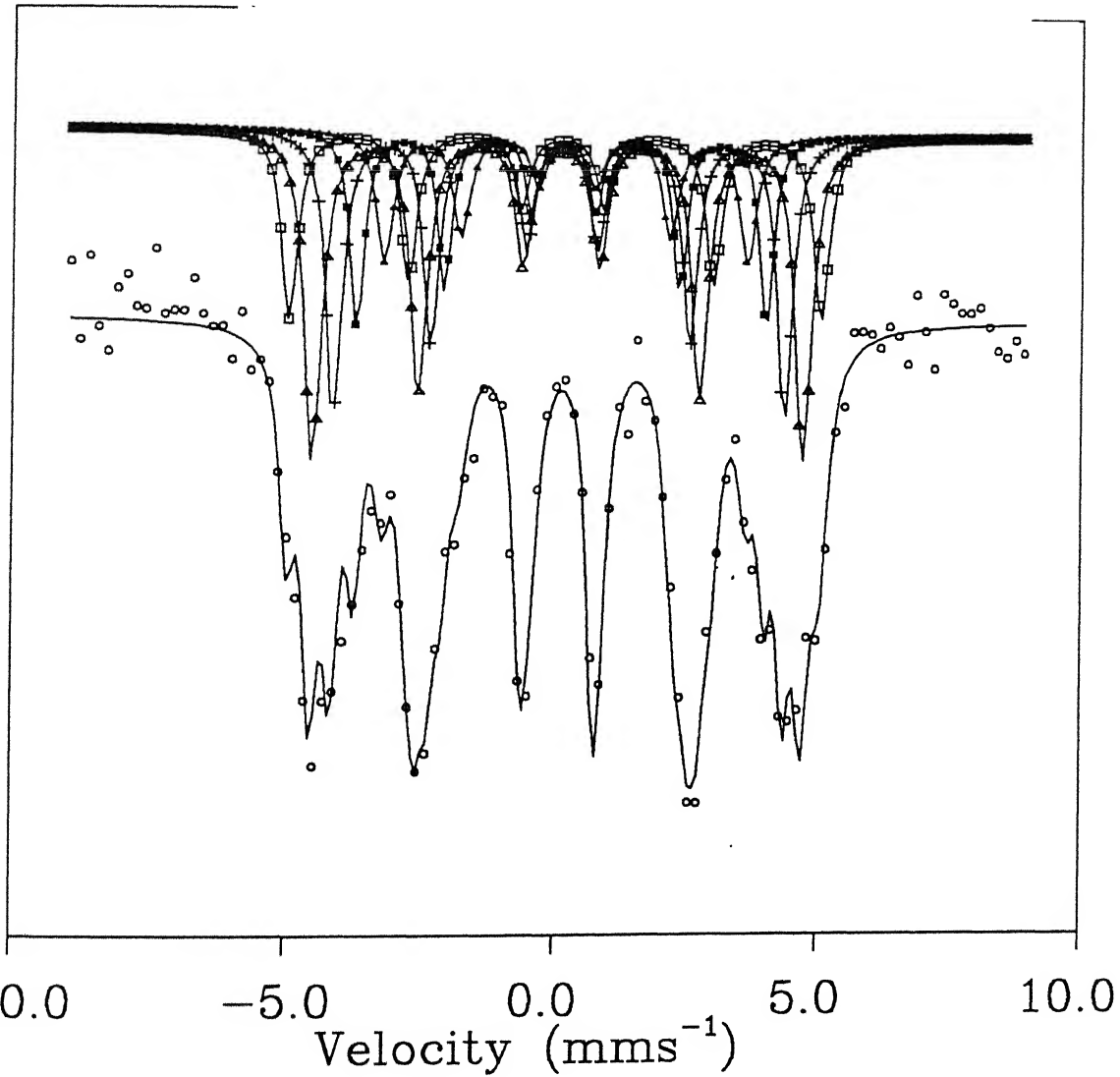


**Fig. 4.4.** Mössbauer spectra of the sample AA1. Open circles (lower spectrum) represent the experimental data points. The upper Figure shows the five subspectra providing the best fit with □, Δ, +, ■ and ▲ representing sites I, II, III, IV and V (see Table 4.2) respectively.

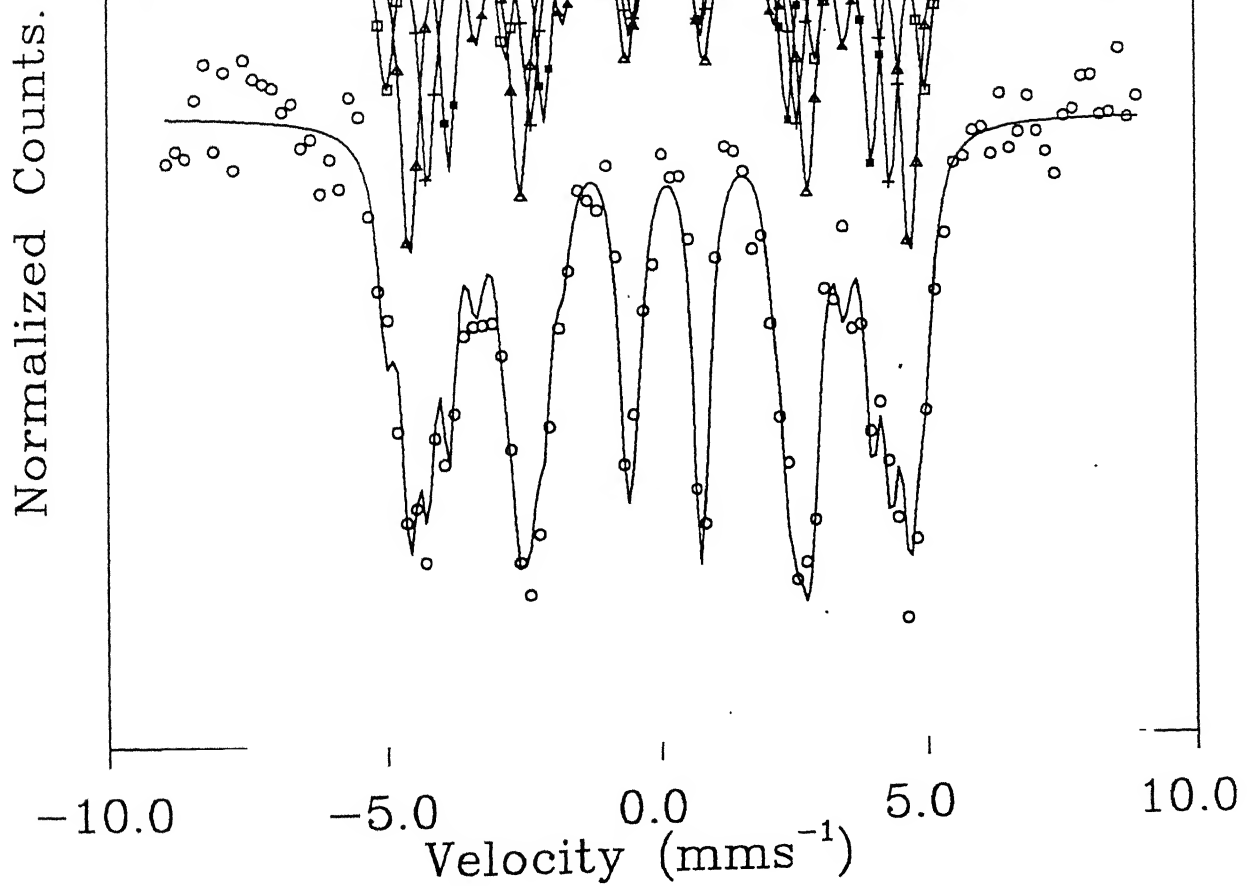


**Fig. 4.5.** Mössbauer spectra of the sample AA2. Open circles (lower spectrum) represent the experimental data points. The upper figure shows the five subspectra providing the best fit with  $\square$ ,  $\Delta$ , +, ■ and  $\blacktriangle$  representing sites I, II, III, IV and V (see Table 4.2) respectively.

Normalized Counts.

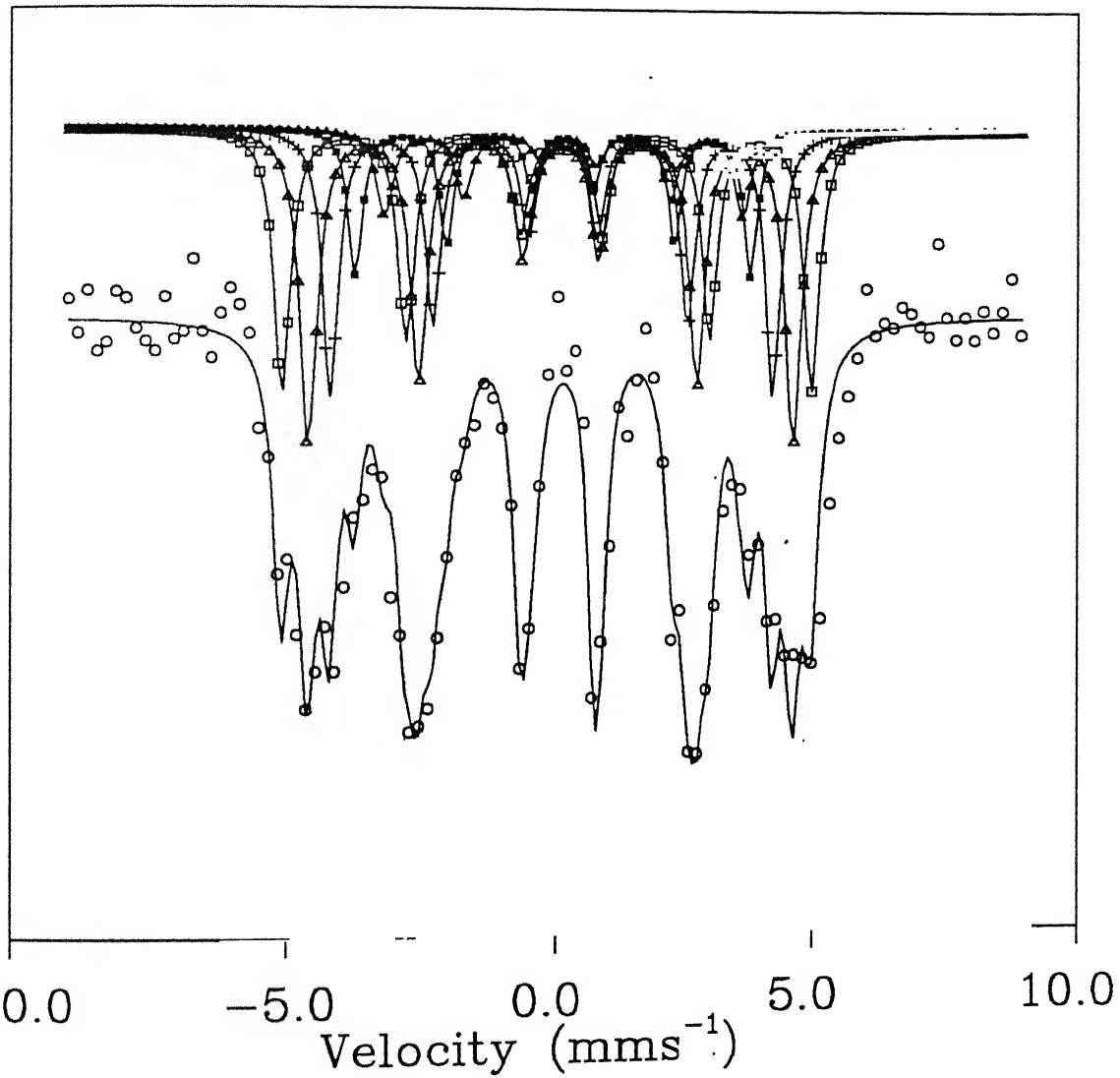
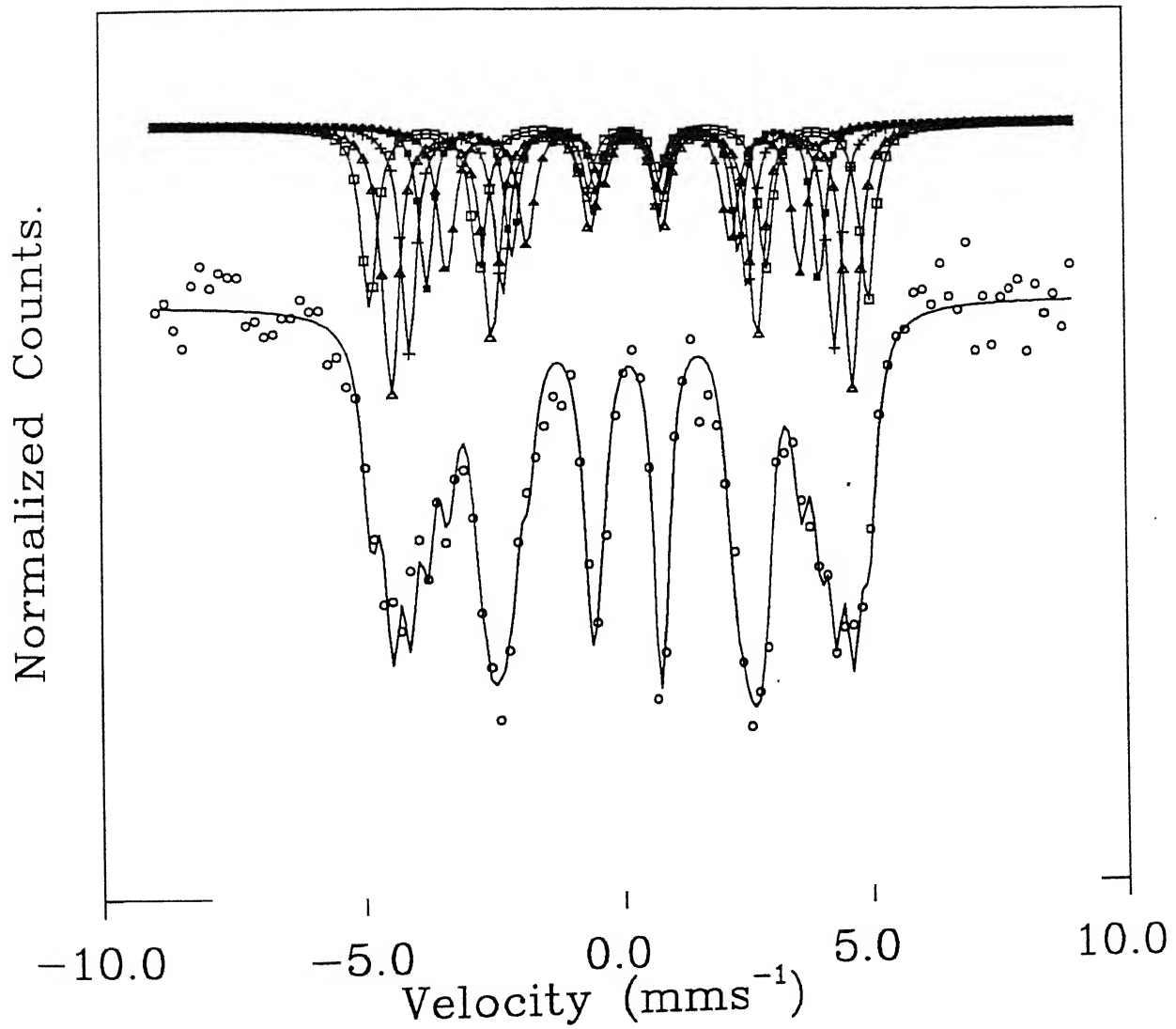
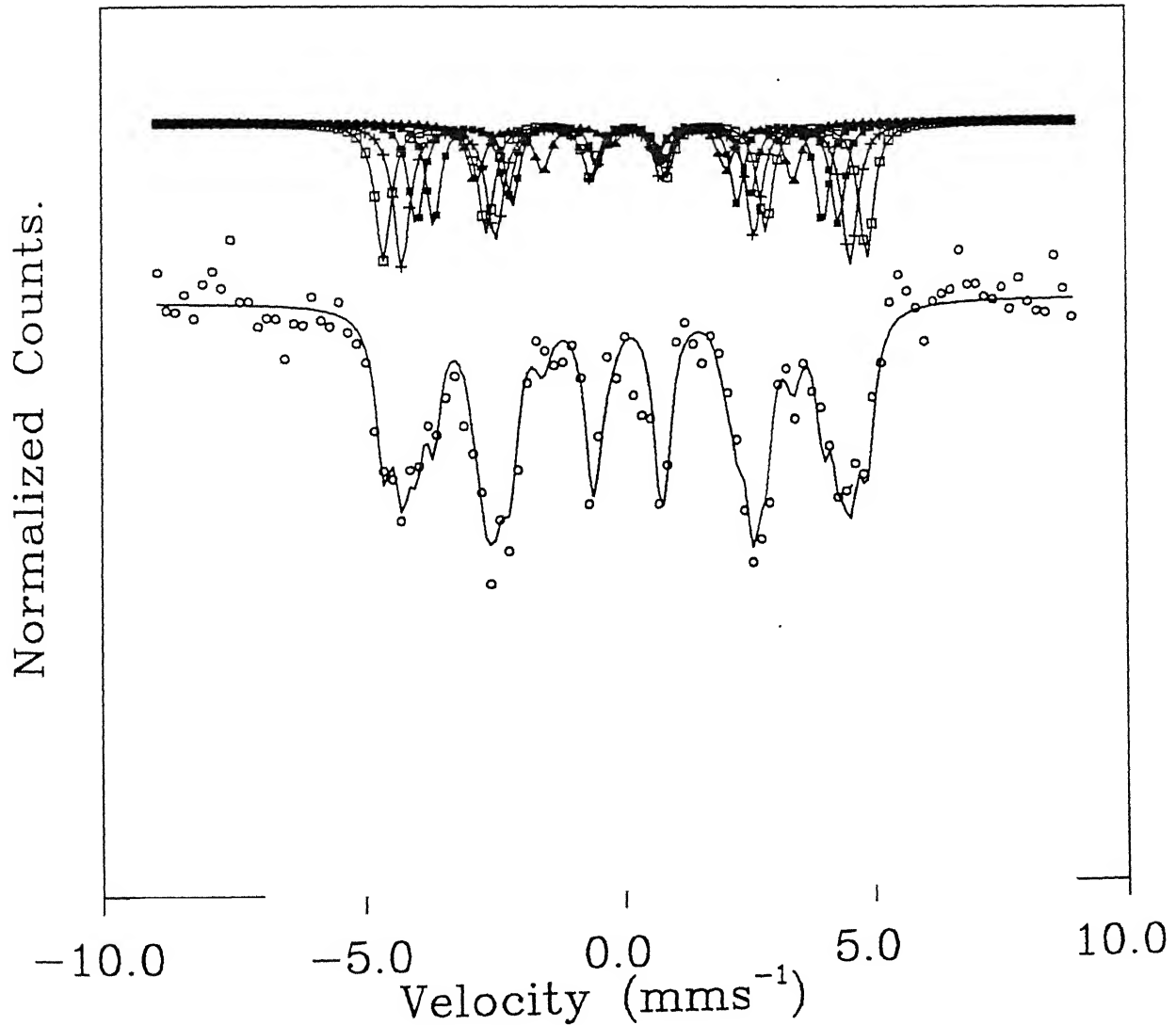


Fig. 4.6. Mössbauer spectra of the sample AA3. Open circles (lower spectrum) represent the experimental data points. The upper Figure shows the five subspectra providing the best fit with  $\square$ ,  $\Delta$ , +, ■ and  $\blacktriangle$  representing sites I, II, III, IV and V (see Table 4.2) respectively.



**Fig. 4.7.** Mössbauer spectra of the sample AA4. Open circles (lower spectrum) represent the experimental data points. The upper Figure shows the five subspectra providing the best fit with  $\square$ ,  $\Delta$ , +, ■ and ▲ representing sites I, II, III, IV and V (see Table 4.2) respectively.



**Fig. 4.8.** Mössbauer spectra of the sample AA5. Open circles (lower spectrum) represent the experimental data points. The upper figure shows the five subspectra providing the best fit with □, Δ, +, ■ and ▲ representing sites I, II, III, IV and V (see Table 4.2) respectively.

Table 4.2. Mössbauer parameters ( $H$ ,  $\Gamma$ , intensity) of samples AA1-AA5 measured at room temperature and the proposed assignment of configurations giving rise to each of the hyperfine magnetic field.

| Sample | Site | $H$<br>(a)<br>in kOe | $\Gamma$<br>(b) | Intensity<br>% (c) | Assignment (d)  |
|--------|------|----------------------|-----------------|--------------------|---|
| AA1    | I    | 310                  | 0.37            | 17                 | $(7\text{Fe} + 1\text{Al})\text{nn} + 6\text{Fe nnn}$<br>and<br>$8\text{Fe nn} + (4\text{Fe} + 2\text{Al})\text{nnn}$ |
|        | II   | 286                  | 0.38            | 31                 | $(6\text{Fe} + 2\text{Al})\text{nn} + 6\text{Fe nnn}$<br>and<br>$8\text{Fe nn} + (2\text{Fe} + 4\text{Al})\text{nnn}$ |
|        | III  | 264                  | 0.37            | 24                 | $(5\text{Fe} + 3\text{Al})\text{nn} + 6\text{Fe nnn}$<br>and<br>$8\text{Fe nn} + 6\text{Al nnn}$                      |
|        | IV   | 240                  | 0.30            | 15                 | $(4\text{Fe} + 4\text{Al})\text{nn} + 6\text{Fe nnn}$   |
|        | V    | 214                  | 0.38            | 13                 | $(3\text{Fe} + 5\text{Al})\text{nn} + 6\text{Fe nnn}$   |
| AA2    | I    | 309                  | 0.36            | 15                 | $(7\text{Fe} + 1\text{Al})\text{nn} + 6\text{Fe nnn}$<br>and<br>$8\text{Fe nn} + (4\text{Fe} + 2\text{Al})\text{nnn}$ |
|        | II   | 288                  | 0.38            | 32                 | $(6\text{Fe} + 2\text{Al})\text{nn} + 6\text{Fe nnn}$<br>and<br>$8\text{Fe nn} + (2\text{Fe} + 4\text{Al})\text{nnn}$ |
|        | III  | 266                  | 0.34            | 22                 | $(5\text{Fe} + 3\text{Al})\text{nn} + 6\text{Fe nnn}$<br>and<br>$8\text{Fe nn} + 6\text{Al nnn}$                      |
|        | IV   | 243                  | 0.31            | 19                 | $(4\text{Fe} + 4\text{Al})\text{nn} + 6\text{Fe nnn}$   |
|        | V    | 212                  | 0.38            | 12                 | $(3\text{Fe} + 5\text{Al})\text{nn} + 6\text{Fe nnn}$   |
| AA3    | I    | 311                  | 0.36            | 25                 | $(7\text{Fe} + 1\text{Al})\text{nn} + 6\text{Fe nnn}$<br>and<br>$8\text{Fe nn} + (4\text{Fe} + 2\text{Al})\text{nnn}$ |
|        | II   | 286                  | 0.38            | 31                 | $(6\text{Fe} + 2\text{Al})\text{nn} + 6\text{Fe nnn}$<br>and<br>$8\text{Fe nn} + (2\text{Fe} + 4\text{Al})\text{nnn}$ |
|        | III  | 261                  | 0.34            | 23                 | $(5\text{Fe} + 3\text{Al})\text{nn} + 6\text{Fe nnn}$<br>and<br>$8\text{Fe nn} + 6\text{Al nnn}$                      |
|        | IV   | 234                  | 0.31            | 12                 | $(4\text{Fe} + 4\text{Al})\text{nn} + 6\text{Fe nnn}$   |
|        | V    | 213                  | 0.38            | 9                  | $(3\text{Fe} + 5\text{Al})\text{nn} + 6\text{Fe nnn}$   |

Table 4.2. (Continued)

| Sample | Site | H <sup>(a)</sup><br>in kOe | $\Gamma$ <sup>(b)</sup> | Intensity<br>% (c) | Assignment <sup>(d)</sup>   |
|--------|------|----------------------------|-------------------------|--------------------|---|
| AA4    | I    | 304                        | 0.36                    | 19                 | $(7\text{Fe} + 1\text{Al})\text{nn} + 6\text{Fe nnn}$<br>and<br>$8\text{Fe nn} + (4\text{Fe} + 2\text{Al})\text{nnn}$ |
|        | II   | 282                        | 0.38                    | 29                 | $(6\text{Fe} + 2\text{Al})\text{nn} + 6\text{Fe nnn}$<br>and<br>$8\text{Fe nn} + (2\text{Fe} + 4\text{Al})\text{nnn}$ |
|        | III  | 260                        | 0.34                    | 22                 | $(5\text{Fe} + 3\text{Al})\text{nn} + 6\text{Fe nnn}$<br>and<br>$8\text{Fe nn} + 6\text{Al nnn}$                      |
|        | IV   | 241                        | 0.31                    | 14                 | $(4\text{Fe} + 4\text{Al})\text{nn} + 6\text{Fe nnn}$   |
|        | V    | 217                        | 0.38                    | 16                 | $(3\text{Fe} + 5\text{Al})\text{nn} + 6\text{Fe nnn}$   |
| AA5    | I    | 295                        | 0.36                    | 25                 | $8\text{Fe nn} + (3\text{Fe} + 3\text{Al})\text{nnn}$   |
|        | II   | 273                        | 0.38                    | 28                 | $8\text{Fe nn} + (1\text{Fe} + 5\text{Al})\text{nnn}$   |
|        | III  | 257                        | 0.34                    | 18                 | $(5\text{Fe} + 3\text{Al})\text{nn} + 6\text{Fe nnn}$<br>and<br>$8\text{Fe nn} + 6\text{Al nnn}$                      |
|        | IV   | 237                        | 0.31                    | 17                 | $(4\text{Fe} + 4\text{Al})\text{nn} + 6\text{Fe nnn}$   |
|        | V    | 194                        | 0.38                    | 12                 | $(2\text{Fe} + 6\text{Al})\text{nn} + 6\text{Fe nnn}$   |

(a) H = Hyperfine magnetic field at the  $^{57}\text{Fe}$  nucleus in units of kOe: Typical error is  $\pm 4\text{kOe}$ .

(b)  $\Gamma$  (FWHM) = Full width at half maximum of the spectral line, values in  $\text{mms}^{-1}$ . Typical error is  $\pm 0.01 \text{ mms}^{-1}$ .

(c) The area values are given as percentages. Typical error is  $\pm 1\%$ .

(d) Proposed Fe atom configuration: nn = nearest neighbour, nnn = next nearest neighbour.

observed for pure  $\alpha$ -Fe. It is interesting to note that for the Fe - 21.2 at% Al Stearns (Fig.2, ref. [4]) also observed five values of the hyperfine field H. To facilitate a comparison of the five H-values observed by us for each of the different samples we have plotted them in Fig.4.9 so that each vertical column shows the H-values obtained for a particular sample. It is observed that the set of H-values observed for the first four samples AA1, AA2, AA3 and AA4 (all containing 24 at% Al) agree among each other within the experimental error. The H-values for the Fe + 25 at% Al alloy (sample AA5), however, shows a different set. This aspect will be discussed later.

It is observed from Table 4.2 that the subspectra yield H-values lying in the range  $H = 318 - 197$  kOe. Using Mössbauer spectroscopy, Stearns [16] has shown how the hyperfine magnetic field H at the Fe nuclei in Fe-Al alloys depends upon the number of Al atoms in the surrounding coordination spheres. Similar approach has been used by the other workers [16-22] to explain the results for H observed by Mössbauer spectroscopy in Fe-Al system. While Stearns [16] interpreted the results in terms of the effect of solute atoms in the first five neighbour shells, Perez Alcazar and Galvao da Silva [21] considered the effect of first (nn) and second (nnn) neighbouring shells. These workers assumed that the 8Fe nn + 6Fe nnn configuration gives  $H_o = 330$  kOe but this field is reduced to  $H = H_o - n_1 \Delta H_1 - n_2 \Delta H_2$  where  $n_1$  and  $n_2$  are the number of Al atoms in the 8 nearest (nn) and the 6 next nearest (nnn) neighbour sites of Fe. Following Stearns [16] they first used  $\Delta H_1 = 24$  kOe (being the reduction in H for each Fe atom

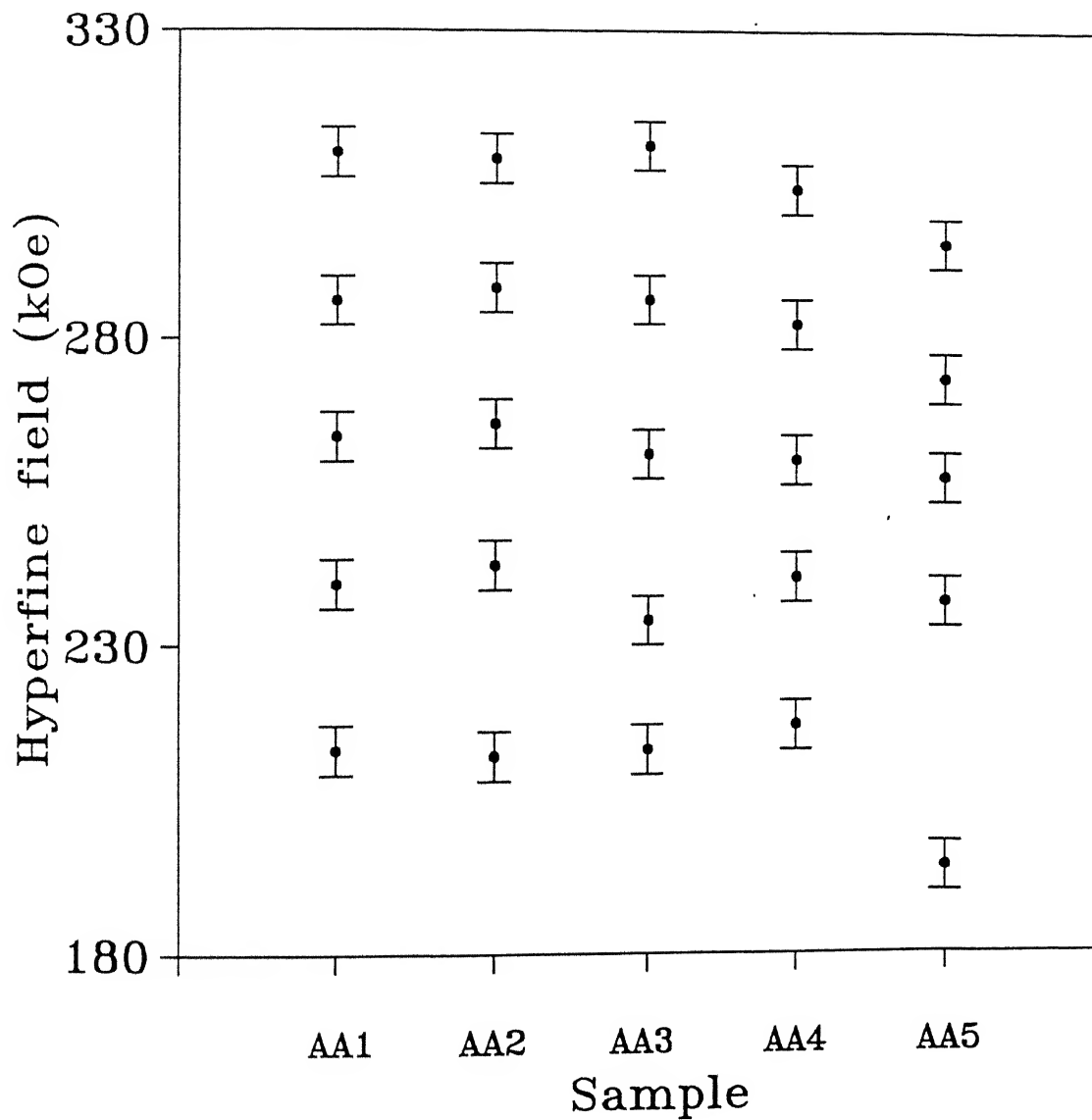


Fig. 4.9. Variation of hperfine field of different sites in samples AA1 - AA5.

substituted by Al in the nn site) and  $\Delta H_2 = 11$  kOe (being the reduction in H for each Fe atom substituted by Al in the nnn site). The probability of finding  $n_1$  Al atoms in the first Fe shell and  $n_2$  in the second Fe shell was given [21] by the binomial distribution

$$P(n_1, n_2) = C_8^{n_1} C_6^{n_2} q^{n_1+n_2} (1-q)^{14-n_1-n_2} \quad (1)$$

where q is the Al concentration and  $C_i^j$  are binomial coefficients.

In order to interpret their experimental data better Perez Alcazar and Galvao da Silva [21] used another empirical relation

$$H = H_0 (1 - \alpha n_1 - \beta n_2) \quad (2)$$

where  $H_0 = 330$  kOe,  $\alpha$  being the value corresponding to  $\Delta H_1 = 24$  kOe (in agreement with Stearns [16]) and  $\beta = 1.5\%$  (which gave  $\Delta H_2 = 5$  kOe). Yeluskov et al. [22] considered only the effects of nn atoms and found that the local hyperfine field H depended nonlinearly on the number of nn Al atoms, the fourth and next (upto eight) nn atom causing H to change by a greater extent than the first three atoms as shown in Fig.4.10.

In order to facilitate the interpretation of the present results (Table 4.2) we have collated the values of H predicted by the above three different models in Table 4.3. Some other experimental results are also included in Table 4.3 for the sake of completeness.

The data presented in Table 4.3 have been used to propose assignments for the Fe-atom configurations responsible for giving rise to each of the five subspectra observed in the present work. While making these assignments we have kept in mind two facts: (i)

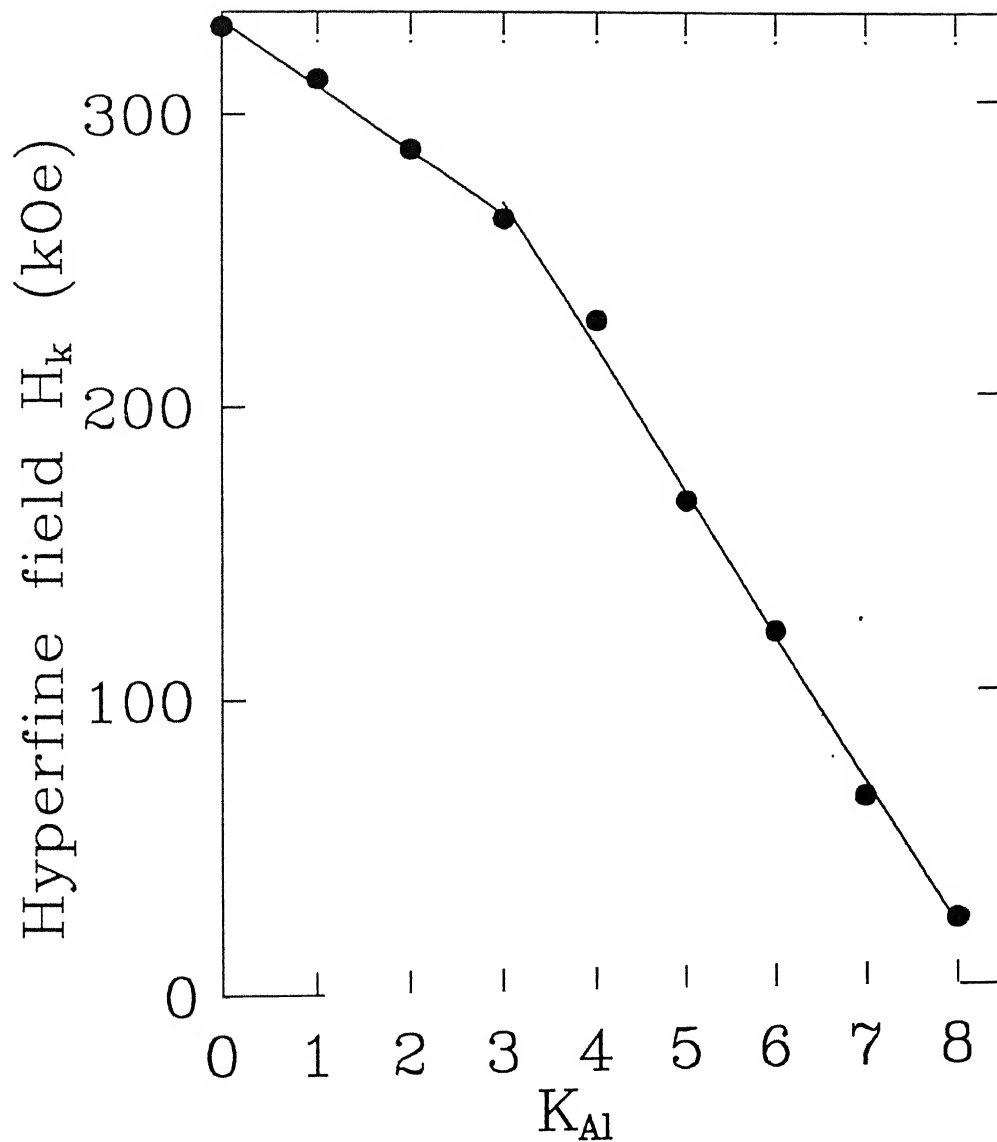


Fig. 4.10. Dependence of local hyperfine field  $H_k$  on the number of K nearest-neighbour Al atoms of the Fe atoms [taken from ref. 22].

Table 4.3. Magnetic hyperfine field values for different Fe atom configuration in Fe-Al alloys as proposed by different workers. All values are in kOe.

| Label | Configuration          | References |     |     |        |
|-------|------------------------|------------|-----|-----|--------|
|       |                        | a          | b   | c   | Others |
| 1.    | 8Fe nn + 6Fe nnn       | 330        | 330 | 330 |        |
| 2.    | (7Fe+1Al) nn + 6Fe nnn | 306        | 306 | 312 |        |
| 3.    | (6Fe+2Al) nn + 6Fe nnn | 282        | 282 | 288 |        |
| 4.    | (5Fe+3Al) nn + 6Fe nnn | 258        | 258 | 264 | 261(d) |
| 5.    | (4Fe+4Al) nn + 6Fe nnn | 234        | 234 | 229 | 230(e) |
| 6.    | (3Fe+5Al) nn + 6Fe nnn | 210        | 210 | 167 |        |
| 7.    | (2Fe+6Al) nn + 6Fe nnn | 186        | 186 | 122 |        |
| 8.    | (1Fe+7Al) nn + 6Fe nnn | 162        | 162 | 65  |        |
| 9.    | 8Fe nn + (5Fe+1Al) nnn | 319        | 325 |     |        |
| 10.   | 8Fe nn + (4Fe+2Al) nnn | 308        | 320 |     |        |
| 11.   | 8Fe nn + (3Fe+3Al) nnn | 297        | 315 |     |        |
| 12.   | 8Fe nn + (2Fe+4Al) nnn | 286        | 310 |     |        |
| 13.   | 8Fe nn + (1Fe+5Al) nnn | 275        | 305 |     |        |
| 14.   | 8Fe nn + 6Al nnn (DO3) | 264        | 300 |     | 300(e) |

(a) Ref. [16] with  $\Delta H_1 = 24$  kOe,  $\Delta H_2 = 11$  kOe.

(b) Ref. [21] with  $\Delta H_1 = 24$  kOe,  $\Delta H_2 = 5$  kOe.

(c) Fig.4.8 of Ref. [22]

(d) Ref. [3].

(e) Ref. [5].

The models used by us in preparing Table 4.3 are empirical in nature and the values of the parameters  $\Delta H_1$ ,  $\Delta H_2$ ,  $\alpha$ ,  $\beta$  might be approximate in nature. The values stated for various parameters in the literature [16-22] are by no means unique and the situation in this regard is not completely clear yet. Nevertheless these models provide an existing basis for identifying the configurations responsible for each H-value.

We shall now discuss the results for each sample separately.

#### 4.3.1.2. Sample AA1; Fe-24 at% Al processed by route 1.

The highest value of hyperfine magnetic field, H, observed for the AA1 sample is  $(310 \pm 4)$  kOe and we have assigned it to the configuration around an Fe atom to be  $(7\text{Fe} + 1\text{Al})$  nn + 6Fe nnn (i.e. in which one nn Fe atom is replaced by one Al atom). It is seen from Table 4.3 that the possibility of the 8 Fe nn +  $(4\text{Fe} + 2\text{Al})$  nnn configuration is also there but with lower probability. The second H value,  $(286 \pm 4)$  kOe is attributed to the configuration  $(6\text{Fe} + 2\text{Al})$  nn + 6 Fe nnn along with a possible existence of 8Fe nn +  $(2\text{Fe} + 4\text{Al})$  nnn again with lower probability. The assignments for the other 3 values,  $(269 \pm 4)$ ,  $(240 \pm 4)$  and  $(214 \pm 4)$  kOe are as shown in Table 4.2. It should be noted that if the possibility of Al atoms occupying the nnn sites is ignored, the assignments for the five H-values for AA1 fall in the pattern  $(8 - n_1)\text{Fe}$  nn +  $n_1\text{Al}$  nn + 6Fe nnn, with  $n_1 = 1, 2, 3, 4$  and 5 respectively. Considering the straightforward nature of route 1 in which the sample was ice-quenched from the disordered  $\alpha$ -phase at  $1000^\circ\text{C}$ , the above pattern might be possible.

**4.3.1.3. AA2 to AA4 samples:- Fe-24 at% Al processed by routes 2, 3 and 4.**

The H-values determined for these three samples agree, within experimental errors, with those obtained for the AA1 sample although the relative intensities are different. This indicates that going down the vertical line in the phase diagram, same configurations are precipitated although their relative population (or the volume fraction of different phases) is determined by the cooling rate and other details of the processing route.

**4.3.1.4. AA5 sample: Fe-25 at% Al processed by route 5.**

The H-values obtained for this sample are  $(295 \pm 4)$  kOe,  $(273 \pm 4)$ ,  $(257 \pm 4)$ ,  $(237 \pm 4)$  and  $(194 \pm 4)$  kOe. While the two values, viz.  $(257 \pm 4)$  and  $(237 \pm 4)$  kOe, agree with those obtained for samples AA1-AA4 within experimental error, the other three H-values are different. This suggests that sample AA5 having a different (25 at% Al compared to 24 at% Al of samples AA1-AA4) composition and more elaborate processing route has given rise to different configurations, as shown in Table 4.2. The ratio of intensities for the configurations giving rise to  $H = 257 \pm 4$  kOe and  $H = 237 \pm 4$  kOe is  $\sim 1$  for the AA5 sample while it is in the range  $\sim 1.2 - 1.5$  for samples AA1 - AA4 respectively. The linewidths for the 5 subspectra for each sample follows a similar pattern, with the  $(4\text{Fe} + 4\text{Al})$  nn + 6Fe nnn showing about 20% less value compared to other configurations.

Previous studies [21-22] of the hyperfine fields in the Fe-Al alloys have shown that the behaviour of average hyperfine field,  $\langle H \rangle$ , has provided useful information. While the individual

H-values (the five values determined in Table 4.2) are seen at a microscopic scale through Mössbauer effect, in other phenomena the average field  $\langle H \rangle$ , seen on a macroscopic scale could become more important. One method of determining  $\langle H \rangle$  is to use the relation

$$\langle H \rangle = \int HP(H) dH / \int P(H) dH \quad (3)$$

where  $P(H)$  is the function describing the hyperfine field distribution. Keeping this in mind we analyzed the Mössbauer spectra of each of samples AA1-AA5 by Window's method [25] described in Chapter 2. The  $P(H)$  distributions so obtained are presented in Fig.4.11 while the values of  $\langle H \rangle$  calculated with (3) are shown in Table 4.4. Also given in Table 4.4 are the values of single average isomer shift (or  $\langle IS \rangle$ ) relative to  $\alpha$ -Fe obtained for the five samples.

The  $P(H)$  distributions shown in Fig.4.11 do not show any sharp structures and each of them shows a broad inverted bell-type shape. The broad and asymmetric nature of these distributions suggest that they are composite in nature being built by the distributions contributed by each of the five H-values (Table 4.2). It is interesting to point out that the hyperfine field distributions obtained by Perez Alcazar and Galvao de Silva [21] for  $Fe_{1-q}Al_q$  ( $q = 0.15, 0.2$  and  $0.225$ ) and by Yeluskov et al. [22] for Fe-23.5 at% Al showed similar shapes. Further the value of  $\langle H \rangle$  obtained [21] for  $Fe_{1-q}Al_q$  decreased from  $\langle H \rangle = 323.95$  for  $q = 0.025$  to  $\langle H \rangle = 272.10$  for  $q = 0.225$ . In the present case the  $P(H)$  distributions for the samples AA1, AA2, AA3 and AA4 were asymmetrical with the ratio of the halfwidths at half maximum,  $\Delta H_1$  (on the left side):  $\Delta H_2$  (on the right side) being about 1.35. On

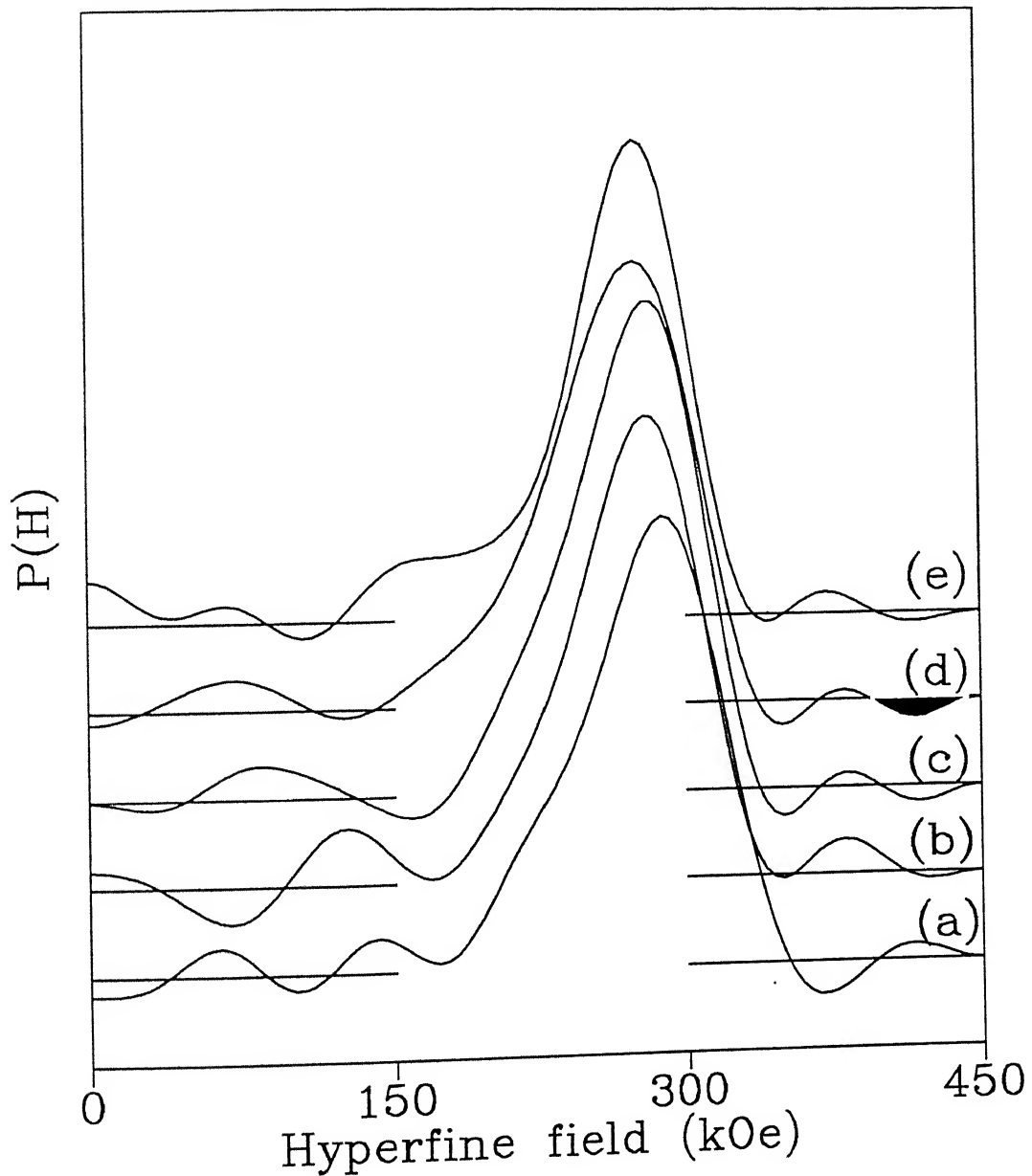


Fig. 4.11. Hyperfine field distributions in (a) AA1, (b) AA2, (c) AA3, (d) AA4 and (e) AA5 samples.

the other hand the dominant peak in the  $P(H)$  for the AA5 sample is fairly symmetrical although it shows a broad bulge in the lower ( $H=145-190$  kOe) field region. It may be pointed out that the least-squares-fit analysis (Table 4.2) did not yield any  $H$ -value lower than 194 kOe. The values of  $H_{peak}$  (the most probable value of  $H$ ) as well as those of  $\langle H \rangle$  appear to decrease in the sequence AA1 to AA5 although the average values of the isomer shift  $\langle IS \rangle$  remain almost constant. Although the variations of the cooling rates involved in the process routes 1 to 5 (Table 4.1) cannot be described by a single parameter, an examination of Table 4.1 indicates that the average rate of cooling is different for the five samples and that it decreases in the sequence AA1, AA2....AA5. This would suggest that the average hyperfine field  $\langle H \rangle$ , at the  $^{57}\text{Fe}$  nuclei in these five samples depend on the process route followed, with  $\langle H \rangle$  decreasing with decreasing cooling rate. Here it is relevant to point out that Perez Alcazar and Galvao de Silva [21] determined  $P(H)$  for  $\text{Fe}_{0.775}\text{Al}_{0.225}$  before and after a high temperature measurement and found a significant difference in the distributions as well as in  $\langle H \rangle$  and  $H_{peak}$ . These authors concluded from this observation that a partial phase decomposition occurs at high temperatures and the annealing process influences  $P(H)$ ,  $H_{peak}$  and  $\langle H \rangle$ . Our present results support this conclusion,. The decrease in  $\langle H \rangle$  indicates a decrease in the iron magnetic magnetic moment [26] which can be attributed to an increasing electron transfer to the iron unfilled 3d bands [27]. In their Mössbauer spectroscopic studies of the alloys  $\text{Fe}_{44}\text{Ni}_{36}\text{P}_{14}\text{B}_6$  Matteazi and Riontino [28] found that  $\langle H \rangle$  decreases

and  $\langle IS \rangle$  increases with decreasing cooling rate and that this behaviour could be understood in terms of changes in spin and charge density.

#### 4.4. Summary and conclusions

Mössbauer spectra of four samples of Fe + 24 at% Al and one sample of Fe + 25 at% Al are measured at room temperature. The processing route followed in the preparation of each sample differed in their rate of cooling or rapid quenching so that different phase compositions were possible. The hyperfine magnetic fields, H, associated with these phases were obtained by analyzing the Mössbauer spectra and these H-values were used to identify the atomic configurations around the Fe atom. In the case of alloys having 24 at% Al, the atomic configuration assigned for the four samples AA1, AA2, AA3 and AA4 were almost same although the relative populations (i.e. volume-fraction of phases) showed some differences. This behaviour suggested that the nature of the processing route influenced the relative population (or volume fraction) of the phases. In the case of the alloys containing 25 at% Al (sample AA5) the configurations and the relative populations showed differences from the other four samples.

The hyperfine magnetic field distributions,  $P(H)$ , were determined for each sample. Apart from minor differences the distributions for the four samples (AA1 - AA4) containing 24 at% Al appear similar while the  $P(H)$  for the AA5 sample containing 25 at% Al showed a different shape. The average hyperfine magnetic fields  $\langle H \rangle$  and average isomer shifts determined from these results

showed that these quantities depend on the average rate of cooling.

It is concluded the Mössbauer spectroscopic studies are thus useful to understand the microscopic as well as the gross properties of the hyperfine magnetic fields in Fe-Al alloys prepared by different processing routes.

References

- [1] R.Nathans, M.T.Pigott and C.G.Shull, J. Phys. Chem. Solids, 6, 38 (1958).
- [2] A.Arrott and H.Sato, Phys. Rev. 114, 1420 (1959).
- [3] K.Ono, Y.Ishikawa and A.Ito, J.Phys.Soc.Japan, 17, 1747 (1962).
- [4] M.B.Stearns, J.Appl.Phys. 35, 1095 (1964).
- [5] G.P.Huffman amd R.M.Fisher, J.Appl. Phys. 38, 735 (1967).
- [6] U.Gonser and M.Ron in "Applications of Mössbauer Spectroscopy", vol. II, edited by R.L.Cohen (Academic Press, New York, 1980), p. 281.
- [7] S.Nasu, U.Gonser, P.H.Shingu and Y.Murakami, J.Phys. F4, L24 (1974); S.Nasu, U.Gonser and R.S.Preston, Proc. Int. Conf. Appl. Mössbauer Effect, Portoroz, J.Phys. 41, C1-385 (1980) and references cited therein.
- [8] T.M.Srinivasan, H.Claus, R.Viswanathan, P.A.Beck and D.I.Bardos, in "Phase Stability in Metals and Alloys", edited by Rudman et al. (McGraw-Hill, New York, 1967), p.151.
- [9] A.I.Bradley and A.H.Jay, Proc. Roy. Soc. A 136, 210 (1932).
- [10] A.Taylor and R.M.Jones, J.Phys.Chem.Solids, 6, 16 (1958).
- [11] A.Lawley and R.W.Chan, J.Phys. Chem. Solids, 20, 204 (1961).
- [12] H.Warlimont, H.Mühe and H.Gengnagel, Z.Angew. Phys. 26, 847 (1969).
- [13] H.Okamoto and P.A.Beck, Metall. Trans. 2, 569 (1971).
- [14] S.M.Allen and J.W.Cahn, Acta Metallurgica, 23, 1017 (1975).
- [15] O.Kubashewski, "Iron-binary Phase Diagram", (Springer-Verlag, Berlin, 1982), p.5.
- [16] M.B.Stearns, Phys. Rev. 147, 439 (1966).

- [17] L.Cser, J.Ostanevich and L.Pal, Phys.Stat.Sol. 20, 581 (1967); L.Cser, J.Ostanevich and L.Pal, Phys.Stat.Sol. 20, 591 (1967).
- [18] M.R.Lesoille amd P.M.Gielen, Phys.Stat.Sol. 37, 127 (1970).
- [19] R.Hergt, E.Wieser, H.Gengnagel and A.Gladun, Phys. Stat. Sol. 41, 255 (1970).
- [20] I.Vincze and L.Cser, Phys. Status Sol. (b) 50, 709 (1972).
- [21] G.A.Perez Alcazar and E. Galvao da Silva, J.Phys. F: Met. Phys. 17, 2323 (1987).
- [22] E.P.Yelusov, E.V.Voronina and V.A.Barinov, J.Magn. and Magn. Mat. 115, 271 (1992).
- [23] J.C.Wang, D.G.Liu, M.X.Chen and X.X.Cai, Scripta Metallurgica, 25, 2581 (1991).
- [24] K.Vedula in "Intermetallics", (John Wiley & Sons, New York, 1994), vol.2 (Practice).
- [25] B.Window, J.Phys. E4, 401 (1971).
- [26] P.Panissod, J.Durand and J.I.Budnick, Nucl. Instr. and Methods, 199, 99 (1982).
- [27] K.Yamauchi and T.Mizoguchi, J.Phys.Soc.Japan., 39, 541 (1975).
- [28] P.Matteazzi and G.Rioutino, Hyperfine Interactions, 28 971 (1986).

## CHAPTER 5

### Mössbauer spectroscopic study of low alloy steels containing Chromium or Manganese

#### 5.1. Introduction

During the early years following the discovery of Mössbauer effect, most of the Mössbauer spectroscopic studies involved basic research in solid state physics and chemistry and determination of hyperfine interaction parameters in different metals and chemical compounds. Soon the wider potential of this technique was recognised. It was particularly realised that the  $^{57}\text{Fe}$  Mössbauer spectroscopy formed a very straightforward and convenient methodology and that it can have interesting applications in physical metallurgy because iron compounds and iron alloys form several fascinating metallurgical systems. Several excellent reviews describing the applications of Mössbauer spectroscopy to physical metallurgy exist in the literature [1-5]. One particularly interesting class of research problems in physical metallurgy where  $^{57}\text{Fe}$  Mössbauer spectroscopy has been applied extensively is the study of steels. The technique of  $^{57}\text{Fe}$  Mössbauer spectroscopy has been used in steel industry as routine monitoring tool as well as a powerful probe in important metallurgical research. The articles by Huffman and Huggins [6], and by Rao [7], for example, outline these developments. The areas

in steel industry where Mössbauer spectroscopic technique are used are steel-making processes, steel-surface processes, steel-corrosion studies and other metallurgical studies.

Steels are the most widely used commercial alloys and they are based on the interstitial solid solutions of carbon in iron. One can classify steels into three categories: (i) plain carbon steels, which do not contain any other metal added intentionally, (ii) low alloy steels to which upto 5% of foreign metals are added and (iii) high-alloy steels which contain more than 5% of alloying metals. It is usual to alloy iron with other transition metals such as V, Cr, Mn, Ni, Mo and W to produce these alloy steels.

The process of quenching and tempering of plain carbon steel has been investigated with  $^{57}\text{Fe}$  Mössbauer spectroscopy [3]. While high-alloy steels have been widely studied by Mössbauer spectroscopy, there are not many studies of low-alloy steels using Mössbauer spectroscopy. On the other hand the low alloy steels containing refractory carbides belonging to the transition metals of group IV - VI of the periodic table are considered important from the point of view of several industrial applications [8].

Interesting applications of  $^{57}\text{Fe}$  Mössbauer effect to physical metallurgy of low-alloy steels arise from two advantages: (i) the qualitative and quantitative identification of various alloy phases and (ii) investigation of the charge and spin density perturbation caused by the impurity at the host matrix atoms through the hyperfine fields,  $H$ . The latter type of information is possible because an impurity atom when incorporated in a magnetic (host) matrix will influence the charge distribution and spin

density in its environment. In other words the hyperfine interactions of  $^{57}\text{Fe}$  in the low-alloy steels are perturbed by the presence of impurity atoms and carbon atoms. Consequently, the Mössbauer spectra become more complicated, because the spectra now depend on the number and location of the other, non-iron, atoms. It is possible to analyze such complex Mössbauer spectra as a superposition of subspectra arising from various types of iron atoms and by classifying these various iron atoms as (i) iron atoms without nearest-neighbour (nn) or next-nearest-neighbour (nnn) atoms, (ii) iron atoms with one, two, ..... nn atoms etc.

Various authors have used the technique of Mössbauer spectroscopy to study such near-neighbour interactions in binary substitutional  $\alpha\text{-Fe-M}$  (where M  $\Rightarrow$  metal) alloys. Stearns [9] studied the binary substitutional systems of  $\alpha\text{-Fe}$  with various amounts of Al, Si, Mn, V and Cr and determined the hyperfine (or internal magnetic) fields (H) and isomer shifts (IS) of  $^{57}\text{Fe}$  nuclei. Careful analysis of these results allowed her to describe the Mössbauer spectra for these alloys in terms of H and IS at Fe nuclei having the solute atoms in the first, second,..... fifth coordination spheres. The disturbance produced in an iron lattice by Cr atoms was studied by Cranshaw [10] by measuring Mössbauer spectra of the binary Fe - 4.8% Cr alloy. Vincze and Campbell [11] studied Mössbauer spectra of dilute Fe-based alloys having various soluble transition metal impurities and analyzed their results to obtain changes in H and IS at first, second and further neighbour shells. Similar studies were also carried out by Longworth and Window [12] and Dubiel and Zukrowski [13]. Similarly the effects

of near neighbour interaction on the values of the Mössbauer parameters, H, IS etc.in Fe - 4.2 at% C alloys were studied by Moriya et al. [14]. All these studies have demonstrated how Mössbauer spectroscopic technique can distinguish between various simultaneously present iron-bearing phases, and how these various phases can be labelled with various environments. However to our present knowledge no such studies have been reported for low-alloy steels. Such studies should be promising particularly if the solute atom in the low-alloy steels possesses magnetic moment. Keeping this in mind we have studied the low-alloy steels containing 0.6% C and 0.0 - 2.0% (mass percentage) Cr or Mn. These studies described in the present chapter have been carried out using the techniques of Mössbauer spectroscopy and magnetic measurements.

## 5.2. Experimental procedure

The samples of steels containing 0.6% C and (i) 0.0, 0.5, 1.0 and 2.0% Cr and (ii) 0.0, 0.5, 1.0 and 2.0% Mn were prepared from high compressibility sponge iron powder, grade NC 100.24 (HOGANAS AB, Sweden), ferrochrome and ferromanganese powders supplied by Ferroalloys Corporation, India and natural (99.9% pure) graphite. Using these powders premixed pellets were prepared which were then sintered at 1300°C for 1h in dry hydrogen. Full details of the sample preparation and microstructural studies are described elsewhere [15].

The absorbers for Mössbauer spectroscopy were prepared from

powdered (particle-size less than 53 m $\mu$ ) samples and were used to record transmission spectra at room temperature (295 K) with a Mössbauer spectrometer described in Chapter 2.

The analysis of the Mössbauer spectra was carried out with computer programs using two methods. In the first method a least-squares-fitting computer program employing Lorentzian lineshapes for the peaks and an iterative procedure was used. It was assumed that the total Mössbauer spectrum was a superposition of a number of contributing subspectra each having different Mössbauer parameters (i.e. hyperfine field, isomer shift, relative intensity etc.). In the second method we followed the procedure of Window [16] to obtain the hyperfine field distributions P(H) from the measured Mössbauer spectra. Both these methods have been described in Chapter 2.

In addition we have carried out magnetic measurements on the above steel samples by using a vibrating sample magnetometer (155, PAR). The magnetometer was calibrated with the help of a standard Ni sample after the usual saddle-point adjustments. All measurements were carried out at room temperatures.

### 5.3. Results and discussion

#### **5.3.1. Mössbauer spectroscopic studies**

The Mössbauer spectra of various steels containing Cr or Mn measured at room temperature are shown in Figs.5.1 and 5.2 respectively. Each of these spectra was subjected to detailed  $\chi^2$ -tests to obtain a set of parameters that could give the best

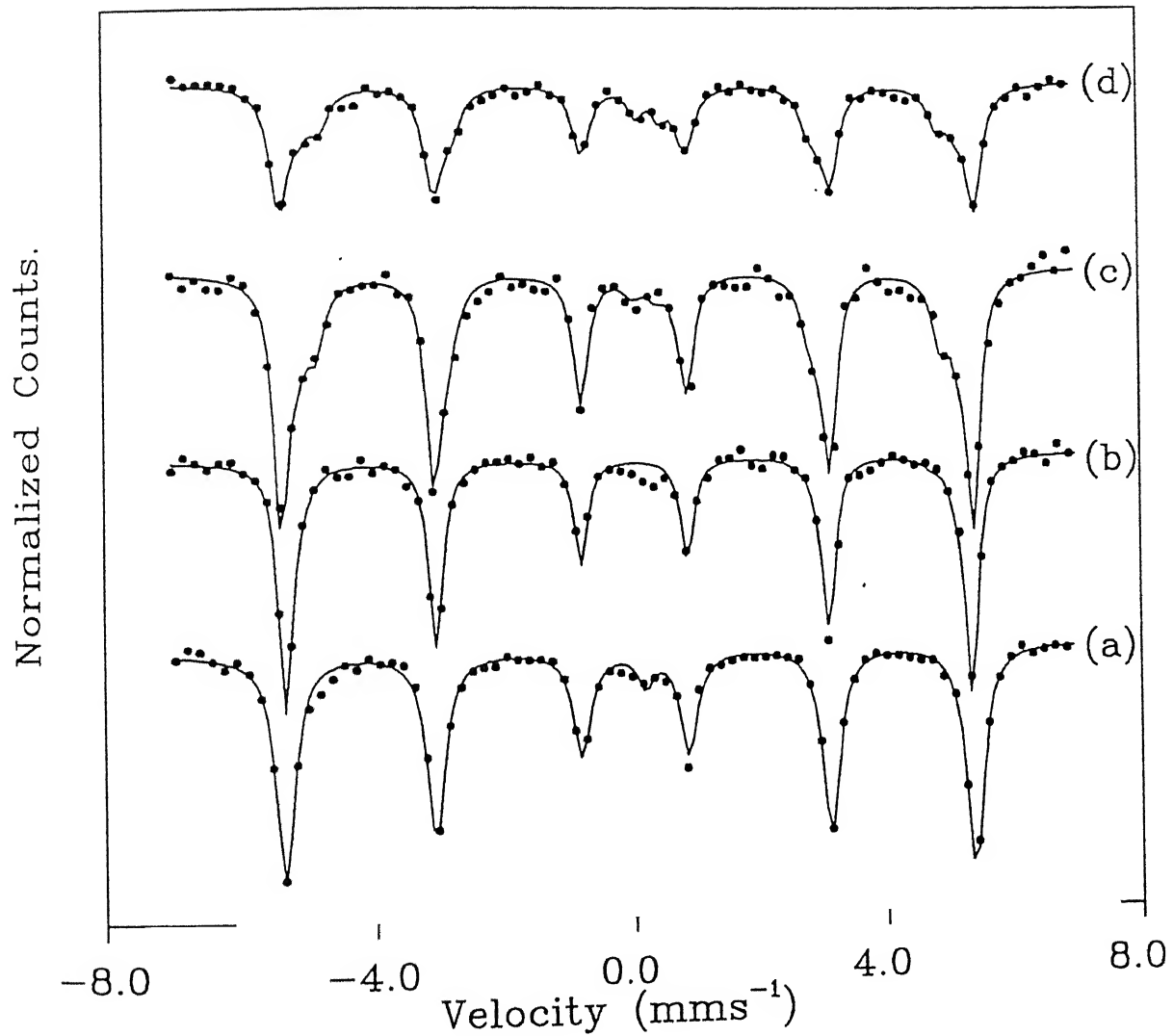


Fig. 5.1.  $^{57}\text{Fe}$  Mössbauer spectra of different Fe-C-Cr steels fitted by using least square fit method. (a) 0.0% Cr, (b) 0.5% Cr, (c) 1.0% Cr, (d) 2.0% Cr.

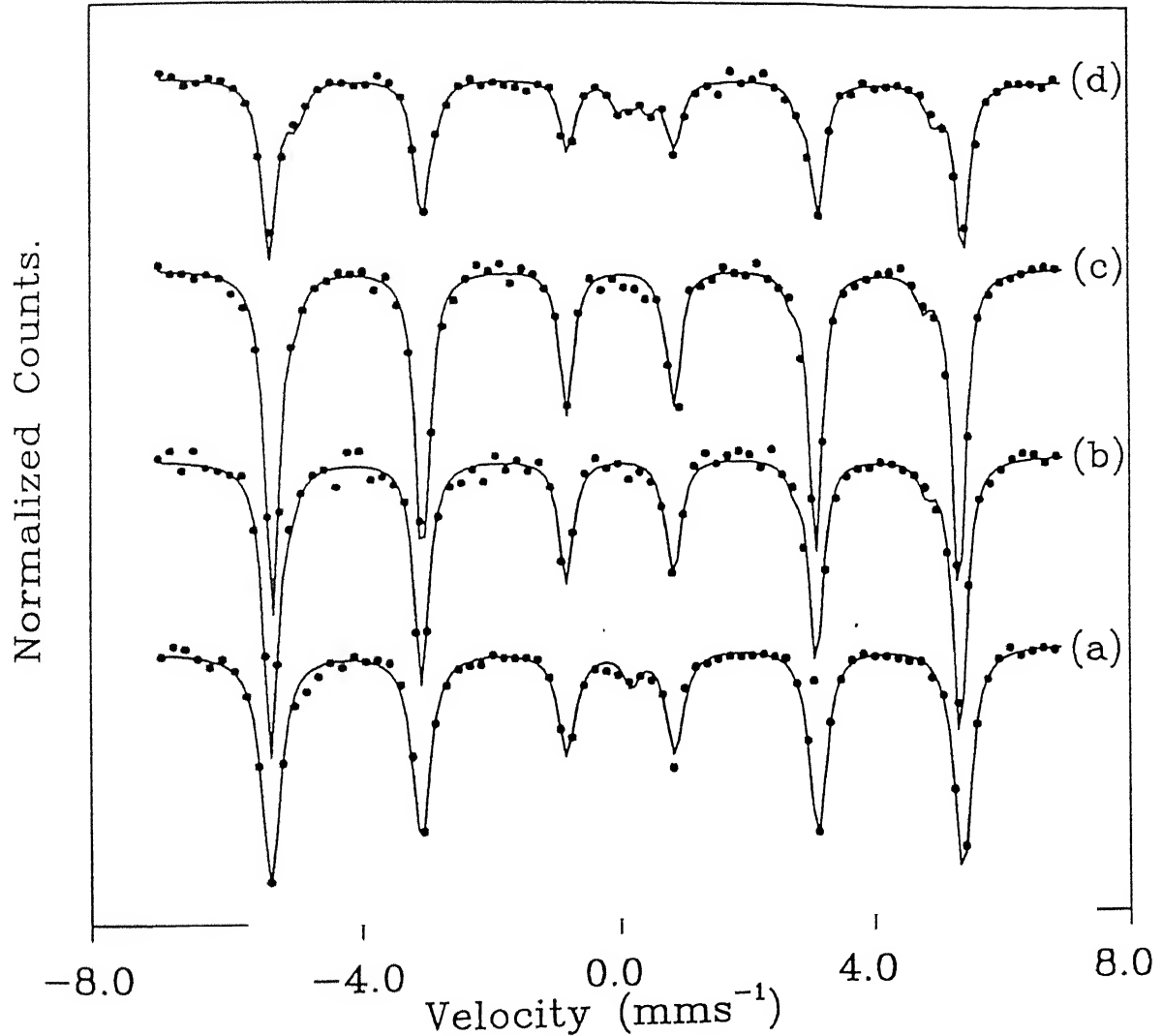


Fig.5.2.  $^{57}\text{Fe}$  Mössbauer spectra of different Fe-C-Mn steels fitted by using least square fit method. (a) 0.0% Mn, (b) 0.5% Mn, (c) 1.0% Mn, (d) 2.0% Mn.

fit for the data. The set of Mössbauer parameters obtained from such an analysis is given in Table 5.1. The present analysis showed that the reference sample (Fe - 0.6% C) could be decomposed into a singlet and one sextet. The singlet is weak (~ 2 %) in intensity and the measured values of IS = 0.16 mms<sup>-1</sup> and quadrupole splitting  $\Delta E$  = 0.0 mms<sup>-1</sup> could not be reconciled with any reported values [17 - 20] for the iron carbides Fe<sub>3</sub>C or Fe<sub>5</sub>C<sub>2</sub>, both of which are known to yield Mössbauer sextets, with H-values in the range H = 110 - 222 kOe. We are unable to identify this singlet. The strong (~ 98 %) sextet is characterized by the value of hyperfine field H = 332 kOe and is attributed to  $\alpha$ -Fe. It has been reported [3] that the hyperfine field of  $\alpha$ -Fe atoms in plain carbon steel differs slightly from the value H = 330 kOe in pure iron [21] and this behaviour is also observed by us.

The present results have shown that addition of Cr (0.5 to 2.0%) to the 0.6% C steel renders the Mössbauer spectrum more complicated (Fig.5.1). The analysis of data has shown the presence of three sextets and one doublet (Table 5.1). The doublet has weak intensity and although its IS and quadrupole splitting ( $\Delta E$ ) could be determined (Table 5.1), we were unable to assign it to any known phases. Among the three sextets, one showing H-values in the range 330 to 334 kOe is identified with  $\alpha$ -Fe while the other two showing H-values around 301 and 318 kOe respectively are assigned to iron atoms having one Cr atom in the first and second neighbouring shells respectively. It is well known [10] that in a binary iron-rich Fe-Cr alloy one observes six-line Mössbauer spectra arising from the Cr atom in the first, second

Table 5.1. Mössbauer parameters of Fe-C, Fe-C-Cr and Fe-C-Mn steels for different mass percentages ( $x$ ) of Cr and Mn.

| Alloying addition ( $x$ ) to Fe - 0.6% C steel | IS<br>( $\text{mm s}^{-1}$ ) | $\Delta E$<br>( $\text{mm s}^{-1}$ ) | H<br>(kOe) | Relative Intensity (%) | Assignment        |
|--|------------------------------|--------------------------------------|------------|------------------------|-------------------|
| 0% Cr(Mn)                                      | 0.16<br>0.01                 | 0.00<br>0.00                         | —<br>331   | 2<br>98                | ?<br>$\alpha$ -Fe |
| 0.5% Cr  | -0.12                        | -0.04                                | 300        | 3                      | 1nn               |
|  | -0.02                        | -0.02                                | 318        | 10                     | 2nn               |
|  | 0.00                         | 0.00                                 | 331        | 87                     | $\alpha$ -Fe      |
| 1.0% Cr  | 0.14                         | 0.37                                 | —          | 3                      | ?                 |
|  | 0.00                         | -0.04                                | 302        | 19                     | 1nn               |
|  | 0.12                         | -0.02                                | 319        | 14                     | 2nn               |
|  | 0.00                         | 0.00                                 | 333        | 64                     | $\alpha$ -Fe      |
| 2.0% Cr  | 0.20                         | 0.37                                 | —          | 5                      | ?                 |
|  | 0.01                         | -0.02                                | 300        | 20                     | 1nn               |
|  | 0.12                         | -0.02                                | 317        | 15                     | 2nn               |
|  | 0.00                         | 0.00                                 | 335        | 60                     | $\alpha$ -Fe      |
| 0.5% Mn  | -0.12                        | 0.00                                 | 305        | 9                      | 1nn               |
|  | 0.00                         | 0.00                                 | 330        | 91                     | $\alpha$ -Fe      |
| 1.0% Mn  | -0.12                        | 0.00                                 | 301        | 8                      | 1nn               |
|  | 0.00                         | 0.00                                 | 329        | 92                     | $\alpha$ -Fe      |
| 2.0% Mn  | 0.16                         | 0.00                                 | —          | 2                      | ?                 |
|  | 0.18                         | 0.50                                 | —          | 5                      | ?                 |
|  | 0.02                         | 0.00                                 | 305        | 17                     | 1nn               |
|  | 0.02                         | 0.00                                 | 332        | 76                     | $\alpha$ -Fe      |

.....nearest neighbour (nn) atoms along with a six-line spectrum arising from iron atoms which are remote from Cr atoms. If the hyperfine field for the latter type of spectrum is  $H$ , the hyperfine fields for spectra arising from first nearest neighbour (1nn), second nearest neighbour (2nn) .... configurations show changes  $\Delta H_1$ ,  $\Delta H_2$  .... from  $H$ . In our least-square-fitting computer program we have used the values of  $\Delta H_1$  and  $\Delta H_2$  reported by Stearns [9] for Fe-Cr system as our initial guess. The finally obtained values  $H \sim 301$  kOe for 1nn and  $H_2 \sim 318$  kOe for 2nn configuration are not much different from the values reported by Stearns [9] and other workers [10-13]. Our analysis also provided data on the changes in the relative populations of different phases as the compositions of Fe-C-Cr alloys is changed. It is observed that the percentages of the 1nn and 2nn phases increase as the percentage composition of Cr is increased from 0.5% to 2.0%, with the 1nn site occupation showing a steeper increase.

Our results for the Mn-containing steels (Fig.5.2, Table 5.1) appear different from those observed for the Cr-containing ones. We have observed only two sextets in the Fe-C-Mn steels with one of them being assigned to the  $\alpha$ -Fe while the other being attributed to the 1nn occupation whose intensity increases with the percentage composition of Mn. In the case of 2% Mn, we observed a weak ( $\sim 2.0\%$ ) singlet and a weak ( $\sim 5.0\%$ ) doublet (Fig.5.2, Table 5.1) which could not be identified with any known phases.

In order to examine how the changes  $\Delta H_1$  and  $\Delta H_2$  in these steels manifest themselves in the hyperfine field distributions,

$P(H)$ , we obtained these distributions by analyzing the Mössbauer spectra with Window's method [16]. The results for  $P(H)$  for the Fe-C-Cr and Fe-C-Mn steels are shown in Figs. 5.3 and 5.4 respectively. The most intense peaks observed at  $H \sim 330$  kOe in these distributions arise out of the  $\alpha$ -Fe phase while the satellite peak at  $H \sim 301$  kOe is ascribed to the 1nn site. In the case of Cr containing steels we have not been able to resolve the  $P(H)$  due to 2nn site from the main ( $\alpha$ -Fe) peak because the former has weaker intensity (Table 5.2) and has H-value ( $\sim 318$  kOe) lying close to  $H \sim 330$  kOe.

The results of magnetic measurements for steel samples containing Cr and Mn are shown in Figs. 5.5 and 5.6 respectively, where appropriate correction for the shape of the sample has been applied [22]. These results show different behaviour for the Cr - and Mn - containing steels. In the case of Cr - containing steels we observe that the saturation magnetic moment per gram decreases with the increase in the Cr amount. This behaviour is ascribed to the fact the magnetic moment per unit atom of Cr is  $0.4 \mu_B$  [12] while the magnetic moment per unit atom of Fe is  $2.216 \mu_B$  [13] and hence the bulk magnetic moment of Cr - steels show lower values compared to Fe + 0.6% C - steels (Fig. 5.5). On the other hand the bulk magnetic moment of Mn-steels show higher values compared to Fe + 0.6% C - steels (Fig. 5.6). It is well known that Mn shows complex structure [14] and it is difficult to quote a specific value for the magnetic moment per unit atom of Mn. The trend of our results (Fig. 5.6) indicates that the magnetic moment per unit atom of Mn may be higher than that for Fe in the steels studied by

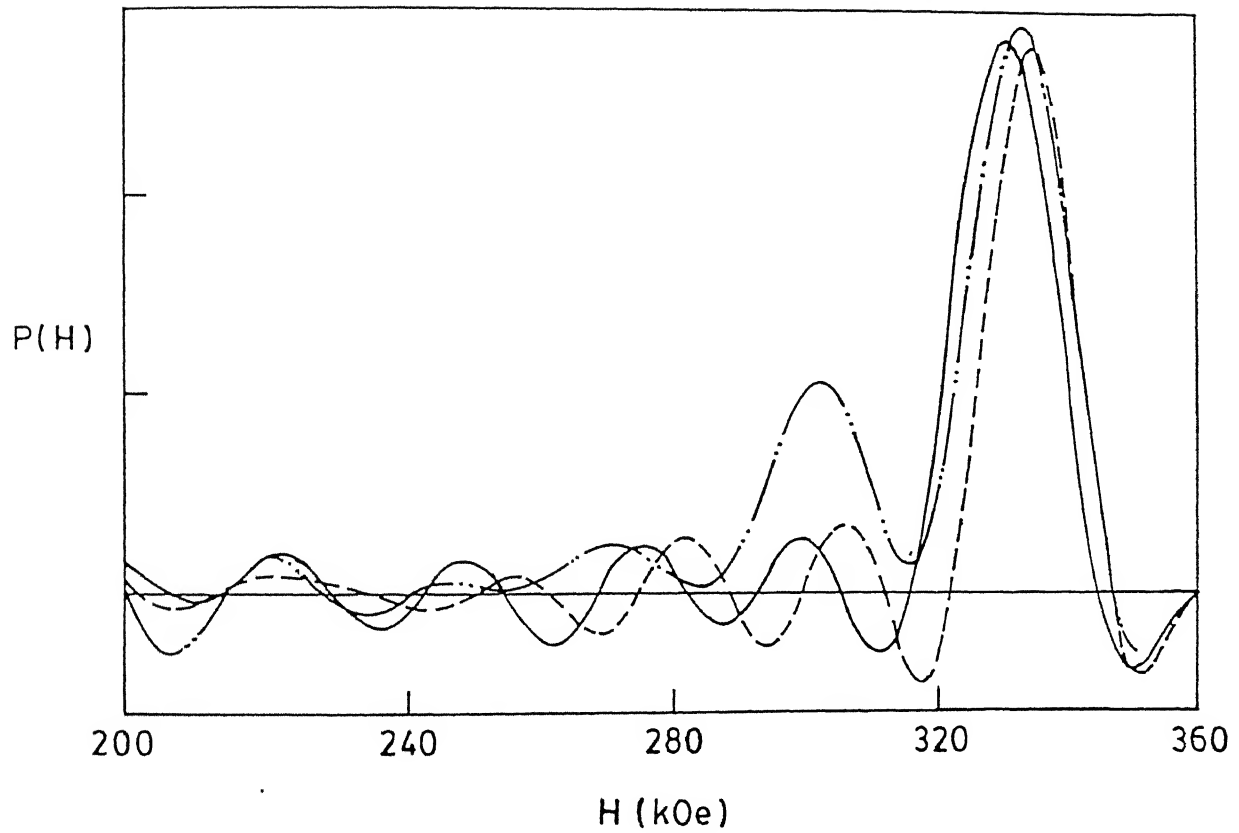


Fig. 5.3. Hyperfine field distribution in Fe-C-Cr steels.

— 0.5% Cr, - - - 1.0% Cr, - . - . - 2.0% Cr.

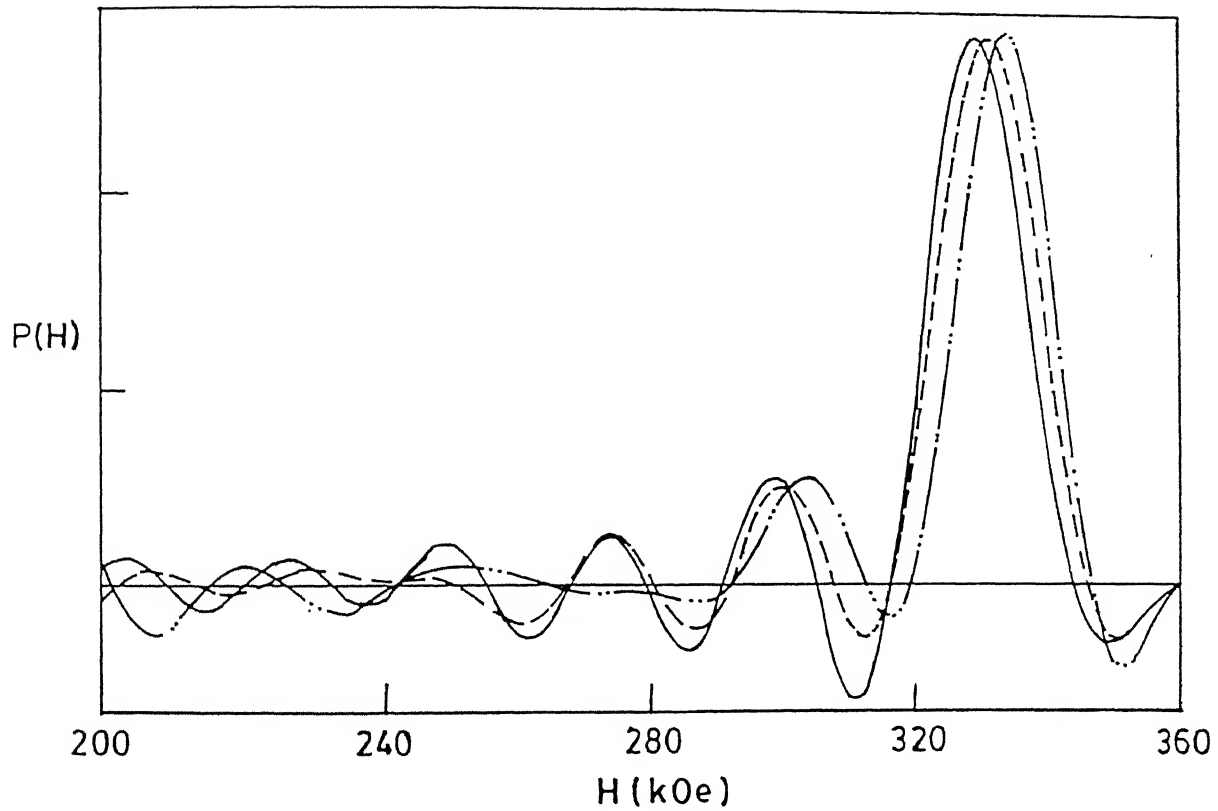


Fig. 5.4. Hyperfine field distribution in Fe-C-Mn steels.

— 0.5% Mn, - - - 1.0% Mn, - . - . - 2.0% Mn.

Table 5.2. Parameters obtained from the analysis of Mössbauer spectra of steel samples by Window's method.  $\Delta H_R$  and  $\Delta H_L$  are the right and left half-width of a peak in the hyperfine field distribution.

| Alloying addition<br>(x) to Fe - 0.6% C<br>steel | Peak 1     |                       |                       | Peak 2     |                       |                       |
|--|------------|-----------------------|-----------------------|------------|-----------------------|-----------------------|
|  | H<br>(kOe) | $\Delta H_R$<br>(kOe) | $\Delta H_L$<br>(kOe) | H<br>(kOe) | $\Delta H_R$<br>(kOe) | $\Delta H_L$<br>(kOe) |
| 0.5% Cr  | 330        | 9                     | 8                     | 300        | 5                     | 5                     |
| 1.0% Cr  | 334        | 7                     | 8                     | 305        | 5                     | 5                     |
| 2.0% Cr  | 334        | 10                    | 8                     | 301        | 7                     | 9                     |
| 0.5% Mn  | 328        | 8                     | 9                     | 298        | 6                     | 6                     |
| 1.0% Mn  | 332        | 8                     | 9                     | 300        | 5                     | 5                     |
| 2.0% Mn  | 334        | 8                     | 9                     | 304        | 6                     | 6                     |

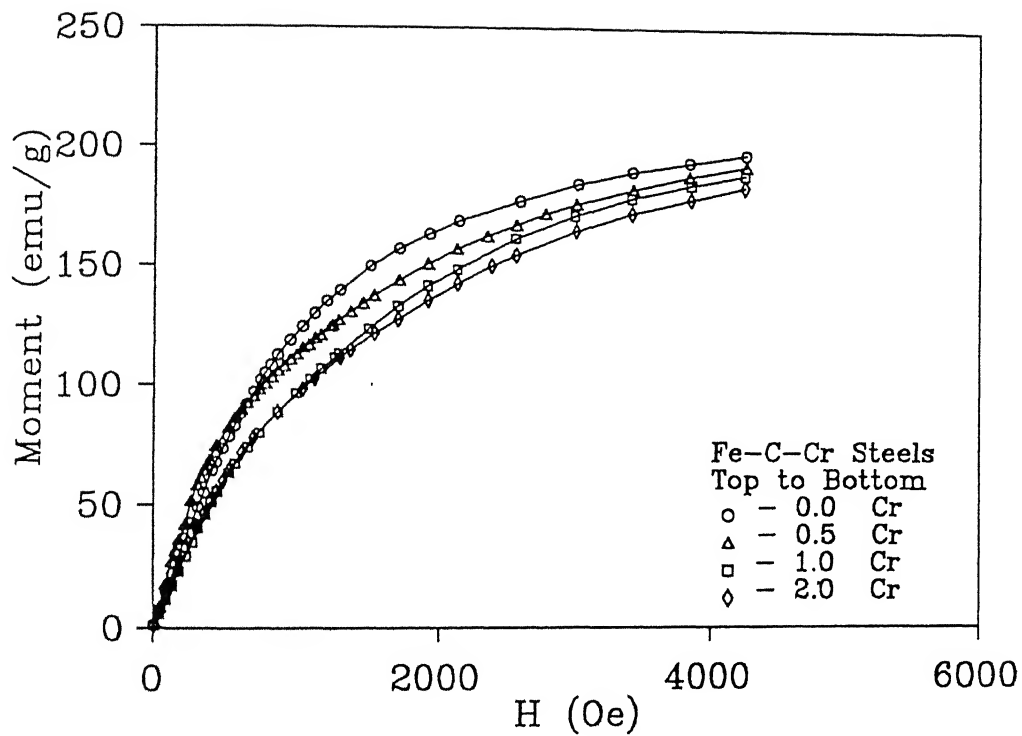


Fig.5.5. Variation of Magnetic moment of Fe atoms under the external magnetic field at room temperature of Fe-C-Cr steels for various compositions : o - 0.0% Cr,  $\Delta$  - 0.5% Cr,  $\square$  - 1.0% Cr,  $\diamond$  - 2.0% Cr.

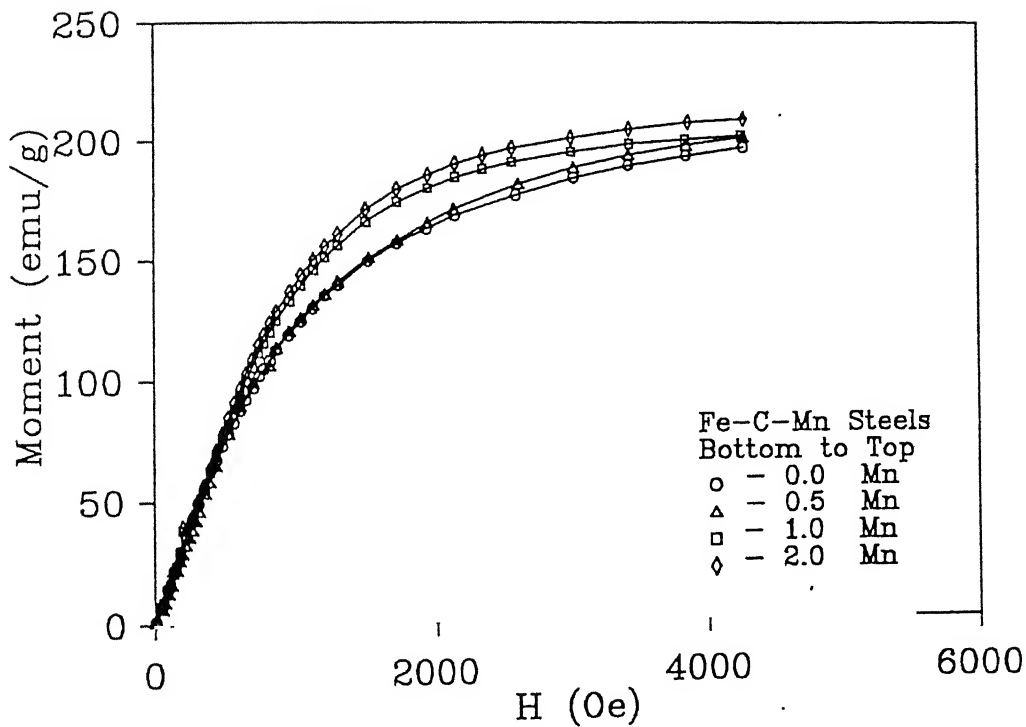


Fig.5.6. Variation of Magnetic moment of Fe atoms under the external magnetic field at room temperature of Fe-C-Mn steels for various compositions :  $\circ$  - 0.0% Mn,  $\Delta$  - 0.5% Mn,  $\square$  - 1.0% Mn,  $\diamond$  - 2.0% Mn.

us.

#### 5.4. Conclusions

Mössbauer spectra have been measured in the Fe - 0.6% C steels containing 0.0 - 2.0 mass percent of Cr or Mn to study the magnetic disturbance around the solute atoms in these steels. Analysis of the observed Mössbauer spectra have allowed us to identify three phases,  $\alpha$  - Fe, 1nn and 2nn, i.e. iron atoms having one Cr atom in the first and second neighbour shells respectively, in the Fe-C-Cr steels and  $\alpha$  - Fe and 1nn in the Fe-C-Mn steels. The plots for the hyperfine field distributions in these steels obtained by Window's method support this identification. The saturation magnetic moment per gram decreases with the increase in the Cr amount while it increases with the increase in the Mn amount.

References

- [1] U.Gonser in "An Introduction to Mössbauer Spectroscopy" edited by L.May, (Plenum Press, New York, 1971), p.155; see also U.Gonser, Mat.Sci.Eng. 3, 1 (1968).
- [2] M.Ron, in "Nuclear Techniques in Basic Metal Industries", published by IAEA, Vienna, 1973, p.493 and p.531.
- [3] F.E.Fujita, in "Topics in Applied Physics", edited by U.Gonser, vol. 5, "Mössbauer Spectroscopy", (Springer-Verlag, Berlin and New York, 1975), p.201.
- [4] L.H.Schwartz, in "Applications of Mössbauer Spectroscopy", edited by R.L.Cohen, (Academic Press, New York, 1976), vol.1, p.37.
- [5] U.Gonser, M.Ackermann, H.J.Bauer, N.Blaes, S.M.Fries, R.Gaa and H.G.Wagner in "Industrial Applications of the Mössbauer Effect", edited by G.J.Long and J.G.Stevens, (Plenum Press, New York, 1986), p.25.
- [6] G.P.Huffman and F.E.Huggins in "Mössbauer Spectroscopy and its Chemical Applications", edited by J.G.Stevens and G.K.Shenoy, Advances in Chemistry Series, 194, 265 (1981); G.P.Huffman and F.E.Huggins, AIP Conference Proceedings, 84, (1982); *ibid* 149, (1982).
- [7] K.R.P.M.Rao in "Industrial Applications of the Mössbauer Effect", edited by G.J.Long and J.G.Stevens, (Plenum Press, New York, 1986), p.153.
- [8] G.S.Upadhyaya, Reviews on High Temperature Metals. 3, 25 (1975).
- [9] M.B.Stearns, Phys.Rev. 147, 439 (1966).

- [10] T.E.Cranshaw, J.Phys.F: Metal Phys. 2, 615 (1972).
- [11] I.Vincze and I.A.Campbell, J.Phys. F: Metal Phys. 3, 647 (1973) .
- [12] G.Longworth and B.Window, J.Phys. F: Metal Phys. 3, 832 (1973) .
- [13] S.M.Dubiel and J.Zukrowski, J.Magn.Magn.Mat. 23, 214 (1981) .
- [14] T.Moriya, H.Ino, F.E.Fujita and Y.Maeda, J.Phys.Soc.Japan, 24, 60 (1968)
- [15] A.Sinha, M.Tech. Thesis, Indian Institute of Technology, Kanpur, India, 1993. (Unpublished) .
- [16] B.Window, J.Phys. E4, 401 (1971) .
- [17] T.Shinjo, F.Itoh, H.Takaki, Y.Nakamura, and N.Shikazono, J.Phys.Soc.Japan, 19, 1252 (1964) .
- [18] M.Ron, H.Shechter, A.A.Hirsch, and S.Niedzwiedz, Phys. Letters, 20, 481 (1966) .
- [19] H.Bernas, I.A.Campbell and R.Fruchart, J.Phys. and Chem. Solids, 28, 17 (1967) .
- [20] J.Danon in "Chemical Applications of Mossbauer Spectroscopy", edited by V.I.Goldanskii and R.H.Herber (Academic Press, New York, 1968), p. 159.
- [21] R.S.Preston, S.S.Hanna and J.Heberle, Phys. Rev. 128, 5 (1968) .
- [22] S.M.Bhagat, S.Haraldson and O.Beckman, J. Phys. Chem. Solids, 38, 593 (1977) .

## CHAPTER 6

### Study of hyperfine field distributions in $\text{Fe}_{79}\text{B}_{16}\text{Si}_5$ and $\text{Fe}_{78}\text{B}_{13}\text{Si}_9$ metallic glasses

#### 6.1. Introduction

In recent years there has been a widespread theoretical, experimental and technological interest among scientists and technologists in the study of metallic glasses produced by rapid quenching of molten metallic alloys [1-7]. Amorphous or glassy solids usually imply the absence of crystalline order or properties. In some disordered alloys, during their preparation by rapid quenching of the alloying constituents from glass or liquid phase, the atoms do not arrange themselves in regular three dimensions, i.e. different atoms irregularly occupy the sites of a regular crystal lattice. The solidification is so rapid (more than  $10^6 \text{ Ks}^{-1}$ ) that atoms are frozen in their liquid configuration. Hence the atomic arrangement of metallic glasses is similar to that of a liquid having the same composition or is like the silicate glasses as far as the long-range periodicity is concerned. Due to the highly disordered or glassy structure of metallic glasses, their physical and chemical properties depend on their structure [1-7]. Many of the unique characteristics of metallic glasses arise out of their amorphous nature. Magnetic properties of iron-based metallic glasses (or amorphous alloys) are such important properties which depend on the structure of the

alloy and which in turn depend on other properties like composition, heat-treatment etc. [8]. One of the most important features of these amorphous alloys is that they can be prepared with different types of compositions using a number of different constituent elements, providing a method to alter or modify their magnetic, mechanical, electrical and corrosion behaviour. The number of the constituents of these types of alloys ranges from two (e.g.  $Fe_xB_{100-x}$ ) to as many as five (e.g.  $Fe_{39}Ni_{39}Mo_4Si_6B_{12}$ ) [8]. Some of these alloy systems behave as very soft magnetic materials, show exceptional hardness, high tensile strengths and almost zero thermal expansion. Such types of different properties, in particular the existence of ferromagnetic property in these alloys (which was thought to be impossible in non-crystalline materials), have rendered them useful in a wide range of technological applications (e.g. transformers, motors, transducers, potential catalysts etc). Basic research in this field is, therefore, very important for improving our understanding of these amorphous materials.

The amorphous state of metallic glass is metastable in nature. Upon annealing these amorphous alloys change from amorphous to crystalline state depending on their composition, annealing temperature and time period of annealing. The magnetic properties in the new crystalline state are different from that of amorphous state. It is, therefore, interesting to enquire how their ferromagnetic properties change from the amorphous state to the crystalline phase depending upon the annealing temperature and time period and how different new phases are being formed. This

kinetic process of crystallization is determined by the temperature and time period of the heat treatment given. Upon annealing, the metallic glasses tend to relax and become denser by atomic rearrangement. The atomic structure of amorphous alloys may be "locally distorted non-stoichiometric quasi-crystalline" [8]. This gives rise to a large number of structurally inequivalent sites [9] in a metallic glass and cause their characteristic magnetic parameters like exchange interactions, magnetic moments, hyperfine fields etc. to have a distribution of values instead of unique values. Further these distributions change if the sample is annealed, the nature of these changes being determined by the composition of the metallic glass, the temperature and time period of annealing. As the temperature of annealing approaches the crystallization temperature the partial crystallization results in the precipitation of other compounds and this evolution process also affects the changes in the above distributions.

Historically, Au-25 at% Si alloy was the first amorphous metallic alloy that was developed and this was followed by the development of Pd-20 at% Si [10-11]. The field of metallic glasses received a big boost after the development of iron - and nickel - bearing metallic glasses which were found to be ferromagnetic. Different kinds of metallic glasses have been developed in the amorphous state during the last three decades. These metallic glasses can be classified into four distinct categories [12]: (a) Transition metal - metalloid (TM-M) glasses which have two subdivisions: the late transition (TL-M) and the early transition metal-metalloid glasses (TE-M). The late transition

metal-metalloid metallic glasses are based mainly upon late transition metals, such as Fe, Co, Ni, Pd or Au, alloyed with a metalloid (a non-metal resembling a metal in some respects) element, such as B, C, P or Si with the system  $Fe_xB_{100-x}$  providing a classic example. In the case of TL-M type glasses the glass formation range of the metalloid elements is about 13 - 26 at%, while in the case of TE-M alloys it is in the range of 15 - 30% (e.g. Ti -  $Si_{15-20}$  or  $Nb_{80}Si_{20}$ ). (b) The second type of metallic glasses combine an early transition metal with a late transition metal (TE-TL), an example being that of  $Nb_{40}Ni_{60}$ . (c) The metallic glasses in the third group consists of simple metals (e.g.  $Ca_{65}Al_{35}$ ). (d) The last type of metallic glasses are formed by combining rare-earth metal (RE) with a transition metal (TM) to form a RE-TM type of glass as for example the Gd-Co system.

The above types of metallic glasses can be prepared by employing different methods, the rapid solidification process (RSP) being the most popular. The RSP technique may be classified into two categories, the spray method and the chill method. The spray method involves atomization of melt before quenching while the chill methods preserve continuity of the melt upto and during quenching. There are several non - RSP or surface methods, which include surface modifications of the substrate to a limited depth. Working details of these methods are described in the literature [1-7].

The iron - based metallic glasses have been studied widely because of the possibility to apply the technique of  $^{57}Fe$  Mössbauer spectroscopy for such studies [8]. It is well known that

Mössbauer spectroscopy has emerged as a sensitive technique to study various properties, especially the magnetic properties, of iron-rich metallic glasses. The glass system  $Fe_xB_{100-x}$  ( $72 \leq x \leq 86$ ) has been the most well-studied system with Mössbauer spectroscopy. Although the binary systems like  $Fe_xB_{100-x}$  are easier for interpreting experimental results theoretically, they do not satisfy the technical requirements of practical applications. Persistent efforts have been made by numerous workers to improve the thermal stability and magnetic properties of the Fe-B system by substituting either another transition metal (e.g. Ni, Co etc.) or another metalloid element (e.g. P, Si etc.) or both. As a result of these extensive studies it was found that the inclusion of Si in the Fe-B system causes improvement in the thermal stability as well as the magnetic properties [13-15]. Following this discovery several workers have investigated the kinetics of crystallization, and electric and magnetic properties of the ternary Fe-B-Si metallic glasses [16-23]. On the technological side the Allied Chemical Company in the U.S.A. reported that the metallic glass  $Fe_{78}B_{13}Si_9$  (METGLASS 260552) has extremely low core loss at distribution and power transformer frequencies and induction.

Keeping this interest in the Fe-B-Si system in mind, the crystallization process of the amorphous  $Fe_{80}B_{20-x}Si_x$  ( $x = 0, 2$  and  $8$ ) [23],  $Fe_{79}B_{16}Si_5$  [24] and  $Fe_{78}B_{13}Si_9$  [24] has been recently studied in our laboratory using X-ray diffraction and Mössbauer spectroscopy. In the latter work [24], we had investigated the phase precipitation in the samples of the metallic glasses

$\text{Fe}_{79}\text{B}_{16}\text{Si}_5$  and  $\text{Fe}_{78}\text{B}_{13}\text{Si}_9$  annealed at different temperatures ( $T_a = 573 - 748 \text{ K}$ ) for various time periods ( $t_a = 1-16 \text{ h}$ ). These studies were helpful to identify the temperature ranges ( $T_a$ ) and annealing durations ( $t_a$ ) in which the amorphous structure of these metallic glasses is retained. This knowledge was useful for studying the diffusion of germanium, palladium, silver and gold atoms in amorphous samples of these metallic glasses using the technique of Rutherford backscattering spectroscopy [24].

Using the Mössbauer parameters and X-ray diffraction data Banerjee et al. [24] were able to identify  $\alpha\text{-Fe}$ ,  $\text{Fe}_3\text{B}$ ,  $\text{Fe}_2\text{B}$  and  $\alpha\text{-}(\text{Fe},\text{Si})$  to be the iron-bearing phases precipitated in the samples of  $\text{Fe}_{79}\text{B}_{16}\text{Si}_5$  and  $\text{Fe}_{78}\text{B}_{13}\text{Si}_9$  annealed above 723 K. In these studies the hyperfine fields,  $H$ , were determined by analyzing the observed Mössbauer spectra with the help of a least-squares-fitting computer program employing Lorentzian shapes for the peaks. It is well known that the Fe-B-Si amorphous alloys contain a large number of structurally and magnetically inequivalent sites. The relative population of these inequivalent sites can be effectively characterized by determining the distribution,  $P(H)$ , of their hyperfine fields. Different methods have been proposed in the literature [25-27] to determine  $P(H)$  from the analysis of observed Mössbauer spectra. It is, therefore, interesting to examine the nature of  $P(H)$  distributions obtained for samples of Fe-B-Si system annealed at different temperatures ( $T_a$ ) for different times and to study the evolution of  $P(H)$  with  $T_a$  and  $t_a$ . Keeping this aim in mind we report here the distributions of hyperfine fields,  $P(H)$ , determined for the

samples of  $\text{Fe}_{79}\text{B}_{16}\text{Si}_5$  and  $\text{Fe}_{78}\text{B}_{13}\text{Si}_9$  annealed in the range  $T_a = 573 - 748$  K for various time periods  $t_a = 1 - 37$  h. Although similar studies on  $\text{Fe}_{79}\text{B}_{16}\text{Si}_5$  [20] and  $\text{Fe}_{78}\text{B}_{13}\text{Si}_9$  [21] have been reported earlier, the present investigations differ from the earlier work in the following two ways:

(i) The previous analysis was based on the Mössbauer spectra recorded at higher temperatures, of  $\text{Fe}_{79}\text{B}_{16}\text{Si}_5$  at  $T = 300, 450$  and  $650$  K [20] and  $\text{Fe}_{78}\text{B}_{13}\text{Si}_9$  at  $T = 296, 380, 600$  and  $650$  K [21]. On the other hand all our Mössbauer measurements were made at room temperatures with samples previously annealed at  $T_a = 573, 623, 673, 723$  and  $748$  K.

(ii) Our study also aimed at examining the effect of the time period of annealing ( $t_a$ ) on the evolution of the distribution of hyperfine fields. Keeping this aim in mind the samples were annealed for different time periods ranging from  $1 - 37$  h. Such time dependence was not studied for these two metallic glasses earlier.

## 6.2. Experimental procedure and data analysis

The samples of the metallic glasses studied, namely,  $\text{Fe}_{79}\text{B}_{16}\text{Si}_5$  (Si5) and  $\text{Fe}_{78}\text{B}_{13}\text{Si}_9$  (Si9) were in the form of ribbons (thickness 0.025 mm) obtained from Goodfellow Metals Ltd, Cambridge, U.K. Absorbers for the Mössbauer spectroscopy were prepared by cutting ribbons of size 8mm x 10mm and placing them on a copper holder. Isothermal ( $T = T_a$ ) annealing of the samples was carried out in a clean and high vacuum ( $< 1 \times 10^{-5}$  mbar) for different time periods ( $t_a$ ) according to the schedule described in

Table 6.1. A separate sample was used at each temperature. The highest temperature used ( $T_a = 748$  K) in the present annealing schedule was below the crystallization temperature ( $T_x$ ) of each glass because the technical information provided by the supplier specified  $T_x = 778$  K for Si5 and  $T_x = 823$  K for Si9 samples.

Mössbauer transmission spectra of the samples were recorded at room temperature ( $T = 295$  K) before annealing (i.e. as-received or as-quenched sample) and after each heat-treatment described in Table 6.1. The instrumental details of the Mössbauer spectrometer have already been described in Chapter 2. All other details of the experimental procedure were same as those described elsewhere [24].

As discussed in Chapter 2, a number of methods have been proposed in the literature [25 - 27] for determining the hyperfine field distributions,  $P(H)$ , from a measured Mössbauer spectrum. Among these the method proposed by Window [25] has been most widely used for metallic glasses [8, 20, 21, 28, 29] and it was adopted in the present work. The details of this method have been described in Chapter 2 and in our analysis we found that a choice of  $N = 15$  (see equation 2.4, Chapter 2) for the amorphous phase and  $N = 20$  for semi-crystalline phase (with  $H_0 = 400$  kOe for both cases) met the optimum conditions for the convergence of the Fourier series expansion. A natural consequence of such a truncated Fourier analysis is the presence of oscillatory features in the  $P(H)$ , especially at the low -  $H$  values. To simplify the analysis we assumed single average isomer shift and negligible

Table 6.1. Details of the heat-treatment schedule

| Sample  | T <sub>a</sub> | t <sub>a</sub>           |
|---|----------------|--------------------------|
| Si5<br>(or Fe <sub>79</sub> B <sub>16</sub> Si <sub>5</sub> ) | 573 K          | 1, 4, 8 and 16 h         |
|   | 623 K          | 1, 2, 4, 8 and 16 h      |
|   | 673 K          | 1, 4, 8 and 16 h         |
|   | 723 K          | 1, 4, 8, 16, 29 and 37 h |
|   | 748 K          | 1, 2, 4, 6 and 8 h       |
| Si9<br>(or Fe <sub>78</sub> B <sub>13</sub> Si <sub>9</sub> ) | 573 K          | 1, 4, 8 and 16 h         |
|   | 623 K          | 1, 2, 4 and 8 h          |
|   | 673 K          | 1, 4, 8 and 16 h         |
|   | 723 K          | 1, 4, 8, 16, 29 and 37 h |
|   | 748 K          | 1, 2, 4, 6 and 8 h       |

electric quadrupole interaction [28,29].

### 6.3. Results and discussion

#### 6.3.1. Study of as-received samples of Si<sub>5</sub> and Si<sub>9</sub>

The results of Mössbauer spectra for the Si<sub>5</sub> and Si<sub>9</sub> samples in the as-received form, and recorded at room temperature are shown in Fig.6.1. These two Mössbauer spectra consisted of six overlapping broadened lines ( $\text{FWHM } \Gamma = 0.9 - 1.1 \text{ mm s}^{-1}$ ) and are characteristic of a typical iron-rich metallic glass [8], the broadening being characteristic of amorphous magnetic solids. The hyperfine field distributions, P(H), obtained for these samples are shown in Fig.6.2 and they show slight asymmetry but otherwise a smooth, well-defined and structureless shape. As pointed out earlier (Sec.6.2) the oscillations observed at the two ends ( $H \sim 25 \text{ kOe}$ ,  $H \sim 375 \text{ kOe}$ ) on either side of the main peak are ascribed to the effects of truncated Fourier analysis and counting statistics [8,9,20,21]. The distributions in Fig.6.2 exhibit one dominant peak and another small peak on its left at about  $H \sim 95 \text{ kOe}$ . All these features agree with those observed by Bhatnagar and Ravi [20,21] who attributed the smaller peak to a particular near-neighbour interaction. Such low-field peaks have also been observed in other ternary metallic systems Fe-Cr-B [30,31] and Fe-W-B [32].

In the case of  $\text{Fe}_{80}\text{Cr}_{15}\text{B}_{15}$  Ganesan et al. [31] attributed the presence of the low-field peak to the weakly coupled Fe atoms dispersed over the alloy with a large number of Cr nearest

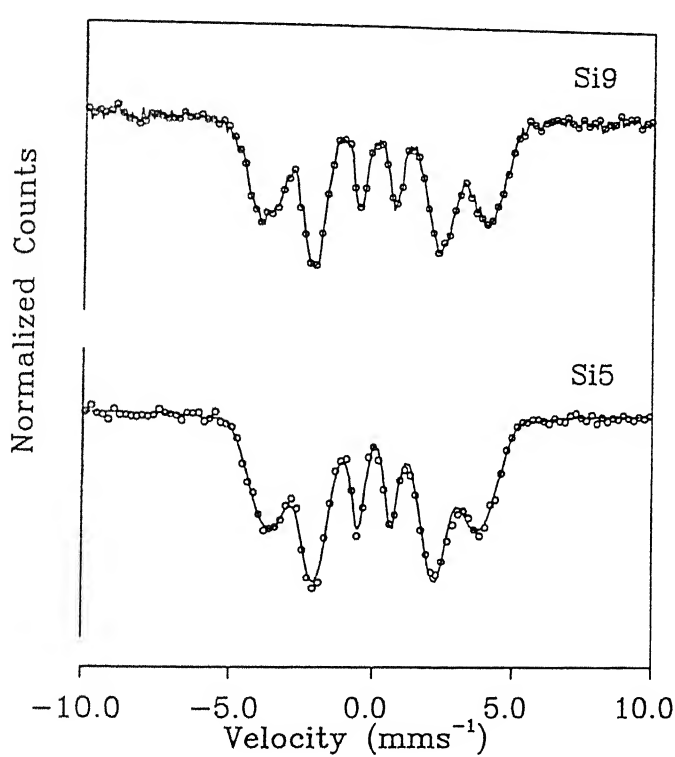


**Fig. 6.1.** Mössbauer spectra of as-received Si5 & Si9 samples.

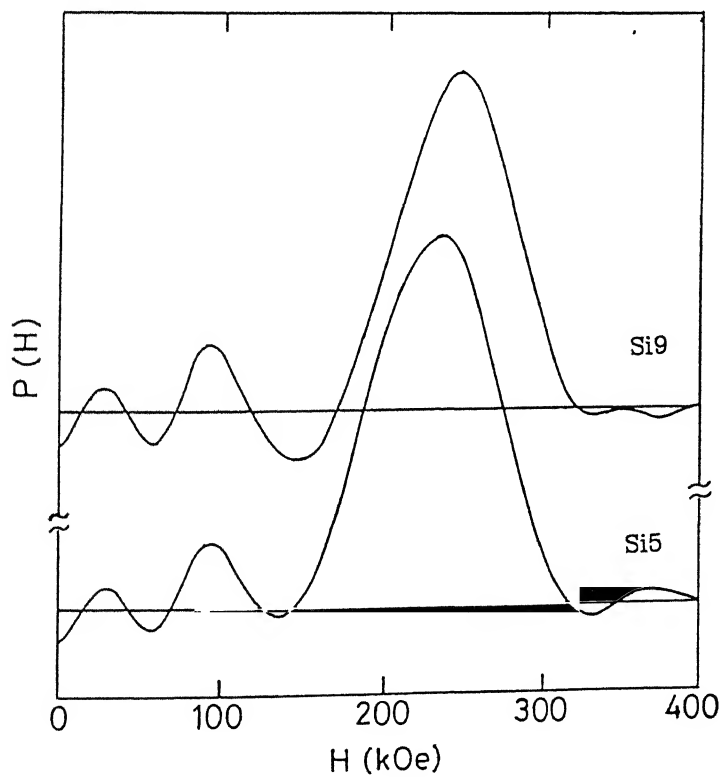


**Fig. 6.2.** P(H) distribution for as-received Si5 & Si9 samples.

neighbours in the form of clusters. A similar explanation involving Si nearest neighbours may be offered in the present case.

In order to discuss the results more effectively, we have characterized the  $P(H)$  distributions in terms of (i) the peak value or the most probable value,  $H_p$ , (ii) the average field  $\langle H \rangle$  defined by  $\langle H \rangle = \int HP(H)dH / \int P(H)dH$ , (iii) two widths  $\Delta H_1$  and  $\Delta H_2$  which are the half-widths at half maxima measured to the left and right of the peak value  $H_p$  respectively. These two widths indicate the amount of asymmetry observed in each peak and (iv) the effective field  $H_{\text{eff}}$  obtained by analyzing the Mössbauer spectra using a least-squares fitting program employing Lorentzian shapes for the peaks.

The analysis of the present results showed that  $\langle H \rangle = 227.6$  kOe and  $H_p = 239.0$  kOe for the dominant peak of Si5 sample (Fig.6.1) while the values for Si9 sample were  $\langle H \rangle = 245.5$  kOe and  $H_p = 251.0$  kOe. These values compare well with the values of  $H_{\text{eff}} = 235$  kOe for Si5 and  $H_{\text{eff}} = 247$  kOe for Si9 reported earlier [24]. The value of  $\Delta H_1$  was found to be slightly larger than  $\Delta H_2$  for both the samples.

### **6.3.2. Study of heat-treated samples**

#### **6.3.2.1. $\text{Fe}_{79}\text{B}_{16}\text{Si}_5$ (or Si5)**

The samples of Si5 were annealed at different temperatures ( $T_a$ ) for various time periods ( $t_a$ ) according to the schedule described in Table 6.1, and their Mössbauer spectra were analyzed

to obtain the  $P(H)$  distributions. The results for the Si5 samples isothermally annealed at  $T_a = 573, 623, 673, 723$  and  $748\text{ K}$  for different time periods are shown in Figs.6.3 - 6.7 respectively. It is observed that the  $P(H)$  distributions for  $T_a = 573, 623$  and  $673\text{ K}$  are similar to that for the as-received sample (Fig.6.1), even when  $t_a$  was raised from 1 to 16 h. Close examination of the finer changes observed in the  $P(H)$  distribution as  $t_a$  was increased from 1 h to 16 h (for  $T_a = 573, 623$  and  $673\text{ K}$ ) showed the following behaviour for the dominant peak:

- (i) The  $H_p$  - values shifted to slightly higher values and
- (ii) A slight bulge developed on the left wing of the dominant peak thus increasing the asymmetry (or the  $\Delta H_1/\Delta H_2$  values).

It may be pointed out that Ganesan et al. [32] had observed similar behaviour for the isothermally annealed samples of  $\text{Fe}_{75}\text{W}_5\text{B}_{20}$  metallic glass at  $T_a = 478\text{ K}$ . It is further observed that the low-field peak persisted for  $T_a = 573, 623$  and  $673\text{ K}$  although its peak position showed a slight shift depending on the value of  $t_a$ . Similar observation was reported for  $\text{Fe}_{75}\text{W}_5\text{B}_{20}$  [32]. This overall behaviour indicated that the samples of Si5 annealed at  $T_a = 573, 623$  and  $673\text{ K}$  retained their amorphous nature and this is in agreement with the conclusions drawn from the previous X-ray diffraction and Mössbauer spectroscopic studies [24].

As the annealing temperature is raised to  $723\text{ K}$ , the  $P(H)$  distributions (Fig.6.6) retain their similarity with those shown for the as-received sample (Fig.6.2) only for  $t_a = 1\text{ h}$  and  $4\text{ h}$ . An increase in  $t_a$  beyond  $4\text{ h}$  (at  $T_a = 723\text{ K}$ ) changes the structure of the  $P(H)$  distributions as shown in Fig.6.6. At  $t_a = 8\text{ h}$ ,  $P(H)$

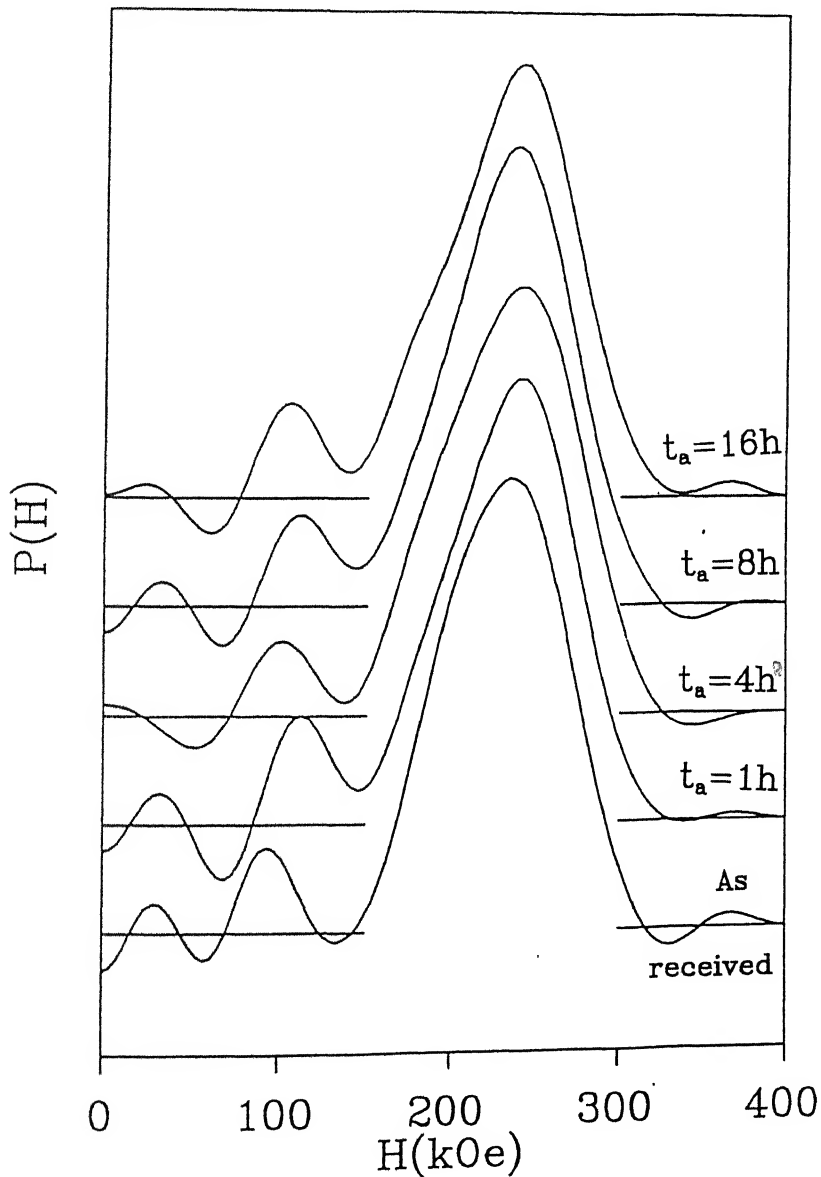


Fig. 6.3.  $P(H)$  distribution for Si5 sample annealed at 573 K (300 °C) for different  $t_a$ .

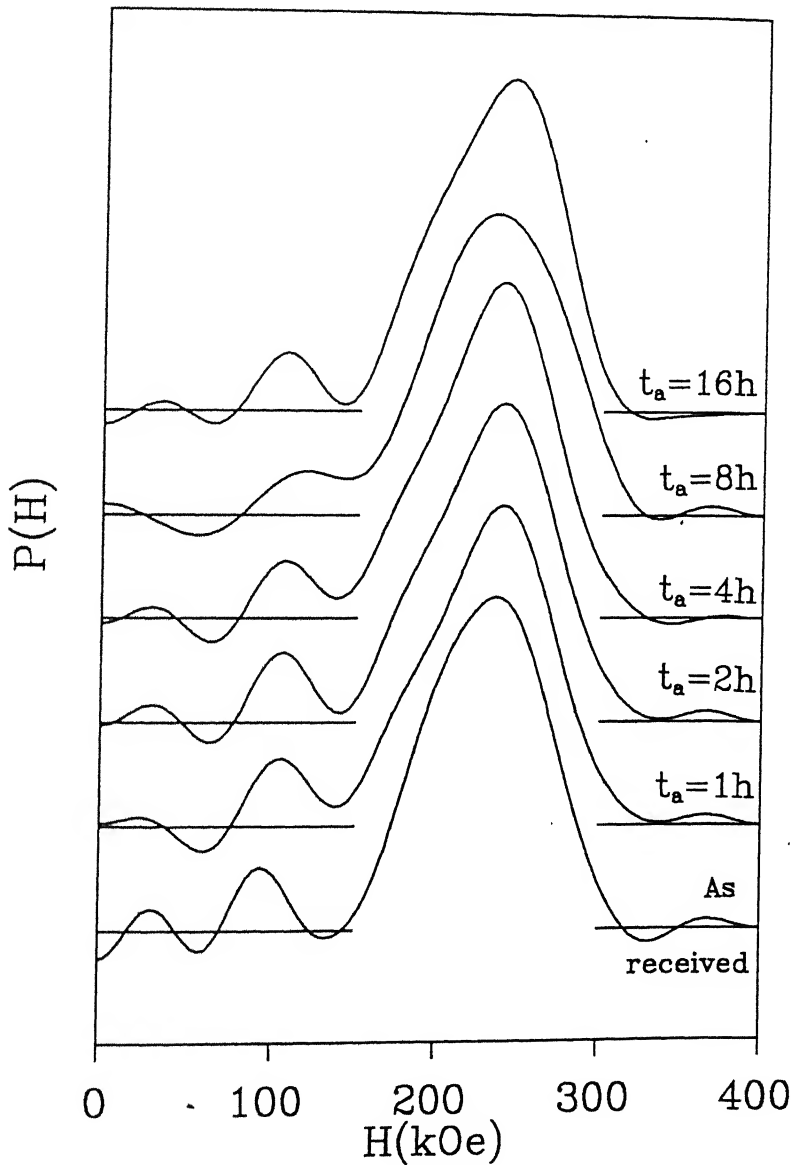
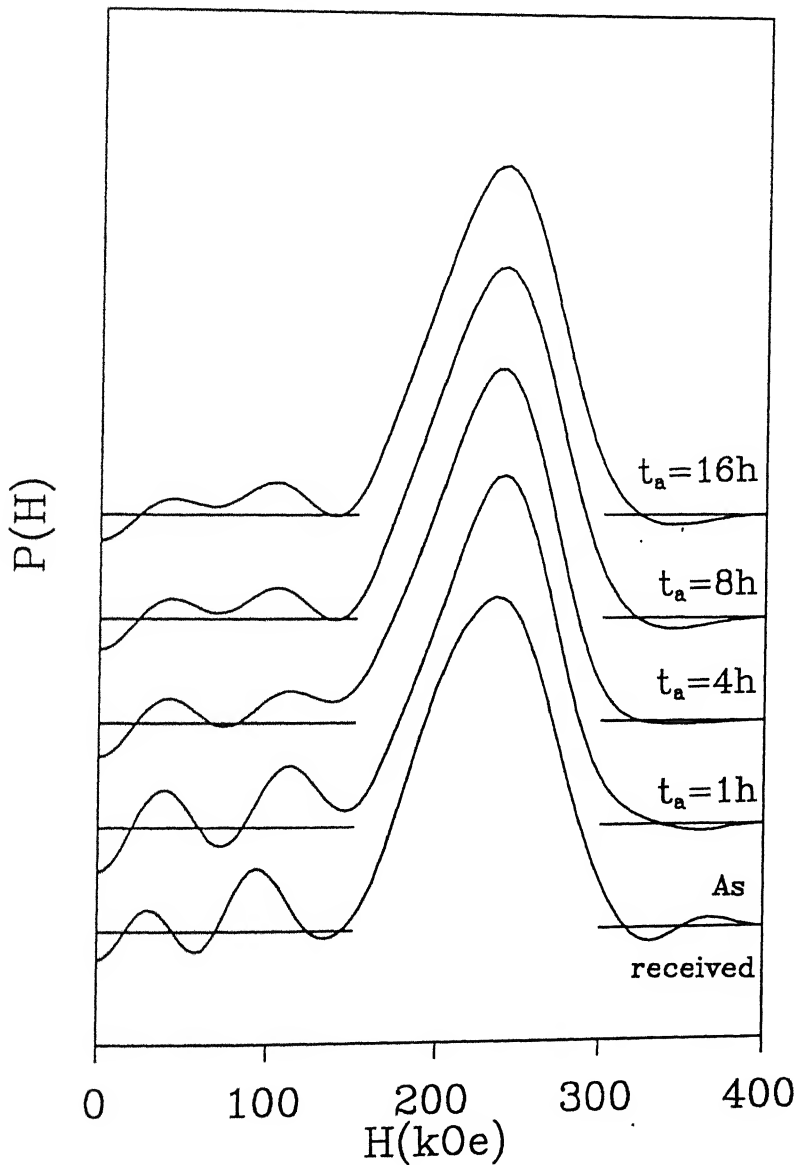


Fig. 6.4.  $P(H)$  distribution for Si5 samples annealed at 623 K (350 °C) for different  $t_a$ .



**Fig. 6.5.**  $P(H)$  distribution for Si5 samples annealed at 673 K (400 °C) for different  $t_a$ .

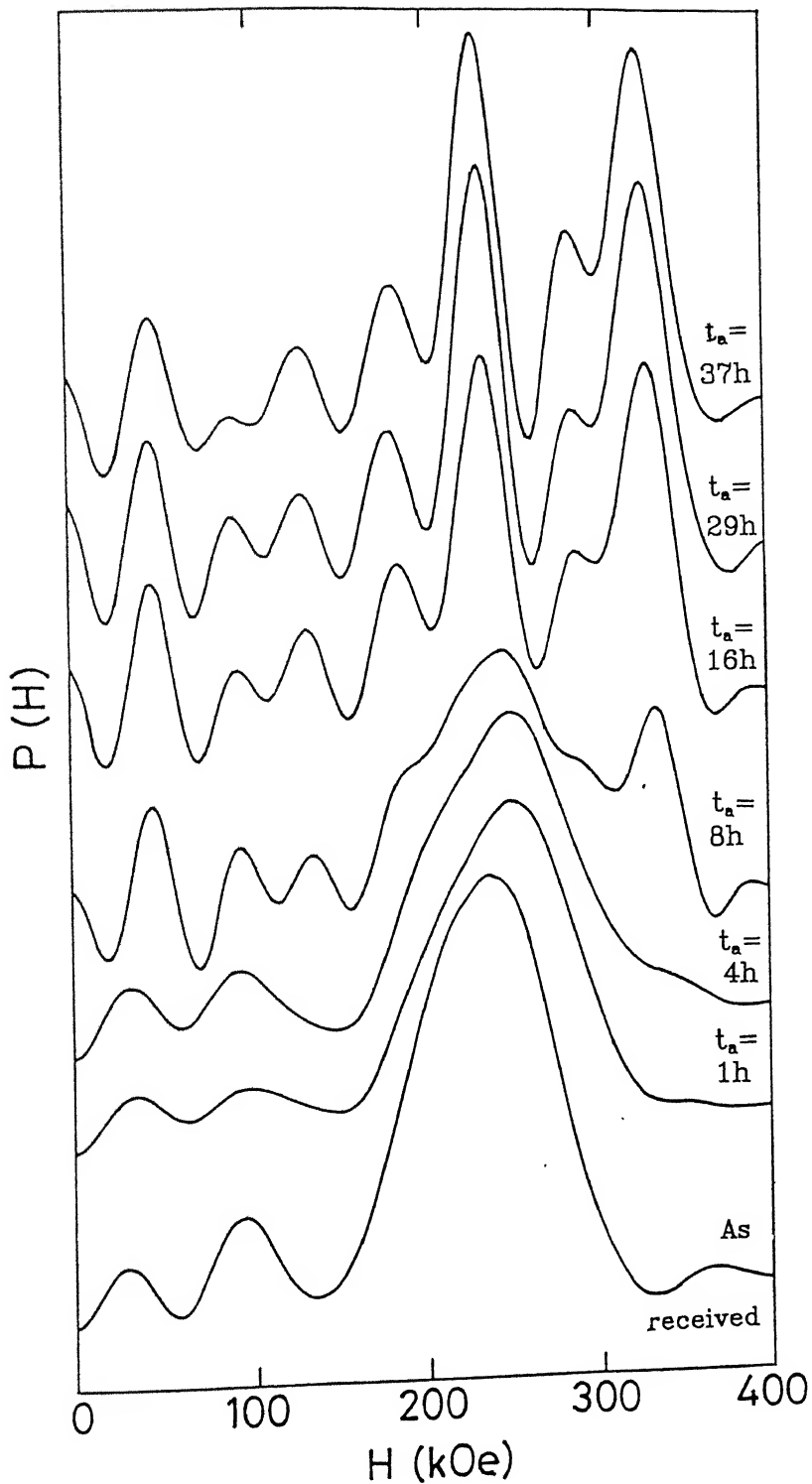


Fig. 6.6.  $P(H)$  distribution for Si5 samples annealed at 723 K (450 °C) for different  $t_a$ .

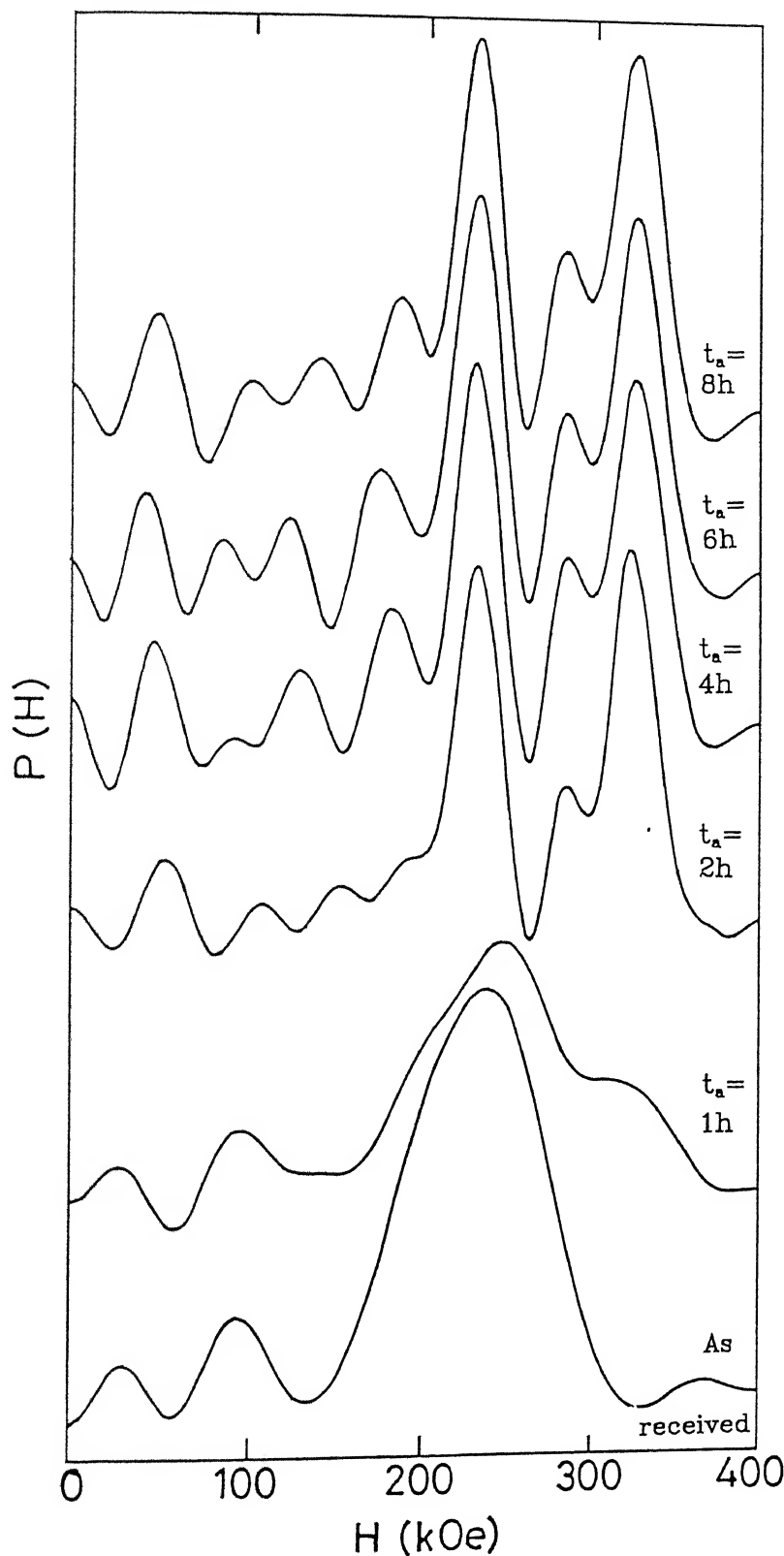


Fig. 6.7.  $P(H)$  distribution for Si5 samples annealed at 748 K (475 °C) for different  $t_a$ .

appears to pass through a transition stage and appears to settle into a new shape at  $t_a = 16$  h which is retained even when  $t_a$  is raised to 29 h and 37 h (Fig.6.6). It has been reported earlier [22,24] that different phases of  $\text{Fe}_3\text{B}$ ,  $\text{Fe}_2\text{B}$ ,  $\alpha$ -Fe and  $\alpha$ -(Fe,Si) evolve during the crystallization of the Si5 and Si9 metallic glasses. Our observations showed that the Mössbauer spectra recorded for the Si5 sample annealed at  $T_a = 723$  K for  $t_a = 16$  h was complicated (Fig.6.8) and could be fitted into eight subspectra using the least-squares fitting program. The values of the Mössbauer parameters obtained for these subspectra have already been reported [24]. This analysis indicated a formation of the phases  $\alpha$ -Fe,  $\text{Fe}_3\text{B}$ ,  $\text{Fe}_2\text{B}$  and  $\alpha$ -(Fe,Si). The phase  $\text{Fe}_3\text{B}$  appears to have been formed at three iron sites, having  $H = 226$ , 265 and 288 kOe. On the other hand the  $\text{Fe}_2\text{B}$  phase show H-values corresponding to two iron sites (with the two values lying very close at  $H = 231.7$  kOe and  $H = 242.0$  kOe), and an average value of  $H = 237$  kOe is usually considered. Previous work [22,24] has shown that silicon in the  $\alpha$ -(Fe,Si)solid solution is situated at different nearest neighbour (nn) iron atom sites. As a result the values of  $H$  in  $\alpha$ -(Fe,Si) solid solution are expected to depend on the nearest neighbour distributions e.g. 8, 7, 6, 5 and 4 nearest neighbour iron atom sites. Further the atomic percent of silicon in the  $\alpha$ -(Fe,Si) can change these H-values. Taking all these aspects into account, one can expect that the  $P(H)$  curves for Si5 annealed at  $T_a = 723$  K for  $t_a \geq 16$  h and at  $T_a = 748$  K for  $t_a \geq 2$  h should receive contributions from several H - values, some of which could be very close. This prediction is vindicated by the

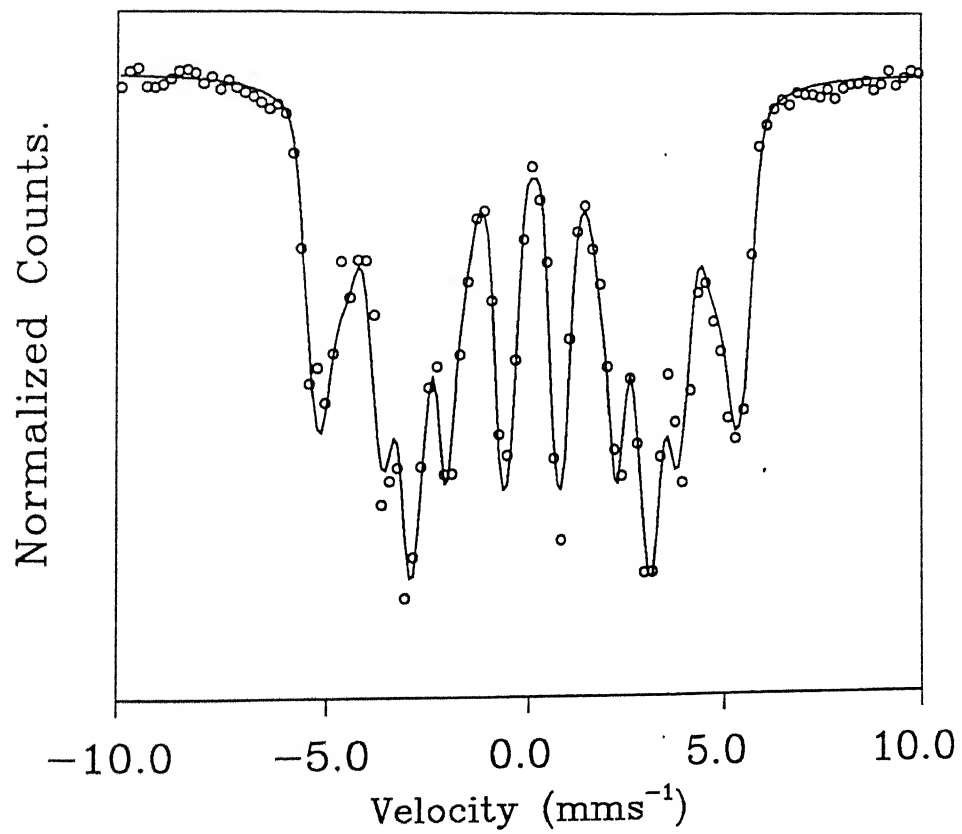


Fig. 6.8. Mössbauer spectrum of Si5 sample annealed at 723 K (450°C) for 16h.

structure in the  $P(H)$  curves shown in Figs.6.6 and 6.7. The distributions corresponding to  $T_a = 723$  K and  $t_a = 16, 29$  and  $37$  h and  $T_a = 748$  K and  $t_a = 4, 6$  and  $8$  h show four dominant peaks in the region  $H = 150 - 400$  kOe and these peaks might be composite peaks arising out of two or more overlapping  $P(H)$  distributions. At this stage it may be appropriate to draw attention to the work of Hesse and Rübartsch [27] who examined the problem of the evaluation of hyperfine field distributions  $P(H)$  from overlapped Mössbauer spectra. These workers [27] considered the case of a  $P(H)$  distribution consisting of two sharp field values. Application of Window's method [25] showed that a smaller value of  $N$  ( $N = 15$ ) does not resolve these two sharp fields but keeps the oscillations low. Increasing the value of  $N$  to 35 could resolve the two fields but introduced larger oscillations, although the  $\chi^2$ -values were reduced. Keeping these results in mind we tested our procedure by using different values of  $N$  for determining  $P(H)$  for samples in which precipitation of phases are expected to give discrete  $H$ -values. These tests allowed us to optimise a choice of  $N$  to be  $N = 20$  so that fair amount of resolution was possible without bringing in large oscillations or larger  $\chi^2$ -values. We feel that this choice of  $N = 20$  corresponds to a situation somewhat similar to the curve B, Fig.2(c) in the paper by Hesse and Rübartsch [27]. In other words the discrete  $H$ -values contributed by different phases have not been completely resolved in our results (Figs.6.6 and 6.7) and this explains why we observe 4 instead 8  $H$  - values.

A small peak appears to have developed around  $H_p \sim 135$  kOe

while the peak at  $H_p \sim 100$  kOe observed for the as-prepared sample appears to grow weaker with  $t_a$ . Following Ganesan et al.[31,32] we attributed these smaller peaks to the effect of Fe atoms surrounded by a large number of Si atoms although we are not sure whether these peaks are artifacts of truncation of Fourier series. In order to understand the four dominant peaks in the central region  $H = 150 - 350$  kOe an attempt was made to "peel off" these distributions so that the values for their  $H_p$ , widths (FWHM) and intensities could be quantitatively obtained. The results of this analysis are shown in Table 6.2, and they show that the four dominant peaks occur around  $H_p \sim 317, 276, 222$  and  $170$  kOe once the process of crystallization of the amorphous alloys (Si5) has advanced. The values of FWHM are not constant during the stage  $t_a = 8$  to  $37$  h (at  $T_a = 723$  K) and this indicates that some of these four peaks are still composite. This is to be expected because the analysis by the least-square fitting yielded eight sub-spectra (having H-values lying close to each other) while the "peeling off" procedure gave only four peaks. An attempt to decompose these peaks further was given up because the resulting  $\chi^2$ -values were becoming worse. These results thus show that the sensitivities of the two methods of analysis (i) Window's method and (ii) least-square-fitting are different. While Window's method can offer information about the distributions of hyperfine fields, it cannot unambiguously resolve the question of which iron-bearing phases have precipitated. Consequently we can use the results of previous analysis [24] to conclude that the  $H_p$  - values shown in Table 6.2 - correspond to the iron-bearing phases in the following

Table 6.2. Summary of parameters of peaks decomposed from the P(H) curves for Si5 shown in Figs. 6.6. and 6.7.

| T <sub>a</sub><br>(K) | t <sub>a</sub><br>(h) | H <sub>p</sub><br>(kOe) | FWHM<br>(kOe) | Inten-<br>sity<br>(%) | T <sub>a</sub><br>(K) | t <sub>a</sub><br>(h) | H <sub>p</sub><br>(kOe) | FWHM<br>(kOe) | Inten-<br>sity<br>(%) |
|-----------------------|-----------------------|-------------------------|---------------|-----------------------|-----------------------|-----------------------|-------------------------|---------------|-----------------------|
| 723                   | 8                     | 323                     | 20            | 16                    | 748                   | 2                     | 313                     | 27            | 46                    |
|                       |                       | 294                     | 32            | 10                    |                       |                       | 273                     | 16            | 10                    |
|                       |                       | 228                     | 66            | 69                    |                       |                       | 219                     | 24            | 39                    |
|                       |                       | 174                     | 20            | 5                     |                       |                       | 181                     | 17            | 5                     |
| 723                   | 16                    | 320                     | 27            | 35                    | 748                   | 4                     | 317                     | 28            | 41                    |
|                       |                       | 280                     | 24            | 19                    |                       |                       | 276                     | 18            | 13                    |
|                       |                       | 224                     | 26            | 35                    |                       |                       | 221                     | 23            | 35                    |
|                       |                       | 174                     | 21            | 11                    |                       |                       | 171                     | 21            | 11                    |
| 723                   | 29                    | 318                     | 30            | 44                    | 748                   | 6                     | 318                     | 28            | 41                    |
|                       |                       | 277                     | 18            | 10                    |                       |                       | 276                     | 17            | 12                    |
|                       |                       | 222                     | 23            | 37                    |                       |                       | 222                     | 24            | 38                    |
|                       |                       | 169                     | 18            | 9                     |                       |                       | 167                     | 22            | 9                     |
| 723                   | 37                    | 313                     | 26            | 40                    | 748                   | 8                     | 317                     | 27            | 41                    |
|                       |                       | 269                     | 27            | 14                    |                       |                       | 275                     | 18            | 13                    |
|                       |                       | 229                     | 26            | 35                    |                       |                       | 222                     | 22            | 36                    |
|                       |                       | 183                     | 18            | 11                    |                       |                       | 176                     | 22            | 10                    |

way:

- (i)  $H_p \sim 313 - 323$  kOe:  $\alpha$ -Fe,  $\alpha$ -(Fe, Si 8nn),  $\alpha$ -(Fe, Si 7nn)
- (ii)  $H_p \sim 269 - 294$  kOe:  $\alpha$ -(Fe, Si 6nn), t -  $Fe_3B$
- (iii)  $H_p \sim 221 - 229$  kOe:  $\alpha$ -(Fe, Si 5nn),  $Fe_2B$ , t- $Fe_3B$ ,  $\alpha$ -(Fe, Si 4nn)
- (iv)  $H_p \sim 167 - 183$  kOe:  $\alpha$ -(Fe, Si other nn ?)

To further examine the evolution of the hyperfine magnetic field  $H$  and the distributions  $P(H)$  better we shall first discuss the results for Si5 sample in the range  $T_a = 573 - 673$  K during which  $Fe_{79}B_{16}Si_5$  metallic glass retains its amorphous nature [24]. The value of  $H_{eff}$ ,  $H_p$  and  $\langle H \rangle$  determined for  $T_a = 573, 623, 673$  and 723 K for different values of  $t_a$  are summarized in Table 6.3, where the values of  $H_{eff}$  are taken from Table I of Ref. [24]. The values of  $H_p$  and  $\langle H \rangle$  correspond to the peak positions and the average values obtained from  $P(H)$  as discussed in Sec.3.1. It is observed that there is a close correspondence between the  $H_{eff}$  - values obtained by least-squares analysis reported earlier [24] and  $H_p$  - values obtained in the present work. The values of  $\langle H \rangle$  are consistently lower than the  $H_{eff}$  or  $H_p$  values because of the asymmetric shape of the dominant peak as well as because of low -  $H$  peaks in the  $P(H)$  distributions. To further bring out the evolution of  $\langle H \rangle$  with  $t_a$  we have plotted in Fig.6.9(a) the values of  $\langle H \rangle$  against  $t_a$  observed for each of the temperature ( $T_a$ , see Table 6.1) studied by us. It is observed that at a given  $T_a$ , within the experimental error, the observed values of  $\langle H \rangle$  do not vary with  $t_a$  and that they lie in the range  $\langle H \rangle = 226 \pm 4$  kOe for  $T_a = 573, 623$  and 673 K. Previous measurements [24] have shown

Table 6.3. Results for  $H_{eff}$ ,  $H_p$ ,  $\langle H \rangle$ ,  $\Delta H_1$  and  $\Delta H_2$  for the  $Fe_{79}B_{16}Si_5$  metallic glass for different annealing temperatures ( $T_a$ ) and time periods ( $t_a$ ). The errors in  $H_{eff}$ ,  $H_p$  and  $\langle H \rangle$  are typically  $\pm 4kOe$ .

| $T_a$ | $t_a$<br>(hr) | $H_{eff}$<br>(kOe) | Window's Method |                     |              |              |
|-------|---------------|--------------------|-----------------|---------------------|--------------|--------------|
|       |               |                    | $H_p$           | $\langle H \rangle$ | $\Delta H_1$ | $\Delta H_2$ |
| 573 K | 1             | 242                | 239             | 228                 | 48           | 41           |
|       | 4             | 243                | 245             | 228                 | 59           | 37           |
|       | 8             | 235                | 235             | 225                 | 46           | 40           |
|       | 16            | 240                | 241             | 226                 | 52           | 37           |
| 623 K | 1             | 237                | 231             | 222                 | 46           | 41           |
|       | 2             | 239                | 237             | 224                 | 49           | 42           |
|       | 4             | 238                | 240             | 226                 | 49           | 37           |
|       | 8             | 240                | 240             | 231                 | 58           | 43           |
|       | 16            | 239                | 245             | 226                 | 59           | 36           |
| 673 K | 1             | 240                | 239             | 226                 | 44           | 38           |
|       | 4             | 239                | 240             | 226                 | 53           | 36           |
|       | 8             | 240                | 240             | 228                 | 49           | 39           |
|       | 16            | 239                | 244             | 231                 | 59           | 34           |
| 723 K | 1             | 242                | 246             | 234                 | 52           | 42           |
|       | 4             | —                  | 247             | 238                 | 54           | 39           |

that a transformation from amorphous to crystalline state begins in the Si5 sample at  $T_a = 723$  K when  $t_a \geq 4$  h. In order to examine how the observed values of  $\langle H \rangle$  vary with  $t_a$  during this partial decomposition we have plotted in Fig. 6.9(b) the variation of  $\langle H \rangle$  with  $t_a$  for  $T = 723$  and 748 K. These results show that for  $T_a = 723$  K,  $\langle H \rangle$  increases smoothly but significantly for short annealing time periods ( $t_a \leq 16$  h), and then remains constant at about  $\langle H \rangle = 264$  kOe upto  $t_a = 39$  h. On the other hand at  $T_a = 748$  h the values of  $\langle H \rangle$  remain constant around  $\langle H \rangle = 263$  kOe beyond  $t_a \geq 2$  h. Koshimura and Takahashi [33] had observed a similar time-evolution of  $\langle H \rangle$  in the binary amorphous  $Fe_{83}B_{17}$  alloy by Mössbauer spectroscopy and have attempted to explain their results using a model of clusters [34,35] and structural relaxation in amorphous alloys as indicated in Fig.6.10. We feel that the present studies provide interesting results for the ternary amorphous alloys  $Fe_{79}B_{16}Si_5$  and should prove useful for attempting a theoretical explanation in terms of structural relaxation.

In order to understand the evolution of  $P(H)$  for the Si5 sample in terms of the phases precipitated during the annealing, we have plotted the difference  $[P(H)_{t=t_a} - P(H)_{t=0}]$  versus  $H$  for different values of  $t_a$  at  $T_a = 723$  and 748 K in Figs.6.11(a) and (b) respectively. It is observed that the field components around  $H = 200$  kOe and  $H = 258$  kOe decrease with annealing time period ( $t_a$ ) while the components around  $H = 230$  kOe (with low intensity) and  $H = 327$  kOe (with higher intensity) increase with  $t_a$ . The vertical arrows in Fig.6.11 indicate the  $H$  - value characteristic of  $\alpha$ -Fe. The behaviour observed in Fig.6.11 can be understood in

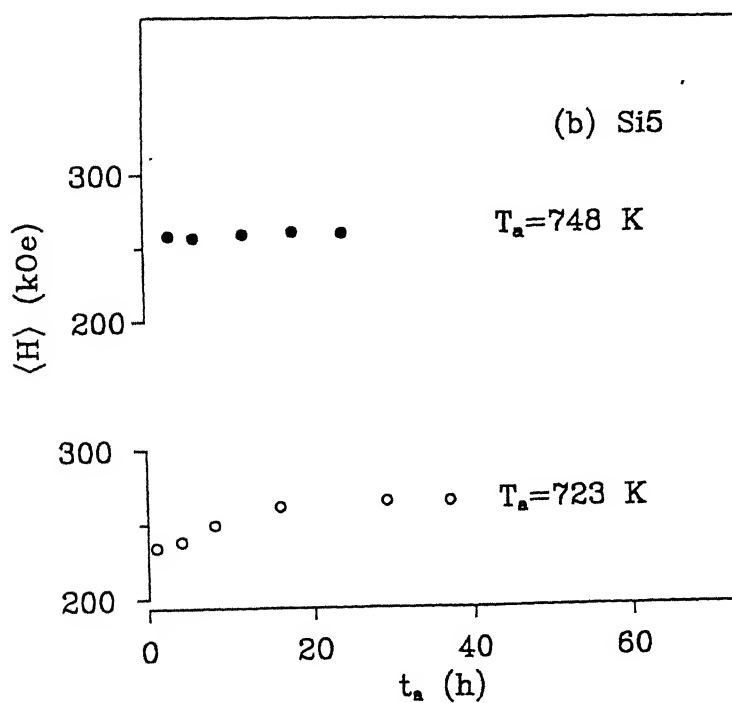
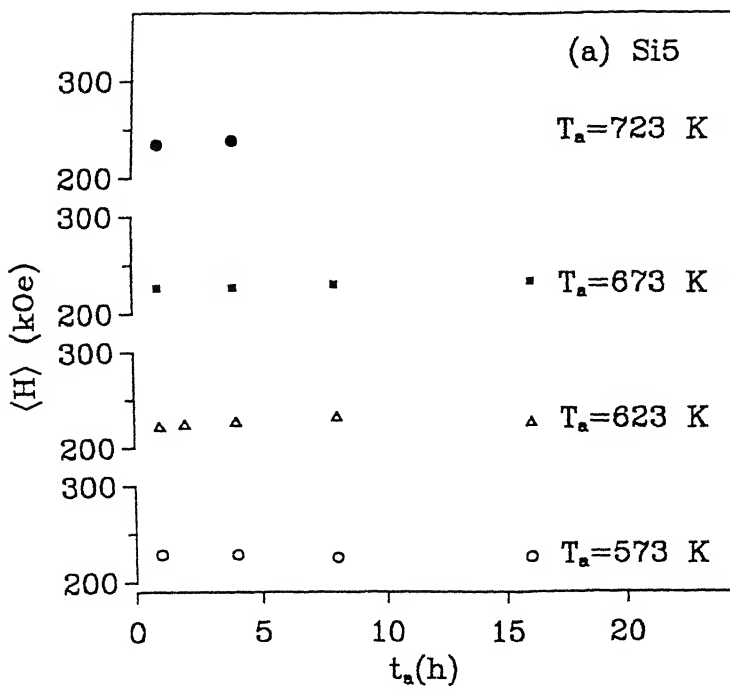
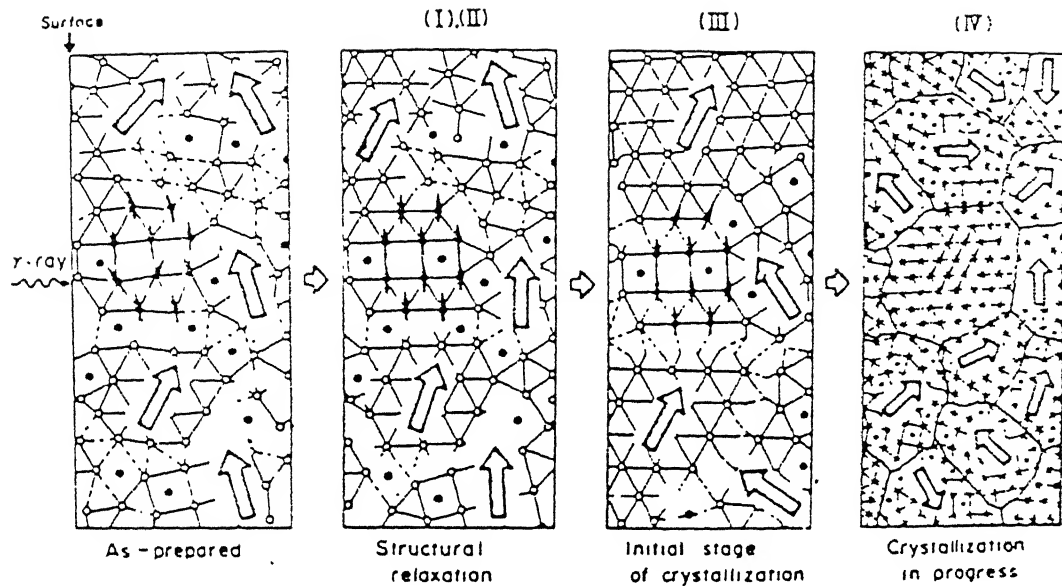


Fig. 6.9. (a) Dependence of  $\langle H \rangle$  for the  $Fe_{79}B_{16}Si_5$  metallic glasses on annealing time period ( $t_a$ ) at (i)  $T_a = 573$  K ( $\circ$ ) ; (ii)  $T_a = 623$  K ( $\Delta$ ) ; (iii)  $T_a = 673$  K ( $\blacksquare$ ) and (iv)  $T_a = 723$  K ( $\bullet$ ) ; (b) Dependence of  $\langle H \rangle$  for the  $Fe_{79}B_{16}Si_5$  metallic glasses on annealing time period ( $t_a$ ) at (i)  $T_a = 723$  K ( $\circ$ ) and (ii)  $T_a = 748$  K ( $\bullet$ ) .



**Fig. 6.10.** A model for structural relaxation in amorphous alloys. (The small arrows indicate the spin direction of Fe atoms and the empty arrows shows the average direction of magnetization in a cluster). [Taken from ref.33].

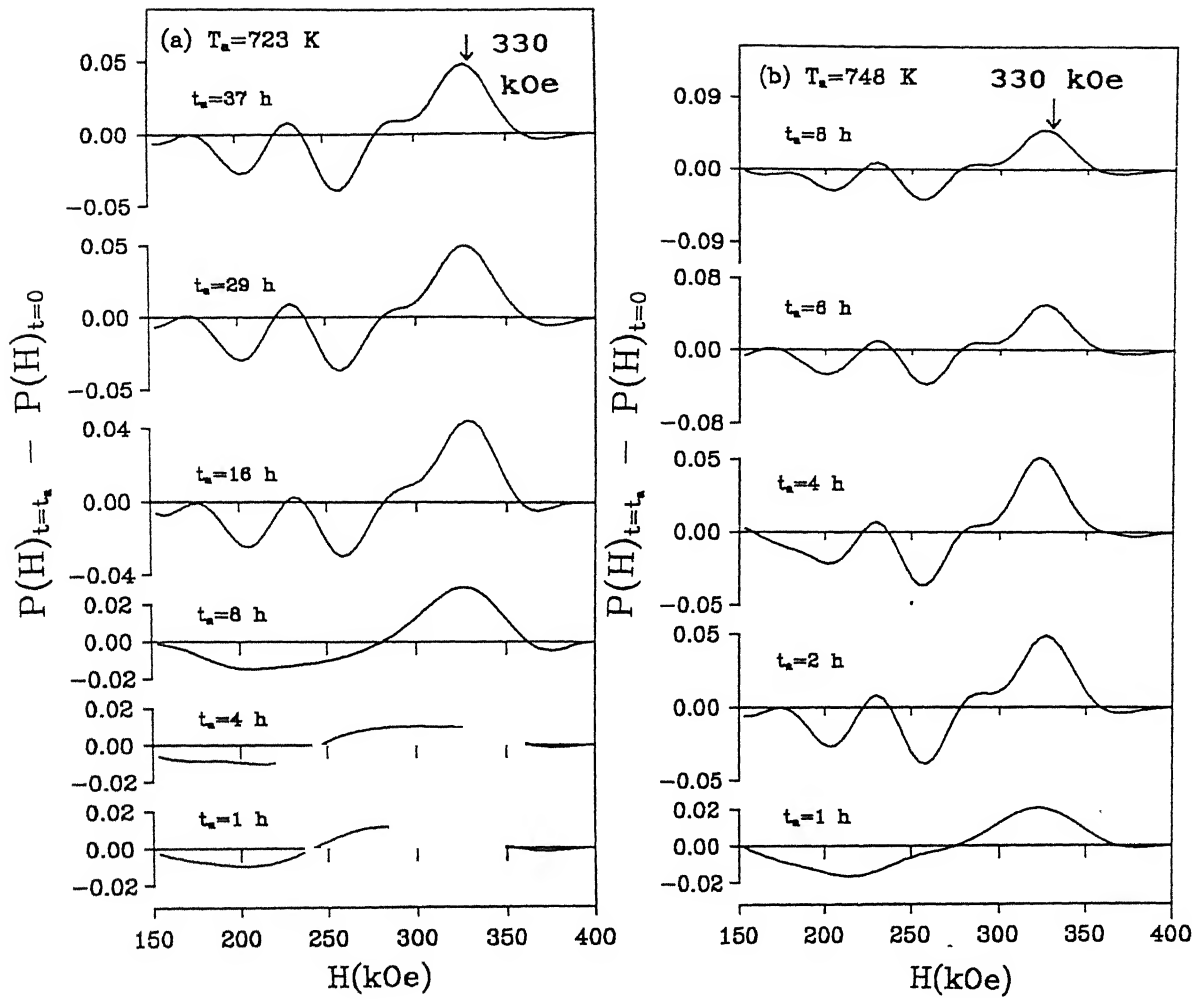


Fig. 6.11. Difference in  $P(H)$  for  $\text{Fe}_{79}\text{B}_{16}\text{Si}_5$  between  $t = t_a$  (after annealing) and  $t = 0$  (before annealing) at (a)  $T_a = 723$  K and (b)  $T_a = 748$  K.

terms of the phase precipitation results reported earlier [24] where it was concluded that the crystallization of  $\text{Fe}_{79}\text{B}_{16}\text{Si}_5$  occurred in two stages. In the first stage  $\alpha$ -(Fe,Si) and metastable  $\text{Fe}_3\text{B}$  are formed while further heating (higher  $T_a$  or  $t_a$ ) leads to the second stage involving the decomposition of the metastable  $\text{Fe}_3\text{B}$  into the stable phases  $\text{Fe}_2\text{B}$  and  $\alpha$ -Fe (i.e.  $\text{Fe}_3\text{B} \rightarrow \text{Fe}_2\text{B} + \alpha\text{-Fe}$ ). The reported values of average H for  $\alpha$ -(Fe,Si 4nn),  $\text{Fe}_3\text{B}$  and  $\text{Fe}_2\text{B}$  and  $\alpha$ -Fe are 201, 259, 237 and 330 kOe (see Table III, Ref. [24]). Using these results, the plots in Fig.6.11 can be interpreted to indicate that as  $t_a$  increases (at  $T_a = 723$  or  $748$  K) the volume fraction of  $\alpha$ -(Fe,Si 4nn) and  $\text{Fe}_3\text{B}$  phases decreases and that of  $\text{Fe}_2\text{B}$  and  $\alpha$ -Fe phases increase. The results also suggest that perhaps  $\alpha$ -(Fe,Si 4nn) phase transform with  $t_a$  to  $\alpha$ -(Fe,Si 7nn) and (or)  $\alpha$ -(Fe, Si 8nn), since the H - values of the latter two phases are closer to (but less than) 330 kOe. The data analysis shown in Fig.6.11 thus indicates that a close examination of the time evolution of P(H) provides valuable information about the kinetics of crystallization (and phase precipitation) in a metallic glass.

### 6.3.2.2. $\text{Fe}_{78}\text{B}_{13}\text{Si}_9$ (or Si9)

The schedule used for the annealing of the Si9 samples is already shown in Table 6.1. The results for the P(H) distributions obtained from the Mössbauer spectra of Si9 samples annealed at  $T_a = 573, 623, 673, 723$  and  $748$  K for different time periods are shown in Figs.6.12 - 6.16 respectively. It is observed that the

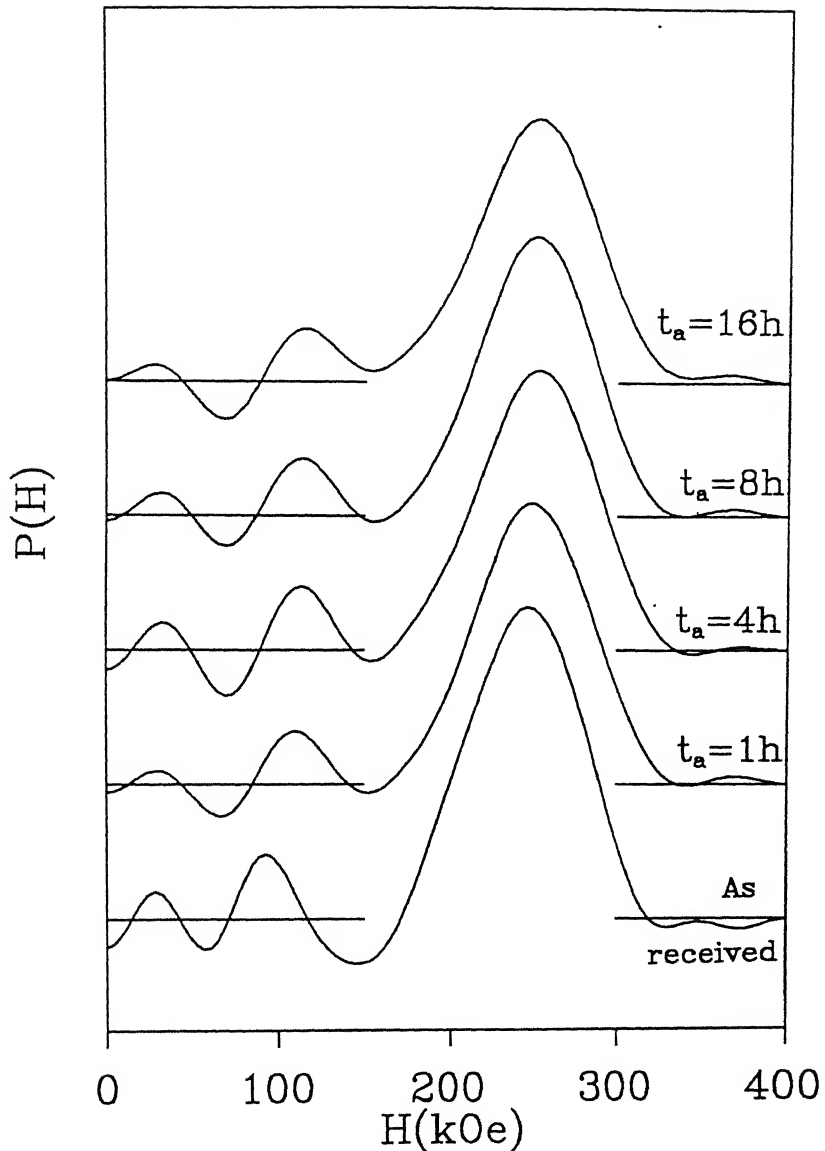


Fig. 6.12.  $P(H)$  distribution for Si9 sample annealed at 573 K (300 °C) for different  $t_a$ .

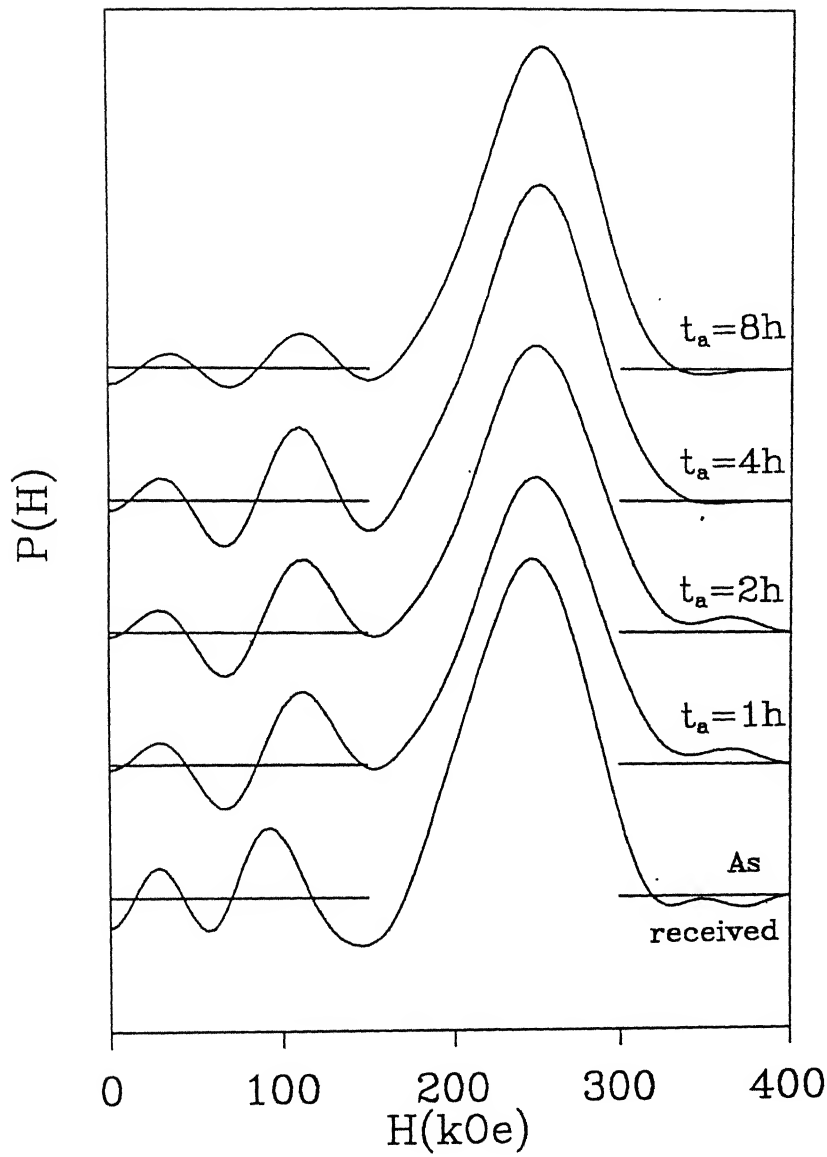


Fig. 6.13.  $P(H)$  distribution for Si9 samples annealed at 623 K (350 °C) for different  $t_a$ .

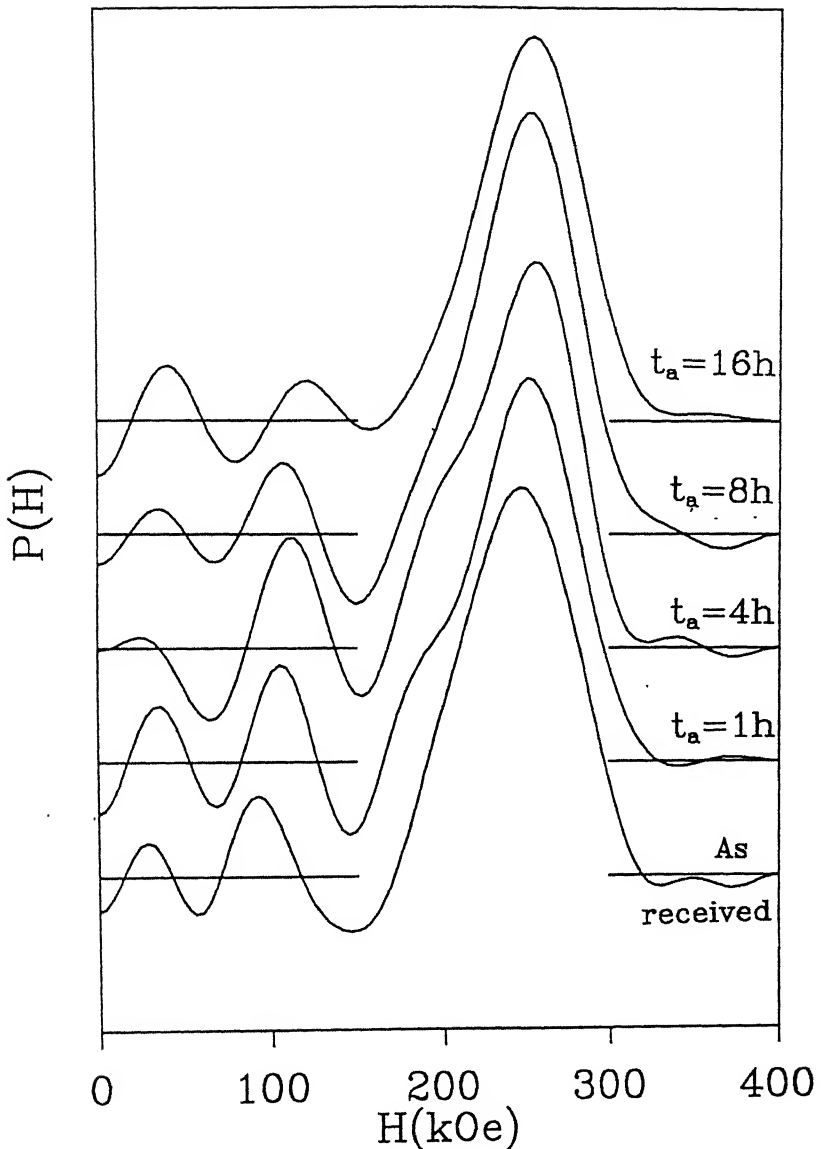


Fig.6.14.  $P(H)$  distribution for Si9 samples annealed at 673 K (400 °C) for different  $t_a$ .

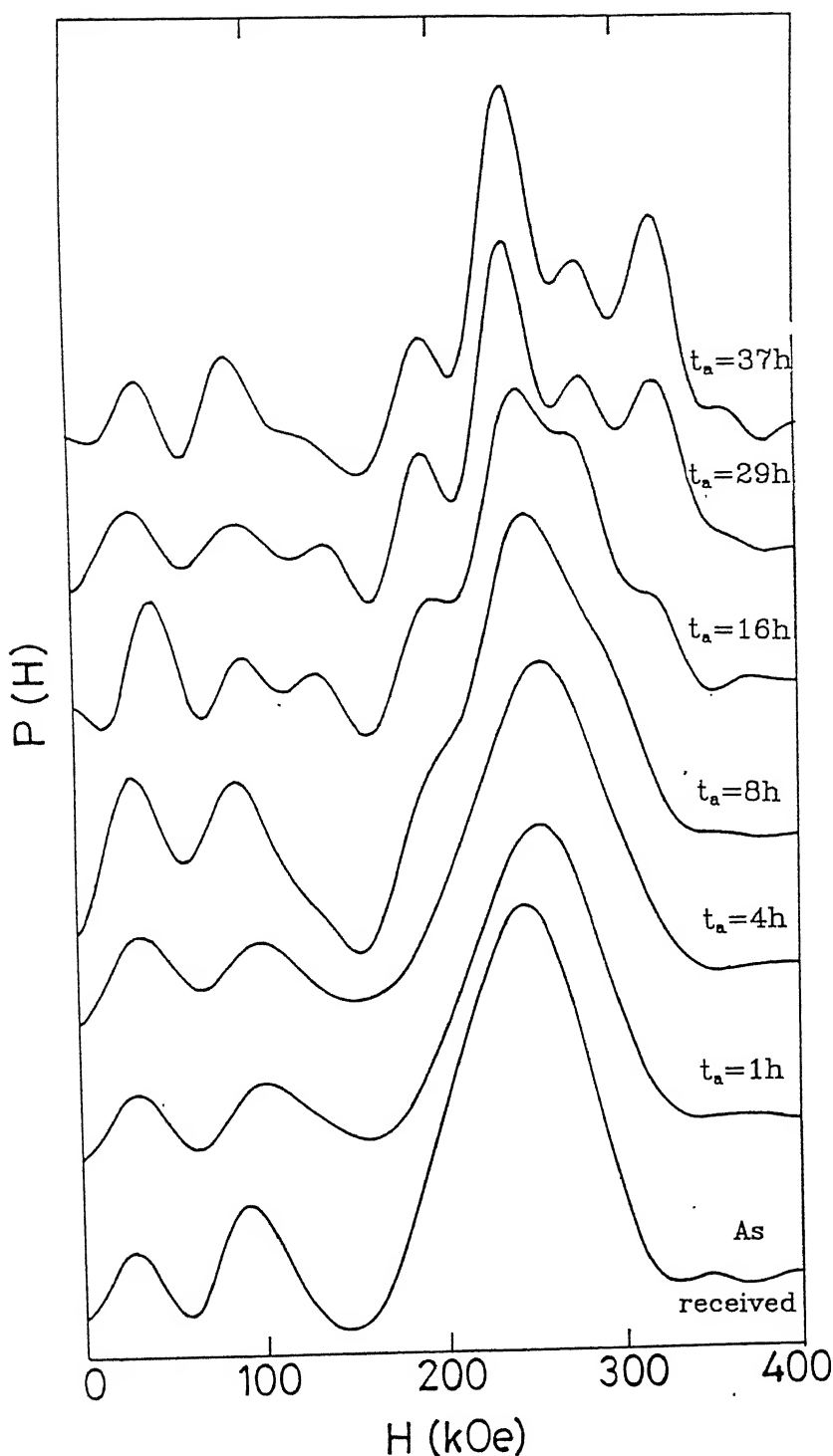


Fig. 6.15.  $P(H)$  distribution for Si9 samples annealed at 723 K (450 °C) for different  $t_a$ .

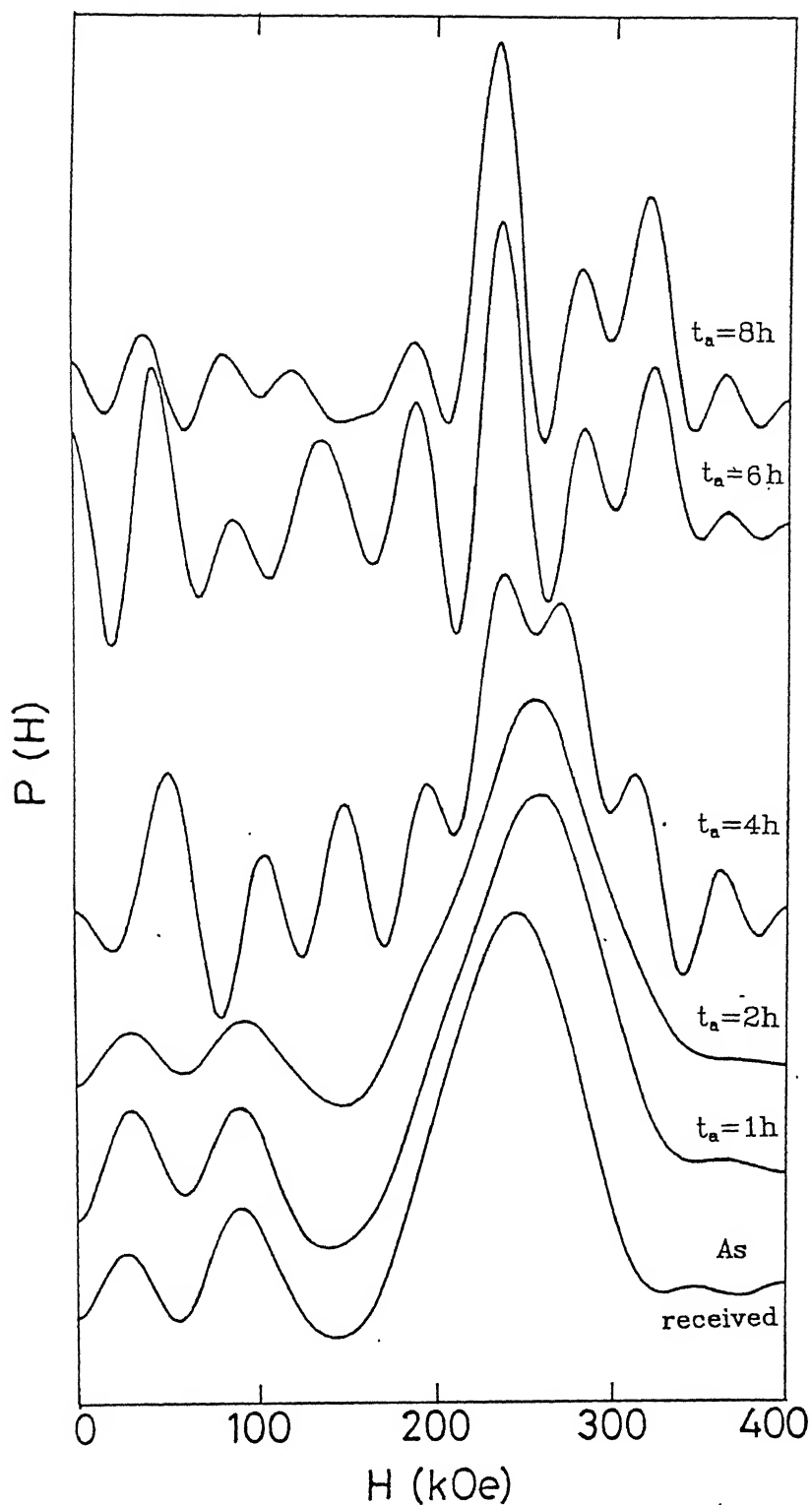


Fig. 6.16.  $P(H)$  distribution for Si9 samples annealed at 748 K (475 °C) for different  $t_a$ .

$P(H)$  distributions for  $T_a = 573, 623$  and  $673\text{ K}$  (Figs.6.12 - 6.14) are similar in shape to that for the as-received sample (Fig.6.2), with the minor changes occurring with  $t_a$  being explained in a manner similar to that used for Si5 in Sec.6.3.2.1. The shape of the  $P(H)$  distribution starts to change only at  $T_a = 723\text{ K}$  when  $t_a \geq 8\text{ h}$  and appears to settle into a new shape when  $t_a = 29\text{ h}$  or  $37\text{ h}$ . The values of  $H_p$ , FWHM and intensities for the Si9 samples obtained by the 'peeling off' method are summarised in Table 6.4. It is noted that the new shape of  $P(H)$  for the Si9 samples (curve g, Fig.6.15) is different from the shape of the corresponding  $P(H)$  curve for the Si5 samples (curve g, Fig.6.6). Both these curves indicate the presence of four overlapping and dominant peaks in the region  $H=150-400\text{ kOe}$ . Their relative intensities are different, even though the values of  $H_p$  and FWHM are same (Tables 6.2 and 6.4). This behaviour indicates that the kinetics of crystallization of the Fe-B-Si glasses depend on their composition. Same conclusion has been drawn from previous studies [23,24]. The  $P(H)$  distributions for the Si9 samples annealed at  $748\text{ K}$  (Fig.6.16) show the presence of precipitated phases only when  $t_a \geq 4\text{ h}$ . The values of  $H_p$ , FWHM, and intensity obtained for Si9 for  $T_a = 748\text{ K}$ ,  $t_a = 8\text{ h}$  (Table 6.4) show slight differences when compared with similar results for Si5 (Table 6.2). It is also noticed that the dominant peaks in the  $P(H)$  distributions for Si9 at  $T_a = 748\text{ K}$  have not resolved any better and the general trends shown in Fig.6.7 (Si5) and Fig.6.16 (Si9) are similar. The results for Si9 show, once again, that the evolution of  $P(H)$  curves follows the kinetics of crystallization. The  $H_p$ -values shown for

Table 6.4. Summary of parameters of peaks decomposed from the P(H) curves for Si9 shown in Figs. 6.15. and 6.16.

| T <sub>a</sub><br>(K) | t <sub>a</sub><br>(h) | H <sub>p</sub><br>(kOe) | FWHM<br>(kOe) | Inten-<br>sity<br>(%) | T <sub>a</sub><br>(K) | t <sub>a</sub><br>(h) | H <sub>p</sub><br>(kOe) | FWHM<br>(kOe) | Inten-<br>sity<br>(%) |
|-----------------------|-----------------------|-------------------------|---------------|-----------------------|-----------------------|-----------------------|-------------------------|---------------|-----------------------|
| 723                   | 16                    | 308                     | 32            | 14                    | 748                   | 6                     | 314                     | 20            | 28                    |
|                       |                       | 269                     | 28            | 28                    |                       |                       | 276                     | 13            | 13                    |
|                       |                       | 234                     | 35            | 50                    |                       |                       | 229                     | 16            | 44                    |
|                       |                       | 187                     | 20            | 8                     |                       |                       | 179                     | 13            | 15                    |
| 723                   | 29                    | 313                     | 33            | 27                    | 748                   | 8                     | 310                     | 20            | 30                    |
|                       |                       | 269                     | 26            | 22                    |                       |                       | 275                     | 15            | 15                    |
|                       |                       | 229                     | 26            | 42                    |                       |                       | 226                     | 18            | 50                    |
|                       |                       | 183                     | 17            | 9                     |                       |                       | 178                     | 13            | 5                     |
| 723                   | 37                    | 313                     | 26            | 27                    |                       |                       |                         |               |                       |
|                       |                       | 269                     | 27            | 21                    |                       |                       |                         |               |                       |
|                       |                       | 229                     | 26            | 44                    |                       |                       |                         |               |                       |
|                       |                       | 183                     | 18            | 8                     |                       |                       |                         |               |                       |

Si9 in Table 6.5 can be related to different iron-bearing phases in the following manner:

- (i)  $H_p \sim 310 - 314$  kOe:  $\alpha$ -Fe,  $\alpha$ -(Fe, Si 8nn),  $\alpha$ -(Fe, Si 7nn).
- (ii)  $H_p \sim 270 - 276$  kOe:  $\alpha$ -(Fe, Si 6nn), t- $Fe_3B$ .
- (iii)  $H_p \sim 226 - 229$  kOe:  $\alpha$ -(Fe, Si 5nn),  $Fe_2B$ , t- $Fe_3B$ ,  $\alpha$ -(Fe, Si 4nn).
- (iv)  $H_p \sim 178 - 183$  kOe:  $\alpha$ -(Fe, Si other nn ?)

We shall now examine the evolution of H and P(H) for the  $Fe_{78}B_{13}Si_9$  (Si9) metallic glasses in a manner described for the Si5 samples in the previous section. The values of  $H_{eff}$ ,  $H_p$  and  $\langle H \rangle$  determined for  $T_a = 573, 623, 673$  and  $723$  K for different values of  $t_a$  are summarized in Table 6.5. Once again we observe that there is a close correspondence between the values of  $H_{eff}$  and  $H_p$  and that the values of  $\langle H \rangle$  are consistently lower than  $H_{eff}$  or  $H_p$  values. The reason for this behaviour have been discussed in the previous section. The variation of  $\langle H \rangle$  with  $t_a$  for the Si9 samples in the temperature range  $T = 573 - 723$  K (during which these metallic glasses remain amorphous) is shown in Fig.6.17 (a) and it is observed that the  $\langle H \rangle$  - values remain constant with  $t_a$  in this temperature range. It is noted that for a given  $T_a$  and  $t_a$ , the  $\langle H \rangle$  values for the Si9 sample are slightly higher than those for the Si5 sample. Similar increase in H with increasing silicon concentration has been reported in the literature [36-38] and it has been ascribed to the strain caused during the replacement of a small metalloid (boron) by a larger metalloid (silicon) atom in the interstitial site.

Table 6.5. Results for  $H_{eff}$ ,  $H_p$ ,  $\langle H \rangle$ ,  $\Delta H_1$  and  $\Delta H_2$  for the  $Fe_{78}B_{13}Si_9$  metallic glass for different annealing temperatures ( $T_a$ ) and time periods ( $t_a$ ). The errors in  $H_{eff}$ ,  $H_p$  and  $\langle H \rangle$  are typically  $\pm 4kOe$ .

| $T_a$ | $t_a$<br>(hr) | $H_{eff}$<br>(kOe) | Window's Method |                     |              |              |
|-------|---------------|--------------------|-----------------|---------------------|--------------|--------------|
|       |               |                    | $H_p$           | $\langle H \rangle$ | $\Delta H_1$ | $\Delta H_2$ |
| 573 K | 1             | 252                | 251             | 246                 | 42           | 41           |
|       | 4             | 255                | 253             | 247                 | 46           | 39           |
|       | 8             | 252                | 252             | 241                 | 44           | 39           |
|       | 16            | 254                | 254             | 244                 | 47           | 35           |
| 623 K | 1             | 250                | 249             | 243                 | 42           | 39           |
|       | 2             | 252                | 253             | 245                 | 47           | 36           |
|       | 4             | 254                | 252             | 247                 | 44           | 37           |
|       | 8             | 254                | 253             | 248                 | 41           | 39           |
| 673 K | 1             | 252                | 262             | 244                 | 54           | 22           |
|       | 4             | 251                | 266             | 249                 | 49           | 27           |
|       | 8             | 255                | 257             | 248                 | 45           | 27           |
|       | 16            | 255                | 255             | 251                 | 42           | 34           |
| 723 K | 1             | 261                | 255             | 250                 | 41           | 41           |
|       | 4             | 258                | 258             | 253                 | 42           | 41           |
|       | 8             | 255                | 252             | 255                 | 41           | 47           |
|       | 16            | 253                | —               | 260                 | —            | —            |

Previous results [24] have indicated that the crystallization process in the  $\text{Fe}_{78}\text{B}_{13}\text{Si}_9$  commences at  $T_a = 748$  K and  $t_a = 1$  h. The variation of  $\langle H \rangle$  with  $t_a$  observed by us for the Si9 sample for  $T_a = 723$  and 748 K is shown in Fig.6.17(b) and it shows that at  $T_a = 723$  K,  $\langle H \rangle$  increases by smaller amount (compared to Si5, see Fig.6.9(b)) at small annealing time periods before reaching a plateau. At  $T_a = 748$  K,  $\langle H \rangle$  remains constant around  $\langle H \rangle = 259$  kOe for  $t_a = 1-8$  h. This saturation value  $\langle H \rangle = 259$  kOe for the Si9 sample is slightly lower than the corresponding value  $\langle H \rangle = 263$  kOe observed for the Si5 sample, and this difference could be attributed to lower percentage of Fe in the Si9 sample which gives rise to lower fraction of  $\alpha$ -Fe during the crystallization.

Following the analysis presented at the end of Sec.6.3.2.1, we present our results for the difference  $[P(H)_{t=t_a} - P(H)_{t=0}]$  versus H for the Si9 sample for different values of  $t_a$  at  $T_a = 723$  K and  $T_a = 748$  K in Figs.6.18(a) and (b) respectively. The results show that in the case of Si9 samples, the field components around  $H = 210$  kOe and  $H = 258$  kOe show a decrease with  $t_a$  and this decrease is more prominent at higher  $t_a$ . An increase in the component around  $H = 236$  kOe is more marked at  $T_a = 748$  K with  $t_a \geq 6$  h. The component around  $H = 324$  kOe is observed at  $T_a = 723$  K for  $t_a \geq 29$  h and at  $T_a = 748$  K for  $T_a = 748$  K for  $t_a \geq 6$  h. The general trend of these results for the Si9 sample is same as that observed for the Si5 sample and can be understood using same arguments.

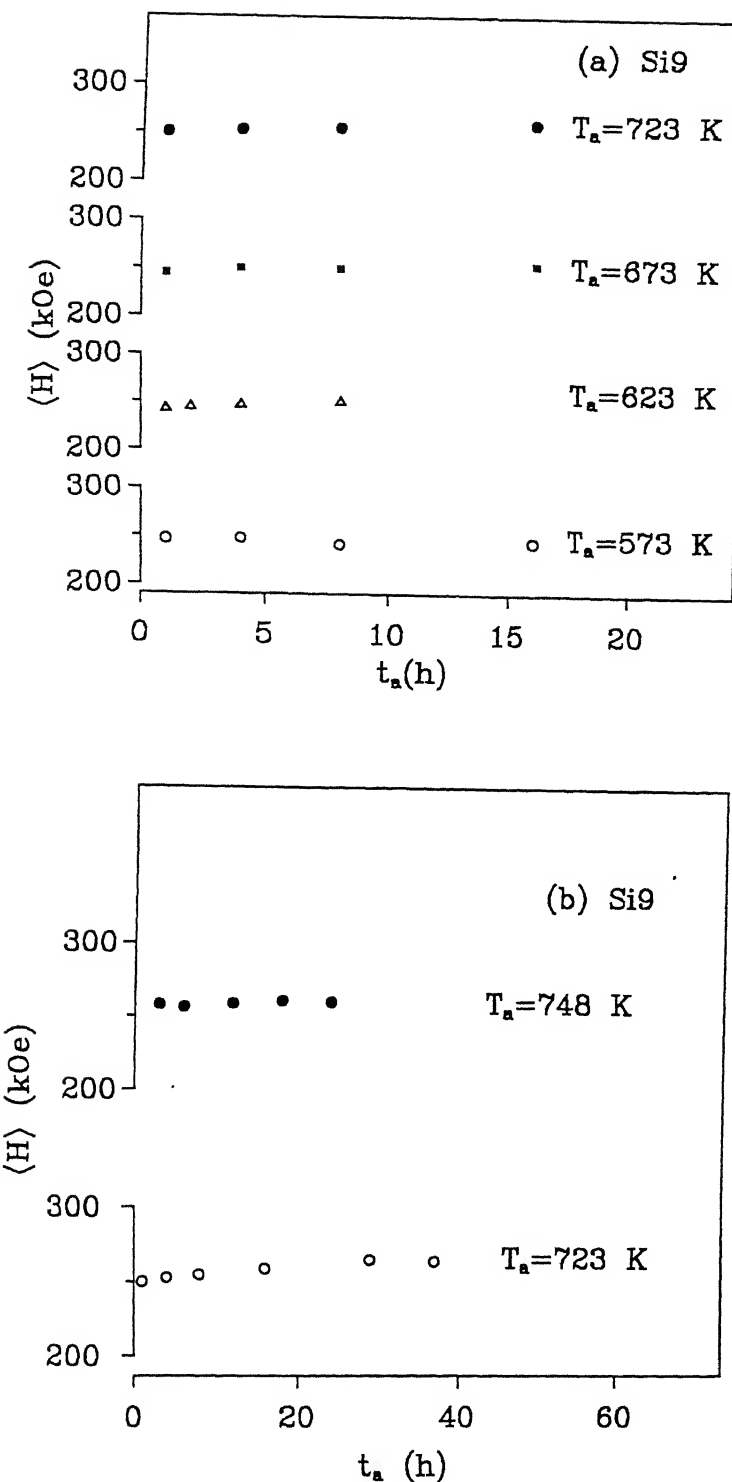
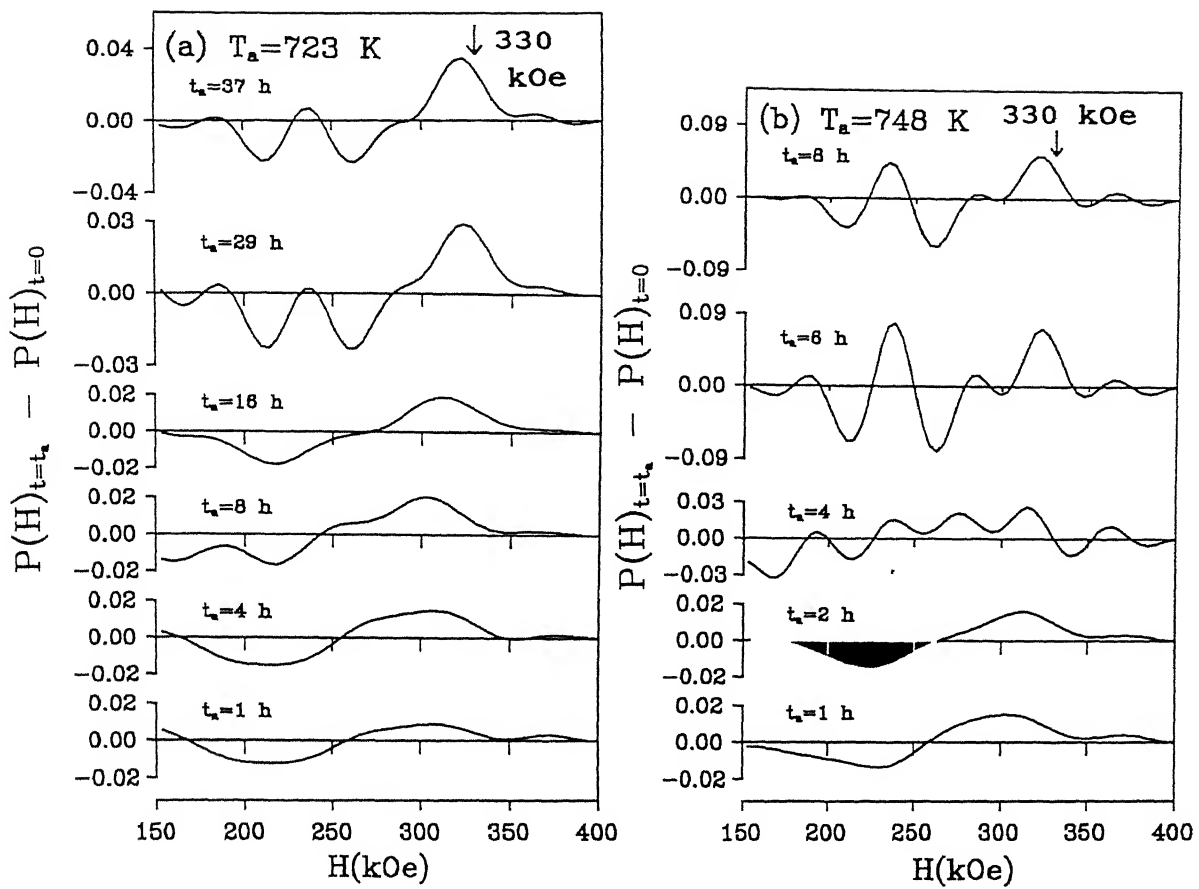


Fig. 6.17. (a) Dependence of  $\langle H \rangle$  for the  $Fe_{78}B_{13}Si_9$  metallic glasses on annealing time period ( $t_a$ ) at (i)  $T_a = 573$  K (○); (ii)  $T_a = 623$  K ( $\Delta$ ); (iii)  $T_a = 673$  K (■) and (iv)  $T_a = 723$  K (●); (b) Dependence of  $\langle H \rangle$  for the  $Fe_{78}B_{13}Si_9$  metallic glasses on annealing time period ( $t_a$ ) at (i)  $T_a = 723$  K (○) and (ii)  $T_a = 748$  K (●).



**Fig. 6.18.** Difference in  $P(H)$  for  $\text{Fe}_{78}\text{B}_{13}\text{Si}_9$  between  $t = t_a$  (after annealing) and  $t = 0$  (before annealing) at (a)  $T_a = 723 \text{ K}$  and (b)  $T_a = 748 \text{ K}$ .

#### 6.4. Conclusions

The Mössbauer spectra of samples of  $\text{Fe}_{79}\text{B}_{16}\text{Si}_5$  and  $\text{Fe}_{78}\text{B}_{13}\text{Si}_9$  in the as-prepared form and after isothermally annealing them at 573, 623, 673, 723 and 748 K for different time periods have been analyzed by Window's method to obtain the hyperfine field distributions  $P(H)$ . The results for these distributions are analyzed in the light of earlier phase precipitation studies of these metallic glasses involving X-ray diffraction and the determination of Mössbauer parameters using the least squares-fitting. It is observed that evolution of the  $P(H)$  distributions in these metallic glasses follow their kinetics of crystallization. The onset of crystallization changes the shape of the  $P(H)$  distributions. The maximum temperature ( $T_a = 748\text{K}$ ) used in the present annealing was less than the respective crystallization temperature and hence the crystallization process was incomplete. Nevertheless the  $P(H)$  curves showed four dominant peaks at  $T_a = 748\text{ K}$  which appear composite. It was not possible to decompose them any further. Keeping this in mind, these four peaks were assigned to the phases precipitated with the help of the assignments arrived earlier with the help of X-ray diffraction and Mössbauer parameters. The analysis of the different curves,  $[P(H)_{t=t_a} - P(H)_{t=0}]$  has supported the transformation of the metastable  $\text{Fe}_3\text{B}$  into stable  $\text{Fe}_2\text{B}$  and  $\alpha\text{-Fe}$  during the crystallization process. The present study thus gives an interesting picture of how the hyperfine field distributions in a

Fe-B-Si metallic glass change with annealing time, keeping the annealing temperature constant but below the crystallization temperature.

References

- [1] Amorphous Magnetism, edited by H.O.Hooper and A.M.de Graff, (Plenum Press, New York, 1973).
- [2] Amorphous Magnetism II, edited by R.A.Levy and R.Hasegawa, (Plenum Press, New York, 1977).
- [3] Rapidly Quenched Metals III, edited by B.Cantor (The Metals Society, London, 1978), Vols. 1 and 2.
- [4] Proceedings of the Conference on Metallic Glasses: Science and Technology, edited by C.Hargitai, I.Bakonyi and T.Kemeny (Kultura, Budapest, 1981).
- [5] Glassy Metals: Magnetic, Chemical and Structural Properties, edited by R.Hasegawa (C.R.C.Press, Florida, 1983).
- [6] Amorphous Metallic Alloys, edited by F.E.Luborsky (Butterworth, London, 1983).
- [7] Metallic Glasses: Production, Properties and Applications, edited by T.R.Anantharaman (Trans Tech, Aedermannsdorf, 1984).
- [8] A.K.Bhatnagar, Hyperfine Interactions, 24-26, 637 (1985).
- [9] C.L.Chien, Phys. Rev. B 18, 1003 (1978).
- [10] P.Duwez, R.H.Willens and W.Klement, J.Appl.Phys. 31, 1136 (1960).
- [11] W.Klement, R.H.Willens and P.Duwez, Nature, 187, 869 (1960).
- [12] A.H.Davies in Ref. [6], Chapter 2.
- [13] T.Kemeny, I.Vincze, B.Fogarassy and S.Arajs, Phys. Rev. B 20 476 (1979).
- [14] A.S.Schaafsma, H.Snijders, F.van der Woude, J.Drijver and S.Radelaar, Phys. Rev. B 20, 4423 (1979).

- [15] M.W.Ruckman, R.A.Levy, A.Kessler and R.Hasegawa, J.Non-Cryst. Solids, 40, 393 (1080).
  - [16] T.Kemeny, I.Vincze, H.A.Davies, I.W.Donald and A.Lovas, Central Research Institute for Physics, Budapest, Hungary, Report No. KFKI - 1980 - 103 (Unpublished).
  - [17] H.N.Ok and A.H.Morrish, Phys. Rev. B 22, 4215 (1980); H.N.Ok and A.H.Morrish, J.Phys. F11, 495 (1981); H.N.Ok, K.S.Baek and C.S.Kim, Phys. Rev. B 24, 6600 (1981).
  - [18] J.M.Dubois, M.Bastick, G.La Caer and C.Tete, Rev. Phys. Appl. 15, 1103 (1980).
  - [19] I.W.Donald, T.Kemeny and H.A.Davies, J.Phys. F11, L31 (1981).
  - [20] A.K.Bhatnagar and N.Ravi, J.Non-Cryst. Solids, 56, 237 (1983).
  - [21] A.K.Bhatnagar and N.Ravi, Phys. Rev. B 28, 359 (1983).
  - [22] T.Nagarajan, U.Chidambaram Asari, S.Srinivasan, V.Sridharan and A.Narayanasamy, Mater. Sci. Engg. 97, 355 (1988).
  - [23] R.Singhal, U.C.Johri and R.M.Singru, J.Mater. Sci. 28, 975 (1993); see also R.Singhal, Ph.D. Thesis, Indian Institute of Technology, Kanpur, India (1993), Unpublished.
  - [24] N.Banerjee, U.C.Johri, V.N.Kulkarni and R.M.Singru, J.Mater. Sci. 30, 417 (1995); see also N.Banerjee, Ph.D. Thesis, Indian Institute of Technology, Kanpur, India (1995), Unpublished.
  - [25] B.Window, J.Phys. E: Sci. Instrum. 4, 401 (1971).
  - [26] T.E.Sharon and C.C.Tsuei, Solid State Commun. 9, 1923 (1971); T.E.Sharon and C.C.Tsuei, Phys. Rev. B 5, 1047 (1971).

(1972).

- [27] J.Hesse and A.Rübartsch, J.Phys., E: Sci. Instrum. 7, 526 (1974).
- [28] C.L.Chien, J. Hyperfine Interactions, 4, 869 (1974).
- [29] C.L.Chien, D.Musser, F.E.Luborsky and J.L.Walter, J.Phys. F: Metal Phys. 8, 2407 (1978).
- [30] Boliang Yu, J.M.D.Coey, M.Oliver and J.O.Ström-Olsen, J.Appl.Phys. 55, 1748 (1984).
- [31] K.Ganesan, A.Narayanasamy, G.Konczos and T.Nagarajan, J. Magn. Magn. Mat. 116, 189 (1992).
- [32] K.Ganesan, A.Narayanasamy and T.Nagarajan, J.Phys. Condens. Matter, 2, 4227 (1990).
- [33] M.Koshimura and M.Takahashi, Proc. Int. Conf. Rapidly Quenched Metals (Sendai, 1981).
- [34] M.Koshimura, A.Abe, M.Takahashi, S.Inawashiro and S.Katsura, Proc. Int. Conf. Rapidly Quenched Metals (Sendai, 1981).
- [35] M.Takahashi, S.Ishio and T.Miyazaki, Sci. Rep. Tohoku Univ. 28A, 299 (1980).
- [36] M.Taniwaki and M.Maeda, Mater. Sci. Eng. 99, 47 (1988).
- [37] U.Gonser, M.Ghafari, M.Ackermann, H.P.Klein, J.Baur and H.G.Wagner in "Proceedings of the 4th International Conference on Rapidly Quenched Metala", edited by T.Masumoto and K.Suzuki (Japan Institute of Metals, Sendai, 1982), p.639.
- [38] L.Haggstrom, L.Granas, R.Wappling and S.Devanarayanan, Phys. Scripta, 7, 125 (1973).

## CHAPTER 7

### Study of the roasting of chalcopyrite minerals by Mössbauer spectroscopy

#### 7.1. Introduction

It is well known that  $^{57}\text{Fe}$  Mössbauer spectroscopy is a very sensitive and useful technique available for identifying and determining the relative amounts of different iron compounds present in complex materials [1]. In particular,  $^{57}\text{Fe}$  Mössbauer spectroscopy has been applied for the analysis of iron-bearing mineral ores both in their as-found state and after thermal and chemical beneficiation process [2-4]. One useful application of such studies involves the monitoring of the kinetics of ore dressing of minerals so that the degree and nature of conversion from one iron compound to another can be ascertained at each stage of ore dressing. In an earlier study [5] of kinetics of the roasting process of pyrite minerals, carried out in our laboratory the  $^{57}\text{Fe}$  Mössbauer spectra and X-ray diffraction of pyrite minerals roasted at  $(610 \pm 5)^\circ\text{C}$  for time periods  $t = 0.0, 0.5, 1.0, 2.0, 5.0, 15.0, 30.0$  and  $60.0$  mins. were observed and these studies provided valuable understanding of the kinetics of roasting and indicated an optimum time period ( $t$ ) for an efficient transformation of pyrite into the magnetic oxides  $\alpha\text{-Fe}_2\text{O}_3$  and  $\gamma\text{-Fe}_2\text{O}_3$ . In the present study we have investigated the kinetics of roasting of the copper bearing mineral, chalcopyrite, at  $(500 \pm 5)^\circ\text{C}$  and  $(650 \pm 5)^\circ\text{C}$  for different time periods using the

techniques of  $^{57}\text{Fe}$  Mössbauer spectroscopy and X-ray diffraction.

Among the copper-bearing minerals chalcopyrite is one of the most abundant forms and it contains copper, iron and sulfur in almost equal parts. The name 'chalcopyrite' comes from the greek word for copper "chalkos" and stands for copper-containing pyrite and has the chemical formula  $\text{CuFeS}_2$ . Extraction of copper from chalcopyrite involves two stages [6]: i) smelting and ii) refining. In the first operation (i.e. smelting) crude copper is separated while the second operation involves refining the copper to a pure metal ( $> 99.9\%$ ) Cu. The initial stages involved in the smelting operation consists of crushing and grinding the mineral ores followed by floatation and partial oxidation.

The process involved during the partial oxidation carries out a roasting of the concentrate mineral ore under strictly controlled temperature range and limited flow of air with an aim of eliminating some of the sulfur. In the stages subsequent to partial oxidation the roasted material is heated in a reverberatory furnace at much higher ( $\sim 1200^\circ\text{C}$ ) temperatures [6]. In view of this, study of roasting (at  $T < 650^\circ\text{C}$ ) of chalcopyrite can lead to new and better methods for extracting copper. Another important aspect of these studies is to develop a copper-extraction process which can emit least amount of air pollutants and water-pollutants. It is, therefore, important to study the kinetics of the roasting process of chalcopyrite minerals by identifying different compounds formed during the roasting.

As pointed out  $^{57}\text{Fe}$  Mössbauer spectroscopy is an important technique for identifying different iron compounds using Mössbauer

parameters such as isomer shift, quadrupole splitting and internal magnetic field. A number of studies of structural and electronic properties of chalcopyrite have been performed using Mössbauer spectroscopic technique [7-10].

In the present work we report the results of our studies of the kinetics of the roasting of chalcopyrite samples roasted at two temperatures for different intervals of time. Mössbauer spectra have been measured at room temperature for chalcopyrite samples roasted at  $(500 \pm 5)^\circ\text{C}$  for time intervals  $t = 1.0, 2.0, 3.0, 5.0, 10.0, 15.0, 20.0, 40.0$  and 60.0 mins. and at  $(650 \pm 5)^\circ\text{C}$  for time intervals  $t = 1.0, 2.5, 3.0, 5.0$  and 10.0 mins. The choice of these temperatures was made on the basis of the existing data on chalcopyrite [6]. The analysis of the measured spectra was carried out to identify the particular iron compound formed by using Mössbauer parameters. In addition X-ray diffraction spectra were measured for the samples to further identify the compounds.

## 7.2. Experiment

The samples of chalcopyrite were obtained from Hindusthan Copper Ltd., Mosabani mines (near Ghatsila, Bihar State, India). Powdered samples were taken and roasted in a small porcelain boat in a controlled air stream at  $(500 \pm 5)^\circ\text{C}$  for  $t = 1.0, 2.0, 5.0, 10.0, 15.0, 20.0, 40.0$  and 60.0 and at  $(650 \pm 5)^\circ\text{C}$  for  $t = 1.0, 2.5, 3.0, 5.0$  and 10.0 mins. After the roasting the sample material was quickly poured and quenched on alumina held at room temperature. After cooling the sample material of about 50 mg was spread uniformly between two thin layers of cello tape to form absorbers for Mössbauer studies.

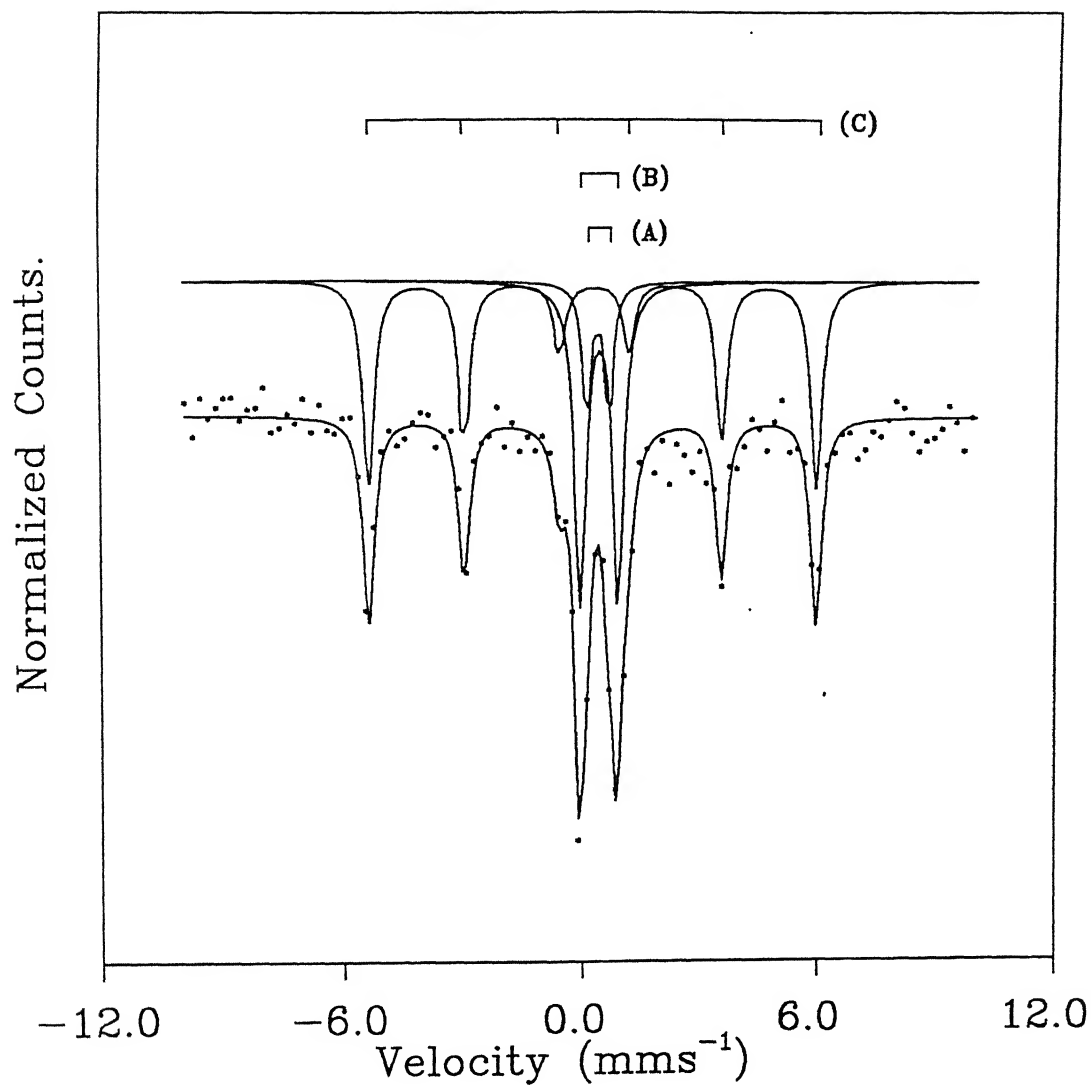


Fig. 7.1. Room temperature Mössbauer spectrum of the chalcopyrite mineral in the as received form.

150

Table 7.1. Roasting of chalcopyrite at  $(500 \pm 5)^\circ\text{C}$  for different time intervals. Values of Mössbauer parameters and assignments<sup>†</sup> of different compounds.

| Time of roasting (mins) | IS ( $\text{mms}^{-1}$ ) (a) | $\Delta E$ ( $\text{mms}^{-1}$ ) (b) | H (kOe) (c) | Assignment                       | Relative Intensity (%) | References |
|-------------------------|------------------------------|--------------------------------------|-------------|----------------------------------|------------------------|------------|
| 0.0                     | 0.31                         | 0.58                                 | —           | Pyrite                           | 18                     | 4          |
|                         | 0.37                         | 1.10                                 | —           | See Text                         | 31                     | 14         |
|                         | 0.24                         | 0.00                                 | 352         | Chalcopyrite                     | 51                     | 7          |
| 1.0                     | 0.48                         | —                                    | —           | $\text{Fe}_2(\text{SO}_4)_3$     | v.weak                 | 4,11       |
|                         | 0.32                         | 0.59                                 | —           | Pyrite                           | 15                     | 4          |
|                         | 0.38                         | 1.10                                 | —           | See Text                         | 30                     | 14         |
|                         | 1.25                         | 2.88                                 | —           | $\text{FeSO}_4$                  | 7                      | 4,12       |
|                         | 0.24                         | 0.00                                 | 352         | Chalcopyrite                     | 48                     | 7          |
| 2.0                     | 0.46                         | —                                    | —           | $\text{Fe}_2(\text{SO}_4)_3$     | v.weak                 | 4,11       |
|                         | 0.32                         | 0.58                                 | —           | Pyrite                           | 16                     | 4          |
|                         | 0.38                         | 1.10                                 | —           | See Text                         | 30                     | 14         |
|                         | 1.25                         | 2.88                                 | —           | $\text{FeSO}_4$                  | 7                      | 4,12       |
|                         | 0.24                         | 0.01                                 | 352         | Chalcopyrite                     | 47                     | 7          |
| 3.0                     | 0.48                         | —                                    | —           | $\text{Fe}_2(\text{SO}_4)_3$     | v.weak                 | 4,11       |
|                         | 0.32                         | 0.58                                 | —           | Pyrite                           | 15                     | 4          |
|                         | 0.40                         | 1.12                                 | —           | See Text                         | 30                     | 14         |
|                         | 1.25                         | 2.83                                 | —           | $\text{FeSO}_4$                  | 6                      | 4,12       |
|                         | 0.24                         | 0.01                                 | 352         | Chalcopyrite                     | 49                     | 7          |
| 5.0                     | 0.47                         | —                                    | —           | $\text{Fe}_2(\text{SO}_4)_3$     | 5                      | 4,11       |
|                         | 0.33                         | 0.60                                 | —           | Pyrite                           | 27                     | 4          |
|                         | 0.40                         | 1.10                                 | —           | See Text                         | 13                     | 14         |
|                         | 1.23                         | 2.92                                 | —           | $\text{FeSO}_4$                  | 30                     | 4,12       |
|                         | 0.30                         | 0.00                                 | 355         | Chalcopyrite                     | 14                     | 7          |
|                         | 0.32                         | 0.12                                 | 513         | $\alpha - \text{Fe}_2\text{O}_3$ | 11                     | 13         |
| 10.0                    | 0.47                         | —                                    | —           | $\text{Fe}_2(\text{SO}_4)_3$     | 6                      | 4,11       |
|                         | 0.33                         | 0.62                                 | —           | Pyrite                           | 19                     | 4          |
|                         | 0.40                         | 1.10                                 | —           | See Text                         | 9                      | 14         |
|                         | 1.23                         | 2.88                                 | —           | $\text{FeSO}_4$                  | 36                     | 4,12       |
|                         | 0.30                         | 0.00                                 | 355         | Chalcopyrite                     | 11                     | 7          |
|                         | 0.32                         | 0.12                                 | 513         | $\alpha - \text{Fe}_2\text{O}_3$ | 17                     | 13         |

Continued on the next page

Table 7.1. (Continued)

| Time of roasting (mins) | IS ( $\text{mms}^{-1}$ ) (a) | $\Delta E$ ( $\text{mms}^{-1}$ ) (b) | H (kOe) (c) | Assignment                       | Relative Intensity (%) | References |
|-------------------------|------------------------------|--------------------------------------|-------------|----------------------------------|------------------------|------------|
| 15.0                    | 0.46                         | —                                    | —           | $\text{Fe}_2(\text{SO}_4)_3$     | 6                      | 4, 11      |
|                         | 0.32                         | 0.62                                 | —           | Pyrite                           | 22                     | 4          |
|                         | 0.40                         | 1.10                                 | —           | See Text                         | 15                     | 14         |
|                         | 1.22                         | 2.93                                 | —           | $\text{FeSO}_4$                  | 33                     | 4, 12      |
|                         | 0.30                         | 0.00                                 | 355         | Chalcopyrite                     | 13                     | 7          |
|                         | 0.22                         | 0.12                                 | 513         | $\alpha - \text{Fe}_2\text{O}_3$ | 11                     | 13         |
| 20.0                    | 0.46                         | —                                    | —           | $\text{Fe}_2(\text{SO}_4)_3$     | 3                      | 4, 11      |
|                         | 0.32                         | 0.62                                 | —           | Pyrite                           | 25                     | 4          |
|                         | 0.36                         | 1.10                                 | —           | See Text                         | 12                     | 14         |
|                         | 1.22                         | 2.89                                 | —           | $\text{FeSO}_4$                  | 28                     | 4, 12      |
|                         | 0.30                         | 0.00                                 | 355         | Chalcopyrite                     | 13                     | 7          |
|                         | 0.35                         | 0.12                                 | 509         | $\alpha - \text{Fe}_2\text{O}_3$ | 19                     | 13         |
| 40.0                    | 0.46                         | —                                    | —           | $\text{Fe}_2(\text{SO}_4)_3$     | 3                      | 4, 11      |
|                         | 0.32                         | 0.62                                 | —           | Pyrite                           | 16                     | 4          |
|                         | 0.37                         | 1.10                                 | —           | See Text                         | 6                      | 14         |
|                         | 1.24                         | 2.85                                 | —           | $\text{FeSO}_4$                  | 36                     | 4, 12      |
|                         | 0.32                         | 0.12                                 | 513         | $\alpha - \text{Fe}_2\text{O}_3$ | 39                     | 13         |

† The summary of Mössbauer parameters of iron-sulphur compounds as reported by Huffman and Huggins [4] has been used in some of these assignments.

- (a) Reported with respect to  $\alpha - \text{Fe}$ ; Error ( $\pm 0.02$ );  
 (b) Error ( $\pm 0.02$ ); (c) Error ( $\pm 4$  kOe).

developed in the Mössbauer spectrum of chalcopyrite as a result of mechanical grinding. In our case some grinding was carried out during the purification of chalcopyrite sample and we feel that the doublet having  $IS = 0.37 \text{ mms}^{-1}$  and  $\Delta E = 1.10 \text{ mms}^{-1}$  observed by us could be ascribed to the effect of the mechanical activation of the sample. It may be pointed out that the Mössbauer spectrum of the mineral jarosite  $MFe_3(OH)_6(SO_4)_2$  where  $M = H_3O, Na, K$ , is observed to produce a doublet having  $IS = 0.38 - 0.39 \text{ mms}^{-1}$  and  $\Delta E = 1.0 - 1.1 \text{ mms}^{-1}$  [15]. However the X-ray diffraction spectra recorded by us did not reveal the presence of jarosite in our sample. In view of this observation we have ruled out the presence of jarosite in our sample. We further point out that although different measurements of the Mössbauer spectra of natural chalcopyrite have reported a sextet, the value of the hyperfine field,  $H$ , is observed to lie in the range  $H = 320 - 356 \text{ kOe}$  depending on the sample used. Thus the values of  $H$  reported for chalcopyrite at room temperatures have been  $356 \text{ kOe}$  [7],  $356 \pm 5 \text{ kOe}$  [16] and  $325 \pm 10 \text{ kOe}$  [17]. The origin of this variation has been explained by Lipka et al. [14] in terms of the influence of the mechanical activation of the sample. It has been pointed out by Lipka et al. [14] that mechanical activation performed during the sample preparation can reduce the  $H$  - value of chalcopyrite from  $353 \text{ kOe}$  to  $302 \text{ kOe}$  depending on the activation time. In their report Raj et al. [17] do not indicate the nature and time period of mechanical activation but it is likely that lower  $H$  - value observed by them is an effect brought in by the mechanical treatment involved during the sample preparation. During our measurement we avoided any further mechanical treatment and our

results give a value of  $H = 352 \pm 5$  kOe which agrees with other results. In other words the amount (i.e. pressure and time period) of mechanical grinding involved in the purification of our chalcopyrite samples was responsible for the presence of the doublet phase but it did not cause any lowering of the  $H$ -value. It is known that chalcopyrite has a magnetically ordered structure and neutron diffraction studies [18] have shown it to be an antiferromagnetic with the  $\mu_{\text{eff}}$  for Fe equal to  $3.85 \mu_B$ . The value of  $H_1 \sim 352$  kOe suggests that in chalcopyrite magnetically ordered  $\text{Fe}^{3+}$  ions of high spin state are located at tetrahedral positions.

Returning to our analysis of our as-received sample (Fig. 7.1 and Table 7.1) we conclude that it contains chalcopyrite, pyrite and a doublet phase of chalcopyrite. Pyrite is one of the naturally occurring impurities in this mineral. The X-ray diffraction results confirm this conclusion in that we have observed peak corresponding to chalcopyrite with strong intensity and that for pyrite with weak intensity.

### 7.3.2. Samples roasted at $(500 \pm 5)^\circ\text{C}$ for different time intervals $t = 1.0, 2.0, 3.0, 5.0, 10.0, 15.0, 20.0, 40.0$ and $60.0$ mins.

Mössbauer spectra measured at room temperature for chalcopyrite samples roasted at  $(500 \pm 5)^\circ\text{C}$  for different time intervals  $t = 1.0, 2.0, 3.0, 5.0, 10.0, 15.0, 20.0, 40.0$  and  $60.0$  mins. are shown in Fig. 7.2 and the corresponding Mössbauer parameters obtained by the computer program are presented in Table 7.1. It is observed that the Mössbauer spectra for samples roasted at  $(500 \pm 5)^\circ\text{C}$  become more complicated and can be decomposed into one singlet, three doublets and one or two sextets depending on

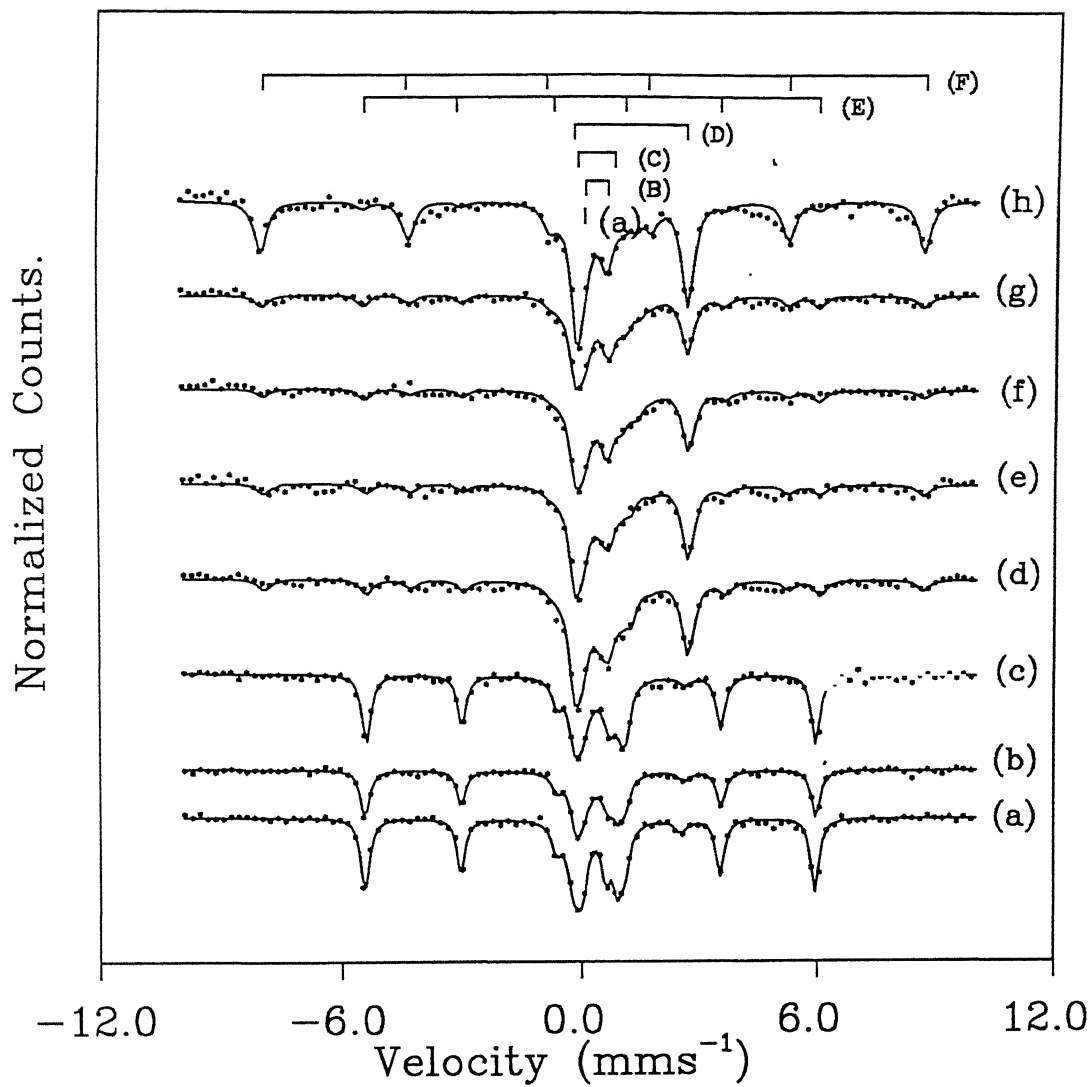
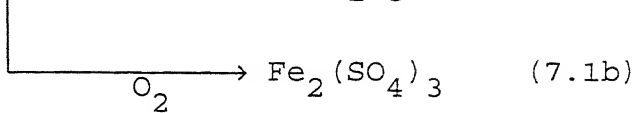
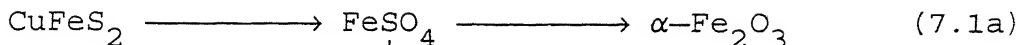


**Fig. 7.2.** Room temperature Mössbauer spectra of chalcopyrite samples roasted at  $(500 \pm 5)^\circ\text{C}$  for different time intervals  $t =$  (a) 1.0, (b) 2.0, (c) 3.0, (d) 5.0, (e) 10.0, (f) 15.0, (g) 20.0 and (h) 40.0 min. The zero of the velocity scale refers to the centre of the inner peaks of  $\alpha$ -Fe Mössbauer spectrum. The lines at the top indicate the characteristic peak positions in the Mössbauer spectra of (A)  $\text{Fe}_2(\text{SO}_4)_3$ , (B) pyrite, (C) see text, (D)  $\text{FeSO}_4$ , (E) chalcopyrite and (F)  $\alpha\text{-Fe}_2\text{O}_3$ .

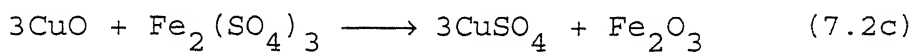
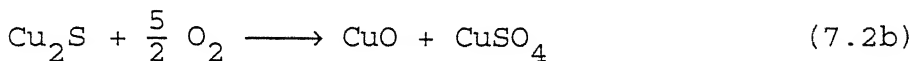
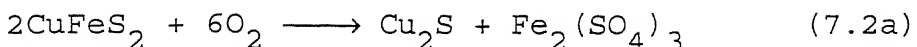
the period of roasting. It is observed that the roasting of chalcopyrite for a time period  $t = 1\text{-}3$  mins. introduces a singlet spectrum in the observed Mössbauer spectra. The identification of this singlet spectrum (as well as of other subspectra) could be made using the summary of Mössbauer parameters of iron sulphur compounds as reported by Huffman and Huggins [4] and DeBenedetti et al. [11]. Such an exercise has helped us to ascribe this singlet line to the iron compound  $\text{Fe}_2(\text{SO}_4)_3$ . Since the intensity of this singlet line is very weak for  $t = 1\text{-}3$  mins., we conclude that the compound  $\text{Fe}_2(\text{SO}_4)_3$  is formed in very small amounts when the roasting period is  $t = 1\text{-}3$  mins. Coming to the identification of the three doublets observed by us for  $t = 1\text{-}3$  mins., two doublets could be ascribed to pyrite and to the effect of grinding as already discussed for the results of the as-prepared sample. The third doublet (Table 7.1) observed by us is ascribed to the iron compound  $\text{FeSO}_4$ . Only one sextet is observed for the roasting period  $t = 1\text{-}3$  mins. and it is identified with chalcopyrite. The pattern of our observations, therefore, shows that the as-prepared sample indicates the presence of pyrite and chalcopyrite while the process of roasting for  $t = 1\text{-}3$  mins. leads to the formation of new compounds,  $\text{Fe}_2(\text{SO}_4)_3$  and  $\text{FeSO}_4$ . If the roasting period is increased beyond  $t = 3$  mins. we observe one more sextet in the Mössbauer spectrum [Table 7.1] and it is easily identified to be due to the iron compound  $\alpha\text{-Fe}_2\text{O}_3$ .

We suggest a possible mechanism to explain the formation of the different iron compounds observed by us by proposing a

reaction



It may be pointed out that Razouk [19] has proposed the following mechanism for the oxidation of chalcopyrite,



and it supports our observations.

The results shown in Table 7.1 also indicate an approximate estimate of the percentages of different phases present in each spectrum. We wish to point out that it is difficult to determine the percentages of different phases very accurately because of the statistical quality of the data and because the peak positions due to various phases overlap each other. The percentage values for the different phases shown in Table 7.1 are, therefore, crude estimates. Nevertheless these estimates and an analysis of the Mössbauer spectra and that of X-ray data have enabled us to construct the following sequence during the roasting of chalcopyrite at  $(500 \pm 5)^\circ\text{C}$ .

During the roasting of chalcopyrite at  $(500 \pm 5)^\circ\text{C}$ , the compounds  $\text{Fe}_2(\text{SO}_4)_3$  and  $\text{FeSO}_4$  appear to be formed for  $t \leq 3$  mins. The phase  $\alpha\text{-Fe}_2\text{O}_3$  appears to be formed for  $t \geq 5$  mins. The amount of chalcopyrite decreases faster after  $t = 3$  mins. and chalcopyrite appears to have been fully transformed when a roasting period of  $t = 40$  mins. is reached. These results are

supported by our X-ray powder diffraction data. During this period the amounts of  $\text{FeSO}_4$  and  $\alpha\text{-Fe}_2\text{O}_3$  grow while that of  $\text{Fe}_2(\text{SO}_4)_3$  remains almost constant for  $t = 5\text{-}40$  mins. We further note that by the time chalcopyrite is fully transformed by roasting it at  $500^\circ\text{C}$  for  $t \geq 40$  min, the only magnetic phase that is remaining is  $\alpha\text{-Fe}_2\text{O}_3$  and it can be taken out by magnetic separation.

### 7.3.3. Samples roasted at $(650 \pm 5)^\circ\text{C}$ for $t = 1.0, 2.5, 3.0, 5.0$ and $10.0$ min.

Mössbauer spectra measured at room temperature for chalcopyrite samples roasted at  $(650 \pm 5)^\circ\text{C}$  for different time intervals  $t = 1.0, 2.5, 3.0, 5.0$  and  $10.0$  mins are shown in Fig. 7.3 and the corresponding Mössbauer parameters obtained by the computer program are shown in Table 7.2. It is observed that at this higher temperature, the transformation of pyrite and chalcopyrite (observed in the as-prepared sample) does not begin until the roasting time is  $t = 2.5$  mins. The Mössbauer spectra observed in the range  $t = 2.5 - 10.0$  mins. were analyzed into subspectra, and their Mössbauer parameters were used to identify the iron compounds formed as done earlier. In the time period  $t = 2.5\text{-}5.0$  mins. the roasting process appears to lead to the formation of  $\text{FeSO}_4$  and  $\alpha\text{-Fe}_2\text{O}_3$  and if the roasting time period reaches  $10.0$  mins. the sample is completely converted to  $\alpha\text{-Fe}_2\text{O}_3$ . These results were supported by our X-ray powder diffraction data.

The above transformations observed by us suggest that the kinetics of the roasting of chalcopyrite may proceed in the

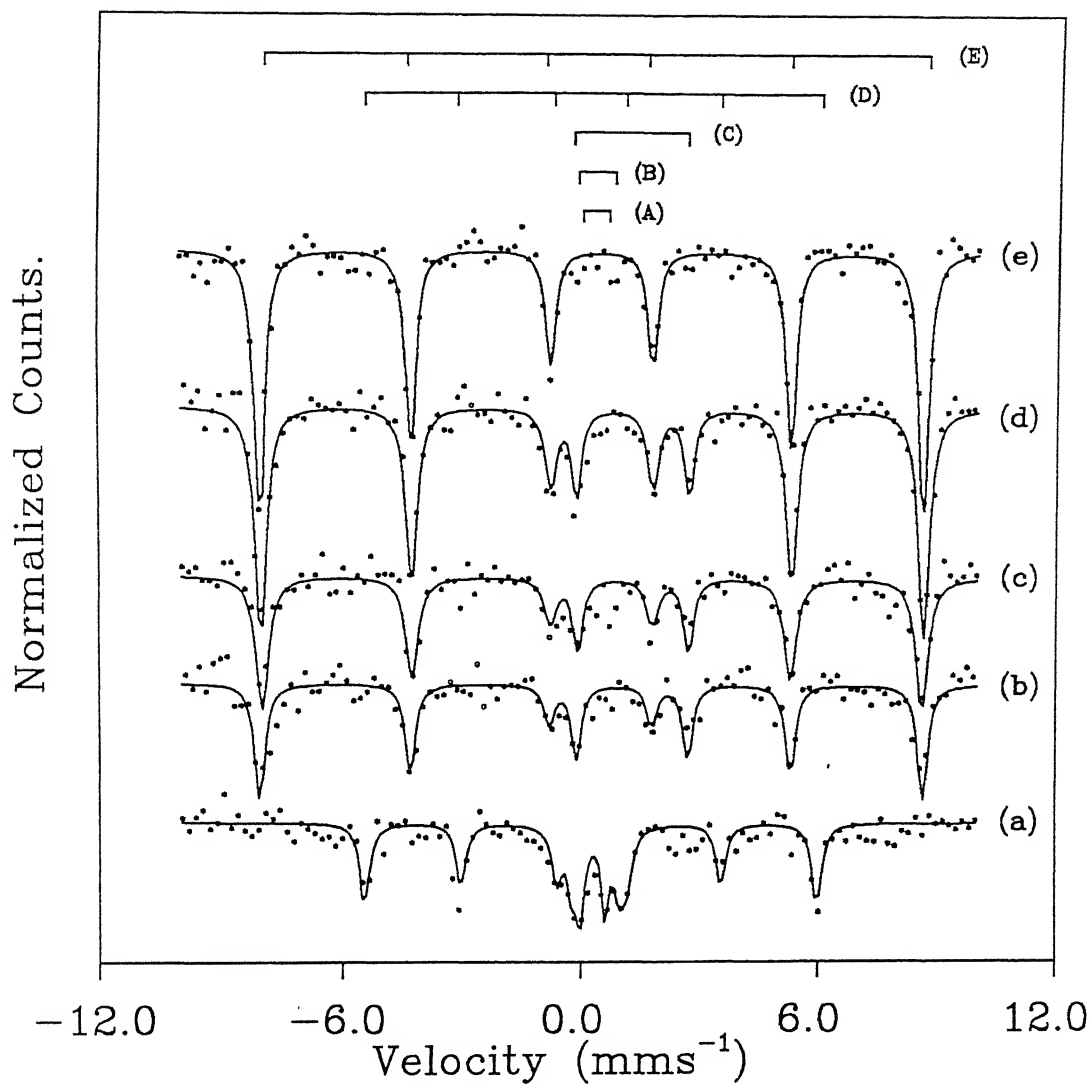


**Fig. 7.3.** Room temperature Mössbauer spectra of chalcopyrite samples roasted at  $(650 \pm 5)^\circ\text{C}$  for different time intervals  $t =$  (a) 1.0, (b) 2.5, (c) 3.0, (d) 5.0, (e) 10.0. The zero of the velocity scale to the centre of the peaks of  $\alpha\text{-Fe}$  Mössbauer spectrum. The lines at the top indicate the characteristic peak positions in the Mössbauer spectra of (A) pyrite, (B) see text, (C)  $\text{FeSO}_4$ , (D) chalcopyrite and (E)  $\alpha\text{-Fe}_2\text{O}_3$ .

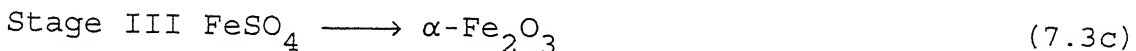
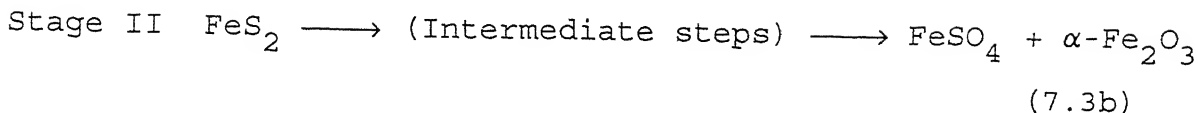
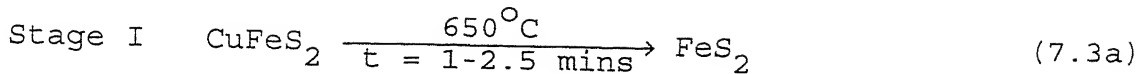
Table 7.2. Roasting of chalcopyrite at  $(650 \pm 5)^\circ\text{C}$  for different time intervals. Values of Mössbauer parameters and assignments<sup>†</sup> of different compounds.

| Time of roasting (mins) | IS ( $\text{mms}^{-1}$ ) (a) | $\Delta E$ ( $\text{mms}^{-1}$ ) (b) | H (kOe) (c) | Assignment                       | Relative Intensity (%) | References |
|-------------------------|------------------------------|--------------------------------------|-------------|----------------------------------|------------------------|------------|
| 0.0                     | 0.31                         | 0.58                                 | —           | Pyrite                           | 18                     | 4          |
|                         | 0.37                         | 1.10                                 | —           | see text                         | 31                     | 14         |
|                         | 0.24                         | 0.00                                 | 352         | Chalcopyrite                     | 51                     | 7          |
| 1.0                     | 0.30                         | 0.62                                 | —           | Pyrite                           | 19                     | 4          |
|                         | 0.37                         | 1.16                                 | —           | see text                         | 30                     | 14         |
|                         | 0.24                         | 0.00                                 | 354         | Chalcopyrite                     | 51                     | 7          |
| 2.5                     | 1.26                         | 2.84                                 | —           | $\text{FeSO}_4$                  | 23                     | 4, 12      |
|                         | 0.25                         | 0.20                                 | 516         | $\alpha - \text{Fe}_2\text{O}_3$ | 77                     | 13         |
| 3.0                     | 1.27                         | 2.83                                 | —           | $\text{FeSO}_4$                  | 18                     | 4, 12      |
|                         | 0.27                         | 0.18                                 | 513         | $\alpha - \text{Fe}_2\text{O}_3$ | 82                     | 13         |
| 5.0                     | 1.25                         | 2.88                                 | —           | $\text{FeSO}_4$                  | 13                     | 4, 12      |
|                         | 0.27                         | 0.19                                 | 514         | $\alpha - \text{Fe}_2\text{O}_3$ | 87                     | 13         |
| 10.0                    | 0.27                         | 0.19                                 | 514         | $\alpha - \text{Fe}_2\text{O}_3$ | 100                    | 13         |

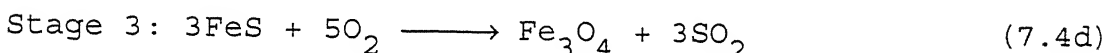
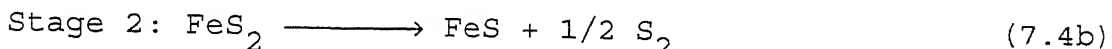
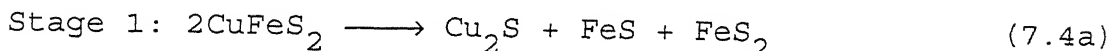
<sup>†</sup> The summary of Mössbauer parameters of iron-sulphur compounds as reported by Huffman and Huggins [4] has been used in some of these assignments.

- (a) Reported with respect to  $\alpha - \text{Fe}$ ; Error ( $\pm 0.02$ );
- (b) Error ( $\pm 0.02$ ); (c) Error ( $\pm 4$  kOe).

following stages:



The above kinetics of roasting of chalcopyrite at  $650^\circ\text{C}$  is supported by the scheme suggested by Leung [20]



The above two schemes are not identical and our observed results do not show the presence of FeS and  $\text{Fe}_3\text{O}_4$ . It is known that the iron compound FeS gives rise to a six-line Mössbauer spectrum having  $\text{IS} = 0.76 \text{ mms}^{-1}$ ,  $\Delta E = -0.07 \text{ mms}^{-1}$  and  $H = 310 \text{ kOe}$  [4] while the compound  $\text{Fe}_3\text{O}_4$  (magnetite) yields two six-line Mössbauer spectra at room temperatures having  $H = 450-463 \text{ kOe}$  (octahedral B-sites) and  $H = 491-500 \text{ kOe}$  (tetrahedral A-sites) [13]. Examination of Fig.7.3 does not reveal the presence of the subspectra which could be attributed to either FeS or  $\text{Fe}_3\text{O}_4$ . We suggest that our measurements might have missed them because the present roasting was carried out at discrete values of  $t$ . It is known [5] that the precise nature of sulphide formed is determined by the time period for which the roasting is carried out and that  $\text{FeS}_2$  and  $\text{Fe}_3\text{O}_4$  can be thermally oxidised into  $\alpha\text{-Fe}_2\text{O}_3$  [13].

Keeping all these aspects in mind we feel that the scheme (stages I-III, equations 7.3) suggested by us is tenable and it explains the results of present measurements.

#### 7.4. Conclusions

In summary we have been able to show in this work that  $^{57}\text{Fe}$  Mössbauer spectroscopy combined with X-ray diffraction method can provide useful information on the kinetics of the roasting process of chalcopyrite minerals. Iron compounds formed at different stages of roasting ( $T = 500 \pm 5^\circ\text{C}$  and  $650 \pm 5^\circ\text{C}$ , for different time periods) have been identified and a possible scheme of transformations has been suggested to explain the observed kinetics.

References

- [1] G.M.Bancroft, Mössbauer Spectroscopy, John Wiley and Sons, New York, 1973.
- [2] Industrial Applications of the Mössbauer Effect, Eds. Y.Nakamura, T.Shinjo, S.Nasu, Nuclear Instrum. & Methods, B 76, 1-417 (1993); Industrial Applications of the Mössbauer Effect, Eds. G.J.Long and J.G.Stevens, Plenum Press, New York, 1985.
- [3] Mössbauer Spectroscopy and its Chemical Applications, Eds. J.G.Stevens and G.K.Shenoy, Advances in Chemistry Series, 194, (1981).
- [4] G.P.Huffman and F.E.Huggins, Fuel, 57, 592 (1978). 5.  
A.Prasad, R.M.Singru and A.K.Biswas, Phys., Stat. Sol.(a). 87, 267 (1985).
- [6] Faith Habasi, Chalcopyrite, its Chemistry and Metallurgy, McGraw - Hill Inc., New York (1978).
- [7] N.N.Greenwood and H.J.Whitfield, J.Chem.Soc.(A). 1697, (1968).
- [8] F.Aramu, T.Bressani and P.Manca, Nuovo Cimento, L1B, 370 (1967).
- [9] D.Raj and S.P.Puri, Nuovo Cimento, LXB, 261 (1969).
- [10] Hang Nam Ok and Chul Sung Kim, Nuovo Cimento, 28B, 138 (1975).
- [11] S. DeBenedetti, G.Lang and R.Ingalls, Phys.Rev.Letters, 6, 261 (1961).
- [12] A.Vertes and B.Zsoldos, Acta Chim. Acad. Sci. Hung., 65, 261 (1970).

- [13] Sat P. Taneja and Colin H.W. Jones, Fuel, 63, 695 (1984).
- [14] Jozef Lipka, Marcel Miglierini, Josef Sitek, Peter Balaz and Klara Tkacova, Nucl. Instr. and Methods, B 76, 183 (1993).
- [15] David A. Cole, Gary W. Simmons, Richard G. Herman, Kamil Klier and Ilona Czako-Nagy, Fuel, 66, 1240 (1987).
- [16] J.Piekoszewski, J.Suwalski and S.Ligenza, Phys. Stat. Sol. 29, K99 (1968).
- [17] D.Raj, K.Chandra and S.P.Puri, J. Phys. Soc. Japan, 24, 39 (1968).
- [18] G.Donnay, L.M.Corlise, J.D.H.Donnay, N.Elliott and J.M.Hastings, Phys. Rev. 112, 1917 (1958).
- [19] R.I.Razouk, J.Appl.Chem.(London), 15, 191 (1965).
- [20] L.S.Leung, Metallurgical Transactions, 6B, 341 (1975).

A 123637

A Date Slip 132637

This book is to be returned on the  
date last stamped.

PHY-1986 D. BAN. NO. 5